LIÈGE université
STAR Institute
Sciences

LPAP
Laboratoire de Physique Atmosphérique & Planétaire

Ultraviolet auroral emissions associated with plasma injections in Jupiter's magnetosphere

Thesis submitted in partial fulfillment of the requirements for the degree of Doctor of Philosophy in the Faculty of Sciences

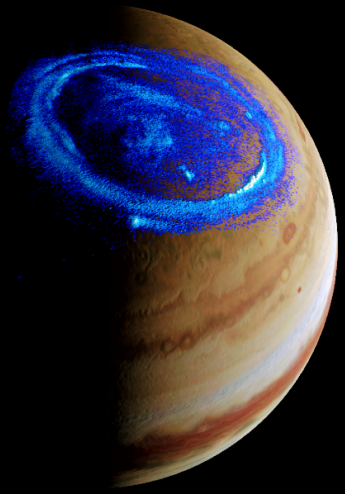

Maïté Dumont

LIÈGE université
STAR Institute
Sciences

LPAP
Laboratoire de Physique Atmosphérique & Planétaire

Ultraviolet auroral emissions associated with plasma injections in Jupiter's magnetosphere

Thesis submitted in partial fulfillment of the requirements for the degree of Doctor of Philosophy in the Faculty of Sciences

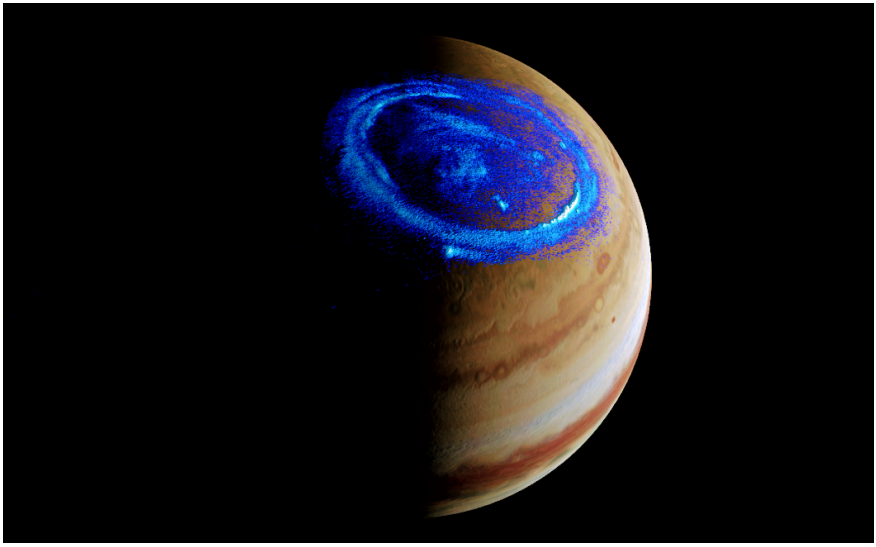

Maïté Dumont

Thesis jury members

Jury president:

Prof. Michaël De Becker

STAR institute, Université de Liège

Thesis director:

Prof. Denis Grodent

STAR institute, Université de Liège

Examinators:

Assoc. Prof. Bertrand Bonfond

STAR institute, Université de Liège

Prof. Jean-Claude Gérard

STAR institute, Université de Liège

Prof. Vincent Hue

Institut Origines, Université d'Aix-Marseille

Prof. Viviane Pierrard

Institut royal d'Aéronomie Spatiale de Belgique

Date of oral presentation: 28 september 2023

©Maïté Dumont, 2023

À la petite fille de 10 ans
qui rêvait de devenir
astrophysicienne.

"We don’t read and write poetry because it’s cute. We read and write poetry because we are members of the human race. And the human race is filled with passion. And medicine, law, business, engineering, these are noble pursuits and necessary to sustain life. But poetry, beauty, romance, love, these are what we stay alive for."

Dead poets society

"Climb the mountain not to plant your flag, but to embrace the challenge, enjoy the air, and behold the view. Climb it so you can see the world, not so the world can see you ."

David McCullough Jr.

Contents

Summary

This thesis focuses on the auroral signatures of plasma injections in Jupiter's ultraviolet emissions. We are mainly interested in low latitude auroral structures sharing the same characteristics as the particular Jovian auroral feature that Mauk et al. (2002) interpreted, for the first time, as the signature of an injection of hot plasma in the magnetosphere.

In a first study, the characteristics of ultraviolet auroral structures located in the outer emissions were studied using data from the Hubble Space Telescope. On average, one structure is observed each day, although several auroral structures are sometimes observed simultaneously over a wide range of local times. The characteristics of these structures, such as their size in the ionosphere, their position in the magnetosphere, their emitted power and their lifetime, are analysed. The positions of these auroral structures were projected in the equatorial plane along magnetic field lines, allowing their observed characteristics to be compared with those of the magnetospheric injections detected by the Galileo spacecraft. The auroral structures are present at all System III longitudes, and Io's orbit appears to be the lower limit of radial detection. In addition, a comparison was made between the magnetic flux associated with these structures and estimates of the outgoing flux linked to the radial transport of plasma in the magneto-

sphere. The magnetic flux associated with the structures could account for at least one third of this flux. This comparative study shows that the auroral structures are most probably related to magnetospheric injections.

In a second study, the motion of the auroral signatures of plasma injections, present in the Hubble Space Telescope data, was examined. The results suggest that the injected plasma moves planetward and lags behind corotation. The characteristics of the structures were then compared with simulations of auroral precipitation based on pitch angle scattering. The lifetime of the auroral structures is between a half and a full rotation of Jupiter. Ultraviolet spectrally resolved images acquired with the Hubble Space Telescope were used to highlight the energy-dependent drift of the electrons in auroral injection signatures. A comparison between the observations and the simulations suggests that the structures are around 3 hours old. Finally, the analysis was extended to larger, less structured outer emissions possibly associated with younger plasma injections. The motion and evolution of these structures are similar to those of the small and compact ones considered in the first part of this second study.

Finally, the last study is based on data collected by Juno-UVS during the first 18 perijoves. The relation between the ultraviolet auroral structures and the auroral signatures of plasma injections was established on the basis of the shift between the brightness peak and the colour ratio peak present in these structures. This shift was automatically detected in the outer emissions. A statistical analysis of their position, in the ionosphere and in the equatorial plane, was carried out. These auroral structures appear in each perijove. The detection rate of the young structures appears to be correlated to the magnetic field strength. On the other hand, such a behavior is not consistent with expectation from pitch angle scattering, the efficiency

of which is inversely proportional to the magnetic field strength. We therefore suggest that these detections are more compatible with the acceleration process due to Alfvén waves, a process that is more effective when the field is stronger in the acceleration zone. In the magnetosphere, the structures are observed at all System III equatorial longitudes, which is in agreement with previous studies obtained with the Galileo spacecraft and the Hubble Space Telescope. Looking at the positions in local time, mature structures are present at all local times. On the other hand, young structures are more present on the dawn region, suggesting that some of the structures are associated with dawn storms. This observation led us to propose two possible processes to explain the injection phenomenon, the first associated with the dawn storm phenomenon, the second with a local-time-homogeneous plasma interchange process. Finally, structures were detected up to 30 R_J, with a detection peak for young structures found at a greater radial distance ($\sim$12 R_J) than the one of more mature structures (9 R_J); this behaviour probably reflects the inward radial motion of the injected plasma in the equatorial plane

These three studies thus shed light on the magnetospheric and ionospheric processes that may be involved in plasma injections and their auroral signatures in Jupiter's magnetosphere.

Résumé

Cette thèse se concentre sur les signatures aurorales d'injections de plasma dans les émissions ultraviolettes de Jupiter. Nous nous intéressons principalement aux structures aurorales à basse latitude partageant les mêmes caractéristiques que la signature aurorale jovienne que Mauk et al. (2002) ont interprétée, pour la première fois, comme la signature d'une injection de plasma chaud dans la magnétosphère.

Dans une première étude, les caractéristiques des structures aurorales ultraviolettes situées à l'extérieure de l'émission principale ont été étudiées grâce à des données du Télescope Spatial Hubble. En moyenne, une structure est observée chaque jour, cependant il arrive que plusieurs structures aurorales soient observées simultanément sur une large gamme de temps locaux. Les propriétés de ces structures, telles que leur taille dans l'ionosphère, leur position dans la magnétosphère, leur puissance émise et leur durée de vie ont été analysées. Les positions de ces structures aurorales ont été projetées dans le plan équatorial le long des lignes de champ magnétique, ce qui a permis de comparer leurs propriétés observées avec celles des injections magnétosphériques détectées par la sonde Galileo. Les structures aurorales étudiées sont présentes à toutes les longitudes Système III et l'orbite d'Io semble être la limite inférieure de détection radiale. De plus, une com-

paraison entre le flux magnétique associé à ces structures dans l'aurore et les estimations du flux sortant lié au transport radial du plasma dans la magnétosphère a été réalisée. Le flux magnétique associé aux structures pourrait représenter au moins un tier du flux sortant. Cette étude comparative montre que les structures aurorales étudiées sont très probablement liées à des injections magnétosphériques.

Dans une deuxième étude, les mouvement des signatures aurorales des injections de plasma présentes dans les données du Télescope Spatial Hubble ont été examinés. Les résultats obtenus suggèrent que le plasma injecté se déplace vers la planète et présente un retard par rapport à la corotation. Ensuite les caractéristiques des structures ont été comparées avec des simulations de précipitations aurorales liées à la diffusion en angles d'attaque. La durée de vie des structures aurorales se situe entre une demi-rotation et une rotation complète de Jupiter. Des images spectralement résolues dans l'ultraviolet, acquises avec le Télescope Spatial Hubble, ont été utilisées pour mettre en évidence la dérive des particules en fonction de leur énergie dans ces structures. La comparaison entre les observations et les simulations suggère que les structures étudiées sont âgées d'environ 3 heures. Enfin, l'analyse a été étendue aux émissions extérieures plus grandes et moins structurées, qui pourraient être associées à des injections de plasma plus récentes. Le mouvement et l'évolution de ces structures sont similaires à ceux des émissions compactes et de petite taille étudiées dans la première partie de cette deuxième étude.

Enfin la dernière étude est basée sur les données recueillies par Juno-UVS au cours des 18 premiers périjoves. Le lien entre les structures aurorales ultraviolettes et les signatures aurorales d'injections de plasma a été établi en se basant sur le décalage entre le pic de brillance et le pic de rapport

de couleur présents dans ces structures. Ce décalage a été détecté de façon automatique dans les émissions externes. Une analyse statistique de leur position, dans l'ionosphère et dans le plan équatorial, a été réalisée. Ces structures aurorales apparaissent dans chaque périjove. Le taux de détection des jeunes structures semble être corrélé à l'intensité du champ magnétique. D'autre part, ce comportement n'est pas cohérent avec les attentes de la diffusion en angles d'attaque, dont l'efficacité est inversement proportionnelle à l'intensité du champ magnétique. Nous suggérons donc que ces détections sont plus compatibles avec le processus d'accélération dû aux ondes d'Alfvén, un processus qui est plus efficace lorsque le champ est plus fort dans la zone d'accélération. Dans la magnétosphère, les structures étudiées sont observées à toutes les longitudes équatoriales Système III, ce qui est en accord avec les études précédentes obtenues avec la sonde Galileo et le Télescope Spatial Hubble. En examinant les positions en temps local, les structures matures sont présentes à tous les temps locaux. Par contre, les jeunes structures sont davantage présentes du côté de l'aube, ce qui suggère qu'une partie des structures semble associée aux "dawn storms". Cette observation nous a conduit à proposer deux processus possibles pour expliquer le phénomène d'injection, le premier associé au phénomène de "dawn storm", le second associé à un processus d'échange de plasma homogène en temps local. Enfin, des structures ont été détectées jusqu'à 30 R_J, les structures jeunes présentent un pic de détection ($\sim$12 R_J) à une plus grande distance radiale que le pic de détection pour les structures matures (9 R_J); ce comportement reflète probablement le mouvement radial vers l'intérieur du plasma injecté dans le plan équatorial.

Ces trois études mettent ainsi en lumière les processus magnétosphériques et ionosphériques pouvant être impliqués dans les injections de plasma et leurs signatures aurorales dans la magnétosphère de Jupiter.

1 Jupiter and its auroral emissions

This introductory chapter briefly reviews our current knowledge of the Jovian system, the structure and dynamics of the Jovian magnetosphere as well as the auroral emissions, more specifically the ultraviolet (UV) emissions.

1.1 The planet Jupiter

The fifth planet from the Sun, Jupiter was born 4.5 billion years ago from the solar nebula that gave rise to our planetary system. Known to astronomers since antiquity, Jupiter is a gas giant planet (like Saturn), which implies a hydrogen-helium planet (more than 87 % of the total mass (Guillot et al. 2004))[1] and no solid surface, unlike the telluric planets (i.e. Mercury, Venus, Earth and Mars). By convention, the surface of Jupiter is defined where the pressure reaches 1 bar, roughly corresponding to the visible ammonia clouds top. Jupiter orbits the Sun at a mean distance of 778 million km (~ 5.2 Astronomical Unit (AU), 1 AU is the average Earth-Sun distance : 1 AU = 149,597,870.7 km (https://www.iau.org/) and its sidereal

[1] Other chemical compounds are also present in small quantities : methane, ammonia, hydrogen sulfide, water, etc. (Atreya et al. 2003).

orbit period is 11.862 years.

As an emblematic feature of this planet, Jupiter shelters a storm that has been raging for more than 400 years: the Great Red Spot. The Great Red Spot is a huge and swirling cloud ensemble with wind speeds of up to 640 km/h (Figure 1.1). Jupiter's atmosphere consists mainly of hydrogen and helium. The outermost clouds are most likely made of ammonia ice, the middle layer is probably made of ammonium hydrosulphide crystals, and finally the innermost layer is probably made of water ice and water vapour (https://solarsystem.nasa.gov/). It is a striped canvas with many storms moving across the giant planet, their colours varying in shades of white, yellow, brown and red, all due to the composition of each zone.

In the solar system, Jupiter is the record holder, to mention only the most outstanding. First of all, it is the largest planet in the solar system with an equatorial radius of 71,492 km ± 4 km (https://lasp.colorado.edu/), which by definition corresponds to 1 Jovian radius (R_J). Its equatorial radius is almost 11 times that of the Earth. Second, Jupiter has the fastest rotation of all the planets in the solar system. It has a spin period of 9h 55m 29.711s = 9.92492 hours (or angular velocity of 1.76×10^{-4} rad/s = 870.536°/day), which results in a large equatorial bulge (its polar radius, which is smaller than its equatorial radius, is 66,854 km). Third, it is the most massive planet in the solar system with a mass (1.8982 10^{27} kg) being more than twice the combined mass of all the other planets in the solar system combined. Fourth, Jupiter has the largest lunar ensemble for a planet in the solar system. As of 22 February 2023, Jupiter has 95 moons with confirmed orbits (https://ssd.jpl.nasa.gov/, https://www.minorplanetcenter.net/). The four largest moons were discovered by Galileo in 1610 and are commonly known as the Galilean satellites. Io (the most volcanically active object in

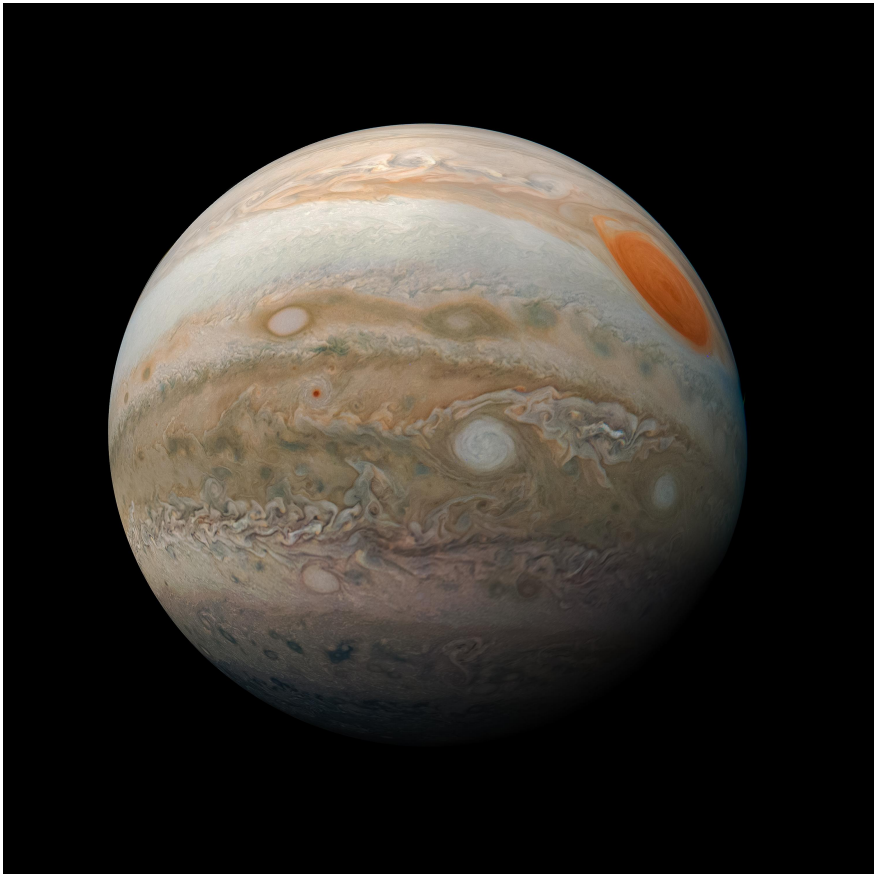

Figure 1.1 – Jupiter and its great red spot and turbulent southern hemisphere were captured by NASA's Juno spacecraft. Credits: Kevin M. Gill/NASA/JPL-Caltech.

the solar system), Europa, Ganymede (the largest moon in the solar system, larger than the planet Mercury) and Callisto. The last three may contain oceans of liquid water beneath their icy crusts. Jupiter possesses a large collection of moons thanks to the planet's massive size and gravitational pull, which is the strongest of any planet in the Solar System. Finally, Jupiter is unique, not only because of its size, fast rotation, mass or number of satellites, but also because it has the strongest intrinsic planetary magnetic field in the solar system with a surface magnetic flux density ranging from 2 Gauss[2], near the equator, to 20 Gauss, near the north pole (Connerney et al. 2018). This corresponds to a magnetic moment of 2.83×10^{20} T m^3, about 20,000 times larger than that of the Earth.

1.2 First observations of aurora on Jupiter

Jupiter is a remarkable planet for many reasons, but the one that led me to carry out this thesis is that Jupiter exhibits very intense, incessant auroral emissions. More specifically, its emitted UV auroral power is about 10^{12} W, which is 100 times more intense than on Earth (Grodent 2015).

For more than 40 years, planetary astronomers have been studying Jupiter's aurorae. Actually, the first observation of Jupiter's UV aurorae was made in 1979 by the Voyager 1 spacecraft (Broadfoot et al. 1979). This spacecraft was launched by NASA in September 1977 to explore the outer solar system and interstellar space beyond the Sun's heliosphere. During its flyby of Jupiter, Voyager 1 highlighted a thin ring of light on Jupiter's nightside that looked like an stretched-out version of the aurorae on Earth, and the auroral

[2] 1 Gauss = 10^{-4} Tesla $\Leftrightarrow$ 1G = $10^{-4}T$

emissions of H_2 and H were clearly identified (Broadfoot et al. 1979).

In the spring of the same year, the first fully imaging X-ray telescope was launched by NASA: the Einstein X-Ray Observatory. It detected the first X-ray emissions from Jupiter's aurorae (Metzger et al. 1983). X-ray observations revealed auroral bands and curtains larger than the Earth itself. From the late 1980s, infrared (IR) auroral emissions were identified by Earth-based telescopes (at Mauna Kea, Hawaii): the NASA Infrared Telescope Facility and the Canada-France-Hawaii Observatory. These auroral emissions were associated with CH_4, C_2H_2 and H_3^+ (Caldwell et al. 1988, Kostiuk et al. 1993, Drossart et al. 1989).

It was not until the 1990s that new observations of Jupiter's UV aurorae were obtained (Dols et al. 1992). These observations were made by the Hubble Space Telescope (HST). Over the past three decades, the study of these aurorae observed by HST became one of the fields of expertise of the Laboratory for Planetary and Atmospheric Physics (LPAP) at the University of Liège, where I carried out this thesis. During my research, I focused on the auroral emissions of Jupiter in the UV range. Before going on with the explanation of the aurorae, I will briefly describe the main magnetospheric regions of Jupiter and their dynamics, and then develop the auroral processes and the morphology of the UV aurorae.

1.3 The magnetosphere of Jupiter

The study of Jupiter's plasma sources as well as the understanding of the configuration and dynamics of the Jovian magnetosphere are essential to the understanding of the plasma injection phenomenon, which is at the

heart of this thesis.

Jupiter's magnetosphere has been studied for more than 40 years and has been visited by 9 spacecrafts (https://solarsystem.nasa.gov/). Seven spacecraft have flown over the planet and two orbited it for several years. Pioneer 10 (1973) and Pioneer 11 (1974) revealed the extent of Jupiter's magnetosphere and measured energetic ions and electrons in situ; Voyager 1 (1979) revealed Io's amazing volcanic activity; subsequent crossings of Jupiter's magnetosphere by Voyager 2 (1980), Ulysses (1992), Cassini (2000) and New Horizons (2007) provided additional data. The first orbiter was the Galileo probe, which orbited Jupiter 33 times between 1995 and 2003, mapping the structures of the equatorial magnetosphere and observing their temporal variability. The latest is Juno, which was inserted into polar orbit around Jupiter in 2016, and is still providing unprecedented auroral data that I am using in this thesis (Chapter 8). In the near future, the next probes will be Europa-Clipper and the JUICE spacecrafts, the latter was successfully launched on 14 April 2023 and is set to be inserted in orbit around Jupiter in July 2031. Measurements/observations from these missions, as well as from ground-based and Earth-orbiting telescopes, have been used to derive internal magnetic field models (e.g. Hess et al. 2011, Connerney et al. 2022) and current disk models (e.g. Pensionerov et al. 2019, Connerney et al. 2020).

Before describing Jupiter's magnetosphere, it is important to recall that the planets of our Solar System do not orbit in a vacuum, but are immersed in the interplanetary medium traversed by the solar wind, which constantly escapes from the Sun's corona. The solar wind consists of a supersonic, low density plasma, mainly composed of protons and electrons, with traces of helium and heavier ions. The solar wind plasma carries the solar mag-

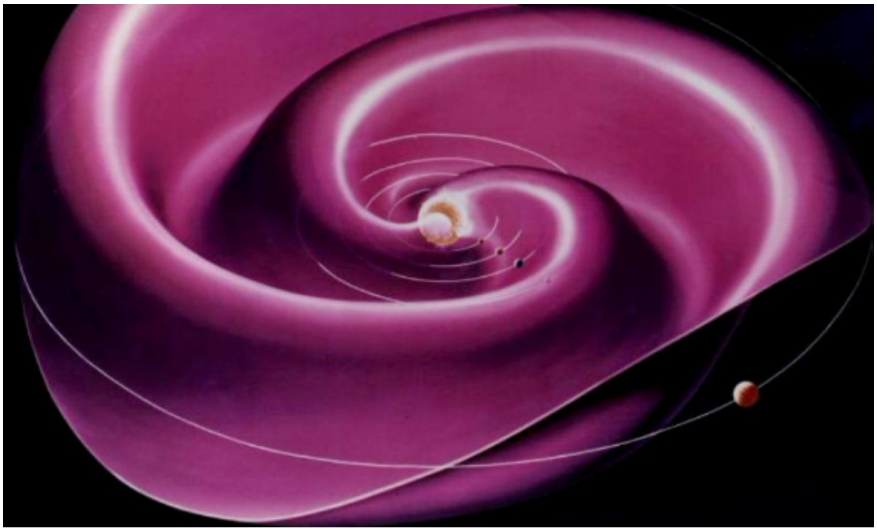

Figure 1.2 – Artist's rendering of the configuration of the current sheet of the heliosphere interplanetary space. Mercury, Venus, Earth, Mars and Jupiter (far right) are visible. Credit: Werner Heil, NASA artists, developed by Prof. John Wilcox.

netic field giving rise to the interplanetary magnetic field (IMF). Due to the rotation of the Sun, the magnetic field streamlines take a spiral shape known as the Parker spiral (as illustrated in Figure 1.2) with the synodic period of the Carrington rotation averaging to 27.2753 days (Parker 1958). The fluctuations of the solar wind will move in the IMF.

The planetary magnetic field acts as an obstacle to the solar wind flow. In a very general approach, the magnetosphere of a planet is the region surrounding it in which the forces associated with the planetary magnetic field prevail over all other forces. The magnetic field of the planet deflects the solar wind generating a boundary between the magnetosphere and the interplanetary medium dominated by the solar wind. This boundary is called magnetopause and it corresponds to a thin layer in which strong surface

currents flow to isolate the magnetospheric plasma from the IMF. The magnetosphere has a "day side" (facing the Sun) where the pressure exerted by the solar wind compresses the planetary magnetic field lines, while the "night side" has an elongated tail extending very far away from the planet because the interaction with the moving IMF stretches the magnetosphere into a very long cylindrical magnetic tail, extending more than 1000 planetary radii downstream of the planet. In addition, the dynamic solar wind pressure (SWP) can be approximated by $P_{SW} = \rho v^2$ (where ρ is the density and v is the velocity of the solar wind, which varies over time (Feldman et al. 2005)) and the density decreases as r^{-2}, where r is the distance from the Sun. The SWP varies with time, causing a modification of the size of the magnetopause. We can use a power law to relate the distances from the magnetopause (R_{MP}) to the SWP : $R_{MP} \propto P_{SW}^{-\alpha}$, in Jupiter's magnetosphere, the α parameter varies between 1/3.8 and 1/5.5 (Huddleston et al. 1998).Thus the magnetopause moves closer to the planet if SWP increases giving rise to a compressed magnetosphere, and conversely, moves away from it if the pressure exerted by the solar wind decreases leading to an expanded magnetosphere (e.g. Vogt et al. 2015). Since the velocity of the solar wind is supersonic, its collision with an obstacle, like a planetary magnetic field, forms a permanent bow shock upstream of the obstacle. Beyond this shock, the solar wind plasma is rapidly decelerated to subsonic velocities, heated and deviated to bypass the planet, while partially penetrating the magnetosphere. It heats the solar wind plasma, forces it to bypass the planet, while partially penetrating the magnetosphere. For the Earth, the cusps are the regions above the magnetic poles where the solar wind plasma has direct access to the ionosphere. In the case of Jupiter, the situation is slightly different. Zhang et al. (2021) suggest that Jupiter may not have a completely open polar cap because the rate of large-scale reconnection does not appear to be fast enough to produce it (Desroche et al.

2012, Masters 2017). In addition, Delamere and Bagenal (2010, 2013) have argued that there are very few polar field lines interconnected with the IMF.

Following the discovery of the magnetic field of Jupiter, the hypothesis of the existence of a magnetosphere has been proposed as the result of the interaction between the planetary magnetic field and the solar wind. The magnetosphere of Jupiter is characterised by the following three elements (Khurana et al. 2004):

1. Jupiter has the strongest intrinsic planetary magnetic field in the solar system, strong enough to balance the dynamic pressure exerted by the stellar wind.

2. Its principal internal plasma source populating the magnetosphere originates from the volcanism of Io.

3. Jupiter has a rotationally-driven magnetosphere and most of the energy comes from the rapid rotation of the planet.

1.3.1 Jupiter's magnetic field and magnetic field models

Jupiter's magnetic field was revealed in 1955, when a very intense radio radiation emitted by Jupiter at 22.2 MHz (λ = 13.5 m) was detected (Burke and Franklin 1955). The presence of this radiation revealed the existence of the magnetic field but also the order of magnitude of its surface intensity. The frequency peak of these radiations characterizes a maximum field of $\sim$ 14 Gauss at the surface of the planet (i.e., about 20 times the maximum value of the Earth surface filed). In 1958, a radio emission superimposed on the thermal emission of the planet was detected from observations at higher frequency (λ = 3, 4, 10.3, 21 and 68 cm). This radiation was interpreted as a synchrotron emission of extremely energetic electrons (ranging from a

few MeV to several tens of MeV) trapped in radiation belts, similar to the van Allen belts on Earth (Drake and Hvatum 1959, Field 1959). This deduction was obtained from the spatial distribution of this radiation around the planet and its wavelength range.

In situ measurements provided by the magnetometers of the Pioneer 10 (July 1973) and 11 (December 1974) and Voyager 1 (March 1979) and 2 (July 1979) probes have revealed more precise data on the magnetic field and its asymmetries. This magnetic field has, first of all, been described by a magnetic dipole with its axis tilted, towards the Jovian longitude of 201°, by around 10.8° with respect to the rotation spin axis of the planet. Moreover, the dipole center is located at about one tenth of Jovian radius from the center of the planet. This asymmetry explains the different values of the maximum magnetic flux density along the Io footpath in the last magnetic field model (JRM33, briefly described below): 20 Gauss in the north and 12 Gauss in the south (Connerney et al. 2022). Unlike the Earth, the magnetic north is located in the northern hemisphere. The first internal magnetic field model was built by adjusting the magnetic measurements from Pioneers magnetometers data (Smith et al. 1976) to the fourth degree, with only the dipolar part considered as significant and giving rise to the "D4 model" (Divine and Garrett 1983). Subsequently, other models with higher terms were proposed, based on magnetospheric and auroral data.

For a good understanding of the plasma injection phenomenon through the auroral emissions, the knowledge of the magnetic field configuration is essential. The magnetic field models enable us to relate auroral events to their location in the equatorial plane of the magnetosphere, by following magnetic field lines. During this thesis, two magnetic field models have been used: Voyager Io Pioneer Anomaly Longitude (VIPAL) (Hess et al.

2011) and Juno Reference Model through Perijove 9 (JRM09) (Connerney et al. 2018). In order to describe these models, it seems useful to tell the chronology of the evolution of internal magnetic field models, which led to the development of these two models :

- VIP4 [3] is a model of Jupiter's internal magnetic field developed in 1998 (Connerney et al. 1998). This model uses magnetic observations from four spacecrafts and the location of Io's footprints (see Section 1.4.3.3) as constraints. Subsequent observations with better resolution revealed that the locations of the satellite footprints (Io, Europa and Ganymede) predicted by this model do not correspond precisely to the observations.

- Grodent et al. (2003b) has highlighted an internal magnetic field anomaly that locally distorts the surface magnetic field, specifically in the region of the auroral kink (Figure 1.8 in Section 1.4.3) between 80° and 150° System III (SIII) in the north. In the anomaly region, the surface magnetic field is weaker and the dipole inclination is higher relative to the rotation axis. The Grodent anomaly model (GAM) is the magnetic field model proposed by Grodent et al. (2008). This model aims at increasing the agreement between the VIP4 model and the observed satellite footprints by including the previously discovered magnetic anomaly. It consists of adding to a fourth degree order spherical harmonic model a small dipole located under the surface in order to reproduce the localized magnetic anomaly. Indeed, the model shows a good agreement with the auroral footpaths of Io, Europa and Ganymede in the northern hemisphere. As the model has only been constrained by measurements in the northern hemisphere,

[3] VIP4 is the abbreviation for Voyager, Io, Pionner observations and a spherical harmonic expansion of order and degree 4

this model is only suitable for this hemisphere. In what follows, the term "anomaly" refers to this specific depletion of the magnetic field in the northern polar region.

- The VIPAL magnetic field model (Hess et al. 2011) is a fifth-degree and fifth-order spherical harmonic decomposition of the Jovian magnetic field model. This model is similar to the VIP4 internal magnetic field model, in the sense that it a multipolar development of the magnetic field constrained by Pionners and Voyagers magnetic field measurements and remote sensing measurements of the Io footprint. It however differs from VIP4 because it uses more accurate HST UV measurements and it is constrained by the actual Io footprint position (longitude + latitude) rather than its mean contour. Contrary to GAM, it did not use the footprints of Europa and Ganymede. Its higher accuracy allows for a better fit of magnetic anomaly without the addition of a low surface dipole. This model is applicable to both hemispheres. I choose the VIPAL model for the analysis of HST data because it was the most accurate internal magnetic field model at the time. It was the model that best predicted the satellite footprints, located in the zone closest to the previously established zone of the injection signatures (Mauk et al. 1999) discussed in this thesis. Even if some structures could be detected beyond the orbit of Ganymede, we kept the same magnetic field model for the sake of consistency.

- The JRM09 model based on observations of the magnetic field made by the magnetometer (MAG) on board the Juno spacecraft is a spherical harmonic model of degree 10 for the internal magnetic field (Connerney et al. 2018). It is described as a provisional model, since it is based on Juno's first nine polar orbits. However, the first fully global coverage of Jupiter's magnetic field was acquired after the first eight

orbits. This model takes hemispheric asymmetry into account, as well as anomalies such as the one at high northern latitudes, for example.

- The JRM33 model is based on data acquired by Juno spacecraft up to mid-April 2021 (i.e. up to and including PJ33). During the acquisition of these data, the equatorial crossings were separated by $\sim 11^\circ$ in longitude. The magnetic field was modelled with a spherical harmonic of degree 18. This model provides a very detailed view of a planetary dynamo (with a dynamo core radius of 0.81 Rj), the first time a model has provided such an accurate view of Jupiter's dynamo (Connerney et al. 2022). However, JRM33 was not used in my analysis of the Juno data (Chapter 8) because this model was not available yet when this analysis was performed.

1.3.2 Magnetospheric configuration, dynamics and plasma sources

In general, the Jovian magnetosphere can be divided into three distinct regions: the inner, middle and outer magnetosphere.

The inner magnetosphere is located below 10 R_J, where the magnetic field is almost dipolar. This region of the magnetosphere shelters the satellite Io (orbiting at 5.9 R_J) and its plasma torus, consisting of heavy ions and electrons, which is approximately corotating with the planet's magnetic field and is located between 5 and 8 R_J. This torus contains several million tons of cold plasma, whose energy is less than 100 eV for the core of the ion distribution. Around a ton of material is injected every second into the magnetosphere by the active volcanism of Io (mainly SO_2, as well as atoms and dust of Na). From this neutral material, charged particles are produced as a result of partial ionization by the Sun's extreme ultraviolet (EUV) ra-

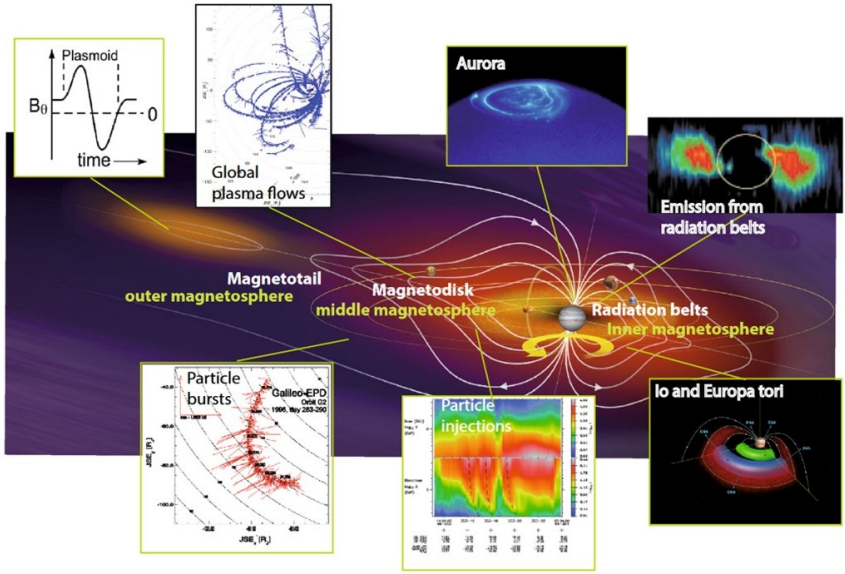

Figure 1.3 – Basic configuration of the Jovian magnetosphere and typical electromagnetic emissions and particle fluxes observed remotely from Earth orbit observatories and/or from in situ spacecraft. (Krupp 2014).

diation and collisions with surrounding energetic particles (S^+, O^+, etc., and as many electrons). The pick-up phenomenon takes place as soon as the ions are formed: they are instantly captured by the magnetic field and carried away by the rotation (Bolton et al. 2015). Iogenic plasma is the main source of plasma in Jupiter's magnetosphere (Figure 1.3). However, it should be pointed out that this is not the only source of plasma in the magnetosphere, atomic oxygen is produced by energetic magnetospheric particles bombarding the icy surface of Europa (Bagenal et al. 1992). Europa's contribution to the magnetospheric plasma is much smaller than that of Io. The contributions from Ganymede and Callisto are even smaller. The total amount of plasma estimated for these three satellites is less than 20

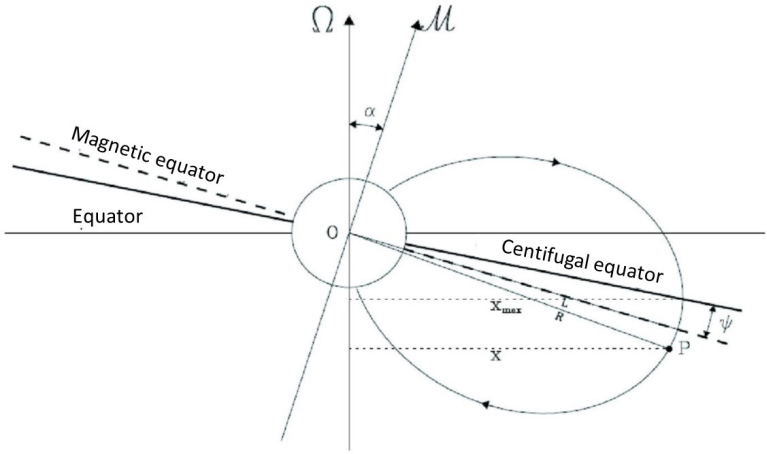

Figure 1.4 – The centrifugal equator is drawn here in a meridian plane containing the axis of the magnetic moment $\vec{M}$ of a centred dipole, inclined by an angle α to the planetary rotation axis of vector $\vec{\Omega}$. The centrifugal equator is defined as the location of the points furthest from the axis of rotation on each field line. The angle Ψ formed by the magnetic equator and the centrifugal equator reaches its maximum in this plane $(\vec{\Omega}, \vec{M})$ and is $\sim \alpha/3$ for a small angle α (Hill et al. 1974) (for Jupiter, $\Psi \sim 3.2°$). A point P in the magnetosphere is easily identified from the magnetic field by the "equatorial (or dipolar) magnetic radius" L of the field line to which it belongs, and in relation to a corotating plasma (torus) by its centrifugal latitude (angle to the local centrifugal equator), adapted from Moncuquet (1997)

kg/s (Cooper et al. 2001). There are also light ions coming from Jupiter's ionosphere (H^+, H_2^+ and H_3^+ , $\sim$ 20 kg/s) (Hamilton et al. 1981), but also from an external source : the solar wind (mainly H^+ and He^{++}), at a rate of a few tens of kilograms per second (Delamere and Bagenal 2003).

Because of the centrifugal force, the iogenic plasma slowly diffuses radially outward, forming the plasma disk. We note that the effects of the plasma on the magnetic field are minimal due to the strong internal magnetic field and the low temperature of the plasma torus. The plasma parameter β, which is

the ratio between the kinetic pressure (P) and the magnetic pressure (B^2/μ_0) inside the plasma, is expressed as follows :

$$\beta = \frac{nk_BT}{B^2/\mu_0} \tag{1.1}$$

where n is the number density, k_B is the Boltzmann constant, T is the temperature, B is the magnetic field[4] and μ_0 is the permeability of the vacuum. Thus, in the inner magnetosphere, β values are less than unity (Mauk et al. 2004). The effects of the magnetic field dominate over the kinetic pressure of the plasma. On the other hand, the effect of the magnetic field on the distribution and the energy of the plasma is important. Indeed, the charged particles moving in the magnetic field are subject to the Lorentz force. This implies that the spatial distribution of the particles is governed by the magnetic field and thus that the plasma torus is confined to the centrifugal equator. The centrifugal equator corresponds to the surface defined by the set of field line points located the farthest from the axis of rotation of Jupiter (Figure 1.4). In addition, Tsuchiya et al. (2015) and Yoshioka et al. (2017) showed that the plasma torus can be described using radial and longitudinal profiles of electron density, temperature, and relative ion abundance, and that these parameters vary with the solar wind.

The dynamics of the magnetosphere are mainly driven by the internal plasma source and rapid rotation (Vasyliūnas cycle, Figure 1.5), while the external source (the Sun) plays only a secondary role (Hill et al. 1974, Vasyliūnas 1983, Kivelson and Southwood 2005). Such as the magnetospheric plasma is collision less and extremely conductive, the magnetic Reynolds number (R_m) is much greater than one and the "Frozen-in" approximation can be

[4]The magnetic flux density (B in [T]) is a function of magnetic field intensity (H in [A/m]) : $B = \mu_0.\mu_r.H$, where $\mu_r = 1$ in vacuum

apply. This approximation implies that the only electric field present ($\overrightarrow{E}$) arises from plasma motion and is expressed as a function of the magnetic field ($\overrightarrow{B}$) and the velocity vector ($\overrightarrow{v}$) : $\overrightarrow{E} = -\left(\overrightarrow{v} \times \overrightarrow{B}\right)$. As a result, the magnetic field lines are equipotential ($\overrightarrow{E}.\overrightarrow{B} = 0$). In such an approximation, the magnetic field lines are frozen in the plasma, so they are pulled towards the corotation and ultimately lead to the corotation of the magnetospheric plasma.

When the plasma outflows, the angular momentum is transferred from the ionosphere to the plasma disk by a current system. This current system consists of a radial current in the plasma disc directed outwards from the magnetosphere, a Pedersen current in the ionosphere equatorward and currents aligned with the magnetic field, closing the loop, connecting the plasma disc to the ionosphere and the ionosphere to the plasma disc. As the iogenic plasma flows radially into the plasma disc, the $\vec{j} \times \vec{B}$ force accelerates the magnetospheric plasma to maintain the plasma's corotation with the magnetic field.

The middle magnetosphere extends from about 10 to 40 R_J (Figure 1.3). Above ~15 R_J, in contrast to the inner magnetosphere, the β parameter is greater than one (Mauk et al. 2004) because the kinetic pressure in the plasma is greater than the magnetic pressure.In order to simplify the description of this region, we can distinguish two current systems : the current disk and a meridian currents system. The first one is related to the differential drift of electrons and ions, the associated azimuthal currents induce a radial deformation (stretching) of the field lines (Bagenal et al. 2017). The second one is related to the transmission of the angular momentum from the ionosphere to the magnetosphere (i.e. Cowley and Bunce 2001, Hill 2001).

At the outer edge of the middle magnetosphere, the currents become too small to maintain a significant degree of corotation and the azimuthal velocity in the plasma sheet starts to drop significantly, a phenomenon named corotation breakdown. The radial current in the equatorial plane induces a magnetic field oriented in the azimuthal direction, above and below the plasma sheet, resulting in a bend-back of the magnetic field lines.

The outer magnetosphere extends beyond 40 R_J (Figure 1.3). We can more specifically focus on two remarkable regions of the outer magnetosphere. First, the dayside outer magnetosphere, whose outer boundary is not fixed in time, as the magnetopause stand-off distance varies between ~ 60 and ~ 90 R_J (Joy et al. 2002), depending on the pressure exerted by the solar wind (Section 1.3). In the antisolar direction, the magnetic tail (or magnetotail) has a cross section diameter of 300 to 400 R_J and an estimated length extending beyond 2,5000 R_J, up to the orbit of Saturn (Khurana et al. 2004, McNutt et al. 2007).

1.3.3 Particles Motion

1.3.3.1 Single Particle Motion

In order to explain the phenomena giving rise to the auroral emissions, it seems essential to describe first the motion of a particle under the influence of an electromagnetic field. When a charged particle is placed in a uniform magnetic field, the motion of a particle along a field line is described by the force $\vec{F}$:

$$\vec{F} = q\vec{v} \times \vec{B} \tag{1.2}$$

where q is the charge of the particle, $\vec{v}$ is the velocity and $\vec{B}$ is the magnetic

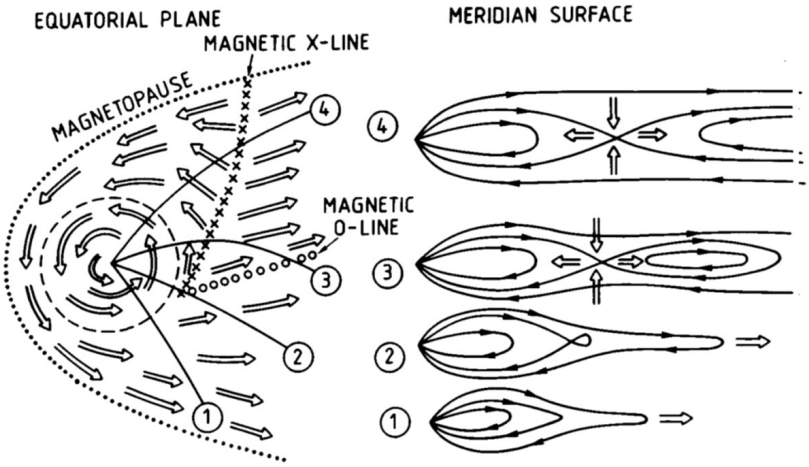

Figure 1.5 – Diagram showing the loading and unloading of the mass. The equatorial plane is shown on the left, and the meridian sections on the right (with the Sun on the left in both views). Illustration from Bolton et al. (2015), adapted from Vasyliūnas (1983).

field.

The definition of this force allows to characterize the motion of the particle in the magnetic field. Indeed, the cross product of the velocity and the magnetic field imposes on the particle a helical motion along the field line, as long as the particle remains trapped on its field line. Moreover the cross product also imposes that the motion of the particle is perpendicular to the velocity and the magnetic field. If the magnetic field is uniform along the z direction ($\vec{B} : (0; 0; B_z)$), the components of the force ($\vec{F} : (F_x; F_y; F_z)$) can be written as follows:

$$F_x = qv_yB_z; \qquad F_y = -qv_xB_z; \qquad F_z = 0 \tag{1.3}$$

If we derive these expressions as a function of time, we obtain the compo-

nents along x and y, the description of a simple harmonic oscillator. Hence, we define the gyroscopic frequency as the angular frequency of this harmonic oscillator :

$$\Omega_c = \frac{|q|B}{m} \tag{1.4}$$

From here, we can characterize the gyration motion of the particle thanks to the radius of the helix. This radius is called gyroradius (R_g) or Larmor radius and is defined as follows:

$$R_g = \frac{v_\perp}{\Omega_c} = \frac{v_\perp m}{|q|B} \tag{1.5}$$

where $v_\perp$ is the particle velocity component perpendicular to the magnetic field. Therefore, the helical motion of the charged particle can be decomposed into the "circular" motion of the particle along the field line, characterized by the Larmor radius, around the guiding center (x_0, y_0), and the displacement along the z-axis with constant velocity. Note that the sign of the charge as well as the mass of the particle have an impact on its motion. Indeed, electrons have a mass much lower than that of ions so they move with a smaller radius. Their charge is negative so they move in the opposite direction of the positive ions.

We can also define the "pitch angle", α, which is the angle between the velocity vector of the particle and the magnetic field vector:

$$\alpha = arctan\left(\frac{v_\perp}{v_\parallel}\right) \tag{1.6}$$

where $v_\parallel$ is the velocity parallel to the magnetic field line.

The presence of an electric field ($\vec{E}$) perpendicular to the magnetic field ($\vec{B}$), results in a drift velocity of the particle perpendicular to the two components of the cross product: $\vec{E} \times \vec{B}$. The electric drift velocity ($\overrightarrow{v_E}$) is such that :

$$\overrightarrow{v_E} = \frac{\vec{E} \times \vec{B}}{B^2} \tag{1.7}$$

The definition of the electric drift velocity, shows that it is not dependent on the charge of the particle, so electrons and ions drift in the same direction and no net current is associated with drift.

In many cases, the motion of the particle in an electromagnetic field can be decomposed into three motions: (1) a gyration around the field line, (2) a bounce along the field line and (3) an azimuthal drift (Figure 1.6). (1) has been explained already, (2) and (3) will be explained latter. Throughout this global motion, the central point around which the particle rotates, called the gyrocenter or guiding center, remains attached to the same magnetic field line. Thus, under these conditions, the"Frozen-in" approximation applies, i.e. the particle remains attached to its field line.

So far, we assumed that the background magnetic field was uniform. However, this approximation does not always hold and one needs to take into the spatial variations of the magnetic field. This is particularly true for a planetary magnetosphere for which the magnetic field rapidly changes close to the planet. The magnetic field is more intense near the planet, which implies the existence of a gradient in magnetic field intensity. This gradient induces a drift, which can be expressed as follows (Baumjohann and et al. 2012):

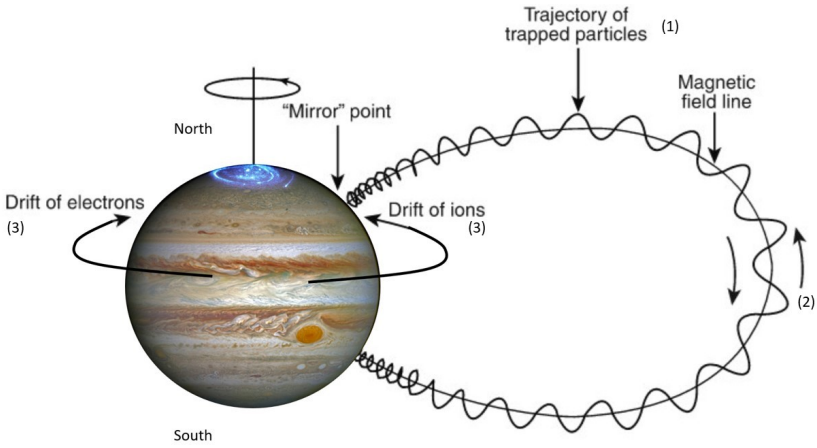

Figure 1.6 – Illustration of the classical motion of a particle trapped along the magnetic field lines around Jupiter, with evidence of the drift in the opposite direction for particles of opposite charge: electrons and positively charged ions. Breakdown of motion into its 3 components: (1) a gyration around the field line, (2) a bounce along the field line and (3) an azimuthal drift. Adapted from Rymer et al. (2007).

$$\overrightarrow{v_{\nabla \vec{B}}} = \frac{m v_{\perp}^2}{2q} \cdot \frac{\vec{B} \times \nabla \vec{B}}{B^3} \tag{1.8}$$

We deduce from this expression that the drift is perpendicular to the magnetic field and its gradient. The drift is therefore in the azimuthal direction around a planet. Given the dependence of the charge in the expression, electrons and positive ions drift in opposite directions, which leads to a net current.

Finally, the particles undergo a curvature drift induced by the curvature of the magnetic field lines. This curvature drift also acts in the azimuthal direction and in opposite directions depending on the particle's positive or

negative charge, therefore producing a net current :

$$\overrightarrow{v_c} = \frac{mv_{\parallel}^2}{qB^2R_c^2}\left(\overrightarrow{R_c} \times \overrightarrow{B}\right) \tag{1.9}$$

where R_c is the local radius of curvature.

The gradient and the curvature drifts are proportional to the energy of the particle (perpendicular to the field for the gradient drift and parallel to the field for the curvature drift), so the larger the speed of the particle, the larger the drift (Kivelson and Russell 1995, Baumjohann and et al. 2012).

It is also known that, in a magnetised plasma, certain physical quantities may be conserved along the trajectory of a charged particle: these are the adiabatic invariants (Baumjohann and et al. 2012). The first invariant is the magnetic moment (μ) of the particle in gyromotion :

$$\mu = \frac{mv_{\perp}^2}{2B} = \frac{mv^2 sin^2(\alpha)}{2B} \tag{1.10}$$

where α is the pitch angle.

Since the magnetic moment of a particle is considered constant over time, the perpendicular velocity must increase when the value of the magnetic field increases. According to the principle of total energy conservation, and if we place ourselves in the case where the energy of the particle is only kinetic, then a perpendicular velocity increase implies a parallel velocity decrease, since :

$$\frac{1}{2}mv^2 = \frac{1}{2}m\left(v_{\parallel}^2 + v_{\perp}^2\right) = constant \tag{1.11}$$

$$\Leftrightarrow v^2 = v_{\parallel}^2 + v_{\perp}^2 = constant \tag{1.12}$$

As the magnetic field increases, the parallel velocity decreases, at the benefit of the perpendicular velocity, until it becomes zero. If this point is high enough above the atmosphere, then the particle can no longer continue its motion along the field line in this direction, so the particle bounces back in the opposite direction towards region where the magnetic field is decreasing. This point of reversal is called mirror point. Mirror points in each hemisphere constitute the extremities of the bouncing motion of the particle along the field line.

Since by definition at the mirror point, the parallel velocity is zero ($v_{\parallel} = v\ cos(\alpha)$), the pitch angle ($\alpha_m$) is 90° at this point. From the definition of the first adiabatic invariant, if B_m is the magnetic flux density at the mirror point, it is expressed as a function of the magnetic flux density (B_i) and the pitch angle (α_i) at any point along the particle's path:

$$\mu = \frac{mv^2 sin^2(90°)}{2B_m} = \frac{mv^2 sin^2(\alpha_i)}{2B_i} \tag{1.13}$$

$$\Leftrightarrow B_m = \frac{B_i}{sin^2(\alpha_i)} \tag{1.14}$$

The mirror point can be located in the atmosphere. In this case, the particles are lost in the atmosphere, and we can determine the critical pitch angle beyond which this happens. From then on, we speak of a loss cone. This critical pitch angle defines the loss cone and can be determined in the equatorial plane:

$$\alpha_{loss\ cone} = arcsin\left(\sqrt{\frac{B_{equator}}{B_{ionosphere}}}\right) \tag{1.15}$$

In the case of a dipole, we can define the distance (r) between the centre of the planet and a given latitude (λ) such that $r = L\ cos^2(\lambda)$, as well as the intensity of the magnetic field at a specific location (Baumjohann and et al. 2012):

$$B = \frac{\mu_0}{4\pi}\frac{M_J}{r^3}\left(1 + 3sin^2\lambda\right)^{1/2} \tag{1.16}$$

where the magnetic dipole moment of Jupiter is M_J is = 1.59×10^{22} A m^2.

When the surface magnetic field is weaker, the altitude of the mirror point is lower. In this case, the number of particles which have a mirror point located in the atmosphere increases. These particles will collide with the neutral atmosphere, eventually leading to brighter aurorae if their energy is sufficient.

1.3.3.2 Motion of trapped particles in Jupiter's magnetosphere

During this thesis I was led to test the hypothesis that the auroral process of plasma injections is associated with pitch angle diffusion and electron scattering by whistler mode waves. For this purpose, I used a simulation based on the Radioti et al. (2013) model, which I transposed from Saturn to Jupiter. Before discussing the results obtained in Chapter 5, I describe the motion of particles trapped in Jupiter's magnetosphere, the motion on which the simulations are based. Most of the following expres-

sions are extracted and/or adapted from Roederer (1970) and Thomsen and Van Allen (1980), although some coefficients have been revised with the help of Dr Elias Roussos and Dr Christopher Paranicas. Unless otherwise noted, all basic formulas are in CGS[5] Gaussian units and all numerical formulas give angular velocities in radian per second, distances in centimeters, and periods in seconds and the kinetic energy E is expressed in MeV.

The simulation describes the motion of a charged particle, specifically an electron, in a Jovian dipole magnetic field. These formulas are expressed as a function of the kinetic energy (E), the McIlwain L-parameter (L)[6] and the equatorial pitch angle (α_{eq}) for a simplified dipolar model of the magnetic field of Jupiter. As we have seen in the case of single particle motion (Section 1.3.3.1), when a charged particle is trapped in a magnetic field, the motion of the particle is a combination of three different motions: (1) gyration around a magnetic field line, (2) latitudinal bounce along the field line, and (3) longitudinal drift perpendicular to the magnetic field line.

Before detailing these motions, two expressions are essential to describe a dipole at a certain magnetic latitude (λ):

- the relation between the local and the equatorial pitch angle, respectively α_l and α_{eq} :

$$sin^2(\alpha_l) = sin^2(\alpha_{eq}) \frac{\sqrt{4 - 3cos^2\lambda}}{cos^6\lambda} \tag{1.17}$$

- the relation between the magnetic flux density at a given magnetic

[5]CGS : Centimeter - Gram - Second

[6]The L-shell or L-value is a parameter describing a set of magnetic field lines which cross the Jupiter's magnetic equator at a number of Jupiter-radii equal to the L-value.

latitude and at the equator, respectively $B(\lambda)$ and B_{eq} :

$$B(\lambda) = B_{eq}\frac{\sqrt{1+3sin^2\lambda}}{cos^6\lambda} \tag{1.18}$$

Following the definition of the first adiabatic invariant, a mirror point is a point where a charged particle trapped in a magnetic field reverses its direction along the magnetic field line. From the equation (1.17), we can determine the mirror points ($\pm\lambda_m$) by solving numerically the equation below :

$$sin^2(\alpha_{eq}) = \frac{cos^6\lambda_m}{\sqrt{4-3cos^2\lambda_m}} \tag{1.19}$$

It should be noted that the latitude of a mirror point depends only on the equatorial pitch angle but not on the equatorial distance of the magnetic field line.

Gyration motion

The relativistically corrected angular gyrofrequency of a charged particle, in the equatorial plane where $B = B_o L^{-3}$, is given by

$$\omega_g = \frac{qBc}{E+mc^2} = \frac{qB_oc}{(E+mc^2)L^3} = \frac{3.852\ 10^7}{(E+mc^2)L^3} \tag{1.20}$$

The equatorial gyroperiod is defined as follow :

$$T_g = \frac{2\pi}{\omega_g} = 1.631\ 10^{-7}(E+mc^2)L^3 \tag{1.21}$$

Ultimately, we may compute the equatorial gyroradius (radius of the cylin-

drical surface on which the particle's helical radius lies) :

$$r_g = \frac{\beta c sin(\alpha_{eq})}{\omega_g} = 778.816 \sqrt{E(E + 2mc^2)} L^3 \tag{1.22}$$

Bounce motion

The bounce period, T_b, is the time (expressed in seconds) required for a particle to make a round trip between the two mirror points. The bounce period and the latitude of the mirror points, λ_m, are the most important parameters to describe the latitudinal bounce motion.

As described before, λ_m can be estimated by solving the equation (1.19). As for the bounce period (T_b), it is estimated by solving the following integral along the field line of length s for a complete bounce between the mirror points :

$$T_b = \oint \frac{ds}{v_{\|}} \tag{1.23}$$

Approximating the Jovian magnetic field by a dipole, this integral can be reduced to

$$T_b = 0.954 \frac{L(E + mc^2)}{\sqrt{E(E + 2mc^2)}} H(\alpha_{eq}) \tag{1.24}$$

where mc^2 is the rest energy of the particle, the value is 0.511 Mev for electrons and c is the speed of light, equals to 2.99 10^{10} cm s^{-1} and Lenchek et al. (1961) approximated the parameter $H(\alpha_{eq})$ by the following expression :

$$H(\alpha_{eq}) = 1.38 - 0.32(sin(\alpha_{eq}) + \sqrt{sin(\alpha_{eq})}) \tag{1.25}$$

Table 1.1 – Typical bounce period (T_b) values for electrons at Jupiter

L-shell	Mirror latitude (deg)	E = 1 Mev T_b (sec)	E=0.5 Mev T_b (sec)	E = 0.1 Mev T_b (sec)
5	20	4.323	4.716	7.423
	45	5.678	6.194	9.750
	70	6.672	7.277	11.455
10	20	8.647	9.431	14.846
	45	11.357	12.387	19.500
	70	13.343	14.554	22.910
15	20	12.970	14.147	22.269
	45	17.035	18.581	29.250
	70	20.015	21.831	34.365
20	20	17.293	18.862	29.692
	45	22.714	24.774	38.999
	70	26.687	29.108	45.820

As an indication, the values of the bounce periods (T_b), expressed in seconds, are given in Table 1.1. These values have been taken for electrons with energies between 0.1 and 1 Mev, for mirror latitudes between 20° and 70° and finally for L-shell between 5 and 20.

Longitudinal drift

Finally the last component of the motion of the electrons, studied by Lew (1961), is the longitudinal drifts in dipole fields. The bounce averaged angular velocity of the guiding center of a particle is expressed as :

$$\omega_{gc} = \frac{3mc^3\beta^2\gamma LF(\lambda_m)}{2qB_0R_J^2G(\lambda_m)} \tag{1.26}$$

where

$$F(\lambda_m) = \oint \frac{(1-sin^4\lambda)}{(1+3sin^2\lambda)^{3/2}} \frac{2-(B(\lambda)/B(\lambda_m))}{\sqrt{1-(B(\lambda)/B(\lambda_m))}} cos\lambda \, d\lambda$$

$$G(\lambda_m) = \oint \frac{\sqrt{(1+3sin^2\lambda)}}{\sqrt{1-(B(\lambda)/B(\lambda_m))}} cos\lambda \, d\lambda$$

By developing these integrals, $F(\lambda_m)$ and $G(\lambda_m)$, over a complete latitudinal bounce period, we obtain the parameter $(\frac{F}{G})$ and we can rewrite the equation (1.26), for which we take the convention that the longitudinal velocity is positive for eastward drifts (in the corotating direction) and negative for westward drifts. This implies that the negative sign corresponds to electrons. We obtain for Jupiter the following equation :

$$\omega_{gc} = \frac{-1.4998\ 10^{14} LE(E + 2mc^2)}{B_0 R_J^2} \left(\frac{F}{G}\right) \tag{1.27}$$

The parameter $\left(\frac{F}{G}\right)^{-1}$ can be approximated as follow:

$$\left(\frac{F}{G}\right)^{-1} = (1.04675 + 0.45333 sin^2\lambda_m - 0.04675 e^{-6.34568 sin^2\lambda_m}) \tag{1.28}$$

1.4 The Jovian aurorae

In general, auroral emissions are generated by the excitation of atoms and molecules in the upper atmosphere by energetic electrons and ions precipitating towards the planet along the magnetic field lines. In the case of Jupiter, the upper atmosphere is mainly composed of atomic and molecular hydrogen. Aurorae are the observed signatures of the electromagnetic

coupling (in very broad sense) between the magnetosphere and the ionosphere of the planet. Auroral emissions can be produced in a wide range of wavelengths. Jupiter's aurorae are observed in the UV, radio, IR, visible, and X-ray (e.g. Grodent 2015). By observing and modeling auroral emissions at different wavelengths, we learn more about the characteristics of the auroral atmosphere, and the different mechanisms that are transporting and transforming the energy in the magnetosphere-ionosphere system. Indeed, the auroral emissions provide a global and instantaneous image of the whole magnetosphere, thus allowing the study of magnetospheric phenomena through the observations of these emissions. During this thesis, I worked on the UV aurorae observed in the polar regions of Jupiter with HST and the Juno spacecraft. In the following sections, I describe the atmosphere, the auroral processes and the morphology of UV auroral emissions.

1.4.1 Atmosphere of Jupiter

Jupiter's atmosphere is a gaseous envelope mainly consisting of H_2 (86%) and He (∼14%). It also contains traces of methane, water vapour, ammonia, and small quantities of carbon, nitrogen, oxygen and sulfur (Taylor et al. 2007). Jupiter's atmosphere can be divided into several layers (Figure 1.7):

- The troposphere, which is the layer just above the 1-bar pressure level and contains the clouds. It is heated by an energy source internal to the planet.
- The stratosphere, where the temperature increases with altitude, thanks to the absorption of near infrared (NIR) radiation by methane (Moses et al. 2004).

- The thermosphere, where temperatures are high but densities low. This last layer absorbs EUV solar radiation as well as charged magnetospheric particles near the magnetic poles, causing the dissociation and ionisation of thermospheric molecules and thus the appearance of the ionosphere. The ionosphere is the region of the upper atmosphere, mostly overlapping the thermosphere, which contains a significant proportion of ions and free electrons.

- The exosphere is the ultimate layer of the atmosphere. Its upper limit is undefined as this region gradually blends with the interplanetary medium. In this region, collisions between atmospheric particles become so rare that they can be neglected and particles can follow parabolic, elliptic or hyperbolic paths in the gravity field. This region is also the warmest part of the atmosphere and is characterized by a constant temperature profile driven by heat conduction which, for Jupiter, reaches 900 K at mid latitudes and more in the auroral regions (Grodent et al. 2001).

A notable feature of Jupiter's thermosphere is its relatively pure chemical composition, with molecular diffusion isolating most species at low altitudes. Its main constituents, in order of abundance, are H_2, which is light, and He, which is inert and plays a very limited role in atmospheric chemistry. This makes the chemistry of this atmospheric layer fairly straightforward. At low altitudes H_2 is the most abundant constituent, but it dissociates at high altitudes (i.e. in the thermosphere) under the effect of UV radiation, and atomic hydrogen H then becomes dominant (Yelle and Miller 2007). However UV radiations and the precipitation of auroral particles contribute to largely complexifying the chemistry, including minor constituents such as hydrocarbons, in the upper stratosphere and lower thermosphere (Menager et al. 2010, Yelle and Miller 2007).

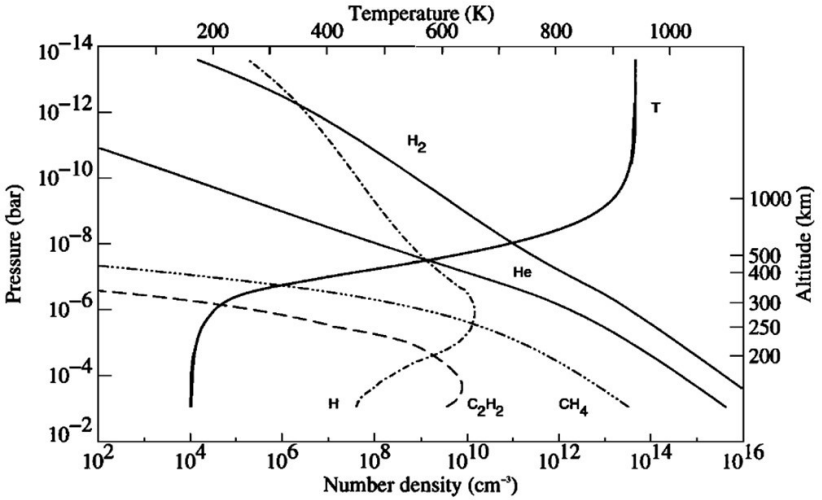

Figure 1.7 – Vertical distributions of main constituents of the upper atmosphere of Jupiter according to the model from Grodent et al. (2001), as well as the related thermal profile, which is an analytical fit to the equatorial temperature profile determined from the Galileo probe data.

Jupiter's UV auroral emissions show the signature of the H Lyman-α line at 121.567 nm and the H_2 Lyman and Werner bands between 90 and 170 nm. Jovian far ultraviolet (FUV) auroral images include emission from the Lyman H_2 band as well as the series of Werner bands, plus the Lyman-α H line. During this thesis, we considered both images including or rejecting the H Lyman line emission (Chapter 3).

1.4.2 Auroral processes

There are several mechanisms by which electrons and ions can precipitate from the magnetosphere into the atmosphere. In this section we present three of them: (1) pitch angle scattering at low latitudes in the magnetosphere; (2) particle acceleration by quasi-static electric potentials (inverted-V) along magnetic field lines and (3) acceleration of particles by plasma waves (Alfvén waves, whistler waves, ...). Once the electrons impact the atmosphere, they can induce excitation, ionisation or dissociation of the neutrals. Jupiter's UV aurora results from the deexcitation of molecular and atomic hydrogen, which relaxes after impact with primary or secondary energetic electrons (Bhardwaj and Gladstone 2000).

The auroral brightness is expressed in kilo-Rayleighs (1 kR = 10^9 photons per second from a 1 cm^{-2} column of atmosphere radiated isotropically into 4π steradian). Auroral brightness is obtained from the number of photon counts detected by the detectors. Conversion factors for instrument counts to brightness and auroral power (in mW/m²) have been determined by Gustin et al. (2012). Jupiter's FUV (120 - 180 nm) auroral emissions are dominated by H Lyman-alpha (H Ly-α), and the Lyman and Werner bands of H_2 (Gustin et al. 2012). Jupiter's atmosphere (Section 1.4.1) contains a layer of hydrocarbons, dominated by methane, which attenuate auroral emissions. The more energetic the particles, the deeper they precipitate and the most energetic ones may deposit most of their energy below the methane homopause. Methane is responsible for the absorption of the auroral emission at wavelengths shorter than 140 nm. Absorption can be estimated from a color ratio (CR). Yung et al. (1982) defined the CR as the ratio between H_2 emission intensity at wavelengths without absorption, between 155 and 162 nm (denoted $I(155-162)$) and emission intensity in a wavelength range

where absorption occurs, between 123 and 130 nm (denoted $I(123-130)$):

$$CR = \frac{I(155-162)}{I(123-130)} \tag{1.29}$$

This CR (other wavelength ranges may be considered) is used to determine the characteristic energy of auroral precipitation and to reveal spatial variations in the amount of methane absorption for different components of the aurora (Gérard et al. 2014).

1.4.2.1 Particle precipitation due to pitch angle scattering

Some wave-particle interactions in the equatorial plane may randomly change the orientation of a particle velocity vector without necessarily changing its total kinetic energy. For example, the parallel velocity may increase at the expense of the perpendicular one, and the particle's pitch angle would fall into the loss cone. As we have seen in Section 1.3.3.1, in that case it means that its mirror point is located into the atmosphere, and thus that the particles will lose its kinetic energy through elastic and inelastic collisions with atmospheric particles. Part of this absorbed energy may then be radiated away by the atmosphere in the form of auroral radiations. It was suggested that wave-particle interactions reinforce the phenomenon of pitch angle scattering, in particular in the diffuse aurora of Jupiter. For example, the whistler mode waves are transverse plasma waves that propagate along the magnetic field and their presence in Jupiter's magnetosphere may also play a role in these pitch angle scattering processes (Kennel et al. 1970). Indeed, the waves disturb the movement of electrons present on the field lines and eventually accelerate them towards the loss cone. However, the quantitative contribution of whistler waves to the generation of the aurora was not clear before Juno. Thanks to the joint observations of three instruments

onboard Juno (Jovian Auroral Distribution Experiment (JADE), Jovian Energetic Particle Detector Instrument (JEDI) and Ultraviolet Spectrograph (UVS)), new quantitative evidence has been provided by Li et al. (2017) and Li et al. (2021), who show that whistler mode waves are probably the main driver of precipitation by pitch angle scattering effectively generating the diffuse aurorae. In addition, Allegrini et al. (2017) also identified loss cone pitch angle distributions in the JADE data that are likely the origin of diffusive aurorae (Mauk et al. 2017).

1.4.2.2 Quasi-static field-aligned potentials

Before Juno, electrons acceleration by quasi-static field-aligned potential was expected to be the main driver for the auroral emissions of Jupiter (e.g. Knight 1973, Ray et al. 2010, Bagenal et al. 2017). In particular, downward electron acceleration by such potentials at the foot of the upward current branch of the current system associated with corotation enforcement was supposed to give rise to the main auroral emission at Jupiter (e.g. Cowley and Bunce 2001, Hill 2001). The typical signature of such quasi-static potentials in charged particle energy spectrograms takes the form of an inverted-V. However, the number of detected inverted-Vs is much lower than expected and the associated energy flux is smaller then the energy flux associated with broad-band energy distribution (Mauk et al. 2018, Mauk et al. 2020, Salveter et al. 2022, Sulaiman et al. 2022, Lorch et al. 2022). Among the different hypothesis to explain the auroral emission associated to inward moving plasma flow, one was involving a current loop related to the inward motion of the injected plasma. In this scenario, the auroral electron are accelerated by a quasi-static potiential in upward (anti-planetward) branch of the current system (Radioti et al. 2010).

1.4.2.3 Acceleration of electrons via wave-particle interaction

Electrons can be accelerated via wave-particle interactions. Among the most studied ones at Jupiter are whistler mode waves and Alfvén waves. For example, Elliott et al. (2018) have discussed the acceleration of electron beams away from the planet by whistler waves in the polar region. On the other hand, Alfvén waves are known to be heavily involved in the generation of the satellite auroral footprints (Bonfond et al. 2009, Hess et al. 2010, Szalay et al. 2018, Sulaiman et al. 2023). These waves appear to be ubiquitous in the Jovian magnetosphere (Mauk and Saur 2007, Lorch et al. 2022) and may be involved in the generation of other components of the Jovian aurora (Saur et al. 2018, Damiano et al. 2019). The magnetometer onboard Juno showed that these Alfvén waves are particularly present on field lines mapping to the inner magnetosphere (Gershman et al. 2019).

1.4.3 Auroral morphology

A large set of observations of Jupiter's UV aurora have been collected by HST since the 1990s as well as by the NASA-Juno mission since 2016. These observations allowed to obtain a lot of information on the UV auroral emissions. The Jovian aurorae are extremely powerful (the UV power emitted is about 10^{12} W, i.e. 100 times more powerful than on Earth and 10 times more powerful than on Saturn). Their morphology is complex, and they vary rapidly, with time scales ranging from seconds to a Jovian rotation ($\sim$ 10 h) (Grodent 2015, Grodent et al. 2018).

Jupiter's aurorae are generally divided into four regions: main emission,

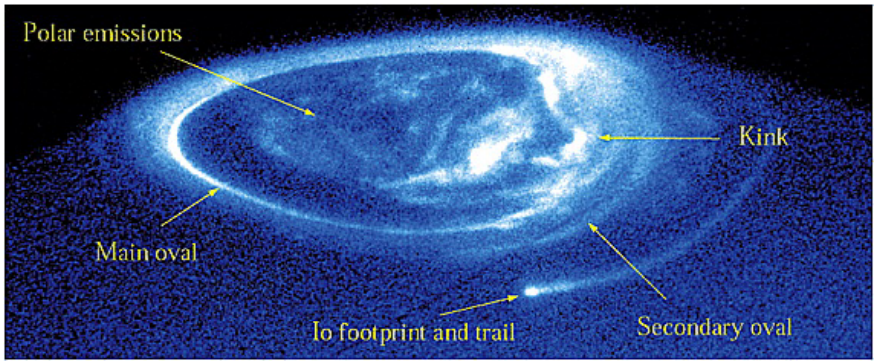

Figure 1.8 – Image taken by HST showing UV auroral emissions at Jupiter's north pole, highlighting some auroral features: the main and secondary ovals, Io's footprint, polar emissions and the "kink" region (the distorted part of the main oval). The outer emissions, like the "Secondary oval", are located beyond the main emission towards the equator (Grodent et al. 2003b).

equatorward emissions, satellite footprints, and polar auroral emissions. The following section describes these four regions.

1.4.3.1 Main emission

Jupiter's main emission is the brightest (one third of the total auroral UV power emitted) and the most stable feature in Jupiter's auroral emissions. It appears as a discontinuous band approximately centered on the magnetic poles. Due to the magnetic anomaly in the northern hemisphere (in the kink region), the emission is distorted in a "bean" shape. According to our current knowledge on this emission, its auroral mechanism is associated with the Field-aligned currents (FAC)s (Cowley and Bunce 2001, Mauk et al. 2018, Kotsiaros et al. 2019, Sulaiman et al. 2022). It was originally suggested to be mainly due to internal processes taking place in the middle magnetosphere approximately between 20-60 R_J

(Clarke et al. 2004, Vogt et al. 2011). It was commonly accepted that the magnetosphere-ionosphere coupling system associated with this emission is related to the breakdown of plasma corotation (Cowley and Bunce 2001, Hill 2001, Southwood and Kivelson 2001). However, Bonfond et al. (2020) highlighted a series of recent observations contradicting the predictive theory of breakdown corotation as a complete explanation for the observed auroral phenomena.

There are observable temporal variations within the main emission as well as variations in Local Time (LT). First, a discontinuity lies between 08 and 13 LT, with variable extent, associated with the compression of the plasma by the solar wind leading to a reduction or inversion of the FACs (Radioti et al. 2008, Chané et al. 2013). Then a small transient patch is observed frequently around 14 LT and associated with intermittent inward plasma flow near 12 LT in the equatorial plane (Palmaerts et al. 2014). Finally, the so-called dawn storms are formed at night, and give rise to a thickening and a significant increase in the brightness of the dawn arc of the main emission. They are relatively frequent, in the observations made by Juno, and seem to last at least 1 to 2 hours (Bonfond et al. 2021). This phenomenon seems to be independent of solar wind fluctuations but is associated with signatures of reconnection, dipolarization and particle acceleration (Yao et al. 2020, Swithenbank-Harris et al. 2021).

1.4.3.2 Polar auroral emissions

Among all the components of the auroral emissions of Jupiter, the polar emissions are the most variable. In the global view of Jupiter's aurora, these emissions are found poleward of the main emission, implying that

these emissions are associated with phenomena occurring beyond 60 R_J. These emissions are subdivided into three different morphological regions: the "swirl region", the "active region" and the "dark region" (Grodent et al. 2008) (Figure 1.9).

At 06 LT, poleward of the main emission lies the dark region. It is a crescent-shaped region devoid of emission (Swithenbank-Harris et al. 2021). Around the magnetic pole, the swirl region consists of many compact and transient structures whose brightness varies strongly from 0 to 200 kR (Grodent et al. 2003b). From 22 LT to 07 LT, they are weak or absent (Greathouse et al. 2021). Finally, in the noon-afternoon sector poleward of the main emission, there is the active region (Pallier and Prange 2001). Some remarkable components are present in the active region. Some of these emissions have been linked to night-side processes such as magneto-tail reconnection, in particular polar spots (Radioti et al. 2008, Haewsantati et al. 2021), or quasi-periodic flashes in the noon-to-dusk sector (Bonfond et al. 2016, Nichols et al. 2017).

1.4.3.3 Satellite footprints

Jupiter has four Galilean moons, in ascending distance from the planet, Io, Europa, Ganymede and Callisto. The first three satellites are associated with auroral footprints (Figure 1.8). These footprints are connected to the satellites by magnetic flux tubes (Clarke et al. 2002). The footprints of these three satellites have tails (Bonfond et al. 2012, 2017) and Io and Ganymede have several spots (Bonfond et al. 2008, Bonfond et al. 2009, 2012, Bonfond et al. 2013a). Thanks to observations in IR made by the Juno spacecraft, Mura et al. (2018) have revealed that the tail of the Io footprint is split

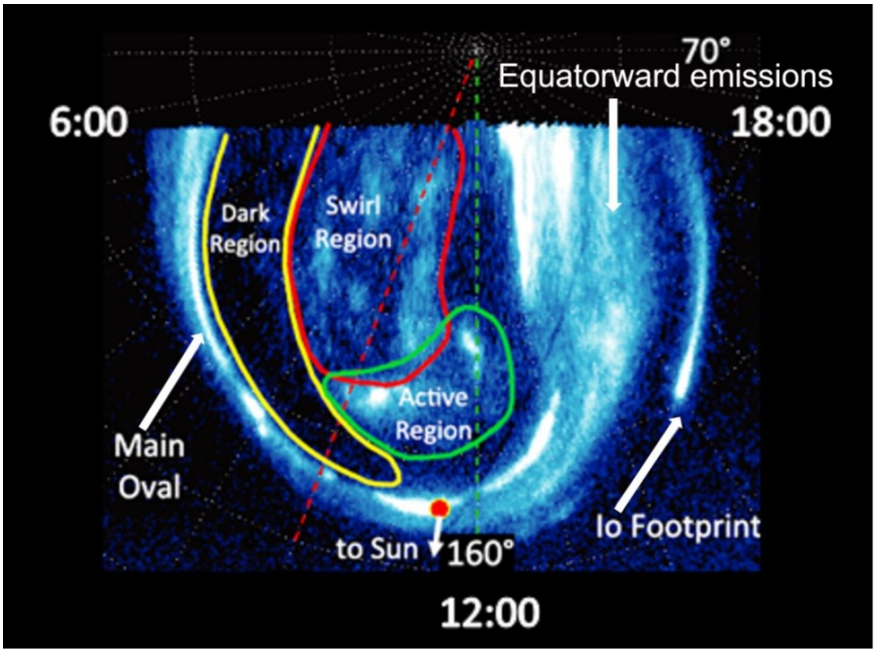

Figure 1.9 – Polar projection of the northern hemisphere of Jupiter's aurorae observed by HST (with a Central Meridian Longitude (CML) of 160°) showing the delineation of the 3 morphologically different regions of the polar emissions: "swirl region" (red), "active region" (green) and "dark region" (yellow). The direction of the Sun(12 LT) is indicated by the white arrow (Vogt et al. 2011), adapted from Grodent et al. (2003b).

into substructures, suggesting that the electromagnetic interaction between Jupiter and its moon is probably more complex than previously anticipated. In the Jovian magnetosphere at a given time, the positions of each satellite are known. Since the instantaneous location of the Galilean moons is known with great accuracy and provided that we have a reliable interpretation of the mechanisms producing their auroral footprints, the precise observation of these simultaneous footprints may be used to constrain models of the magnetic field connecting the moons to Jupiter. This method has

been used in the past to build magnetic field models of Jupiter like VIP4 (Connerney et al. 1998), VIPAL (Hess et al. 2011) or GAM (Vogt et al. 2011) and discussed in Section 1.3.1.

The UV brightness of the Io footprint is around ten times larger than Ganymede's footprint, which is itself around ten times larger than the one of Europa (few kR) (Bonfond et al. 2017). Note also that the brightness of these UV footprints varies with the position of the satellite in the magnetosphere (Gérard et al. 2006).

In 2018, Bhattacharyya et al. 2018 reported a tentative detection of the Callisto footprint, which is particularly difficult due to the proximity of the main emissions.

1.4.3.4 Equatorward emissions

These emissions are located equatorward of the main emission. They are associated with processes occurring in the inner and middle magnetosphere. They consist of diffuse emissions, secondary oval and plasma injection signatures.

The diffuse emissions are broadly distributed in (magnetic) latitude and have a low brightness, as shown in Figure 1.10 (Radioti et al. 2009b). The secondary oval feature is discrete arcs of varying length, and tends to be less bright than the equatorial diffuse emission region (Tomás et al. 2004, Grodent et al. 2003b, Gray et al. 2017). Finally the plasma injection auroral signatures are compact auroral structures. These signatures are the focus of this thesis and are described in detail in the next chapter.

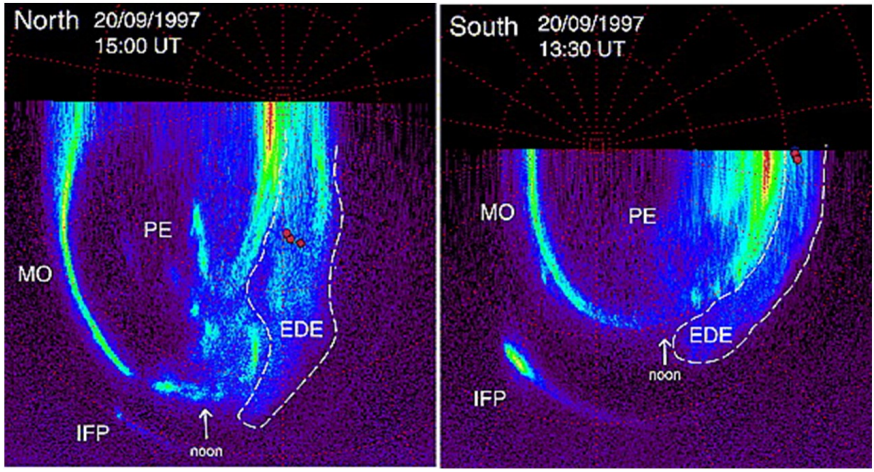

Figure 1.10 – Polar projection of the northern (left) and southern (right) auroral emissions observed by HST (with 12 LT at the bottom and 18 LT at the right). We observe: the main emission (MO), the Io footprint (IFP), the polar emissions (PE) and the region of Equatorward Diffuse Emissions (EDE) (Radioti et al. 2009b).

2 Plasma injections and their auroral signatures

This chapter reviews the current understanding on plasma injections in the Jovian magnetosphere. Before defining a plasma injection in Jupiter's magnetosphere, it should be recalled that plasma injection events were first reported in Earth's magnetosphere in 1971 by DeForest and McIlwain (1971), then in the Jovian magnetosphere in 1997 by Mauk et al. (1997), and finally in the Kronian magnetosphere in 2005 (Burch et al. 2005, Hill et al. 2005, Mauk et al. 2005). Furthermore, the term "plasma injection" used in the case of Jupiter and Saturn refers to plasma injections observed on Earth, which are similar in appearance. For Jupiter and Saturn, although it is commonly used in the literature, there is no agreement on its exact meaning. To clarify the situation, in this thesis, we assume that :

> An injection event is an intensification of high-energy particles that drift azimuthally around the planet under the influence of magnetic gradient and curvature according to their electric charge, mass and energy within a colder background plasma.

2.1 Plasma injection in Earth's magnetosphere

In Earth's magnetosphere, the phenomenon of geomagnetic substorm is a brief (1-3 hours) and powerful process driven by the Sun, involving a transfer of energy from the solar wind to the magnetosphere and leading to disturbances in the magnetosphere, ionosphere and upper atmosphere (Akasofu 1964). In a simplified way, when the IMF turns southward, the interplanetary and terrestrial magnetic field lines can merge at the day-side magnetopause, giving rise to a so called magnetic reconnection. This first reconnection of the magnetopause "opens" the magnetosphere. The reconnected field lines on the day side are transported to the magnetotail, where a new reconnection of the magnetosphere on the night side takes place. This second reconnection "closes" the magnetosphere and creates a circulation in the form of two convection cells, one moving towards the interior of the magnetosphere and the other out into interplanetary space. This circulation is driven by the Dungey cycle (Dungey 1961). It involves the transfer of mass, energy and momentum from the solar wind to the magnetosphere. Typically, a substorm can be divided into three phases (McPherron et al. 1973): growth phase, expansion phase and recovery phase (Figure 2.1 panel a).

If the reconnection rate on the day side is higher than that on the night side, then energy supplied on the day side is greater than the energy released on the night side. As a result, magnetic and plasma energies accumulate in the tail lobe and plasma sheet, forming the growth phase of the substorm. This phase is accompanied by a growing sheet current that stretches the magnetic field lines. About an hour later, the substorm expansion phase begins when the energy accumulation becomes too big and the tail becomes unstable. As a result, the stored energy is released into the near-Earth region and

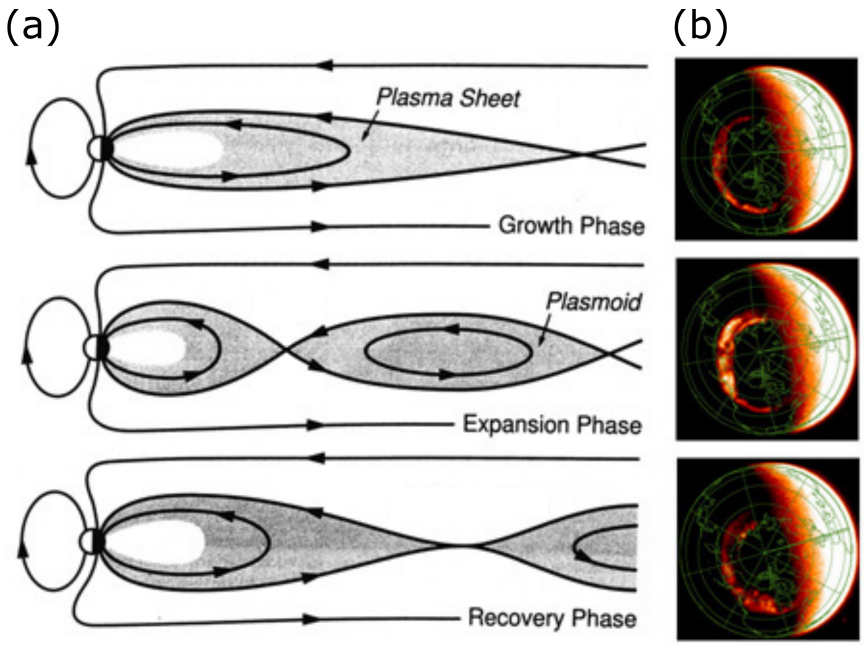

Figure 2.1 – (a) Sketch of the evolution of the plasma sheet during a substorm, adapted from Baumjohann and Treumann (1996). (b) Three auroral images associated with the three substorm phases obtained with the IMAGE WIC instrument on board NASA's IMAGE mission. The Sun is to the left for panel (a) and the right for panel (b). (Image courtesy of Southwest Research Institute website)

energetic particles are injected into the regions around the geostationary orbit. This high energy plasma undergoes magnetic and curvature drifts. When the field lines relax from their stretched state, they move planetward into a more dipolar configuration leading to a dipolarisation of the field. As a result of the planetward motion, there is an energisation of the charged particles in the plasma sheet. This phase lasts between 30 and 60 minutes. Finally, the substorm recovery phase is characterised by the return to the quiet state of the magnetosphere and persists about 1-2 hours. Dur-

ing a substorm, the auroral morphology and emission intensity change as the substorm phase evolves as shown in Figure 2.1 panel b. The energetic plasma injection on Earth is associated with the substorm expansion phase (DeForest and McIlwain 1971, McIlwain 1974, Birn et al. 1997, Pollock et al. 2003). The auroral signature associated with a substorm is the sudden brightening of the aurora on the night side (Ebihara 2019). This is a common phenomenon in the Earth's magnetosphere, occurring at a distance between 5 and 10 Earth radii. The ions and electrons involved in the injection have energies of up to a few hundred keV (Mauk et al. 1997, Yao et al. 2017).

2.2 Plasma injection in the Jovian magnetosphere

Measurements from the Energetic Particles Detector (EPD) on board the Galileo spacecraft provided evidence for the ubiquitous occurrence of plasma injections in the Jovian magnetosphere (Mauk et al. 1997). Figure 2.2 shows three electronic intensifications near 1600, 1730 and 1920 UT, and two ionic intensifications (which are not as well ordered as the electron data) near 1500 and 1620 UT detected by Galileo on 18 December 1996, which are interpreted as injection signatures. More recently, thanks to the JEDI instrument on board the Juno spacecraft, Haggerty et al. (2019) observed plasma injection signatures in the Jovian magnetosphere. However, these new observations were made at higher latitudes than the previous ones demonstrating that hot particles injected near the equatorial plane are travelling along magnetic field lines and may reach the atmosphere where they are likely producing auroral signatures. Haggerty et al. (2019) also highlighted that there is no difference between the frequency of proton injections and that of electron injections meaning that both types of particles

contribute to the injection process.

Two years after the discovery of the Jovian injections, Mauk et al. (1999) performed a statistical analysis of these energy-time dispersed intensifications in the energetic ions and electrons, based on Galileo EPD data. They found that energetic particle injections are commonly observed in the Jovian magnetosphere from 9 to 27 R_J, at all SIII longitudes and all LTs. Two different processes are likely to inject hot particles in a magnetosphere. The first one is related to the interchange instability process, described in Section 2.2.1. The second one involves particle acceleration events related to planetward plasma transport and heating following magnetic reconnection (Krupp et al. 1998), detailed in Section 2.2.2. Moreover, radio emissions and EPD measurements made by Galileo highlight the connection between hot tail inflows at 80–120 R_J and injections in the inner magnetosphere (10–25 R_J (Louarn et al. 2014)). More recently, using HST and Hisaki UV data, Gray et al. (2016) related injections in the inner magnetosphere of Jupiter with hot inflows from magnetotail reconnection. Mauk et al. (1999) proposed a schematic description of the injection phenomenon in Jupiter's magnetosphere (Figure 2.3) in which the cold and dense iogenic plasma moves radially outward as a result of pressure gradients and centrifugal forces and, by virtue of conservation of magnetic flux, are replaced by inward moving flux tubes filled with sparse but energetic plasma.

2.2.1 Interchange instability process

In the Jovian magnetosphere, which is dominated by centrifugal forces, injections are inherent in the radial transport of hot and cold plasma. They are probably the result of centrifugally driven interchange events (Siscoe

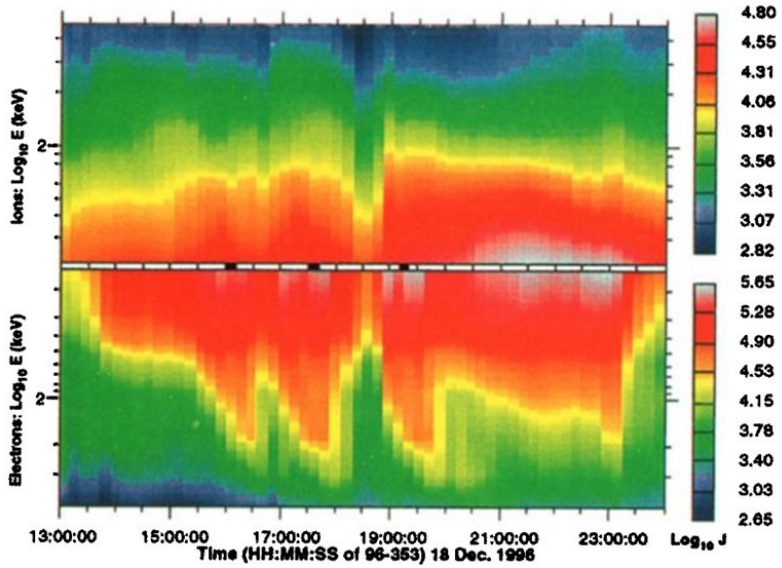

Figure 2.2 – A 12-hour energy-time spectrogram taken on 18 December 1996 in Jupiter's inner magnetosphere by the EPD on board Galileo of energetic ions (regardless of their mass) (top) and energetic electrons (bottom). The colour is coded according to the $\log_{10}$ $(\mathrm{cm}^2.\mathrm{s.sr.keV})^{-1}$ of the particle intensity. Note that the energy scale for electrons is inverted (Mauk et al. 1997). Three electronic intensifications associated with plasma injections clearly appear near 1600, 1730 and 1920 UT.

and Summers 1981). As iogenic plasma rotates around the planet, it is driven centrifugally from the planet. Centrifugal instability therefore leads to spontaneous movement of the flux tubes. This is because the configuration, in which the mass content of the flux tube is higher near the planet than further away, is unstable. As a result, the iogenic plasma moves outwards into the stretched magnetotail under the influence of centrifugal forces and pressure anisotropies (Paranicas et al. 1991). In summary, during an interchange event, distant magnetic flux tubes containing hot and tenuous plasma flow inwards to compensate for the outflowing flux tubes contain-

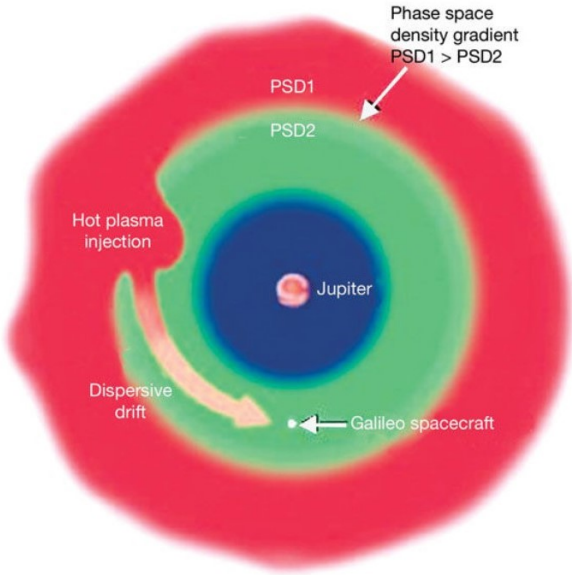

Figure 2.3 – Schematic of injection generation in Jupiter's magnetosphere, where plasma injection (red) occurs. Dispersive drifts then occur due to rotation and the magnetic field gradient causes energy dispersion (Mauk et al. 2002).

ing cold and dense plasma (Ma et al. 2016).

2.2.2 Plasma heating process

As discussed in the previous section, the accumulation of plasma in the torus of Io cannot be maintained indefinitely. This iogneic plasma diffuses radially away from the torus and supplies the magnetodisc with cold and dense plasma. The magnetodisc rotates around Jupiter and consists of plasma confined to the equator, carrying currents that distort the magnetic field into a disc-shaped structure (Kivelson 2015, Delamere et al. 2015). As the magnetic field stretches, Delamere et al. (2015) suggest that radial

transport in the middle and outer magnetosphere is governed by magnetodisc reconnection.

Bagenal and Delamere (2011) have highlighted that the temperature of the ions increases with radial distance, in complete contradiction to the expectation that the plasma cools as it expands to a larger volume. This implies that the expansion is not adiabatic and that energy must be added to the system. There are a number of papers in the literature that investigate the possibility of turbulent heating of Jupiter's magnetodisc using a diffusive transport model (e.g. Saur 2004) or a model based on advective flow, commonly used for solar wind heating (e.g. Ng et al. 2018). Ng et al. (2018) suggest that the advective flow approach is appropriate beyond 10 RJ, where transport becomes rapid and dominated by large-scale motions. In fact, the advective model is more consistent with the observational data obtained by Galileo.

2.2.3 Auroral signatures of plasma injections

Mauk et al. (2002) were the first to associate isolated, patchy auroral UV emission equatorward of the main emission with injections of energetic particles moving in the same flux tube. However, this association was based on a single series of simultaneous observations between the HST and Galileo. They proposed two possible mechanisms for this auroral signature: (1) electron scattering in the loss cone (Section 1.4.2.1), or (2) electron precipitation due to field-aligned currents flowing along the flanks of the injected hot plasma parcel (Section 1.4.2.2).

A number of papers have subsequently been published on plasma injec-

tions, but most of them are based on auroral observations before the injection of Juno in orbit around Jupiter and its wealth of unprecedented in situ data. Before the Juno era, using observations from HST and Galileo, Radioti et al. (2009b) studied auroral equatorward diffuse emissions. Their analysis suggests that some of the diffuse emission components could be related to injection events, indicating that the auroral signatures associated with plasma injections are a common phenomenon. These features, possibly attributed to plasma injection signatures, are observed in both hemispheres (Gérard et al. 2013). Moreover, the association between injections and auroral signatures is further confirmed by the observation and statistics of their location when mapped onto the magnetic equatorial plane (Dumont et al. 2014). The UV auroral signatures of plasma injections are almost fully corotating bright spots with slightly variable size and shape. Most of the time, several such isolated spots may be observed simultaneously, forming groups, but occasionally one single spot may be detected between the main emission and the magnetic footpath of Io. They are so common that in their characterisation of Jupiter's aurorae, Grodent et al. (2018) defined two specific families of auroral morphologies with these "injection" and "strong injection" features.

Nichols et al. (2009) reported an increase in the emitted power in the auroral zones with "patchy emissions". These emissions appear to exhibit the auroral characteristics of injections, i.e. they are at lower latitudes than the main emission and take the form of isolated patches. It should be noted, however, that auroral signatures of plasma injections observed almost simultaneously in both hemisphere have generally not the same power (Gérard et al. 2013). The measurements suggest that the power of these structures decreases with the value of the magnetic field. However, the power is neither proportional to B nor to B^{-1} (Gérard et al. 2013). As for Gray et al. (2017), they propose

that plasma injections act as a source of temperature anisotropy and particle to enhance electron scattering in the aurora and the brightness of the second oval feature (Section 1.4.3.4). Changes in the magnetic field topology around an injection can also generate shear Alfvén waves, accelerating electrons along magnetic field lines and leading to precipitation.

It is assumed that a plasma injection occurs as follows: a flux tube filled with hot plasma is suddenly injected towards the planet, the particles of different energies undergo a differential drift due to the gradients and curvatures of the magnetic field. As shown by in situ measurements of energetic electrons, plasma injection show an increase in the flux of low-energy electrons before the increase in the flux of high-energy electrons (Mauk et al. 2002). Bonfond et al. (2017) were the first to highlight that certain localised auroral features show signs of differential drift with energy. The observed shift is thought to be the auroral counterpart of the differential drift typical of plasma injections into the middle magnetosphere. In other words, the shifts observed between precipitated electrons of different energies, in line with the differential drift expected in plasma injections, indicate that at least some of these outer emissions are caused by injected particles that are assumed to be part of the large-scale plasma transport. Thanks to joint observations by HST and the Hisaki telescope, Kimura et al. (2015) suggested that these emissions are linked to a rapid input of energy into the polar region by the internal plasma circulation ((Vasyliūnas cycle, Vasyliūnas (1983)). Bonfond et al. (2017) also state that if the reported events are correctly interpreted, a reconnection in the magnetospheric tail could succeed to the injections.This implies that in the magnetosphere, ~80 R_J separate the radial distance of the injections (10 R_J) from the radial distance of the reconnection X-line (90 R_J). On the basis of observations from Juno (Bonfond et al. 2017) the radial propagation speeds should be of the

order of 200 km/s. This speed corresponds to the highest value of radial transport speed estimated by Bagenal and Delamere (2011) at these distances (60-200 km/s). This value is also quite close to the Alfvén velocity estimates between Europa and the magnetic tail lobes, respectively, ~160 km/s (Kivelson et al. 2004) and ~350 km/s (Cowley et al. 2015). Bonfond et al. (2017) therefore propose two scenarios. However, they are rather speculative and require new observations to confirm them. The first proposes that, due to the instability of large-scale interchanges, a quantity of cold plasma suddenly migrates outwards in the magnetosphere, and that this cold plasma orbits Jupiter for three quarters of a complete rotation. It would then be released into the tail of the magnetosphere in the form of a plasmoid after reconnection. The second proposes that, in the middle magnetosphere, large-scale plasma injections generate significant perturbations in the magnetic field as they propagate at speeds close to the Alfvén speed towards the outer magnetosphere, then triggering reconnection in the tail.

During HST observations in the spring of 2007, Bonfond et al. (2012) noted an increase in the occurrence of features associated with plasma injections in UV and IR emissions. Bonfond et al. (2012) and Yoshikawa et al. (2017) have suggested that there is an indirect link between Io's volcanic activity and the occurrence rate of injections. Increased volcanic activity would be associated with an increase in the amount of plasma in the middle magnetosphere, which would favour the interchange of flux tubes and increase the rate of plasma injections, into the inner and middle magnetosphere. Bonfond et al. (2012) also report a rather rare phenomenon: on 7 June 2007, a large emission feature (15,000 by 6,000 km) was observed as far away as the predicted location of Io's footprint. When the Io footprint crossed this structure, it became so dim that it was no longer observable. In addition to the link between Io's volcanic activity and the rate at which injections

occur. During the quiet period of Io's volcanism, Kimura et al. (2015) observed a quasi-periodic (5-day) increase in auroral brightness. This 5-day period corresponds to the frequency of particle injection events detected by the Galileo satellite (Louarn et al. 2014). During the period of high Io activity, Yoshioka et al. (2018) observed that the brightness of auroral emission became more intense ~20 days after the onset of the increase in S^+ brightness in the plasma torus. They estimated that the aurora was twice as bright (or even more) than during quiet periods, and therefore estimated that it took about 10 days for the iogenic plasma moving outwards in the magnetosphere to affect the reconnection rate of the magnetosphere (Kimura et al. 2015). The increase in the brightness of S^+ in the iogenic plasma torus, followed by the increase in the brightness of the low-latitude emissions, could give us the global timescale for radial transport in Jupiter's magnetosphere (Louarn et al. 2014, Gray et al. 2016).

If Io's volcanic activity plays a role in the injection process, it is natural also to assess the potential role of the solar wind in this phenomenon. Mauk et al. (1999) suggested that clustered injections of energetic particles could be associated with rarefactions of the solar wind. Kimura et al. (2018) conducted a detailed analysis of auroral and solar wind data during the 2015 volcanic event. They concluded that these auroral brightenings were mainly caused by the increase in Io's mass loading rate.

Finally, Kimura et al. (2017) suggest from auroral observations with Hisaki and HST that auroral injection events and dawn storms may be linked. Thanks to joint observations by HST and Juno, Yao et al. (2020) report that dawn storms and signatures of plasma injections are often observed simultaneously. In addition, Bonfond et al. (2021) observed in UV auroral emissions that dawn storms give rise to plasma injection signatures,

establishing a direct link between dawn storms and auroral signatures of plasma injections. This link is confirmed by Ebert et al. (2021), who conducted a Juno multi-instrument study of dawn storms. They emphasise that the dawn storm emissions were created by processes that mapped to Jupiter's nightside and then migrated in the direction of planetary rotation. The high-latitude energetic electron and ion populations detected simultaneously with depleted lower energies are similar to particle observations in the equatorial magnetosphere associated with dynamical processes driven by interchange events, plasma injections and/or tail reconnection. More specifically, Yao et al. (2020) propose that reconnection in the magnetosphere are associated with dawn auroral storms. This is followed by one or more magnetic dipolarisations that corotate with the planet within a few hours, leading to plasma injections into the inner magnetosphere. These injections can produce multiple auroral signatures at all LT, as observed by HST (Haggerty et al. 2019, Yao et al. 2020). Following the reconnection process that produces the dawn storm, magnetic dipolarisation is triggered, which corotates with the planet and produces plasma injections into the inner region of the magnetosphere, leading to auroral injection signatures in the wide range of local time sectors. The reconnection can produce multiple dipolarisation events within a few hours, resulting in multiple auroral injection signatures (Yao et al. 2020).

2.3 Plasma injections in the Kronian magnetosphere

Plasma injections are also present in Saturn's magnetosphere (Mauk et al. 2005, Hill et al. 2005, Burch et al. 2005), and we can draw some useful conclusions from the similarities between Saturn and Jupiter. Internal sources of neutrals are important in Saturn's magnetosphere, and many of

these neutrals are ionised in the inner magnetosphere. While the volcanic moon Io is the main source of plasma in Jupiter's magnetosphere, the icy moon Enceladus plays a similar role in the Kronian magnetosphere. Many authors have studied the radial motion of injections into Saturn's magnetosphere (e.g. Burch et al. 2005, Hill et al. 2005, Paranicas et al. 2016). The aim of these studies was to quantify the plasma circulation process. The plasma permanently fed by Enceladus is evacuated outwards by the planet's rotation. As a result of this evacuation of plasma from the Kronian satellite, the hottest plasma moves inwards due to the conservation of magnetic flux. The inward motion of the hot plasma is faster than the outward plasma flow (Chen et al. 2010). Two-dimensional simulations based on the Rice convection model (e.g. Liu et al. 2010) show narrow longitudinal hot plasma fingers surrounded by narrow longitudinal cold plasma fingers moving outwards. At this stage, we cannot say whether these are plasma fingers or confined structures like plasma bubbles (Blanc et al. 2015).

The study of plasma injections into Saturn's magnetosphere has revealed the existence of two different types of injection. The first type of injection is associated with centrifugal instabilities, which are mainly observed at low energies. These plasma injections are limited in size (< 1 Saturnian radius (R_S)) and survive less than one rotation of Saturn (Hill et al. 2005). According to Azari et al. (2018), most events last 15 minutes or less. These injection events occur mainly between 6 and 9 R_S (Chen et al. 2010, Kennelly et al. 2013, Azari et al. 2018) and in the afternoon LT sector (Chen and Hill 2008). However, Kennelly et al. (2013) claim that the interchange movement preferentially occurs in the afternoon and midnight sectors. This difference could be due to an inaccuracy in the azimuthal plasma velocity profile used by Chen and Hill (2008).

The second type of injections are mainly associated with high energy electrons (>100 keV). They are larger in size (>1 R_S) and persist for one or more rotations of Saturn (Mauk et al. 2005, Paranicas et al. 2007, 2010). Their energy-time signatures are similar to the previous ones, but are more scattered due to their longer lifetime. These injections preferentially occur between 15 and 20 R_S (Mitchell et al. 2005, 2009) and in the night and morning sectors (Müller et al. 2010). It is widely assumed that these injections are produced by the dipolarisation of the magnetic field lines and the formation of plasmoids in the magnetic tail (Bunce et al. 2005, Hill et al. 2008, Mitchell et al. 2009).

As with Jupiter, the plasma injections present in Saturn's magnetosphere can be associated with auroral signatures. These signatures are produced by scattering processes (Radioti et al. 2013) or by pressure-induced electric currents flowing along the boundaries of the plasma injection cloud (Kivelson and Russell 1995, Radioti et al. 2013, Guo et al. 2018).

3 Instrumentation and data

This chapter discusses the relevant instrumentation and data obtained with the HST's Advanced Camera for Surveys (ACS) and Space Telescope Imaging Spectrograph (STIS), as well as the UVS on board the Juno spacecraft. It is partially based on the studies published by M. Dumont, D. Grodent, A. Radioti, B. Bonfond and J.-C. Gérard in the Journal of Geophysical Research: Space Physics in 2014 (Dumont et al. 2014) and by M. Dumont, D. Grodent, A. Radioti, B. Bonfond, E. Roussos, and C. Paranicas in the Journal of Geophysical Research: Space Physics in 2018 (Dumont et al. 2018).

3.1 Hubble Space Telescope

HST orbits the Earth at around 540 km, which gives it the great advantage of being very little altered by the atmosphere, in particular by the absorption of UV radiation. In addition, HST provides higher resolution than those from ground-based telescopes, in a large wavelength range spanning the UV and visible parts of the spectrum as well as a small portion of the IR spectrum. The first part of this work was carried out using data from HST, and more specifically from ACS and STIS. Mauk et al. (2002) reported that

auroral signatures of injection phenomena were observable on UV images of Jupiter from the HST. This first potential association of the detection of the signature of a magnetospheric injection, based on Galileo in situ particle instruments, with the quasi-simultaneous observation of its auroral UV counterpart, with HST, opened a new era in the study of the injection process in Jupiter's magnetosphere.

3.1.1 Hubble Space Telescope instrumentation

3.1.1.1 Advanced Camera for Surveys

The ACS instrument is composed of three cameras (Table 3.1) and each has specific functions (Ford et al. 1996) (https://hst-docs.stsci.edu/):

1. a wide-field charge coupled device (CCD) camera, with a spectral range of 350-1,100 nm, allows a broad study of the Universe. It is used, for example, to study the nature and distribution of galaxies, which characterise the evolution of the universe.

2. a high-resolution CCD camera capable of capturing detailed images of the sky over a spectral range of 170-1,100 nm. This makes it possible to explore the inner regions of galaxies and search for exoplanets, for example.

3. a solar blind channels (SBC) detector (with a Multi Anode Microchannel Array (MAMA) detector) working in the FUV spectral range (115-170 nm). It was primarily designed to observe hot stars or planets radiating in the UV. The SBC detector was used to acquire the ACS images used in this thesis.

3.1.1.2 Space Telescope Imaging Spectrograph

Covering wavelengths from NIR to FUV, STIS is a general-purpose imaging spectrograph (Woodgate et al. 1998)(https://hst-docs.stsci.edu/). This instrument is made up of three detectors (Table 3.1): a CCD camera and two MAMA detectors, one operating in near ultraviolet (NUV) and the other in FUV.

The key characteristics of ACS/SBC and STIS FUV MAMA detectors are listed in the table 3.1. Note that Jupiter's apparent diameter is 50 arcsec, so the planet is not fully visible in the field of view of these instruments. They capture about a quarter of the Jovian disk. In the HST observations used, the polar region of interest (on the order of 10×10 arcsec^2) is placed in one part of the detector, leaving most of Jupiter's disc outside the detector. This is because sunlight (>170 nm) is backscattered by Jupiter's atmosphere and saturates the ACS and STIS detectors. The polar regions are peculiar in that they contain a hydrocarbon layer that absorbs this UV solar emission and also increases the contrast of the auroral emissions relative to the atmospheric background. In order to project the images, the centre of the planet must be known. To determine this, a limb-fitting procedure is used, which consists of fitting the Jovian limb to a model planetary disk. Using this procedure, each pixel in the initial image is assigned a planetocentric latitude and longitude in SIII (Grodent et al. 2003b).

3.1.2 Hubble Space Telescope data

The HST UV database used in this thesis consists of a set of 1874 high-resolution UV images obtained from 1999 to 2007 with ACS and STIS on board HST (Table 3.2: GO 8171, GO 8657, GO 9657, GO 10140, GO

Table 3.1 – ACS/SBC and STIS FUV MAMA detector characteristics

	ACS/SBC	FUV MAMA
Spectral Response [nm]	115 - 170	115 - 170
Image Size [pixels]	1024×1024	1024×1024
Plate Scale [arcsec^2/pixel]	$\sim 0.034 \times 0.030$	0.0246×0.0247
Field of View [arcsec^2]	34.6×30.5	25.2×25.3

10507 and GO 10862). HST GO (General Observer) observing time is counted in orbits. Each orbit lasts 96 minutes and includes a useful period of time during which Jupiter can be observed: the orbital visibility period, about 45 minutes. The length and timing of the visibility period vary according to the declination of the target and the possible presence of scheduling constraints (https://hst-docs.stsci.edu/hom). Approximately 75% of the data set was obtained during a large HST campaign (GO 10862) that lasted for a few months in 2007 (Clarke et al. 2009). During this campaign, images were captured every day during single orbit or across consecutive multiple orbits. The regularity of the observations during this campaign means that the temporal variation of the elements investigated in this thesis can be analysed more accurately than during the previous campaigns used. We consider images obtained using the Long Pass MgF_2 (F115LP) and the Long Pass CaF_2 (F125LP) filters on ACS and the CLEAR and Strontium Fluoride (SrF2) filters on STIS (Table 3.3). They transmit the UV emissions of H_2 and H in the FUV domain. For each detector, two different filters were used: one allowing H ly-α to pass, i.e. ACS/SBC.F115LP and STIS/FUV.CLEAR, and the other not, i.e.

Table 3.2 – HST programs used

Type ID	Principal Investigator (PI Institution)	Configs	Allocated orbits	Start - End of campaign
GO 8171	John Clarke (Boston University)	STIS/CCD STIS/FUV-MAMA	14	Aug 8, 1999 - Nov 14, 2000
GO 8657	John Clarke (Boston University)	STIS/FUV-MAMA	35	Dec 14, 2000 - Jan 21, 2001
GO 9657	Ronald Elsner (NASA Marshall Space Flight Center)	STIS/FUV-MAMA	5	Feb 24, 2003 - Feb 26, 2003
GO 10140	Denis Grodent (Université de Liège)	ACS/SBC	6	Jan 25, 2005 - Mar 12, 2005
GO 10507	Denis Grodent (Université de Liège)	ACS/SBC	4	Feb 7, 2006 - Apr 14, 2006
GO 10862	John Clarke (Boston University)	ACS/SBC	69	Feb 20, 2007 - Jun 11, 2007
GO 11649	Jean-Claude Gérard (Université de Liège)	STIS/FUV-MAMA	3	Aug 31, 2009 - Sep 11, 2009
GO 12883	Denis Grodent (Université de Liège)	STIS/FUV-MAMA	9	Nov 14, 2012 - Jan 24, 2014
GO 13035	Sarah Badman (Lancaster University)	STIS/FUV-MAMA	20	Jan 1, 2014 - Jan 16, 2014
GO 13402	Jean-Claude Gérard (Université de Liège)	STIS/FUV-MAMA	3	Jan 8, 2014 - Jan 14, 2014
GO 14105	Jonathan Nichols (University of Leicester)	STIS/FUV-MAMA	47	May 16, 2016 - Jul 18, 2016
GO 14634	Denis Grodent (Université de Liège)	STIS/FUV-MAMA STIS/CCD	151	Nov 30, 2016 - Sep 7, 2018

ACS/SBC.F155LP and STIS/FUV.SrF2 (Table 3.3). The conversion from counts per second to brightness or power units is described in Bonfond et al. (2016) and based on the coefficients derived by Gustin et al. (2012).

The study of auroral emissions is facilitated when images of the emissions are projected onto a plane over the geographic pole. SIII coordinates can be associated with this polar projection. The center position of the planet is determined by the limb fitting procedure described by Bonfond et al. (2009). In addition, the luminous contribution of the planet's disc is removed to leave only the auroral emission (Bonfond et al. 2011). It allows to project the images on a polar map fixed in SIII, where structures corotating with the planet may be easily distinguished from those lagging corotation. The accuracy of the projection decreases toward the limb, where the pixels are stretched for geometrical reasons. Accordingly, we excluded from our analyses the features located less than 10° away from the limb plane.

The projections are made at an altitude of 400 km, in agreement with Bonfond et al. (2015), who measured the altitude of the main emissions and found a maximum value of 400 km. They then project at 400 km, as this is a compromise between the satellite footprints at 900 km and the main emissions, which are probably closer to 250 km. We can therefore assume that all the auroral emission is produced in an infinitely thin layer at an altitude of 400 km above the surface (pressure level of 1 bar). However, the vertical extension of the aurora is not taken into account, which leads to uncertainty about the position of the emission in terms of latitude and longitude. In the case of the observations of auroral regions made with Juno described in the following section, the majority of observations are made at closer to nadir, so the conversion of the instantaneous position of the pixels into latitude and longitude is considered to be reliable and relatively independent of the

Table 3.3 – Mean, minimum and maximum wavelengths for filters: ACS/SBC.F115LP, ACS/SBC.F125LP, STIS/FUV.SrF2 and STIS/FUV.CLEAR (Rodrigo and Solano 2020).

Filter ID	λ_{mean} (nm)	λ_{min} (nm)	λ_{max} (nm)
ACS/SBC.F115LP	141.915	115	198.067
ACS/SBC.F125LP	144.921	121.745	198.195
STIS/FUV.SrF2	146.93	124.524	189.818
STIS/FUV.CLEAR	139.178	115	188.842

altitude.

For Earth-based observations of Jupiter's aurora, the viewing geometry of the southern Jovian aurora is less favorable than in the north. In the southern hemisphere, the magnetic pole is relatively close to the jovigraphic pole and a limited amount of the most equatorward emission can be observed, whatever the CML. In the northern hemisphere, the magnetic dipole axis is tilted significantly relative to the spin axis, and when the dipole axis is pointing towards the observer, only a small part of the auroral emission is hidden beyond the limb. The counterpart is that only a very small part of the aurora is visible when the dipole is pointing away. This leads to a strong bias in the CML. The database used contains a limited range of CMLs that optimise the display geometry. The bias was accounted, by normalizing the data (more details in Section 4.3), for in the present analysis which relies on a large set of 1123 images of the northern hemisphere and 751 images of the southern hemisphere.

3.1.3 HST-STIS spectral observations

As we saw in Section 1.4.2, auroral emissions are associated with energetic particles penetrating the planet's upper atmosphere, exciting H and H_2, which then release emissions in the Lyman series of H (in particular Ly-α), as well as in the Lyman and Werner band systems of H_2 (Hue et al. 2019). These two wavelength ranges are used to determine the H_2 CR defined by Yung et al. (1982). As the Lyman and Werner band systems of H_2 are located at wavelengths below 140 nm, this implies that this band is located in the methane absorption region. The CR can be used to determine the characteristic energy of auroral precipitation from the spatial variations in methane absorption for the different components of the aurora. The spatial distribution of CR within the auroral signatures of plasma injections gives us information about the energy distribution of the particles that make them up (Gustin et al. 2016). The higher the CR, the higher the energy of the particles. Spectra of the FUV Jovian auroral emissions are obtained with the STIS FUV-MAMA imaging spectrograph. The processing of these observations has been described by Gérard et al. (2014). Briefly, the spectral images are reconstructed from the time-tag data accumulated during slit scans across the polar regions. Time-tag mode records the positions and arrival times of incoming photons. The G140L grating mode[1] provides a spectral resolution of 1.2 nm. For each HST visit (GO 13402), two images are created, one for short wavelengths, between 123 and 130 nm, and one for long wavelengths, between 155 and 162 nm.

[1]The G140L grating mode is suitable for observations with efficient, spatially resolved spectroscopy offering broad spectral coverage in the UV but where high spectral resolution is not required. A spectral range of 115 to 170 nm is covered in this mode.

3.2 Juno Spacecraft

The last part of my thesis is based on observations from the Juno spacecraft. The Juno spacecraft has been in orbit around Jupiter since 4 July 2016. Juno's prime mission lasted just over 5 years and included 35 science orbits, labelled perijove (PJ) (Figure 3.1). In July 2016, the Juno spacecraft was placed in a highly elliptical polar orbit (e = 0.98) around Jupiter with a period of 53 days. The perijove, the point in the orbit where Juno is closest to Jupiter, is $\sim$ 1.05 R_J and the apojove, the point in the orbit where the spacecraft is farthest from Jupiter, is $\sim$ 113 R_J (Connerney et al. 2018). Typically eight hours near-perijove, it is the most important for Juno's UVS instrument. The oblateness of Jupiter leads to a precession of Juno's orbit, causing the tilt of the semi-major axis with respect to the equatorial plane to move gradually southwards from -4.6° to -33.5° (Figure 3.1 panel (b)) (Bagenal et al. 2017). Initially, the aurora is observed in each hemisphere for four hours during the PJ. However, due to the evolution of the orbits, the spatial coverage of the aurora in the northern hemisphere decreases as the orbits evolve. Finally, the spacecraft's orbit evolved at the end of the prime mission to begin Juno's transition to exploring the Jovian system, with additional flybys of Europa and Io, as well as fly through of Europa's torus and Io. The mission will end in September 2025 (https://www.nasa.gov).

Juno is spin-stabilized with a rate of 2 rotations per minute (i.e. 30 seconds spin periods) and carries ten science instruments, three of which study Jupiter's aurora in three different wavelength ranges: UV, IR and Radio, respectively the UVS the Jupiter InfraRed Auroral Mapping (JIRAM) and the Waves instruments (Gladstone et al. 2017, Mura et al. 2017, Kurth et al. 2017). The use of Juno to study the aurora is extremely useful, as observations at high latitudes in the polar regions gives us access to high resolution

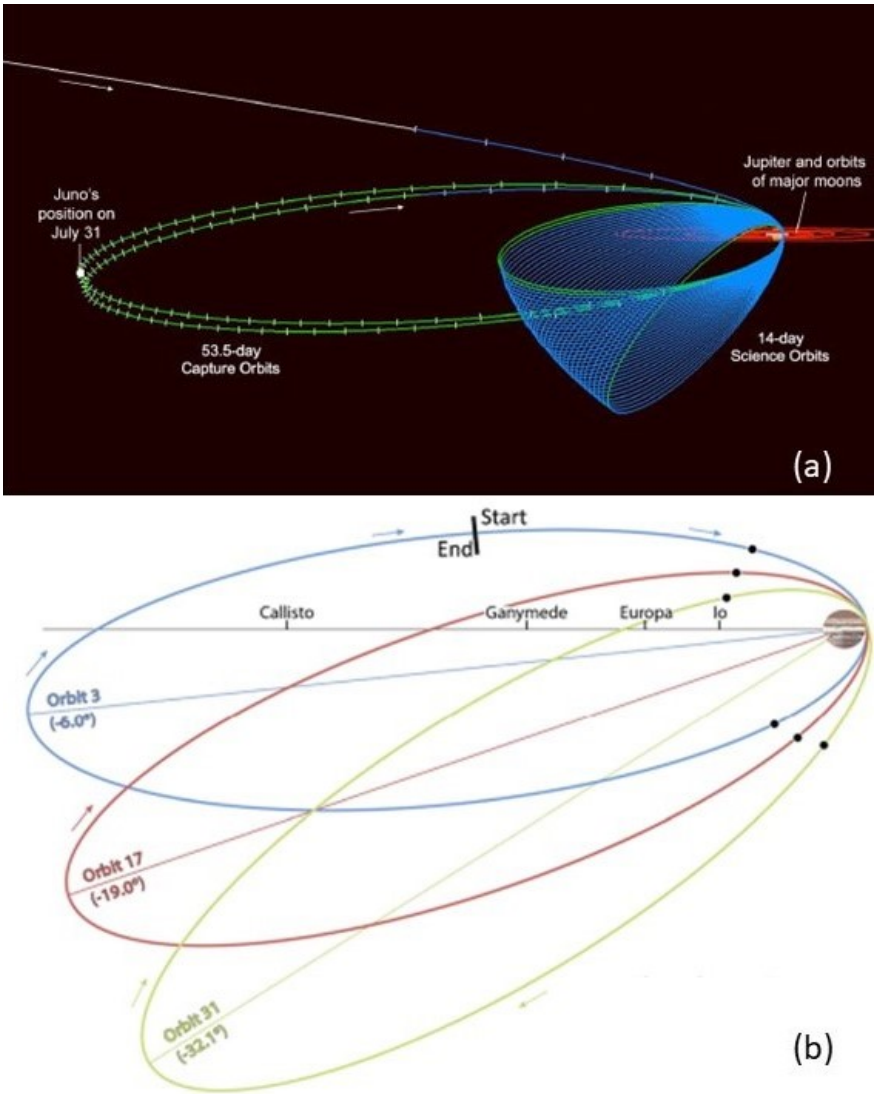

Figure 3.1 – Panel (a) shows Juno's orbits, including its two long and stretched capture orbits. On the left is the spacecraft's position on 31 July. Image credit: NASA / JPL-Caltech. Panel (b) shows the evolution of Juno's orbit over time: PJ3 (December 2016), PJ17 (December 2018) and PJ31 (December 2020). (adapted from Bagenal et al. (2017)).

auroral observations, but also to regions that were previously impossible to observe with an Earth-orbiting satellite, in particular the night-side sector of the polar regions. These observations allow us to complete our knowledge of the auroral signatures of plasma injection in Jupiter's aurorae. Although a lot of unprecedented information on the auroral emissions may be derived from these three instruments.

In this thesis, we focused on the FUV auroral emissions observed with the UVS instrument, using the data from the first 18 PJ, from PJ1 to PJ19 (no scientific data were acquired during PJ2) (Table 3.4).

3.2.1 Juno instrumentation : Ultraviolet Spectrograph

Juno-UVS is a photon-counting imaging spectrograph with a spectral bandpass of 68–210 nm. The spectrograph entrance slit has three contiguous segments with fields of view of 0.2°×2.5°, 0.025°×2°, and 0.2°×2.5°, forming a "dog bone" shaped slit (Gladstone et al. 2017). This instrument was specifically designed to study the Jovian aurora in the UV. Juno-UVS operates in scan mode, scanning Jupiter's auroral regions once per 30-second due to the rotation of spacecraft. A flat scanning mirror is located at the front of the instrument, which allows to observe in directions ±30° perpendicular to the Juno's spin plane. This makes it possible to target different parts of the aurora when Juno is very close to Jupiter and the integrated field of view of UVS is much smaller than the auroral region. This allows different regions of the aurora to be targeted by its controlled position. Successive bands acquired near perijove are then projected onto polar maps and combined to produce near perijove a complete high-resolution reconstructed image of the aurora, as described below (Bonfond et al. 2017).

Table 3.4 – Characteristics of reconstructed FUV spectral image used

PJ	N/S	Date	Start time	Stop time	SIII longitude of Io (deg)	SIII longitude of the Sun (deg)	Juno altitude (R_J)
PJ1	N	27 Aug. 2016	09:51:49	11:21:24	293 - 335	75 - 129	3.75 - 1.84
	S		13:51:39	14:30:36	44 - 62	220 - 244	1.17 - 2.08
PJ3	N	11 Dec. 2016	14:43:50	15:22:16	215 - 233	1 - 24	2.95 - 2.11
	S		17:37:33	18:41:42	295 - 325	106 - 144	0.53 - 2.03
PJ4	N	02 Feb. 2017	11:31:54	12:12:30	200 - 218	299 - 324	1.74 - 0.78
	S		13:38:07	14:20:15	258 - 277	15 - 41	0.69 - 1.69
PJ5	N	27 Mar. 2017	03:55:17	07:07:10	62-151	77-193	5.89-2.19
	S		09:27:46	10:30:27	216 - 245	278 - 316	0.57 - 2.05
PJ6	N	19 May 2017	01:01:35	04:10:50	55 - 142	27 - 141	5.94 - 2.31
	S		06:23:17	07:37:29	204 - 238	221 - 266	0.28 - 2.01
PJ7	N	10-11 Jul. 2017	22:42:46	00:21:00	64 - 110	357 - 57	4.01 - 1.94
	S		02:30:12	03:24:34	169 - 194	135 - 168	0.56 - 1.84
PJ8	N	01 Sep. 2017	20:12:04	20:32:10	68 - 77	321 - 333	2.01 - 1.54
	S		22:24:34	23:18:21	129 - 154	41 - 73	0.56 - 1.84
PJ9	N	24 Oct. 2017	16:25:13	16:56:26	36 - 51	238 - 257	1.56 - 0.81
	S		18:29:10	18:57:23	94 - 107	313 - 330	0.82 - 1.49
PJ10	N	16 Dec. 2017	16:35:59	17:08:08	115 - 129	299 - 318	1.64 - 0.88
	S		18:38:23	19:33:04	171 - 196	13 - 46	0.70 - 1.99
PJ11	N	07 Feb. 2018	12:52:38	13:40:11	85 - 107	218 - 247	1.12 - 0.11
	S		14:39:47	15:40:22	134 - 162	283 - 319	0.86 - 2.28
PJ12	N	01 Apr. 2018	06:28:11	08:03:20	340 - 24	40 - 98	4.12 - 2.14
	S		10:18:11	11:30:17	87 - 120	179 - 223	0.49 - 2.18
PJ13	N	24 May 2018	03:46:08	04:55:09	339 - 11	356 - 39	2.39 - 0.75
	S		06:20:12	07:11:26	50 - 74	90 - 121	0.67 - 1.89
PJ14	N	16 Jul. 2018	02:53:56	04:52:37	28 - 83	19 - 91	3.03 - 0.33
	S		06:03:07	06:58:14	115 - 141	134 - 167	0.80 - 2.10
PJ15	N	06-07 Sep. 2018	23:44:18	00:50:24	14 - 44	319 - 359	1.80 - 0.26
	S		01:52:25	02:38:26	73 - 94	36 - 64	0.68 - 1.78
PJ16	N	29 Oct. 2018	20:08:41	20:49:16	347 - 6	243 -267	1.08 - 0.18
	S		21:55:49	22:46:00	37 - 60	308 - 338	0.89 - 2.08
PJ17	N	21 Dec. 2018	16:17:39	16:54:35	314 - 331	157 - 180	0.72 - 0.07
	S		18:06:14	18:30:01	4 - 15	223 - 237	1.29 - 1.85
PJ18	N	12 Feb. 2019	16:43:02	17:19:10	39 - 56	227 - 249	0.94 - 0.16
	S		18:15:06	18:56:14	81 - 100	283 - 308	0.67 - 1.66
PJ19	N	06 Apr. 2019	11:08:41	11:40:21	318 - 332	79 - 98	1.28 - 0.53
	S		12:58:57	13:55:05	9 - 35	146 - 180	0.77 - 2.09

3.2.2 Juno Ultraviolet Spectrograph data

The instrumental data is an inventory of photon detection events characterised by the X and Y position of the count on the detector. They represent the spectral dimension (i.e. wavelength) and the spatial dimension (i.e. position) along the slit, respectively, forming a 2048×256 (spectral × spatial) pixel matrix. UVS captures swaths of auroral emission every 30 seconds. Their size varies according to the distance between Juno and Jupiter. The images of the aurora are made up of the bands as they are acquired, assembled and projected onto polar maps to obtain a high-resolution image of the aurora as the field of view moves across the planet (Figure 3.2). When the images were generated, the projection altitude was set to 400 km above the planetary surface (Bonfond et al. 2015). To obtain information about the brightness of the aurora, the number of counts is converted into kilo-Rayleighs and linked to the effective surface area determined during the Juno cruise to Jupiter. There is an uncertainty associated with the temporal variability of the effective area which is attempted to be minimised by a calibration factor. By definition, the brightness used in this thesis is the total EUV plus FUV brightness emitted by H_2. However, to scale the entire UV spectrum of the Lyman and Werner bands of H_2, the brightness measured in the 155-162 nm region was multiplied by 8.1, based on an unattenuated H_2 spectrum at 300 K without self-absorption (Bonfond et al. 2017). UVS cannot observe the entire aurora during a single spin in the PJ, so all auroral images are assembled by performing a weighted sum of successive spins, with the most recent spin having a higher weight. Each weighting factor is equal to one tenth of the previous factor. To produce the final brightness map, the weighted sum of the counts is divided by the weighted sum of the

time exposure maps. Gaps in the swaths are observed, either because the buffer memory was saturated (i.e. when particularly intense elements were produced), or because of high radiation levels (i.e. when a count threshold is exceeded, the instrument can be forced to reduce its voltage) (Bonfond et al. 2017, Bonfond et al. 2021).

Finally, it should be pointed out that there are sources of uncertainty affecting estimates of the total auroral emitted power. There are three main sources of uncertainty:

1. systematic calibration uncertainties, associated with the conversion of the measured count rate into luminosity and energy flux of the precipitated electrons , estimated at 16% (Gérard et al. 2019),

2. depending on the number of auroral counts in the region of interest, the uncertainty of the shot noise is less than about 5% for small spots and about 1% for the largest features such as dawn storms,

3. the selection uncertainty, which is a function of the definition of the region of interest and can be up to 15%.

Combination of these three sources of uncertainty amounts to a reasonable estimate of the emitted power uncertainty on the order of 25% (Bonfond et al. 2021).

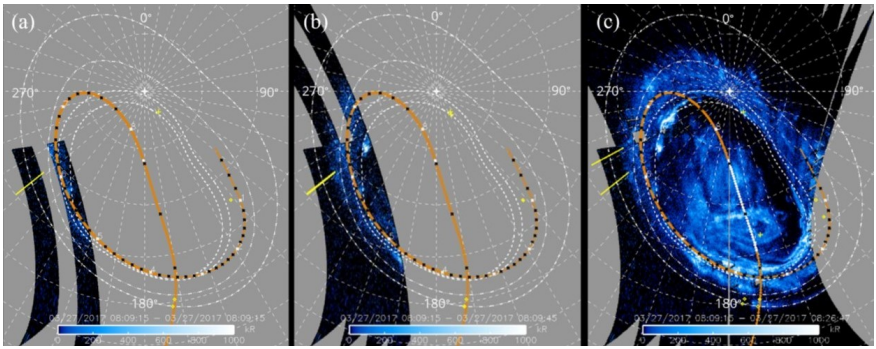

Figure 3.2 – Polar projection of Jupiter's northern aurora observed by Juno-UVS on 27 March 2017 (PJ5). A polar grid (dotted lines) is overlaid with 10° spaced SIII meridians and parallels. The statistical position of the main emissions (Bonfond et al. 2012) is represented by two dotted contours: compressed magnetosphere (innermost) and expanded magnetosphere (outermost). The footpaths of Io and Ganymede are shown as dashed lines. Panel (a) shows an image corresponding a single spin, taken at 08:09:15 Universal Time (UT). The image in panel (b) combines two spins taken at 08:09:15 UT and 08:09:45 UT. And panel (c) shows a complete view of Jupiter's northern aurora, made by combining spins data taken between 08:09:15 UT and 08:26:47 UT. The subsolar longitudes at the beginning and end of the combined data are indicated by the yellow lines. The orange line represents the Juno magnetic footprint according to the JRM09 model (Haewsantati 2022).

4 Jupiter's equatorward auroral features: possible signatures of magnetospheric injections

This chapter is based on the paper written by M. Dumont, D. Grodent, A. Radioti, B. Bonfond and J.-C. Gérard and published in the Journal of Geophysical Research: Space Physics in 2014 (Dumont et al. 2014).

4.1 Introduction

In this chapter, I focus on isolated equatorward auroral features showing the same appearance as the auroral signature of plasma injection previously observed by Mauk et al. (2002). All auroral features analyzed in this chapter were selected, from the HST UV database obtained from 1999 and 2007 with the ACS and the STIS on board of HST (Table 3.2: GO 8171, GO 8657, GO 9657, GO 10140, GO 10507 and GO 10862) and described in Section 3.1.2 . These auroral features satisfy some specific criteria: they are (1) equatorward of the main emission, (2) detached from the main emission (isolated), (3) compact structures (longitudinal mean extent $< 6°$ and latitudinal mean extent $< 3°$) that are not secondary arcs or diffuse emissions, (4) they must evolve regardless of the rest of the auroral emission's

behavior, and (5) they are not satellite footprints. In this study, I excluded the features located less than 10° away from the limb plane, as mentioned in Chapter 3, because the accuracy of the projection decreases towards the limb, where the pixels are stretched for geometric reasons. This means that about 10% of the structures were rejected on this criterion. Application of these criteria resulted in the identification of 130 individual UV auroral features. Figure 4.1 shows the polar projection in SIII coordinates of an image of the northern UV aurora obtained with STIS on 18 December 2000. In this example, the main emission (e.g. Grodent et al. 2003a), the polar emissions (e.g. Grodent et al. 2003c), Ganymede's footprint (e.g. Grodent et al. 2009) are indicated and the region of equatorward emissions (e.g. Radioti et al. 2009b) is the region equatorward of the main emission. In the latter region an isolated patchy auroral structure is highlighted with a yellow square, this equatorward auroral feature fulfils the selection criteria.

More specifically, in this chapter, I statistically investigate the properties of the isolated equatorward auroral features and establish their possible association with magnetospheric plasma injections. To carry out this study, I analyze observations of Jupiter's auroral regions and compare them with statistical results obtained with in situ instruments. I analyze their location, emitted power, lifetime and I compare their observed properties with those of magnetospheric injections detected by the Galileo spacecraft. Moreover, I compare the amount of magnetic flux moving towards and away from the planet in the Jovian magnetosphere, using a combination of remote and in situ observations, to study the importance of plasma transport associated with injection signatures in the Jovian magnetosphere.

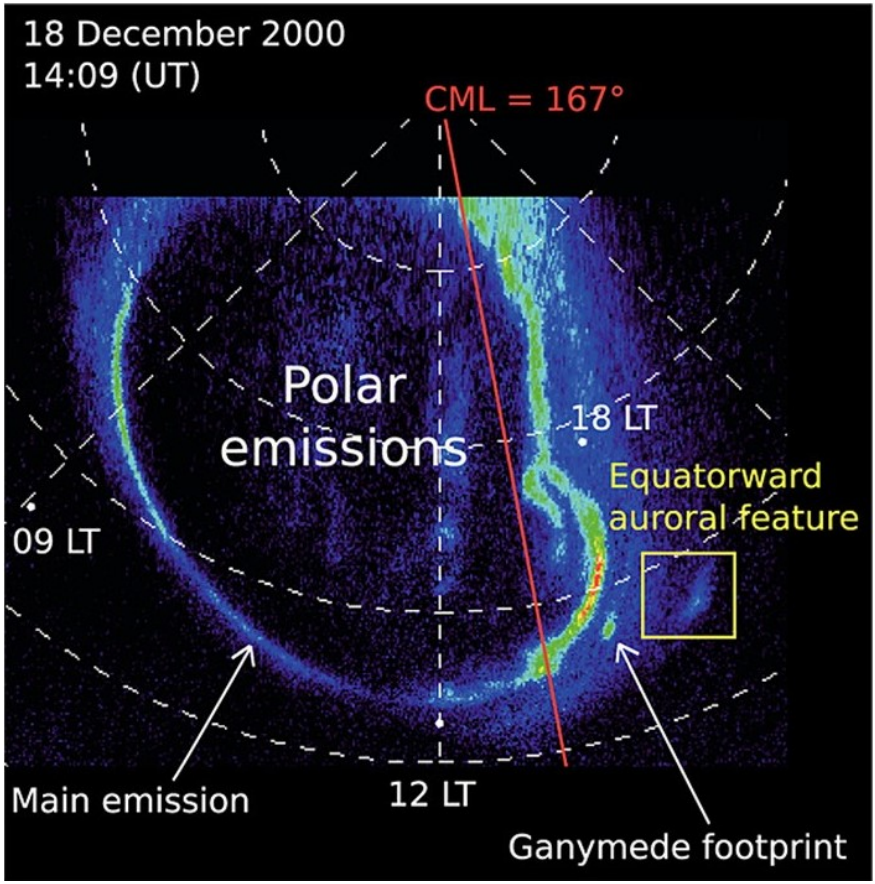

Figure 4.1 – Polar projection of an HST/ STIS image in a reference frame fixed in SIII. The image shows the northern Jovian aurora on 18 December 2000 at 14:09 UT. The central meridian longitude (red line) is 167° SIII. In this particular case, noon (12 LT) is towards the bottom and dusk (18 LT) to the right. The main auroral features are indicated: the main emission, Ganymede footprint, polar emissions and equatorward auroral feature. In this case, the equatorward auroral feature has a latitudinal extent of ~2,083 km and a longitudinal extent of ~ 3,578 km in the ionosphere.

4.2 Analysis of equatorward isolated auroral structures

As mentioned above, 130 auroral features have been identified in the dataset of images acquired between 1999 and 2007 by HST. The complete list of events are available in the Supporting Information of Dumont et al. (2014). These auroral emissions were observed during 52 different days in the northern hemisphere and 33 different days in the southern hemisphere, corresponding to an average number of ~ 1.5 auroral features per day. Figure 4.2 displays a histogram giving the percentage of days during which a certain number of auroral features were visible in the northern (red) and in the southern (blue) hemispheres. The median value is 1 auroral feature per day. In ~ 60% of the cases in the north and ~ 50% of the cases in the south, at least one auroral feature is present. These emissions are relatively frequent since they are observed on average at least every other day. Specifically, days during which only one auroral feature is observed represent 30% of the cases in the north and 20% in the south. Occasionally, up to 8 simultaneous equatorward isolated auroral features are observed both in the northern and southern hemispheres.

Some of the morphological characteristics of the equatorward auroral structures are displayed in Figure 4.3. Panels a and b of Figure 4.3 show the ionospheric azimuthal and latitudinal extent of the auroral features in km. I determine the ionospheric longitudinal and latitudinal extent of the auroral features from the coordinates of the four extreme points of the auroral structure in the northern (red) and in the southern (blue) hemispheres. Both longitudinal and latitudinal dimensions range between 640 km and 15,300 km. The largest auroral structure measures 11,700 km latitudinally and 14,400 km longitudinally. The latitudinal and azimuthal extents of the au-

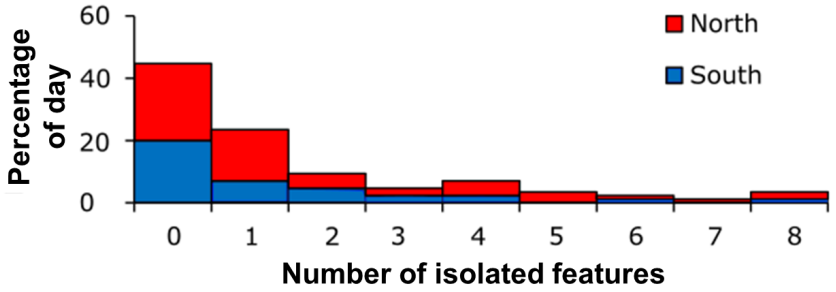

Figure 4.2 – Histogram of isolated transient auroral structures observed in the north (red) and in the south (blue). The percentage of Earth days during which a certain number of isolated auroral features, between 0 and 8, were observed in the database that we considered. On average, more than half of all observations present one or more signatures of isolated equatorward auroral features.

roral features have the same order of magnitude as the auroral structure's extents associated with the auroral signature of an injection (6,000 km by 15,000 km) observed at Jupiter by Bonfond et al. (2012). This latter structure is included in the present data base and represents one of the largest selected structure. Panel c of Figure 4.3 shows the power emitted in the EUV and FUV Lyman and Werner bands by these auroral features inferred from the conversion coefficients given by Gustin et al. (2012). The power ranges from 2 10^{-2} GW to 113 GW, with the majority of the features characterized by an emitted power between 5 and 10 GW. Significant temporal variations of the power (around 50% between minimum and maximum) are systematically observed in the whole dataset. The uncertainty on the count rate and on the background removal was negligible compared to the inaccuracy of the boundary selection procedure of the auroral features. To estimate this uncertainty, each manually selected pixel forming the contour of the feature is replaced with a random direct neighbour and we estimate the power inside this new contour. For each feature of the dataset, we repeat this op-

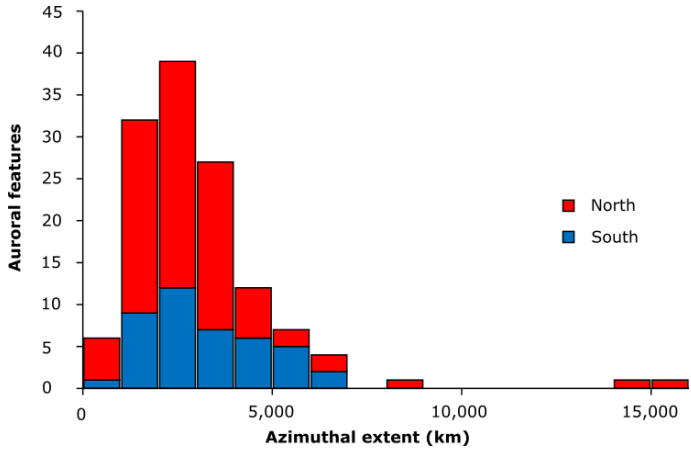
45
40
35
30
25
20
15
10
5
0
Auroral features
North
South
0
5,000
10,000
15,000
Azimuthal extent (km)

(a)

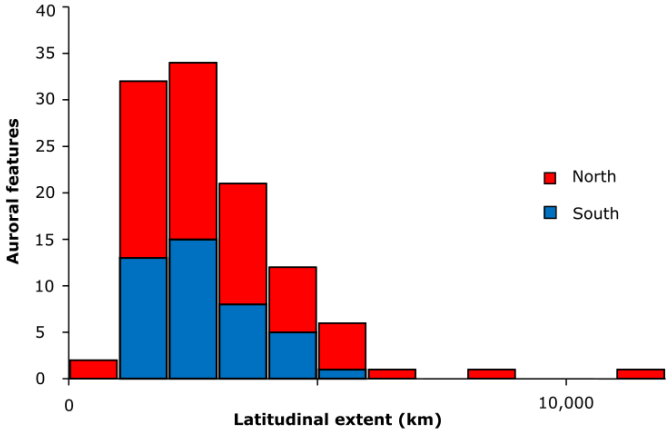
40
35
30
25
20
15
10
5
0
Auroral features
North
South
0
10,000
Latitudinal extent (km)

(b)

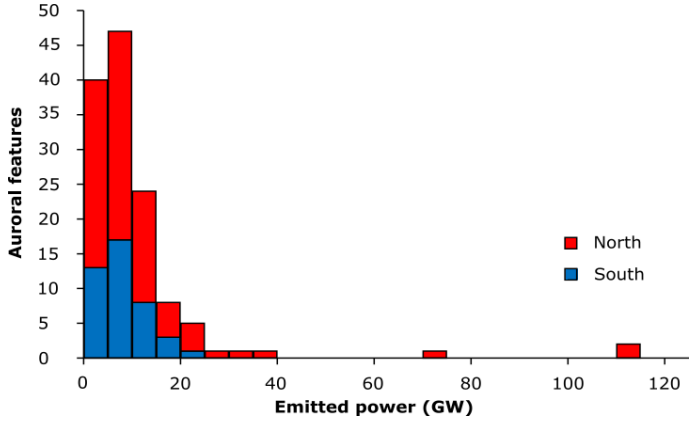

(c)

Figure 4.3 – Histograms displaying the distribution of the auroral features characteristics: (a) azimuthal extent, (b) latitudinal ionospheric extent, both inferred from the auroral UV morphology and (c) power emitted in the EUV+FUV Lyman and Werner bands by the auroral features selected in the north (red) and in the south (blue). Both azimuthal and latitudinal dimensions range between 640 and 15,300 km. The most probable emitted power of the features is between 5 GW and 10 GW.

eration 100 times and we compute the standard deviation of the emitted power, which typically lies around 10% of the initial value. The observed fluctuations are larger than the standard deviation. Thus these variations provide strong evidence that the equatorward auroral features are highly variable. The average time between two consecutive maxima of the emitted power is 8 ± 3 minutes. Such timescale should be compared with the typical periodicity of 18 minutes highlighted by Louarn et al. (2001) for the energetic events they associate with the injection signatures. Using observations from several instruments on board Galileo, Louarn et al. (2001) analysed a strong magnetospheric disturbance characterised by multiple injections of energetic particles into the inner magnetosphere, producing magnetic oscillations correlated with injections of energetic electrons with a periodicity

of 18 minutes, between 10 and 13 R_J. This typical periodicity is thus on the same order of magnitude as the average time between two consecutive maxima of the auroral emitted power. These measurements were not concurrent, which could explain the factor of 2 between the two values.

The observed lifetime of each selected auroral UV feature in the northern and in the southern hemispheres is defined as the time range during which each feature is bright enough to be observed with HST STIS or ACS (with a sensitivity threshold of a few kR, depending on the background level of the planetary disk). The observed lifetime of the auroral features varies between 5 and 213 minutes. 71% of the observed lifetime of the auroral features are between 30 and 50 min corresponding to one orbit time observation (approximately 45 min). If some auroral features have an apparent lifetime shorter than the duration of one HST orbit, this is because they move out of the field of view of the camera before the end of the orbit. In the present data set, we were not able to capture the full life cycle of an equatorward auroral feature in a single orbit. In the very few cases during which several consecutive HST orbits were obtained, auroral signatures persisted throughout the sequence. We performed a brightness (emitted power) analysis similar to that of Radioti et al. (2009a). Unfortunately, the results of the analysis are not totally conclusive since, contrary to the Saturn cases presented by Radioti et al. (2009a), the lifetime of the auroral structures is longer than the observation. As a result, it is not possible to derive Maxwellian full-width-at-half-maximum lifetimes that could have been directly compared with those obtained by Radioti et al. (2009a). Still, this analysis shows that the phenomenon associated with the auroral structures is taking place for long periods of time, presumably on the order of several hours.

4.3 Comparison of auroral emissions with in situ Galileo observations

The aim of this section is to highlight the common properties between the mapped auroral structures and the plasma injections present in the equatorial plane of Jupiter. To make this comparison, we magnetically map the center position of the auroral signatures from the ionosphere to the equatorial plane using the VIPAL magnetic field model (Hess et al. 2011) (more details in Section 1.3.1). VIPAL was the most suitable magnetic field model available, for auroral features appearing between the auroral footpaths of Io and Ganymede, which is the region where most injections studied by Mauk et al. (1999) are located. Panels a and c of Figure 4.4 show the mapped position and radial distance of the auroral features in SIII longitude normalized for all SIII longitudes in the northern (red) and in the southern (blue) hemispheres. This normalization accounts for an observational bias in the selected database resulting from the limited range of CML which was adopted to optimize the viewing geometry. To achieve this, the equatorial plane is divided into 8 sectors of equal size (45°) with the origin of the first sector set to 0°of SIII longitude. The normalization takes into account for the number of times the sectors have been observed in the entire database. In each sector, the number of auroral features is divided by this number. All these values are then normalized so that the total number of observed auroral features is 130. We estimate the probability of the presence of auroral features assuming a binomial distribution and the error bars in panels a and c of Figure 4.4 correspond to the standard deviation of the distribution. The magnetospheric source regions of the selected auroral features appear to be mapped at all longitudes and at radial distances between 7 and 62 R_J. The most probable radial position of the mapped auroral features lies between 10 and 13 R_J, and their most probable equatorial longitude lies

between 45°and 135°, for the northern features, and between 45°and 90°of equatorial longitude for the southern ones. Only 15% of the cases magnetically map beyond 40 R_J. The latter population should be considered with caution since the VIPAL model becomes increasingly inaccurate beyond Ganymede's orbit (15 R_J). Panels b and d of Figure 4.4 show the spatial distribution of energetic particle injections identified by Mauk et al. (1999) in Galileo EPD measurements. They are present at all SIII longitudes, i.e. at no preferential longitude, and at radial distances between $\sim$ 9 R_J and $\sim$ 27 R_J. These two distances are the minimum and maximum radial positions sampled by Galileo during the time periods considered in the in situ study of Mauk et al. (1999), for which, the most probable radial distances were found between 10 and 12 R_J.

Even though HST and Galileo spacecraft observations are not contemporary, the spatial distribution of the events may be compared. When magnetically mapped back in the equatorial plane, the auroral features appear at all SIII longitudes and only beyond Io's orbit. These results are consistent with the finding of Mauk et al. (1999) concerning injections observed in situ. The main difference between the spatial distribution of events inferred from HST and Galileo stems from their different sampling methods. Indeed, HST observations map to a large portion of the dayside magnetosphere but most of the nightside magnetosphere is out of reach of the telescope. On the other hand, the Galileo spacecraft was obviously not able to sample all LTs and all local distances simultaneously. Despite these observation biases, we find that the distributions of the detected features are in good agreement between HST and Galileo observations (Figure 4.4), we suggest that the equatorward auroral features that we considered for this study are possibly associated with energetic particle injections in the Jovian magnetosphere. If the auroral structures studied are connected to

auroral signatures of injections, the present analysis complement the study of Mauk et al. (2002) which was based on one unique case of simultaneous HST and Galileo observations. Assuming that these isolated auroral features are related to plasma injection, this is the first time that injection signatures are observed beyond 27 R_J.

The observations made with interplanetary probes such as Galileo, provide only local properties of the magnetosphere. By contrast, the auroral emissions provide a global picture of the magnetosphere and allow us to perform a more complete statistical study. Importantly in this study, we show, for the first time, that several auroral signatures of injections may be observed simultaneously at different LT sectors, indicating that simultaneous injections may occur at the same time from different locations in the magnetosphere rather than from a unique and localized region in Jupiter's aurora. It should be noted that Radioti et al. (2013) reported more than one auroral signature of injection observed simultaneously in Saturn's aurora. In addition, multifluid MHD simulations of Saturn's magnetospheric plasma flows by Kidder et al. (2009) are showing several simultaneous events. The presence of simultaneous auroral signatures of injections could be the consequence of the interchange instability; since ideal magnetohydrodynamic numerical simulations, such as those of Yang et al. (1994), suggest that the Io torus breaks up into several long fingers implying several injections at different LTs in the equatorial plane. Alternatively, simultaneous injections may result from the long lifetime of some events. Indeed, injections are not necessarily created simultaneously. For example, injections successively generated at the same LT sector will rotate with Jupiter and thus appear at different LTs on HST images.

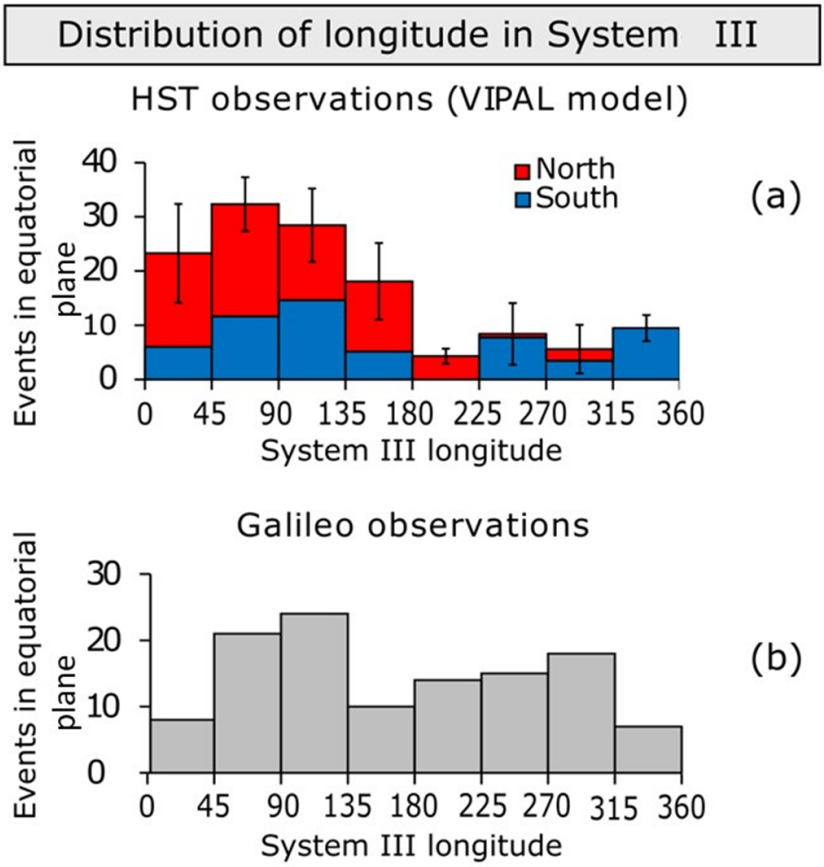
Distribution of longitude in System III
HST observations (VIPAL model)
Events in equatorial plane
North
South
(a)
0
10
20
30
40
0 45 90 135 180 225 270 315 360
System III longitude
Galileo observations
Events in equatorial plane
(b)
0
10
20
30
0 45 90 135 180 225 270 315 360
System III longitude

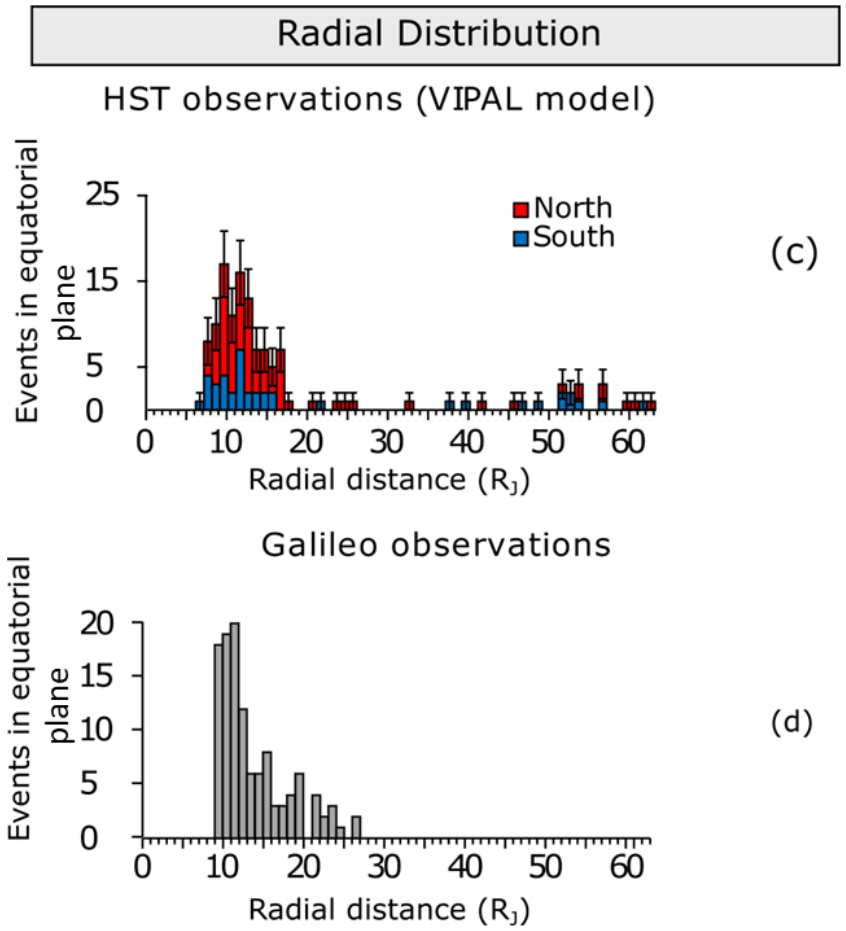

Figure 4.4 – (a) Histogram of the magnetically mapped SIII longitude of the auroral features. (c) Histogram of the radial position of the auroral features. Values in the north and in the south are indicated in red and blue, respectively. The error bars are drawn assuming a binomial law for each bin and they correspond to the standard deviation of the distribution. The most probable radial position of the mapped auroral features is between 10 and 13 R_J. The most probable longitudinal position lies between 45°and 135°in the northern hemisphere and between 45°and 90°in the southern hemisphere. (b) Histogram of the SIII longitude of the energetic particle injections detected by Galileo (adapted from Mauk et al. (1999)). (d) Histogram of the radial position of the energetic particle injections detected by Galileo (adapted from Mauk et al. (2002)). Figures 4b and 4d show that the most probable radial position of the injection events considered by Mauk et al. (1999) is between 10 and 12 R_J and they display no preferential longitude.

4.4 Plasma transport, magnetospheric structures studied and injections

The location of the equatorial source region of the auroral signatures studied is reported in Figure 4.5. Figure 4.5 summarizes the results displayed in Figures 4.2 and 4.4 with the location of mapped structures observed in the north (red diamonds) and in the south (blue squares). These auroral features magnetically map between 7 R_J and 62 R_J. For 71% of the cases in the north and 64% of the south ones, the signatures map between the orbits of Io and Ganymede. Only 12% of the cases in the north and 22% in the south are mapping beyond 40 R_J. The auroral features studied here are never observed inward of the Io footprint. Therefore, the orbit of Io appears as a natural inner boundary for the phenomenon at the origin of the auroral signatures. The phenomenon studied may be related to centrifugal driven interchange events, such as the inward moving interchange driven flux tubes balance the outward flux. In this case, the studied events move in as far as the mass loading does such as the Io's torus is the inner boundary of the phenomenon. From the data set of Mauk et al. (1999), this observation could not be made for injections because the minimal radial position sampled by Galileo in Mauk et al.'s study is 9 R_J.

The azimuthal distribution of the magnetospheric counterpart of the studied auroral structures spans a large LT sector from 06 LT to 20 LT. However, it should be noted that a large LT region is not accessible to HST, owing to Earth-based observing geometry constraints (dashed region in 4.5). We observe 65% of events in the sector between noon and dusk, which represents an average of 11% of events per LT hour. This is significantly more than in the two other sectors (dawn to noon; dusk to midnight) where we observe on average 4.5% of events per LT hour between dawn and noon and 3%

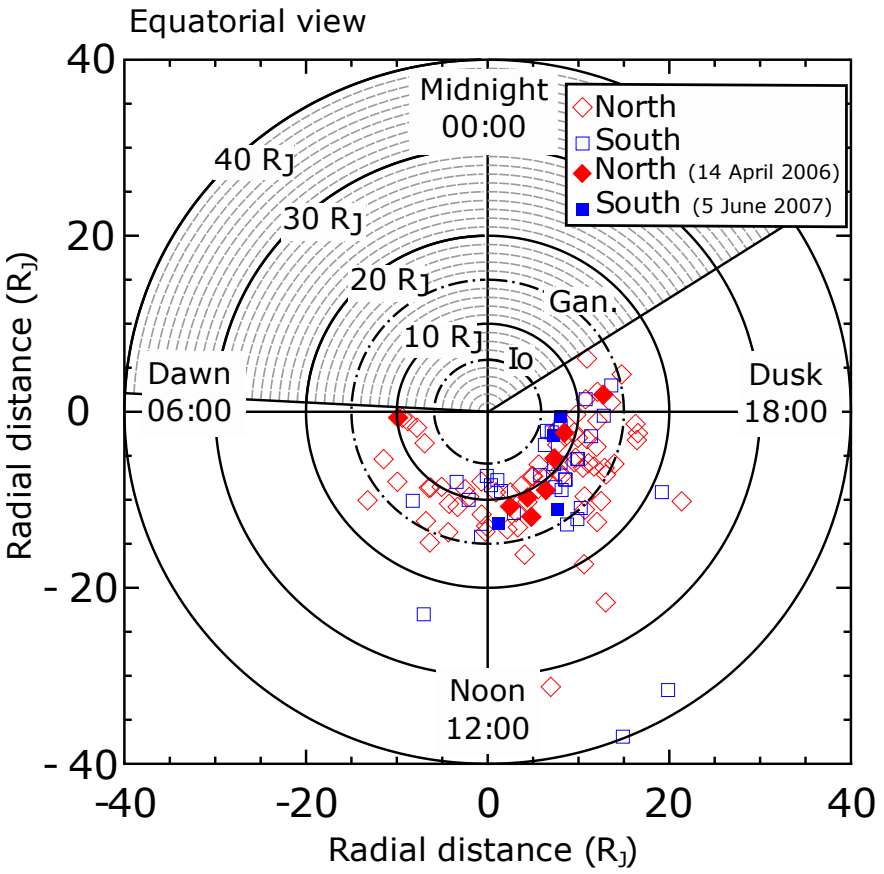

Figure 4.5 – Magnetically mapped LT location (i.e. longitude and radial distance) of the auroral UV features under study in the equatorial plane. Red diamonds and blue squares show the mapped position of the northern and southern auroral features, respectively. The different circles indicate the radial distance, from the orbit of Io to 40 R_J. A wide LT region (dashed region) is not covered by HST images, owing to Earth-based observing geometry. These auroral features magnetically map between 7 R_J and 62 R_J. The LT of the auroral structures covers all values in the sector accessible to HST 06 LT to 20 LT. Red filled diamonds indicate the location of eight distinct features observed simultaneous on 14 April 2006 in the northern hemisphere. Blue filled squares indicate the location of four distinct features observed simultaneous on 5 June 2007 in the southern hemisphere.

of events per local hour between dusk and midnight. We observe a similar behavior in both hemispheres.

For approximately 30% of the dataset, we observe more than one auroral feature on the same HST orbit. Two particular cases are highlighted with filled diamonds and squares in Figure 4.5. The first case corresponds to observations made on 14 April 2006 in the northern hemisphere, where 8 events are observed simultaneously. The second case corresponds to observations obtained on 5 June 2007 in the southern hemisphere during which 4 events were simultaneously observed. We observe that the structures are present simultaneously at different LTs and at different radial distances. The distribution of longitudes in LT for the whole data set was normalized with the same method as that used in Figure 4.5, and shown in Figure 4.6. We observe a relatively uniform distribution of structures mapping to the southern hemisphere. For the northern hemisphere, the most probable longitudes of structures, when mapped in the equatorial plane, lies between 12 LT and 18 LT. However, we note that, due to the biased CML distribution in the northern hemisphere, this sector usually corresponds to the same SIII longitude range located in the magnetic anomaly of the northern pole at Jupiter. We therefore suggest that the overpopulation in this sector, seen in the northern hemisphere only, may be linked to an observational bias associated with the presence of the northern magnetically anomaly, which could make it it easier to discriminate auroral feature detaching from the rest of the emission.

In situ signatures of recently reconnected and inward-moving flux tubes were found at radial distances ranging from 33 to 155 R_J in the tail between 19 and 06 LT (e.g. Vogt et al. 2010, Kronberg et al. 2005). Such flux tubes would map within the main auroral oval and their auroral counterparts

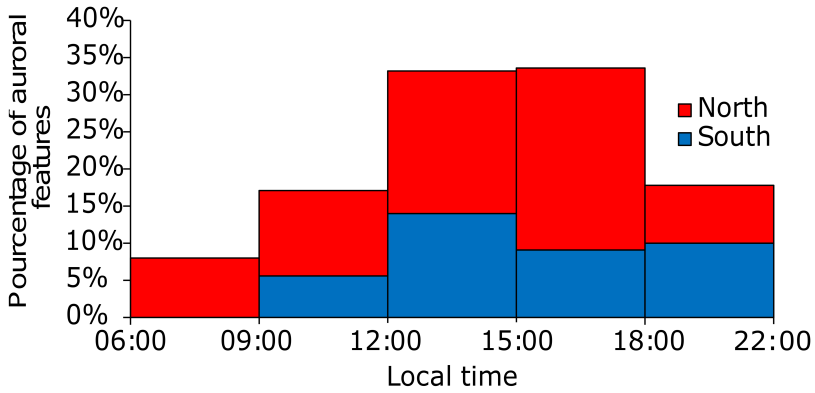

Figure 4.6 – Magnetically mapped LT of the auroral features under study. Observations in the north and south are indicated in red and blue, respectively. The distribution of the mapped structures in the southern hemisphere is relatively uniform in sectors where these structures are visible. The most probable LT sector in the equatorial plane ranges from 12:00 to 18:00 in the north.

are thought to be the polar dawn spots (Radioti et al. 2008, 2010). These structure appear to dissipate within a few (<4) hours as no polar dawn spot has ever been found beyond noon. Alternatively, the low-latitude features discussed in this chapter are seen at all observable LTs, which leave us with only two possible explanations. Either the phenomenon causing them, the interchange instability being the most likely one, can take place at any LT. Or they could still originate from a privileged LT sector. One possible scenario would be that the interchange instability might be enhanced in a specific LT sector, as a result of some topological reconfiguration subsequent to tail reconnection. But then, the lifetime of the heated plasma bubble has to be significantly longer than 4 hours, for their auroral signatures to remain equally observable whatever the LT accessible to HST.

Finally in order to determine the typical radial and azimuthal extent of mag-

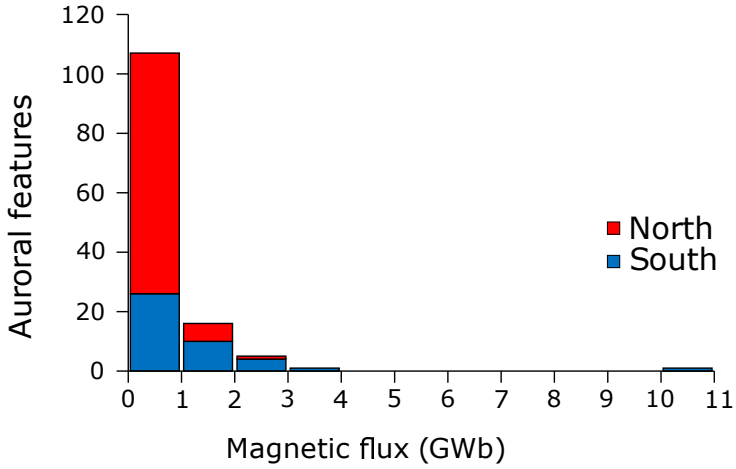

Figure 4.7 – Histogram of the inward magnetic flux associated with auroral features. Contribution from the northern (southern) auroral features is displayed in red (blue).The majority of the auroral features is associated with a magnetic flux between 0.002 GWb and 1 GWb.

netospheric signatures studied in the equatorial plane, we mapped the coordinates of the four extreme points of each auroral structure in the equatorial plane. The radial extent of the events under consideration ranges between 1 and 10 R_J with the majority ($\sim 60\%$) between 1 R_J and 4 R_J. Their typical azimuthal size is between 0.1 R_J and 7 R_J with the majority ($\sim 80\%$) between 0.1 R_J and 3 R_J.

4.4.1 Magnetic flux

During an injection, a parcel of sparse and hot plasma is transported into a region of dense and cold plasma. As heavy plasma moves outward, sparse plasma must be injected inward in the magnetosphere in order to

conserve magnetic flux in this region. In the following, we compare the amount of inward-moving magnetic flux associated with the auroral signatures of magnetospheric structures considered in this study with estimations of the outward-moving flux.

The inward flux associated with each event is estimated by multiplying the surface magnetic field at the center position of the auroral feature by the area subtended by this auroral emission. Figure 4.7 shows the magnetic flux associated with each event in the northern (red) and in the southern (blue) hemispheres. The resulting magnetic flux ranges from 1.9×10^{-3} GWb to 10 GWb with the majority ($\sim 80\%$) between 1.9×10^{-3} GWb and 1 GWb. In one case only, the flux reaches a value as high as 10 GWb. The magnetic flux associated with auroral features observed in the south is generally higher than in the north. The median number of injection per day is 1 (see Section 4.2) so that the mean magnetic flux is approximately 0.65 GWb per event. In our dataset, there is generally only one HST orbit per day and the auroral features are usually visible for the whole orbit. However, there are 16 cases of two or more consecutive HST orbits. For each of those cases, the auroral features under study are seen at the same SIII longitudes all along the sequence. Accordingly, we assume that the typical event duration is at least equal to the maximum observed lifetime ($\sim$ 3.5 hours). With such a typical duration, the mean magnetic flux is $\sim$ 3 GWb and the maximum magnetic flux is $\sim$ 46.5 GWb within these three and a half hours. As far as the outward magnetic flux is concerned, a typical value resulting from the transport of iogenic plasma by flux tube interchange may be calculated using the magnetospheric plasma radial transport velocity and the magnetic field magnitude in the equatorial plane.

$$\phi_{out} = S(t)B(R) \tag{4.1}$$

$$S(t) = \pi(R + [V_r(R) * t])^2 - \pi R^2 \tag{4.2}$$

, where $S(t)$ is the area covered by the radially moving plasma in the equatorial plane in t seconds, $B(R)$ is the value of the magnetic field at radial distance R, and V_r is the radial plasma outflow speed.

According to Bagenal and Delamere (2011), at 20 R_J, V_r is between 6 km/s and 40 km/s and B ~ 15 nT. Following equations 4.1 and 4.2 the estimated outward-moving magnetic flux lies between 82.8 and 273.3 GWb/day. This is one and two orders of magnitude larger, respectively, than the inward magnetic flux inferred from the present auroral analysis. This difference in magnitude may be explained as follows. In the present chapter, we only considered the auroral features strictly matching our selection criteria for calculating the inward moving flux. However, every magnetospheric event might not lead to an auroral signature bright enough to be detected, this detection threshold could explain part of the discrepancy. Moreover, only 40% of the auroral region is seen by HST at once, implying that we do not have the ability to observe all auroral features that would have appeared simultaneously. Finally, only ~ 45 minutes of an HST orbit may be used to observe Jupiter (the time during which HST is in the shadow casted by the Earth). Assuming that the duration of the auroral signatures is ~ 3.5 hours (maximum observed lifetime of auroral features in the few sequences of consecutive HST orbits), this implies that HST could have missed 3 of the signatures that appeared on this particular day. As the observed auroral emissions correspond to 40% of all LT, and if it is hypothesized that the events take place at no preferential longitude, it is reasonable to further multiply the number of observed signatures by 2.5 to obtain the actual total

number of magnetospheric structures present at all longitudes. All in all, we estimate a multiplication factor on the order of 8. With such a correction factor, the mean daily magnetic flux becomes ~ 25 GWb. We note that this flux remains on the low side of the estimated outward flux, meaning that events may account for only 30% of the inward flux. The outward flux must balance the inward flux; and large scale plasma injections are expected to largely contribute to the latter (Krupp et al. 2004). If the selected auroral features are associated with plasma injections in the magnetosphere, then one would expect the related magnetic flux to at least partly balance the outward flux. Indeed, the values that we derive are on the same order of magnitude, even if our injection-related inward flux is three times lower than the outward flux. The underestimation of the inward flux may be -at least in part- related to our five selection criteria of auroral signatures, listed in Section 4.1, which may be too restrictive. Moreover, we cannot exclude that we missed features too faint to be detected.

4.5 Summary and conclusions

In the present analysis, we report the first statistical study of Jovian auroral features possibly associated with signatures of magnetospheric injections, based on HST auroral data from 1999 to 2007. Using the VIPAL magnetic field model, we magnetically map the auroral structures in the equatorial plane and we investigate their characteristics. We examine the possibility that the selected UV auroral features are related to injection events in the Jovian magnetosphere. We show that these equatorward auroral features are common as they appear in more than half of the data sample. Most observations displayed only one unquestionable auroral feature per day. We occasionally observe several auroral structures on the same

image, pointing out to multiple regions of generation of magnetospheric events instead of a localized source region. Generally, the auroral features are visible during the whole observation orbit, and when several consecutive HST orbits were available, the auroral features were systematically observed during the whole sequence. Accordingly, this strongly suggests that their lifetime is greater than 45 minutes. Our analysis shows that the auroral features are seen at all SIII longitude and preferentially map to distances between 7 R_J and 40 R_J. We compare these HST observations with in situ injections signatures obtained from Galileo energetic particle data and we demonstrate that the auroral and in situ measurements are present at the same location in the magnetosphere, indicating that the auroral features under study are most probably signatures of injections. We also note that the lifetime of these auroral structures are consistent with the lifetime of the injections. Moreover, the temporal variations of the emitted power have the same typical timescale (~8 minutes) as those of the injections observed in radio domain (18 minutes) (Louarn et al. 2001). Finally, we estimate the inward moving magnetic flux associated with these auroral signatures and compare it with the outward moving magnetic flux. We estimate that the daily inward moving flux associated with events can account for at least 30% of the outward flux. If the selected structures are signatures of plasma injections in the equatorial plane, then this discrepancy might be the result of too restrictive selection criteria of the auroral features or the underestimation of their lifetime or a problem of detection threshold.

5 Evolution and simulation of the auroral signature of an injection

This chapter is based on the first part of the study by M. Dumont, D. Grodent, A. Radioti, B. Bonfond, E. Roussos, and C. Paranicas that was published in the Journal of Geophysical Research: Space Physics in 2018 (Dumont et al. 2018).

5.1 Introduction

Using HST auroral data from 1999 to 2007, I showed in the Chapter 4 that energetic particle injections in the equatorial plane of Jupiter are associated with isolated equatorward patchy auroral UV emissions. Based on this finding, I was able to report the first statistical study of these auroral structures. However, we are still lacking a global understanding of the mechanism triggering the localized injections, their auroral counterpart, and their association with global scale injection events.

Jupiter's auroral activity is mainly driven by internal processes (Clarke et al. 2009). Io's volcanism is a permanent internal source of plasma that plays a key role in the circulation of charged particles in the Jovian magnetosphere.

The iogenic plasma moves radially outwards and, due to the conservation of magnetic flux, flux tubes filled with sparse but energetic plasma move inwards. In some cases, some large injection events cause sudden and transient brightenings in the auroral emission. Kimura et al. (2015) suggested that these emissions are related to a rapid energy input in the polar region by the internal plasma circulation. According to Bonfond et al. (2012), the increased occurrence of large patches of UV emissions, associated with magnetospheric injection signatures could be explained by the enhancement of volcanic activity on Io. But a number of questions remain. How do the auroral signatures of plasma injections evolve over time? What is the auroral process that produce these auroral signatures? How does the electron energy distribution within these structures evolve? How long can these structures be observed in the auroral emission? How old are these auroral features when they are observed? The aim of this chapter is to address this chain of events by answering these questions.

5.2 Temporal longitudinal and latitudinal evolution of auroral signatures of injections

In this section, I examine sequences of images of Jupiter's aurora observed with HST. A sequence is an observation of Jupiter often made up of several individual images during a HST orbit. The database that we considered consists of a collection of 1874 images of FUV (115-170 nm) Jovian auroral emission taken in 1999 and 2007 with ACS and STIS on the HST, it is described in Section 3.1.2. The sequences used contain auroral structures that fulfil six specific criteria: (1) equatorward of the main emission; (2) well separated from the main emission; (3) compact struc-

tures (mean longitudinal extent <6 ° and mean latitudinal extent <3°) that do not form secondary arcs (Gray et al. 2017) or diffuse emissions (Radioti et al. 2009b); (4) their brightness, size, and level of corotation evolve independently from the rest of the auroral emission, (5) they are not satellite footprints; and (6) the observations display only one auroral feature during an HST orbit. These specific criteria allow us to select a set of cases for which it is possible to characterize the evolution of size and brightness of the auroral feature.

Thirteen sequences meet the criteria defined above, representing almost 10% of the database. Eight sequences show the northern hemisphere and five display the southern hemisphere (Table 5.1). Each sequence contains only one auroral signature of injection that is clearly separated from the rest of the auroral emissions. The auroral injection boundaries are objectively defined with a gradient vector flow active contour algorithm, as described by Xu and Prince (1998). This algorithm identifies the boundaries of the auroral signature of injection based on a fixed percentage (between 5% and 15%) of the maximum brightness in the sequence. This threshold remains fixed within each sequence, but it had to be set manually because the brightness of the features and the brightness of the background outer diffuse emissions differ from one case to another.

The first step of this study consists in determining the temporal evolution of the center position of the auroral signatures of injections during the selected HST sequences. To perform this analysis, we define, for each sequence, an ionospheric reference contour magnetically mapping to a fixed radial distance in the equatorial plane using the VIPAL magnetic field model (Hess et al. 2011). The fixed radial distance is defined such that the ionospheric reference contour passes through the auroral signature of an injection at the

beginning of the observing sequence. As illustrated in the typical example shown in Figure 5.1, we then measure the perpendicular and parallel distances from the reference contour to the center position of the auroral signature of injection on each image of the sequence. This approach shows the spacing of the structures center against the reference contour over time. Indeed, the magnetic field of Jupiter is tilted roughly 10° of its rotation axis, and in the northern hemisphere, it presents relatively small-scale irregularities (e.g., Connerney et al. 2018). Because of these irregularities (e.g. the kink region), it is deceptive and thus inappropriate to measure the spacing of the structures over time in longitude and latitude by using a dipole, even an inclined one. We therefore use the real distances in the auroral emissions compared to a reference contour. Consequently, working with parallel and perpendicular distances relative to such a reference contour allows us to account for the magnetic field asymmetries in the determination of the relation between the motions measured in the ionosphere to motions in the magnetosphere.

Each auroral structure displays a small radial displacement, which corresponds to a planetward motion in the equatorial plane and a longitudinal displacement along the direction of the corotation flow (Table 5.1). An injection is usually associated with radial planetward transport of hot and tenuous plasma in the magnetosphere. Once injected, energetic particles drift azimuthally around Jupiter, as a result of the combined effects of the corotational electric field drift, magnetic gradient, and curvature drifts. The observed movement of the structures is in agreement with the theoretical explanation of the injection phenomenon (see Section 2.2).

Typically during a sequence, the perpendicular and parallel distances between the mapped reference contour and the center position of the auroral

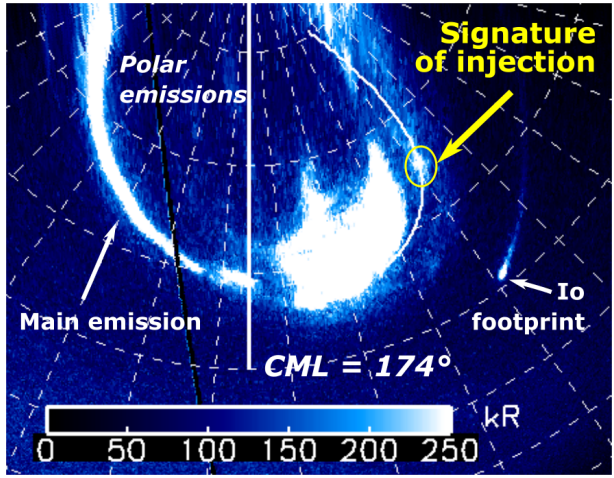
Polar
emissions
Signature
of injection
Main emission
Io
footprint
CML = 174°
kR
0 50 100 150 200 250

(a)

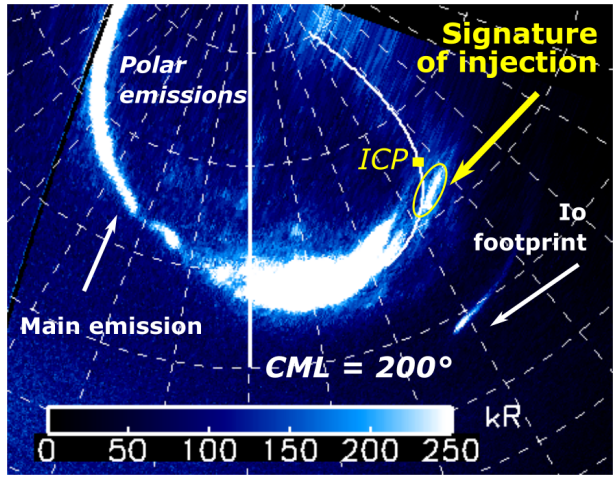
Polar
emissions
Signature
of injection
ICP
Io
footprint
Main emission
CML = 200°
kR
0 50 100 150 200 250

(b)

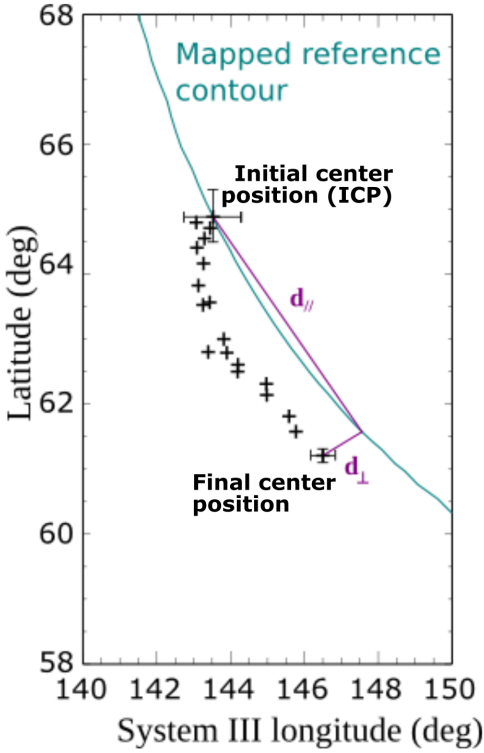

(c)

Figure 5.1 – (a and b) Polar projections of Jupiter's northern UV aurora obtained with ACS on 4 March 2007. They are the first and the last images of the sequence, respectively. The sequence starts at 10:23 UT and ends 43 min later at 11:06 UT. The CML evolves from 174° to 200° SIII. The main auroral features are indicated on the first image: the main auroral emission, Io footprint, polar emissions, and auroral signature of injection. The Initial Center Position (ICP) of the auroral signature is indicated, in (b), with a yellow square. The white contour corresponds to reference contour with a fixed radial distance (41 R_J) in the equatorial plane using the VIPAL magnetic field model. Figure 1c shows the SIII longitude and latitude of the center on each image of the sequence over time. A gap in longitude SIII between the initial and the final center positions of the auroral structure is observed. This gap implies that the structure presents 87% of the fraction of the rigid corotation. $d_{\parallel}$ and $d_{\perp}$ correspond to the parallel and perpendicular distances between initial and final center positions. The pointing uncertainty for the first and the last images of the sequence are defined in the text.

signature of injection (respectively $d_{\parallel}$ and $d_{\perp}$ in Figure 5.1) are on the order of a few hundreds kilometers and, in the most extreme case, a few thousand kilometers. We assume that the pointing and selection inaccuracy is ±2 pixels on the center in the first image, and we set a ±1 pixel uncertainty on the center in the other images. The pointing uncertainty is accounted for only once when estimating distances since it is a systematic error that remains constant over the entire sequence. Overall, the motion of the structures (in SIII) is always larger in the parallel direction than in the perpendicular one. Moreover, the magnetic mapping of these motions, in the equatorial plane, shows that their azimuthal displacement is larger than their radial displacement.

Figure 5.1 gives an obvious example of temporal evolution of an auroral signature of injection during a sequence. Figures 5.1a and 5.1b show polar projections of the first and last images of the sequence taken on 4 March 2007, respectively, with ACS in the northern hemisphere. In order to illustrate the motion of these features in the clearest way possible, we chose the case with the largest azimuthal displacement listed in Table 5.1. The white line corresponds to reference contour mapped in the auroral emission passing through the first center position. Figure 5.1c shows the SIII longitude and latitude of the center on each image of the sequence over time. The motion of the structure is significantly larger than the inaccuracy on the location of its center position. We also verified that this displacement is not a consequence of the slight change of the structure's shape with time. Since the edge of the auroral feature exhibits the same kind of displacement.

All the auroral structures under consideration present a modest level of subcorotation (i.e., between 80 and 90% of rigid corotation) and a small radial movement. It is reasonable to interpret the auroral structures discussed in

this study as mainly associated with old injections, it is suggesting that they are older than one HST sequence. They are considered old on the basis of their low radial velocity and their correspondingly small displacement in latitude during a sequence. Indeed, after an injection event, high-energy electrons are lost into the auroral atmosphere faster than the low-energy ones due to a stronger pitch angle scattering (Schulz and Lanzerotti 1974). As a result, only low-energy electrons remain and their auroral counterpart is close to corotation, in accordance with the observations. In addition, the radial velocity is expected to decrease as the hot plasma approaches the planet (Hill 2016). As a consequence, the observed low equatorward velocities, typically on the order of a few degrees per hour maximum, suggest that here the auroral features under consideration correspond to old injections.

5.3 Simulations of auroral signature of an injection

5.3.1 Electrons drift model

Two processes have been proposed to generate the auroral signatures of magnetospheric injections: (1) pitch angle scattering and (2) field-aligned currents flowing along the flanks of the hot injected plasma bubble (Kivelson and Russell 1995). In this study, we investigate the possibility that the precipitated energy flux may be provided to the ionosphere through electron pitch angle scattering by whistler mode waves, in accordance with previous studies (e.g., Mauk et al. 2002, Radioti et al. 2009b, Kimura et al. 2015). We use a simple model, based on the model used by Radioti et al. (2013) for Saturn which I've adapted for Jupiter, to simulate the evolution of the energy flux with time. From these simulations, we deduce both the

longitudinal extent of the auroral injection signature (Figure 5.3a) and the longitudinal profile of the energy flux (Figure 5.3b). We assume a dipolar magnetic field[1], and we only consider the effects of the injected electrons since, according to Mauk et al. (2002), the ions do not contribute significantly to the precipitated flux.

In the model, electrons are propagating longitudinally under the influence of azimuthal (sub) corotation and gradient/curvature drifts. The simulation does not include the radial drift for the corresponding injected population in the magnetosphere. However, the auroral features that we studied show small radial displacements (Table 5.1). The drift rates of the charged particles due to the gradient and curvature drifts depend on the particles' energy (more details in Section 1.3.3.2). Hence, the longitudinal width of the auroral features is expected to increase with time. For the energies considered in the simulation, the total drift velocity of energetic electrons decreases with energy, as shown in Figure 5.2. Moreover, the brightness of the auroral features should decrease with time because the energy density declines with time. Indeed, the gradient and curvature drifts disperse the total injection energy over a wider region and the injected particles suffer additional losses, due to strong pitch angle scattering, for example.

[1] Although the surface field is difficult to approximate by a dipole (cf. the kink region), this approximation seems possible in the equatorial plane of the magnetosphere where the plasma injections take place.

Table 5.1 – List of the 13 UV sequences observed by HST containing only one auroral signature of injection clearly separated from the rest of the auroral emissions.

Rootname	Date[a] (hemisphere)	CML range[b] (SIII deg)	First center coordinate (SIII deg)	Perpendicular distance between initial and final center positions, $d_\perp$ (uncertainty range; km)	Parallel distance between initial and final center, positions $d_\parallel$ (uncertainty range; km)	
o6bab1oyq	28/12/00 (N)	154 – 176°	128.4°	277 (84 – 317)	931 (462 – 1,145)	Used in Fig. 5.3
o6baa4chq	18/12/00 (N)	167 – 191°	139.9°	175 (128 – 312)	1,117 (732 – 1,355)	
j93ea4eaq	25/04/05 (N)	144 – 168°	136.8°	159 (69 – 315)	1,382 (615 – 1,684)	
j9rlc2wfq	04/03/07 (N)	174 – 200°	143.2°	1,573 (875 – 1,862)	3,723 (3,133 – 4,175)	Used in Fig. 5.1
j9rlc4fpq	06/03/07 (N)	115 – 141°	162.1°	400 (318 – 482)	428 (348 – 617)	
j9rlk9mcq	17/03/07 (N)	169 – 172°	146°	303 (220 – 342)	762 (702 – 1,068)	
j9rld2nzq	13/05/07 (N)	154 – 178°	140.9°	211 (64 – 489)	1,071 (452 – 1,476)	
j9rld5b5q	16/05/07 (N)	185 – 209°	133.5°	1,674 (835 – 2,411)	2,128 (1,811 – 2,304)	
o6ba04btq	18/12/00 (S)	48 – 132°	79.9°	1,760 (721 – 2,136)	545 (500 – 830)	
o6baa2nkq	14/12/00 (S)	22 – 48°	79.8°	437 (427 – 493)	127 (74 – 137)	
o6ba01o9q	28/12/00 (S)	36 – 120°	62.7°	1,389 (881 – 1,557)	2,040 (1,831 – 2,269)	
j9rle9hlq	30/05/07 (S)	7 – 31°	339.3°	189 (109 – 251)	1,204 (1,073 – 1,437)	
j9rlfaalq	11/6/7 (S)	73 – 97°	133.7°	381 (199 – 425)	1,265 (804 – 1,556)	

CML, central meridian longitude

[a]Dates are formatted as day/month/year. [b]Range of SIII longitudes during the observation's sequence.

5.3.2 Comparison of simulations with auroral observations

We use the simulation model described above and compare its outputs with the 13 auroral signatures of injections observed with HST. The simulation procedure accounts for 11 input parameters organized in two distinct sets: (1) six parameters to characterize the observed emissions and (2) five parameters to control the model. The first set of six parameters controls the longitude of the barycenter of the auroral feature in each image, the longitudinal thickness of the first auroral feature in the sequence, the L-shell range in the equatorial plane when t = 0, the number of images in the sequence, the time between two images in the sequence, and a uniform value for the fraction of rigid corotation during a sequence (observed to be between 80 and 90%). The remaining five parameters are directly related to the simulation itself: the number of particles in the simulation, energy range of electrons, spectral index, pitch angle for all particles, and flux scaling factor in $f = f_0 E^{-\kappa}$. The simulation output parameters are the temporal evolution of the auroral brightness and the longitudinal extent of the auroral signature as a function of time.

At the onset time, we impose the following parameters: 10^5 particles isotropically distributed and an electron energy distribution between 20 and 400 keV. The energy range is chosen, in accordance with the in situ measurements in the equatorial plane reported by Mauk et al. (1997) and with the distribution of the electron energy in the auroral emission determined by Gérard et al. (2014).

At each time step, we calculate the longitudinal thickness and the brightness profile normalized to the maximum energy obtained at the onset time from the simulated injection. We compare these simulations with HST ob-

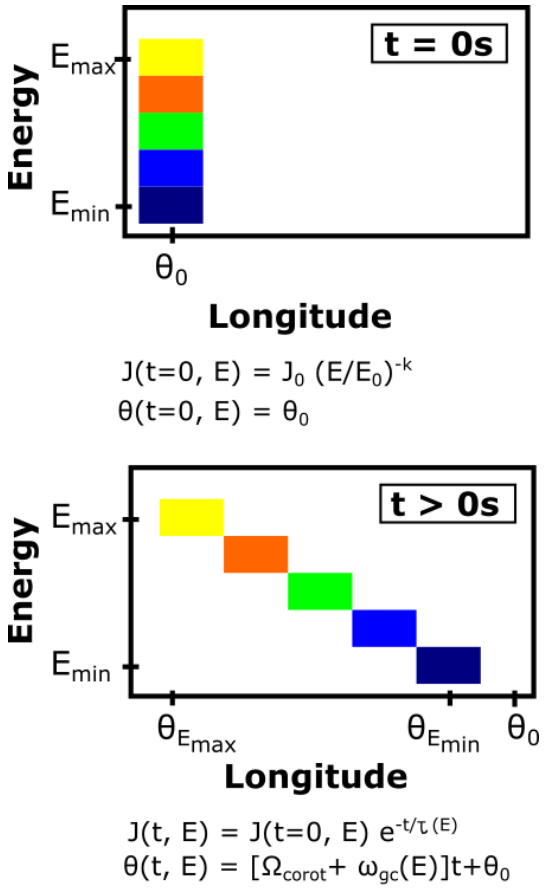

Figure 5.2 – Schematic representation of the electron drift model associated with auroral signature of an injection in the Jovian magnetosphere (adapted from Radioti et al. 2013). We assume that the precipitated energy flux is provided to the ionosphere by pitch angle scattering due to whistler mode waves. At t = 0, electrons are injected at a given longitude θ_0, their energy lies between E_{min} and E_{max}, and their differential flux is $J(t = 0, E) \propto E^{-\kappa}$, where κ is a power law's spectral index. All discrete energy elements of the injected plasma coexist and are represented by different colors. The drift rates of the electrons due to the gradient and curvature drifts depend on the electrons' energy ($\omega_{gc}(E)$) and on the initial bulk fraction of rigid corotation (Ω_{corot}). At t > 0, the longitudinal width of the auroral features increases, $\Delta\theta = \|\theta_{E_{max}} - \theta_{E_{min}}\|$ corresponds to the longitudinal extend of the auroral feature.

servations for each image. Additionally, we note that the simulation output is controlled by the lifetime of the electrons. The differential flux is reduced by a factor of $e^{-t/\tau(E)}$, where $\tau(E)$ is the lifetime of the electrons due to loss processes and ranges between 10^3 and 10^5 s, depending on the electron energy. We adjust the lifetime of the auroral features and the spectral index to reproduce the observations. We observe that the spectral index determines the shape of the brightness profile as a function of longitude. A higher spectral index implies a sharper profile and a slower longitudinal length increase with time. Given the number of parameters we impose, we do not find a unique solution. For each of the 13 structures, we tested different values of the spectral index and we determined the spectral index based on the best fit of the observations with the simulations. We found that the best fit was associated with $\kappa = 3 \pm 0.5$. Indeed, we observe that when the spectral index deviates from 3 ± 0.5, the simulation does not reproduce well the observations. For example, if we use a smaller spectral index, we observe that the longitudinal extent is close to the simulated one but the observed brightness profiles are not reproduced by the simulations. A positive spectral index in the electron distribution implies a larger contribution from low energy electrons.

One of the 13 cases studied is shown in Figure 5.3. This case is particularly interesting because this injection is the only one simultaneously observed with the EPD on board the Galileo spacecraft and with HST (Mauk et al. 2002); thus, we have direct evidence that this auroral feature is associated with an injection. Figure 5.3a shows the observed longitudinal extent of the auroral signature of injection (solid line) and the simulated one (black dashed line) for an injected electron population with spectral index $\kappa = 3$ and an energy range between 20 and 400 keV. The error bars indicate the 1° selection uncertainty for each image. Figure 5.3b shows the normalized

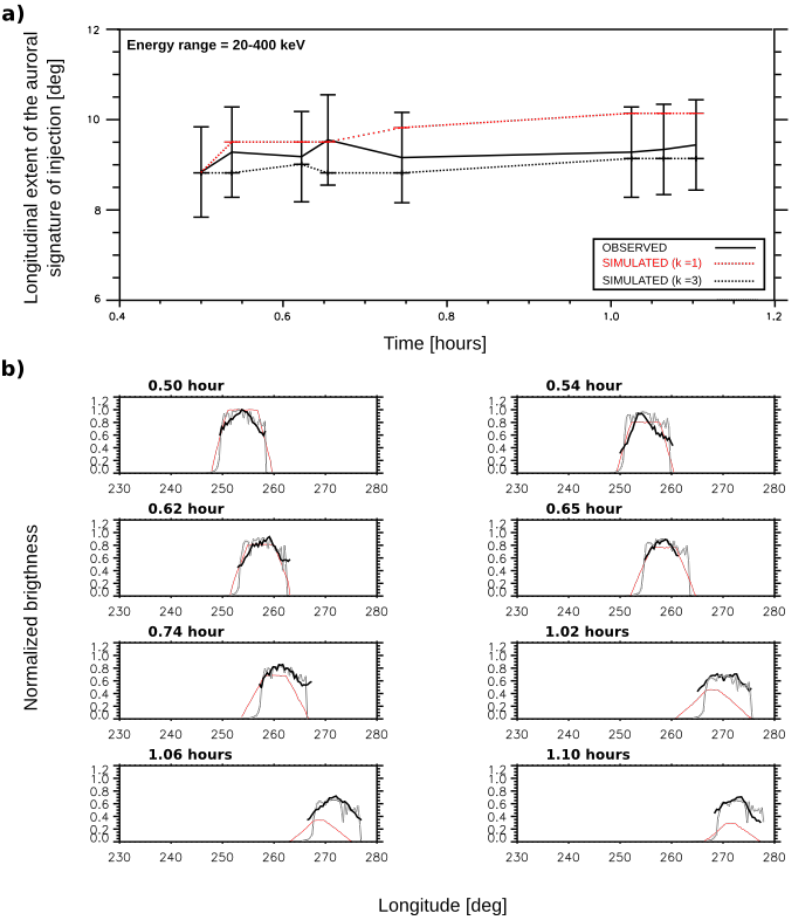

Figure 5.3 – (a) Length of auroral signature of injection (in degree) observed by HST STIS on 28 December 2000 (solid line) as a function of time (in hours). The simulated evolution of the longitudinal extent for an injected electron population is done with a spectral index $\kappa = 3$ (black dashed line), a spectral index $\kappa = 1$ (red dashed line), both with an energy range between 20 and 400 keV. The error bars indicate the 1° selection uncertainty. (b) Normalized brightness as a function of LT (in degree). Each panel corresponds to one image of this sequence. The simulated evolution of the brightness profiles for an injected electron population is done with a spectral index $\kappa = 3$ (grey line), a spectral index $\kappa = 1$ (red line), and energy range between 20 and 400 keV. The time displayed on the top of each panel corresponds to the time elapsed since the presumed beginning of the auroral signature.

observed brightness profiles (solid line) and the simulated energy flux profiles (black dashed line). The observed normalized brightness profiles are taken at constant latitude as a function of LT for each image. Figure 5.3 demonstrates that the simulation is in a relatively good agreement with the observation in terms of length and brightness evolutions. Small inconsistencies are likely related to the determination of the brightness profile, the assumption of an isotropic distribution, and the fact that we did not take the radial displacement of the injected plasma into consideration. In order to illustrate the influence of the value of the spectral index k on the quality of the fit of the simulation output, we show a test case with $\kappa = 1$ (red line in Figure 5.3). Figure 5.3a also shows the simulated longitudinal extent of the auroral signature of injection (red dashed line) for an injected electron population with spectral index $\kappa = 1$ and an energy range between 20 and 400 keV. In Figure 5.3b, the simulated energy flux profiles decreases too rapidly with time compared to the observations. However, it is noticeable that the longitudinal extent of the $\kappa = 1$ case is not significantly different from the observed one nor from the $\kappa = 3$ case. This can be explained by of Jupiter's strong magnetic field which prevents a rapid drift of the particles and the subsequent broadening of the auroral structure, contrary to the Saturn case (Radioti et al. 2013). We carry out similar simulations for the 12 other cases, with similar outcome: the longitudinal extent increases and the brightness decreases over time in similar manner, consistently with the observations.

Electron scattering appears to be the best candidate mechanism for the auroral signatures of plasma injection. This hypothesis is supported by the good agreement between UV observations and our simulations of the auroral brightness. It is noteworthy that Li et al. (2017) used the same mechanism to explain the radial gradient of precipitation energy of the equator-

ward diffuse emissions in Juno observations.

We previously suggested that auroral signatures of injection considered here are associated with old injections. We have always imposed an age of the auroral feature for the first image of the sequence different from 0, meaning that the auroral signature of plasma injection was already present before the beginning of the observation sequence. The age is adjusted in such a way that we have good agreement between the observations and simulations. In our database (Table 5.1), the range of these initial lifetimes is between 10 min and 2 hr. On average, the lifetime of the present structures is around a half rotation of Jupiter (~5 h). In Chapter 4 that the age of the auroral features is longer than the HST observations, but it seldom exceeds the Jupiter's rotation period (~ 10 hr). This is in agreement with the results presented in this chapter. It should be noted that the full life cycle of these auroral features cannot be captured due to the typical HST observing scheme, consisting of a single isolated orbit of ~45 min every 24 hr. However, in certain exceptional cases, some large auroral signatures of injection should have a lifetime larger than the rotation of Jupiter Bonfond et al. 2012. Nonetheless, these cases cannot be explained with the simple model that we used.

5.4 Summary and conclusions

The latitudinal and azimuthal motions of the auroral signatures of plasma injections observed in HST data are compatible with magnetospheric injections moving planetward and lagging corotation. The simulations of the auroral signatures of injected plasma suggest that the auroral features may be caused by electron scattering. The simulations provide a better un-

derstanding of the size, the spectral index, and the evolution of the injected electron population in the Jovian magnetosphere. For example, they show that during a typical HST sequence, the spread of the injection signature due to diffusion is very limited. They also give information on the lifetime of the structures. On average, it ranges between a half and a full rotation of Jupiter, which is in agreement with the statistical results of Chapter 4. We suggest that these auroral signatures of injection are associated with old injections, because they are in quasi-corotation and they present a very small equatorward displacement.

6 Evidence of the energy-dependent drift of the electrons in auroral signatures of injections

This chapter is based on the second part of the study published by M. Dumont, D. Grodent, A. Radioti, B. Bonfond, E. Roussos, and C. Paranicas in the Journal of Geophysical Research: Space Physics in 2018 (Dumont et al. 2018).

6.1 Introduction

As mentioned in the Chapter 5, once energetic plasma particles are injected, they start to drift azimuthally around Jupiter. However, all these energetic particles do not have the same energy, which implies a differential drift as a function of energy.. Measurements from the EPD on board the Galileo spacecraft gave evidence of the ubiquitous occurrence of plasma injections in the Jovian magnetosphere and highlighted a differential drift between the high- and low-energy electron populations (Mauk et al. 1999). In this chapter, I use the spectral scans of the Jovian FUV aurora from HST program GO 13402 collected on 8 January 2014 in the north. The image

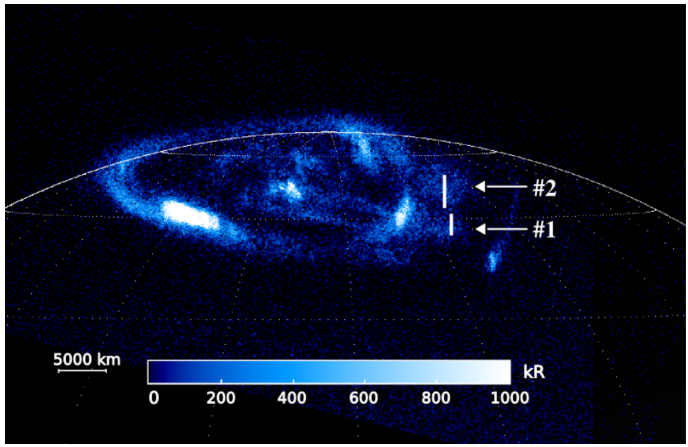
#2
#1
5000 km
kR
0
200
400
600
800
1000

(a)

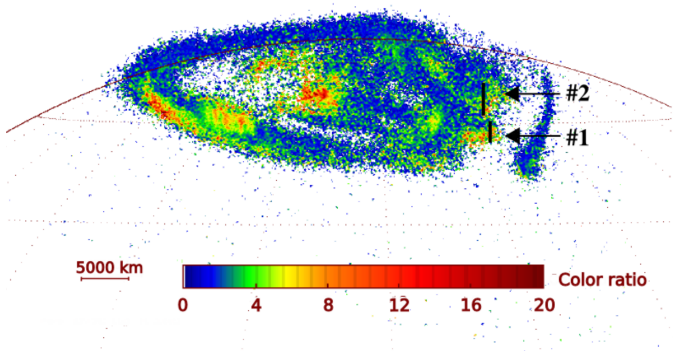
#2
#1
5000 km
Color ratio
0
4
8
12
16
20

(b)

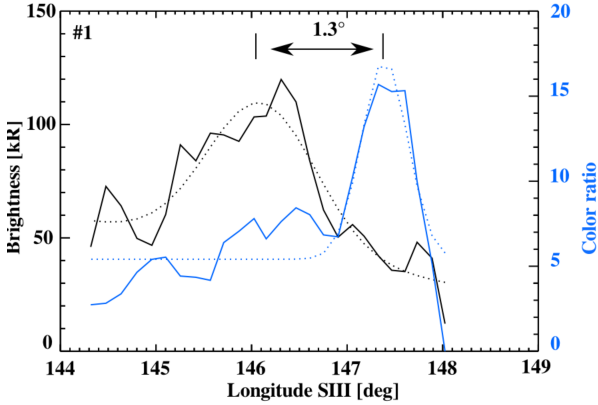
#1
1.3°
Brightness [kR]
Color ratio
Longitude SIII [deg]
150
100
50
0
20
15
10
5
0
144
145
146
147
148
149

(c)

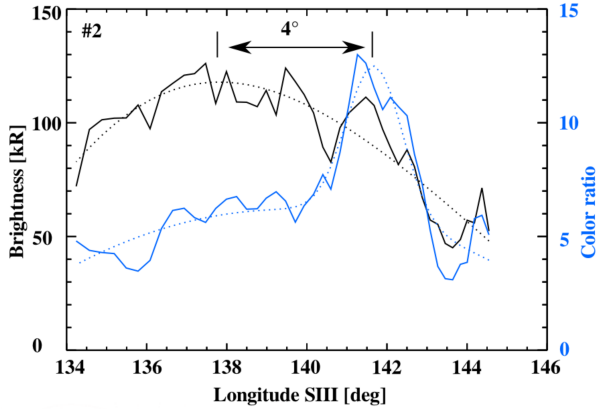
#2
4°
Brightness [kR]
Color ratio
Longitude SIII [deg]
150
100
50
0
15
10
5
0
134
136
138
140
142
144
146

(d)

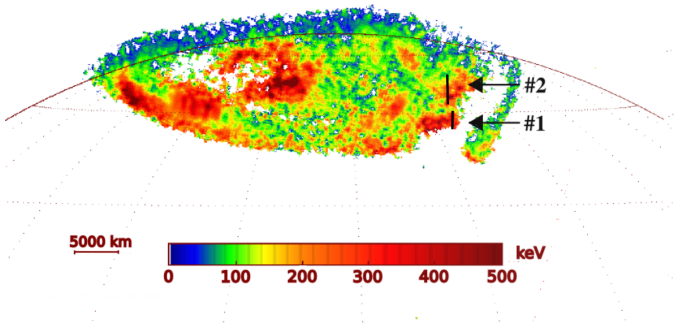

(e)

Figure 6.1 – (a) Reconstructed auroral image based on STIS scan of the northern hemisphere on 8 January 2014. The two white arrows indicate two equatorward auroral features. (b) Corresponding reconstructed image of the CR. The amount of absorption by methane increases from dark blue (low absorption) to red. Therefore, high-energy electrons are in the red regions and low-energy electrons are in the blue regions. The two black arrows indicate two equatorward auroral features corresponding to panel a. (c and d) Brightness and CR profiles across structures 1 and 2 along the white and black lines indicated in panels (a) and (b), respectively. Additionally, Gaussian functions fitting the observed brightness and CR profiles (blue and black dashed lines) show that the brightness maximum does not match the location of CR maximum. Indeed, the offsets are 1.3 and 4° for structures 1 and 2. (e) Corresponding image of electron energies assuming a model atmosphere for which the eddy diffusion coefficient is set to $1.4 \times 10^6 cm^2/s$, adapted from Gérard et al. (2014).

processing of these observations is described in Section 3.1.3. They consist of a continuous time-tagged spatial scan of the polar region, and were designed to cover an area of $24.6'' \times 11.5\ ''^2$ encompassing all the auroral region in the northern hemisphere. They have a CML range of SIII longitudes between 155° and 188°. The purpose of this chapter is to observe the energy-dependent drift of the electrons in auroral signatures of injections and to estimate their age from this property.

Figure 6.1 provides a comparison (a) of the auroral brightness, (b) of the CR, and (e) of the corresponding characteristic electron energies. Figure 6.1a reveals two auroral features located equatorward of the main emission and poleward of the Io footpath (white arrows). These two structures are likely auroral signatures of plasma injections since they are equatorward of the main emission, they form compact structures, and they are not satellite footprints. In these patches of emission, the mean energy is higher than in the surrounding emissions (black arrows in Figure 6.1b). Interestingly, the comparison between the brightness and the CR shows that their maxima are not collocated (Figures 6.1c and 6.1d). In order to be able to define as objectively as possible the offset between the brightness and the CR profiles, I fit them with Gaussian functions (blue and black dashed lines in Figures 6.1c and 6.1d). Using these best fit profiles, offsets of 1.3° and 4° are observed between brightness maximum and CR maximum for structures 1 and 2, respectively. The CR peaks upstream of the feature relative to the plasma rotation direction, as expected for auroral signatures of injections, since the high-energy electrons drift upstream of the low-energy electrons, as shown by in situ measurements (Mauk et al. 1999). This further suggests that these auroral features are indeed related to plasma injection in the equatorial plane. Moreover, based on Juno-UVS observations, Bonfond et al. (2017) highlighted a shift between the brightness peak and the CR peak of several auroral features associated with injections, similar to the ones observed here.

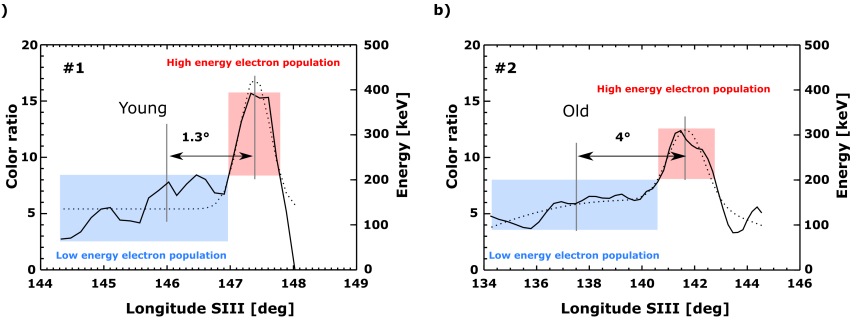

Figure 6.2 – (a and b) CR profiles (black lines) and the Gaussian functions fitting the observed CR profiles (black dashed lines) across structures 1 and 2 along the white and black lines indicated in figure 6.1a and 6.1b, respectively. Assuming a model atmosphere for which the eddy diffusion coefficient is set to $1.4 \times 10^6 cm^2/s$, the electron energies associated with the CR is on the right of each plot. The vertical grey lines correspond to the center position of each energy electron population. The longitude difference between low-energy electron population and high-energy electron population informs us on the age of the auroral feature. These differences are 1.3 and 4° for structures 1 and 2. With the simulation method (described in Section 6.2), I estimate that the age of structures 1 and 2 is around 2 and 3 hr, respectively.

6.2 Simulation of the longitudinal drift from the spectral observations

As suggested above, the equatorward auroral features highlighted in Figure 6.1 display a separation between high and low-energy electron populations. At the onset time, when the plasma is injected, I assume that electrons of different energies are uniformly distributed in the injected plasma. Since the drift velocity of electrons is energy dependent, I use the simulation method described in Section 5.3.1 to estimate the age of the structures. It should be noted that this method does not account for the possibility that contiguous injections may interact or merge as they spread. We use the same data set as Gérard et al. (2014). The relationship between the CR

and the electron energy strongly depends on the assumed vertical distribution of hydrocarbons in the Jovian atmosphere. In the present study, I use the same atmospheric model as Gérard et al. (2014) with an eddy diffusion coefficient set to $1.4\times10^6 cm^2/s$, corresponding to a methane homopause altitude of 320 km (Grodent et al. 2001). With this model, I consider that the low-energy electron population has a CR less than 8 and the high-energy population has a CR higher than 8. These CR ranges correspond to energies between 60 and 200 keV and between 200 and 400 keV, respectively. Based on the location of the contour of the auroral signature, I manually select the low- and high-energy populations from the CR (Figure 6.2). The longitudinal difference of these two populations increases with time and should be zero at the onset time of the injection. Hence, the longitude difference between these two center positions informs us on the age of the auroral feature. We use the simulation described in Section 5.3.1 for the low- and high-energy electrons. The simulation runs until the longitudinal difference between the two populations is equal to the observed difference. In this case, which is based on a single spectrally resolved observation, the κ index cannot be retrieved from the simulation since the evolution of the brightness with time is missing. Assuming $\kappa = 3$ (in accordance with Chapter5), I also prescribe the initial longitudinal extent of the auroral feature and the level of rigid rotation. With this method, I estimate that the age of structures 1 and 2 is around 2 and 3 hr, respectively, that is a factor of 3, at minimum, smaller than one Jovian rotation. This result is consistent with results in Chapter 5 and with the HST observations (Chapter 4).

6.3 Summary and conclusions

The HST spectral observations provide an opportunity to compare the CR and the auroral brightness, and to highlight the energy-dependent drift of the electrons in auroral signatures of injections. Indeed, I observe a shift between the energy maximum and the brightness maximum in auroral structures associated with injection signatures. Since the electron drift velocity is energy dependent, this motion can be attributed, at least in part, to the energy-dependent curvature drift of energetic electrons. Using simulations, the age of these structures was derived and estimated to be a few hours, in agreement with previous results.

7 Position and dynamics of bright patchy auroral emissions

This chapter is based on the last part of the study published by M. Dumont, D. Grodent, A. Radioti, B. Bonfond, E. Roussos, and C. Paranicas in the Journal of Geophysical Research: Space Physics in 2018 (Dumont et al. 2018).

7.1 Introduction

In Chapters 5 and 6, I only considered auroral features obeying to a relatively strict set of selection criteria, meant to permit systematic and reproducible analyses. These auroral structures presented small latitudinal and longitudinal motions. However, some outer emissions, even if they do not exactly meet all the selection criteria defined previously, still exhibit a temporal evolution similar to those described in Chapters 5 and 6. For example, some features are not perfectly separated from the main emission and/or more than one auroral feature are present in the same HST sequence. In this section, I am interested in a subset of these bright patchy auroral emissions, which show a substantial latitudinal motion. These auroral features are equatorward of the main emission but not necessarily well

separated from it. They are more compact than secondary arcs, brighter than diffuse emissions; they are not satellite footprints; and they evolve independently from the rest of the auroral emission's behavior. We analyzed high-resolution UV images from 1999 to 2017 in 11 HST programs (GO 8171, GO 8657, GO 9685, GO 10140, GO 10507, GO 10862, GO 11649, GO 12883, GO 13035, GO 14105, and GO 14634). Table 7.1 lists 42 observations presenting at least one feature fulfilling the criteria set out previously. These bright patchy auroral emissions are frequently seen in both hemispheres. They are mainly present in the noon and dusk sectors. Their presence in these sectors is most probably linked to an observational bias in the collection of data arising from a limited range of CML, which was selected to optimize the HST's viewing geometry (see Chapter 3). Here I do not discuss their presence in the night sector because this sector is not observable by HST. However, Bonfond et al. (2017) highlighted their presence on the nightside in Juno UV observations. We will address those nightside structures observed with Juno-UVS, in Chapter 8.

These events do not overlap with those on Table 5.1, because they do not satisfy all the selection criteria used for Table 5.1 events (i.e., they are not perfectly separated from the main emission and/or more than one auroral feature are present in the same HST sequence).

7.2 HST FUV Time-Tag Observations

These bright patchy auroral emissions showing substantial latitudinal motion have complex boundaries, which are generally impossible to isolate from other auroral emissions. Hence, a statistical study of the movements of these structures is unfeasible in practice. In this section, I carry out the study of a typical case, which features four bright patchy auroral emissions

Table 7.1 – List of the 42 UV sequences observed by HST from 1999 to 2017 showing bright patchy auroral emissions with a substantial latitudinal motion.

HST observation campaign	Rootname	Date[a] (hemisphere)	CML range[b] (SIII deg)	Local time sector
GO 8171	o5hy04hsq	21/9/99 (S)	67 – 87°	Noon
	o5hya4i4q	21/9/99 (N)	122 – 201°	Noon-Dusk
	o5hyb6frq	22/2/00 (N)	63 – 134°	Dusk
GO 8657	o6baa1opq	28/12/00 (S)	96 – 120°	Noon
	o6bab1pbq	28/12/00 (N)	154 – 176°	Dusk
GO 10140	j93e03bvq	18/4/5 (N)	119 – 14°	Noon-Dusk
	j93ea3cdq	18/4/5 (N)	173 – 198°	Noon
	j93e52veq	06/5/5 (N)	124 – 147°	Noon
GO 10507	j9du04ewq	14/4/6 (N)	163 – 188°	Dusk
GO 10862	j9rlb3pyq	23/2/7 (N)	208 – 234°	Noon
	j9rlc8zbq	10/3/7 (S)	234 – 299°	Noon
	j9rlk8hpq	22/3/7 (N)	116 – 123°	Noon
	j9rld3a1q	14/5/7 (N)	119 – 144°	Noon-Dusk
	j9rle3eyq	24/5/7 (S)	3 – 28°	Noon
	j9rle8d9q	29/5/7 (N)	161 – 185°	Noon
	j9rlf3qsq	03/6/7 (N)	189 – 214°	Noon
GO 11649	ob3001xqq	11/9/9 (S)	76 – 103°	Noon - Used in Figure 7.1
GO 12883	oc0v06xhq	24/1/14 (S)	120 – 124°	Dusk
	oc0va6xjq	24/1/14 (N)	130 – 145°	Noon-Dusk
GO 14105	ocx808jjq	21/5/16 (N)	133 – 160°	Noon-Dusk
	ocx812u2q	26/5/16 (N)	196 – 223°	Noon
	ocx816xkq	27/5/16 (N)	168 – 195°	Noon
	ocx817emq	28/5/16 (N)	126 – 153°	Noon
	ocx830rjq	22/6/16 (S)	47 – 74°	Noon-Dusk
	ocx847eyq	18/7/16 (N)	184 – 211°	Dawn-Noon
GO 14634	od8k26q4q	4/12/16 (S)	308 – 332°	Noon
	od8k08q5q	7/12/16 (N)	137 – 161°	Noon-Dusk
	od8k14vrq	14/12/16 (N)	128 – 152°	Noon-Dusk
	od8k27ghq	07/1/17 (S)	322 – 347°	Noon
	od8k30i4q	24/1/17 (N)	122 – 147°	Dusk
	od8k31i4q	24/1/17 (N)	180 – 204°	Noon-Dusk
	od8k67bfq	27/3/17 (S)	53 – 77°	Noon
	od8k68bxq	27/3/17 (N)	111 – 135°	Noon-Dusk
	od8k81roq	19/4/17 (N)	122 – 146°	Noon-Dusk
	od8k82ovq	23/4/17 (N)	167 – 191°	Noon-Dusk
	od8k88hbq	16/5/17 (N)	143 – 168°	Noon-Dusk
	od8k97xzq	19/5/17 (S)	333 – 357°	Dawn
	od8k0ay5q	19/5/17 (S)	30 – 55°	Dawn
	od8k0nh8q	27/5/17 (N)	151 – 176°	Dusk
	od8k0vfzq	10/7/17 (S)	25 – 50°	Noon-Dusk
	od8k0wgcq	11/7/17 (S)	83 – 108°	Noon-Dusk

[a]Dates are formatted as day/month/year.

[b]Range of SIII CML during the observation's sequence.

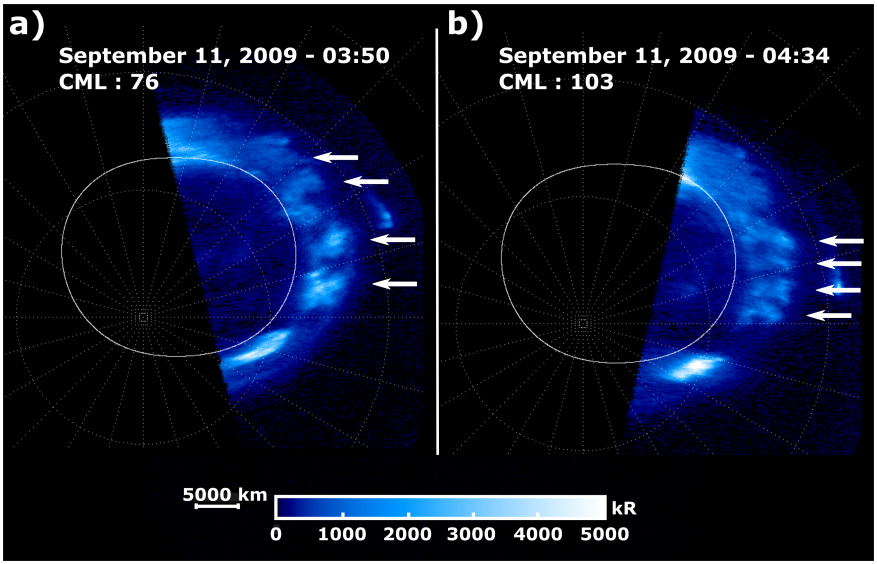

Figure 7.1 – (a and b) Polar projections of Jupiter's southern UV aurora obtained with STIS instrument on 11 September 2009. They are respectively the first and the last image of the sequence. The sequence starts at 03:50 UT, and it ends 44 min later at 04:34 UT. The CML evolves from 76°to 103°SIII. At the beginning of the sequence, the positions of four bright patchy auroral emissions are indicated by white arrows. On the last image, the positions of bright patchy auroral emissions are indicated by white arrows.

with substantial latitudinal motion. This STIS time-tag observation was acquired with the F25SRF2 filter on 11 September 2009 (Bonfond et al. 2011). During this 45-min long sequence, the CML increased from 76 to 103°. We favored a case in the southern hemisphere to avoid the magnetic anomaly present in the northern hemisphere (Grodent et al. 2008). Indeed, while the magnetic anomaly sometimes facilitates the identification of auroral injection signatures, the motion of such a structure could be misinterpreted due to the peculiar field topology in this region. On the first image of the sequence (Figure 7.1a), four equatorward isolated patches of auroral emissions are located in the noon sector(indicated by arrows). Comparison

of the first and the last images of the sequence (Figure 7.1b), ~ 45 min later, illustrates the temporal evolution of the four auroral features during the sequence. These structures are all in quasi-corotation, and they all present a significant equatorward movement. It is particularly noteworthy that they migrate equatorward independently from each other and they ultimately fork over time. This distinctive motion suggests the presence of convection (associated with the bulk motion of the flux tubes filled with energetic plasma) in addition to the diffusion (associated with the energy-dependent drift of the individual particles). The four structures have, respectively, longitudinal displacements of 0.5°, 1.2°, 1.8°, and 2.1° (between 92% and 98% of full corotation) and latitudinal displacements of 0.7°, 0.5°, 0.3°, and 0.2°. These displacements correspond to distances from 750 to 1800 km in the auroral region and to radial velocities from 0.5 to 2 R_J/hr in the equatorial plane.

All the structures referenced in Table 7.1 present the same kind of behavior as the auroral signatures of old injections (i.e., they are equatorward emissions in quasi-corotation) suggesting that they are also associated with the injection process. Their longitudinal motion (in quasi-corotation) is similar to that of the old injections, but their large planetward radial velocities are indicating that they correspond to younger magnetospheric injections. If the radial velocity is very low, it means that the structure is at the end of its journey, which is why I characterize it as an old injection. Alternatively, a plasma injection with a significant radial velocity suggests that the structure is younger than those studied in Chapter 5. However, because of turbulence and plasma inhomogeneities, it is probably not trivial to determine the exact age of the plasma injections only using the radial velocity. Nevertheless, at least qualitatively, the radial speed is expected to be a good indicator of the evolution stage of the plasma injection (Hill 2016).

7.3 Summary and conclusions

So far, I have suggested that the auroral signatures of injection studied were associated with old injections, because they were in quasi-corotation and they presented a very small equatorward displacement. However, there are some equatorward bright patchy auroral features, as shown in this chapter, which present wider azimuthal and radial displacements than observed for the old injections. If the radial speed is indicative of the evolution stage of the plasma injection, then the significant radial speed of the structures suggests that they are related to young magnetospheric injections dominated by magnetosheric convection.

8 Systematic study of outer emissions from Juno spacecraft observations

8.1 Introduction

Between September 2003 and August 2016, the only way to obtain new information about plasma injections into Jupiter's magnetosphere was to study them from Earth, for example using auroral emissions, as I have done and described in previous chapters (Chapters 4, 5, 6 and 7). But the study of auroral phenomena using Earth-orbiting observatories has its limitations. As I mentioned earlier, HST can only observe the portion of Jupiter's aurora that is facing Earth, between dawn and dusk through noon LTs.

On 27 August 2016, NASA's Juno spacecraft made its first orbital flyby of Jupiter, and today the spacecraft continues its successful exploration of the planet and its magnetospheric environment. Thanks to Juno's UVS, we can observe all regions of auroral emission, in both the northern and southern hemispheres, during each PJ used for this study. In other words, the great advantage of using Juno data rather than HST data to study the auroral signatures of the injections is that we can study this phenomenon in all LT sectors and without bias in the CML. So, using Juno's UVS observations, I took the opportunity to study the signatures of plasma injections in Jupiter's

UV auroral emission, in particular in regions that are not accessible to HST.

The aim of this chapter is to verify that, with access to all auroral sectors, the auroral data still corroborates Galileo's in situ study of plasma injections and studies based on the auroral signatures of plasma injections using HST. To this end, I have developed a method for automatic detection of outer emissions based on the presence of a brightness peak and a CR peak. As mentioned in Chapter 6, based on Juno observations, Bonfond et al. (2017) have identified a spatial shift between the location of these two peaks in several auroral features associated with injections. This shift is the result of a differential drift of the particles over time. Finally, all the detections obtained are analysed statistically.

The following questions have been raised and this chapter will try to answer them. Are there preferential zones for the presence of these auroral signatures in SIII coordinates? Do they have preferential radial distances? Does the age of the structures that have been investigated influence their location in LT or SIII longitudes or their radial distance? Finally, given that a plasma injection detected in the magnetosphere does not necessarily give rise to an auroral signature (Haggerty et al. 2019), we wondered whether this behaviour had an impact on the distribution of these structures and more specifically whether the distribution in the northern and southern hemispheres differed.

8.2 Systematic study of the auroral signatures of plasma injections from observations by the Juno spacecraft

This study is based on the first 18 PJ of the Juno spacecraft between 27 August 2016 and 6 May 2019. The reconstruction of the images used is described in section 3.2. We started from the fact that an auroral signature of plasma injection has a brightness signature and a CR signature. As mentioned in previous chapters, in situ measurements of energetic electrons from plasma injections show that high-energy electrons drift upstream of low-energy electrons (Mauk et al. 1999, Clark et al. 2019). The value of CR is greater upstream of the auroral signatures of the injections in relation to the direction of rotation of the plasma. The observed shift is thought to be the auroral counterpart of the differential electron drift (Bonfond et al. 2017). The detection of this shift is an unambiguous evidence that the signatures studied are indeed related to the phenomenon of plasma injection into the equatorial plane of the magnetosphere. In addition, I have already highlighted the shift between the brightness peak and the CR peak in auroral signatures of plasma injections from the HST data. It is understood that an auroral signature of plasma injection can be associated with (1) the collocation of the brightness peak and the CR peak, corresponding to a very recent injection assuming an isotropic distribution: a “young” or “fresh” injection, (2) the brightness peak being located downstream with respect to the CR peak, in which case the electrons have already begun to drift : an ”old” or “mature” injection.

To carry out this study, we decided to look at all outer emissions magnetically mapping between 5 and 30 R_J. Specifically, we used contours with a

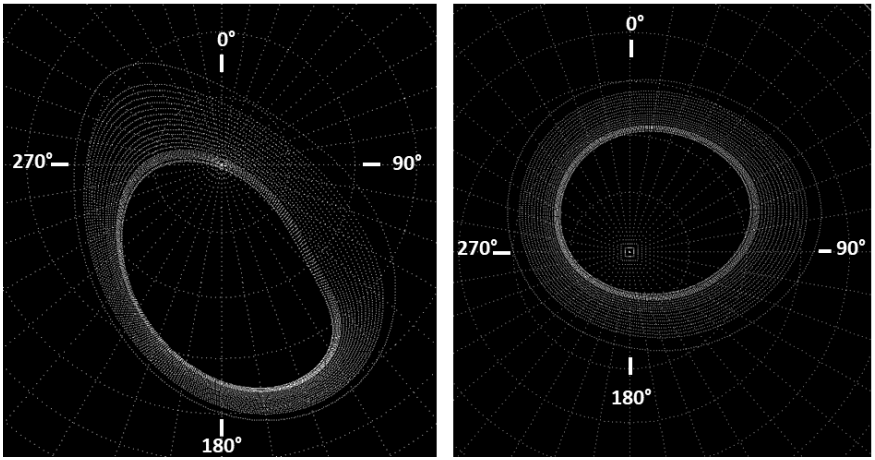

Figure 8.1 – Fixed R_J contours, between 5 and 30 R_J, in the equatorial plane projected into the ionosphere in the northern hemisphere (left), and in the southern hemisphere (right), with 0° SIII at the top, using JRM09 magnetic field model.

fixed equatorial distance (radial distance of the contours used: 5, 5.5, 6, 6.5, 7, 7.5, 8, 8.5, 9, 9.5, 10, 11, 12, 13, 14, 15, 16, 17, 18, 19, 20, 25 and 30 R_J) projected in the ionosphere using JRM09 magnetic field model in order to constrain the location of the injection signatures in the outer auroral region as efficiently as possible (Figure 8.1). We set this radial distance interval on the basis of previous observations, in which one injection signature has so far been detected beyond Io's auroral footpath (5.9 R_J) (Bonfond et al. 2012), and we stopped the detections at the edge of the main emission. We smoothed the images with 1000 km wide circular kernel in the ionosphere. We then measured the brightness and CR along the contours every 0.1° SIII and then smoothed the curves with a five points-wide boxcar kernel.

The aim of the first phase was to test the accuracy of the detections in all the outer emissions. Io's footprint was detected in almost all observations.

However, this was not the case for the footprints of the other satellites. We have removed the auroral region where Io's footprint is present by eliminating all longitudes visited by the footprint during the PJ, on the contours at 5.5 and 6 R_J, to avoid detecting the brightest of Io's footprint. The table 3.4, in Chapter 3, lists the position interval of Io during the observation. The brightness of the Europa and Ganymede footprints is much lower than that of Io, which may explain why they are not detected by the detection method used. The regions where these fortuits have therefore not been removed from the auroral data to minimise the loss of auroral information.

Along each fixed radial distance contour projected into the ionosphere, the brightness and CR peaks were detected. We first imposed the following detection thresholds: a minimum CR of 5, a minimum brightness of 50 kR, with at least 5 kR difference between two brightness extrema, and finally maximum azimuthal extent between two consecutive minima of 20°, consistent with the maximum azimuthal extent determined in Chapter 4. Based on these detection thresholds, we define "Type 1 detections". However, after a simple visual inspection of the polar maps, we noticed that certain auroral structures, which we would naturally have considered to be auroral signatures of plasma injections, fell below our detection thresholds. They were not detected because they were brighter, but their CR was less than 5. This led us to define the thresholds for "Type 2 detection": a minimum CR of 3, a minimum brigthness of 250 kR, with a minimum of 5 kR between the maximum and minimum brigthness, and maximum azimuthal extent between two consecutive minima of 20°. Figure 8.2 shows an example of the Type 1 (panels a and c) and Type 2 (panels b and d) detections obtained for PJ1 in the southern hemisphere in the brightness and CR maps. Panels a and c of Figure 8.2 show that, for example, the structure indicated by the yellow arrow should be associated with an auroral signature of plasma

injection. However, it is not detected at Type 1 detection thresholds. And conversely, panel b of figure 8.2 shows that the structure indicated by the orange arrow is detected at Type 1 detection thresholds, but not at Type 2 detection thresholds. This means that we are working with two different sets of detection thresholds in order to study the auroral signatures of plasma injections as accurately as possible.

8.2.1 Method for clustering detections

As we saw in Chapter 4, the auroral signatures of injections have a latitudinal extent. This implies, as shown in figure 8.2 and also in figures 8.4, 8.5 and 8.6, that multiple detections can be made within the same auroral structure due to their latitudinal extent, i.e. multiple contours crossing the auroral signature. To be consistent with the two previous studies, we want to work in terms of structure rather than detections. To do this, we need to group the detections of brightness peaks by auroral structure using a hierarchical clustering method. This method statistically analyses the detection data and constructs a hierarchy of clusters. In our case, the hierarchical clustering strategy is agglomerative, with each observation starting in its own cluster and pairs of clusters merging as one moves up the hierarchy, with the data presented in the form of a dendrogram (Figure 8.3). In other words, the positions of each brightness peak are used to calculate the distance between them in the aurora, creating a distance matrix. We then need two criteria to know how to combine the groups:

1. The measure of the dissimilarity between sets of detections, in this case the distance between detections of brightness peaks, which is a maximum of 2000 km in the aurora. In the study carried out in Chapter 4, more than 70% of the structures had azimuthal and latitudinal

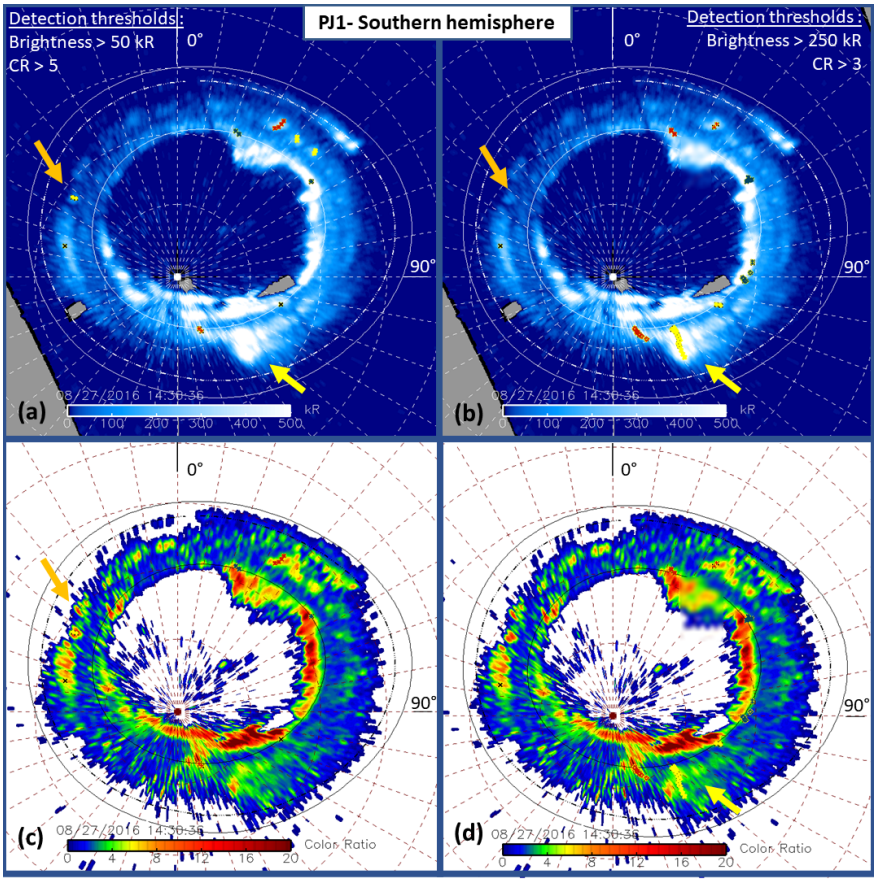

Figure 8.2 – The top two panels (a,b) are the same assemblages of polar projection of the data retrieved during PJ1 on 27 August 2016 between 13:51 and 14:30 for the southern hemisphere (with 0° SIII at the top). The bottom two panels (c, d) are similar maps as in panels a and b but for the CR. The dashed lines are Io's footprint according to JRM09 magnetic field model. The outer contour (solid line) is the contour at 5 RJ and the inner contour (solid line) is the contour at 30 RJ. In the panels (a,c), the detection thresholds are a minimum CR of 5, a minimum brightness of 50 kR. All Type 1 detections are therefore observed, and are represented by crosses. The orange arrow highlights detections made in the same structure. The yellow arrow highlights an area that should be associated with an auroral signature of plasma injection, but no detection has been made with these thresholds. In the panels (b,d), the detection thresholds are a minimum CR of 3, a minimum brightness of 250 kR. All Type 2 detections are therefore observed, and are represented by crosses. The yellow arrow highlights detections made in the same structure. The orange arrow highlights an area that should be associated with an auroral signature of plasma injection, but no detection has been made with these thresholds.

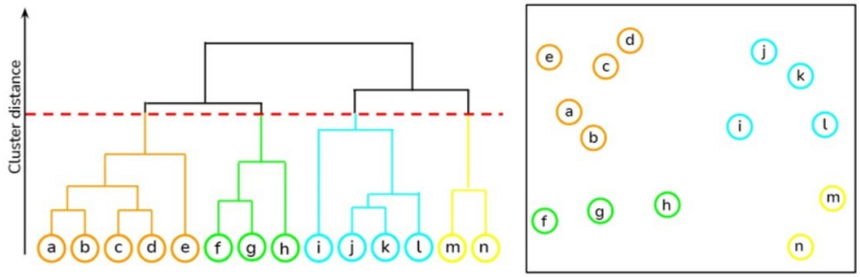

Figure 8.3 – Schematic representation of clustering. On the left, a dendrogram linking the detections according to the distance between them (the dotted red line corresponds to the maximum distance tolerated between 2 detections in the same cluster). On the right, the result of the clustering can be seen using the colour code. (https://towardsdatascience.com/hierarchical-clustering-explained-e59b13846da8)

extents greater than 2000 km.

2. The linking criterion, which specifies the dissimilarity of the sets as a function of the pairwise distances of the observations in the sets. This second criterion influences the shape of the clusters. In our case, we imposed a compact/homogeneous cluster, given the shape of the auroral structures associated with the injection signatures. In other words, we take the weighted average per pair, so that the distance between two clusters is defined as the average distance for all pairs of detections between each cluster, weighted by the number of objects in each cluster.

We applied clustering to all brightness peak detections. We define the position of the structures using the position of the brightest peak in the cluster. As we have seen, we have Type 1 and Type 2 detections which are assimilated to Type 1 and Type 2 structures respectively after clustering. Since

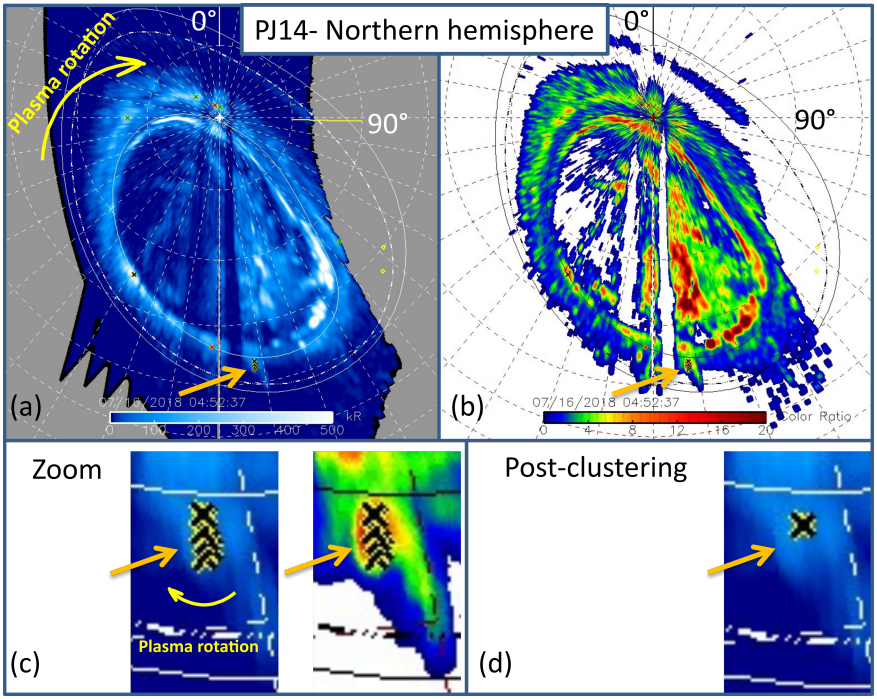

Figure 8.4 – Panel (a) is the assemblage of polar projection of the data retrieved during PJ14 on 16 July 2018 between 02:53 and 04:52 for the northern hemisphere (with 0° SIII at the top). Panel (b) is similar map as in panel (a) but for the CR. The dashed lines are Io's footprint according to JRM09 magnetic field model. The outer contour (solid line) is the contour at 5 R_J and the inner contour (solid line) is the contour at 30 R_J. The orange arrow highlights detections made in the same structure, with a no-shift. Panel (c) zooms in on the region of interest indicated by the orange arrows in the brightness and CR maps on the left and right, respectively. Panel (d) is the zoom on the region of interest in the brightness map after clustering. The black cross corresponds to the position of the brightest detection in the cluster, which defines the position of the detected auroral structure.

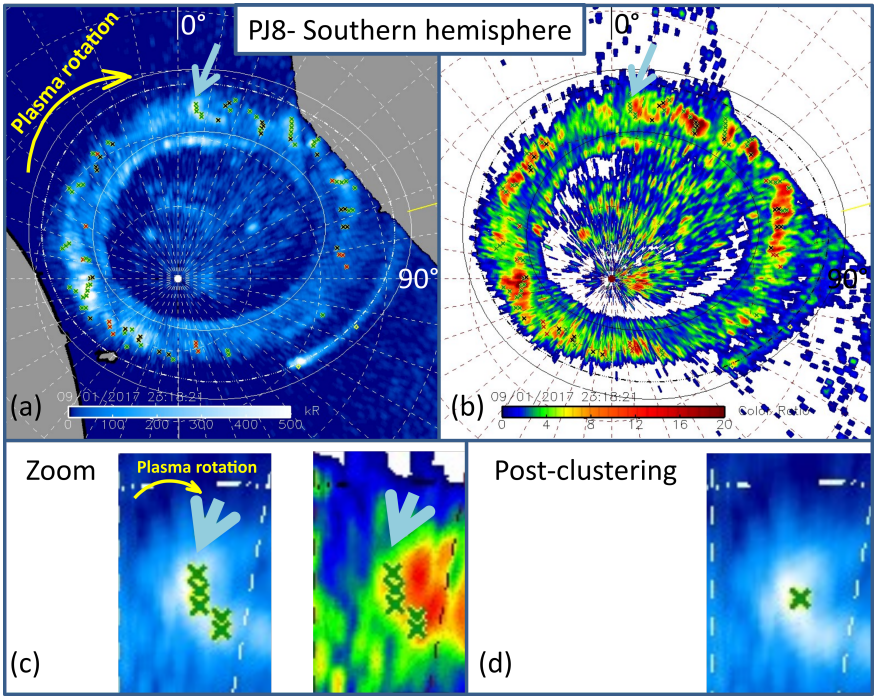

Figure 8.5 – The panel (a) is the assemblage of polar projection of the data retrieved during PJ8 on 1th September 2017 between 22:24 and 23:18 for the southern hemisphere (with 0° SIII at the top). The panel (b) is similar map as in panel (a) but for the CR. The dashed lines are Io's footprint according to JRM09 magnetic field model. The outer contour (solid line) is the contour at 5 R_J and the inner contour (solid line) is the contour at 30 R_J. The blue arrow highlights detections made in the same structure, with a negative shift. Panel (c) zooms in on the region of interest indicated by the blue arrows in the brightness and CR maps on the left and right, respectively. Panel (d) is the zoom on the region of interest in the brightness map after clustering. The green cross corresponds to the position of the brightest detection in the cluster, which defines the position of the detected auroral structure.

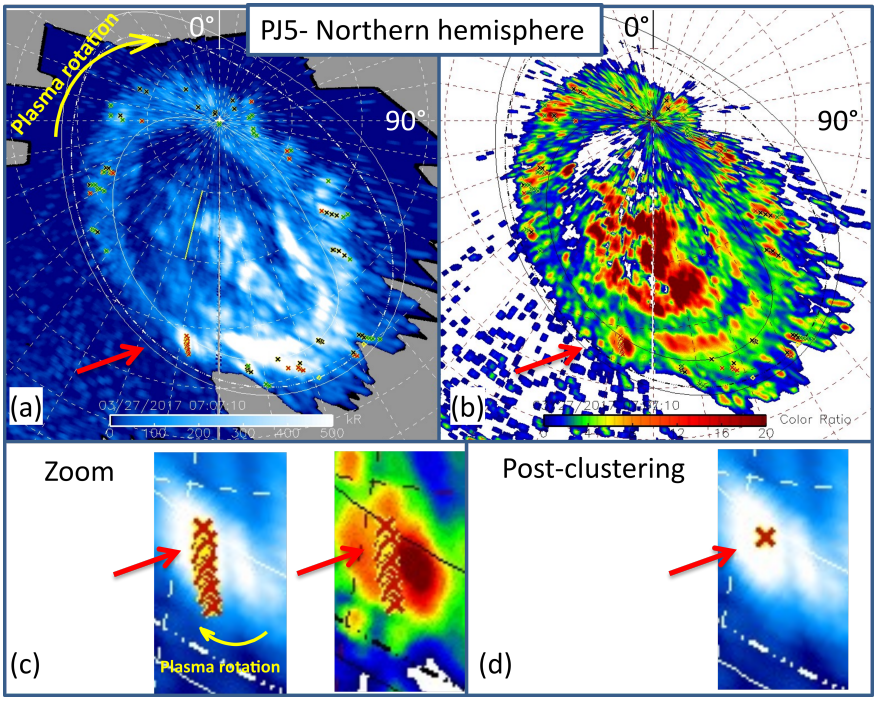

Figure 8.6 – The panel (a) is the assemblage of polar projection of the data retrieved during PJ5 on 27 March 2017 between 03:55 and 07:07 for the northern hemisphere (with 0° SIII at the top). The panel (b) is similar map as in panel (a) but for the CR. The dashed lines are Io's footprint according to JRM09 magnetic field model. The outer contour (solid line) is the contour at 5 R_J and the inner contour (solid line) is the contour at 30 R_J. The red arrow highlights detections made in the same structure, with a positive shift. Panel (c) zooms in on the region of interest indicated by the red arrows in the brightness and CR maps on the left and right, respectively. Panel (d) is the zoom on the region of interest in the brightness map after clustering. The red cross corresponds to the position of the brightest detection in the cluster, which defines the position of the detected auroral structure.

each brightness peak is associated with a CR peak, we define their shift from the magnetospheric coordinates SIII as the difference between the longitude of the brightness peak minus the longitude of the CR peak. The structure shift was defined as the median of the shifts in the same cluster. Three types of shifts are possible: negative, null and positive. As we saw in Chapter 6, the first two can be indeed related to the injection phenomenon. When the plasma is injected, it is assumed that electrons of different energies are uniformly distributed in the injected plasma, so that the brigthness peak and the CR peak are colocalised and their shift is null (Figure 8.4). In this chapter, it may also be referred to as the "no-shift". Over time, a separation occurs between the populations of high and low energy electrons because the high energy electrons (responsible for large CR) drift faster (in longitude) than the low energy electrons (responsible for small CR). This causes the brightness peaks to lie behind the CR peak, resulting in a negative shift between the longitude of the brightness peak and the longitude of the CR peak (Figure 8.5). We have allowed a margin of error so that the no-shift is between ± 0.9°. The aim of this tolerance is to detect positive or negative shifts with a minimum absolute value of 1°. This is consistent with Chapter 6, where we defined a structure with a shift of -1.3° as the young structure. For the positive shift, the brightness peak is upstream of the CR peak (Figure 8.6). Figure 8.7 shows an example of this clustering for PJ1 in the southern hemisphere. For Type 1 structures, in panel (a) of Figure 8.7, eight different auroral structures are observed: five with a no-shift between the brightness peaks and CR, associated with fresh injections (black crosses), and three with the shift typical of an auroral signature of more mature plasma injections (green crosses). For Type 2 structures, eight different auroral structures are observed in panel b of Figure 8.7: four with a shift associated with young injections (black crosses), and four with the shift typical of an auroral signature of more mature plasma injections (green

crosses).

To determine whether our structure distributions are inhomogeneous (homogeneous), i.e. whether statistically there are (or are not) zones of preferential presence as a function of the parameters studied (SIII longitude, LT and radial distance), χ^2 tests are performed. The result is considered homogeneous if the p-value is greater than or equal to 0.1, quasi-homogeneous if this value is between 0.05 and 0.1, and inhomogeneous if the p-value is less than 0.05 (Johnson 2013). Uncertainty bars derived from the shot noise have also been taken into account, i.e. the uncertainty is related to the number of structures detected (N) and is equal to $\pm \sqrt{N}$. Before going any further, we wanted to know whether the application of clustering significantly modified the distribution of detection shifts. Therefore, a χ^2 test was performed on the distribution of the different detection shifts before and after clustering. The result was that clustering did not significantly change the percentages of any of the three shifts examined (χ^2 test, p-value > 0.1).

The structures with a positive shift are related to our assembly method, described in chapter 3. During a PJ, Juno-UVS does not have the capacity to observe all auroral emissions instantaneously. We are therefore forced to assemble the observations by performing a weighted sum of successive spins. These non-simultaneous compilations are then assembled, and it may happen that we observe one part of a structure at a time "t" and while the other part was observed earlier or later, this delay can range from 30 seconds to several hours (Table 3.4). The greater the time lag, the more time the particles have had to drift and the more the CR will vary over time. Finally, we are faced with the detection of energetic structures that have a positive shift between the brightness peak and the CR peak. We have checked each of these positive shifts by looking at the movies reconstructed

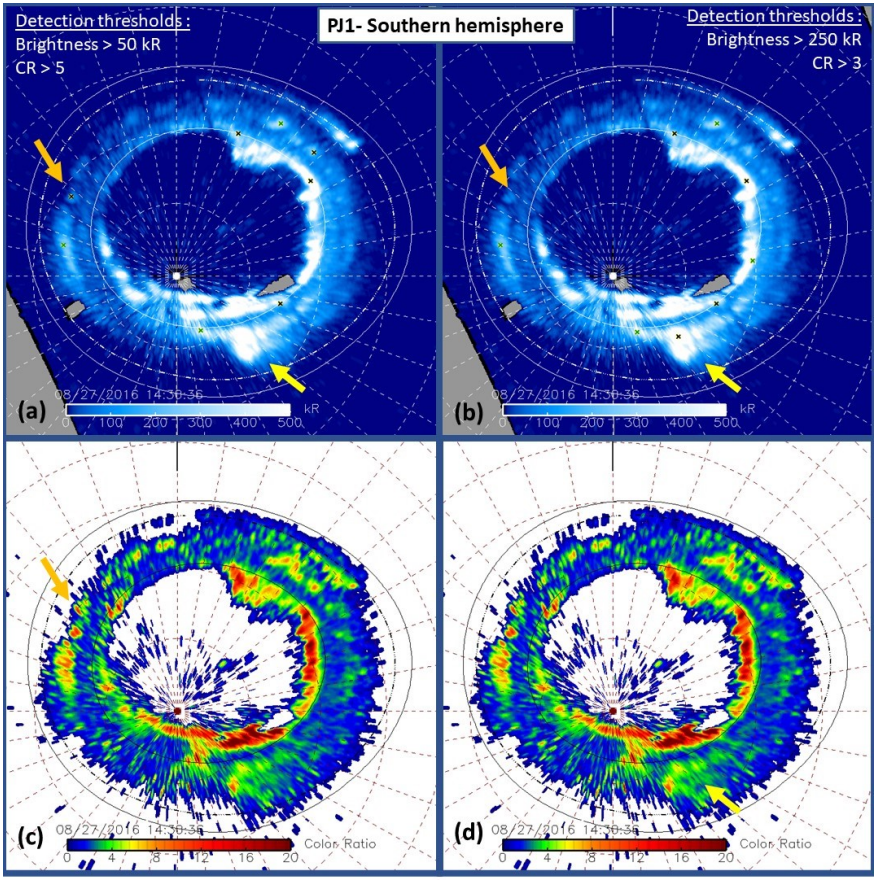

Figure 8.7 – This figure is the same as figure 8.2 after applying the clustering. The top two panels (a,b) are the same assemblages of polar projection of the data retrieved during PJ1 on 27 August 2016 between 13:51 and 14:30 for the southern hemisphere (with 0° SIII at the top). The bottom two panels (c, d) are similar maps as in panels a and b but for the CR. The dashed lines are Io's footprint according to JRM09 magnetic field model. The outer contour (solid line) is the contour at 5 R_J and the inner contour (solid line) is the contour at 30 R_J. In the panels (a,c), the detection thresholds are a minimum CR of 5, a minimum brightness of 50 kR. All Type 1 structures are therefore observed, and are represented by crosses. The yellow arrow highlights an area that should be associated with an injection signature, but no structure has been made with these thresholds. In the panels (b,d), the detection thresholds are a minimum CR of 3, a minimum brightness of 250 kR. All Type 2 structures are therefore observed, and are represented by crosses. The yellow arrow highlights a structure .The orange arrow highlights an area that should be associated with an injection signature, but no structure has been made with these thresholds.

from each PJ. An example of such discontinuity in a Juno UVS sequence is shown in Figure 8.6. After clustering, it is the assembly method that is responsible for the presence of the positive shift.

8.3 Analysis of auroral signatures of plasma injections in the ionosphere

The study of auroral structures associated with plasma injections in Jupiter's magnetosphere is divided into 2 different types of structures: Type 1 structures, corresponding to low brightness (minimum brightness detection > 50 kR) and having a minimum CR of 5, and Type 2 structures, corresponding to higher brightness (minimum brightness detection > 250 kR) and having a minimum CR of 3. Over the 18 PJ considered, 253 Type 1 structures were detected (132 in the north and 121 in the south) and 166 Type 2 structures were detected (92 in the north and 74 in the south). Given the detection thresholds, it is possible for the same structure to be present in both Type 1 and Type 2 structures, provided that its brightness is greater than 250 and its CR is greater than 5.

The analysis of the distribution of the SIII longitudes and shifts of the Type 1 structures in the ionosphere is carried out (Figure 8.8). In the northern hemisphere, an inhomogeneous combined distribution is observed (χ^2 test, p-value < 0.01) (Figure 8.8 panel (b)), with a detection peak between 135° and 180°. In this longitude interval, the peak is mainly due to the presence of auroral structures associated with fresh injections (no-shift) (Figure 8.8 panel (c)). A very few structures (< 9%) are detected between 315° and 90°. The combined distribution in the southern hemisphere (Figure 8.9

panel (b)) is almost homogeneous (χ^2 test, p-value = 0.08). In particular, the distributions of the different types of shift are homogeneous or quasi-homogeneous (χ^2 tests, p-value > 0.08) (Figure 8.9 panels (c), (e) and (f)). It should be noted, however, that the distribution of Type 1 structures with a positive shift, in both hemispheres ((Figures 8.8 and 8.9 panel (d)), appears to be relatively homogeneous, although the χ^2 test may not be meaningful because of the paucity of data points. The distribution of the difference between the number of structures with a negative shift and the number of structures with a positive shift is intended to show that the structures with a negative shift predominate and that the observed phenomenon is real. Indeed, we have shown that structures with a positive shift are associated with the reconstruction of Juno images from UVS. We therefore assumed that, in the worst case, we could erroneously detect as many structures with a positive shift as with a negative shift associated with image reconstruction. This led us to look at the difference between structures with a negative shift and those with a positive shift. If we have more structures with a negative shift than with a positive shift, this is undeniable proof that the structures with a negative shift are real. In the northern hemisphere (panel (f) of Figure 8.8), the distribution of the difference between the number of structures with a negative shift and the number of structures with a positive shift is inhomogeneous, with two zones of presence between [90° ;180°] and [225° ;315°]. In the southern hemisphere (panel (f) of Figure 8.9), their distribution is almost homogeneous (χ^2 test, p-value = 0.09).

As for the detection of Type 2 structures in the northern hemisphere (Figure 8.10), we see an inhomogeneous combined distribution (χ^2 test, p-value < 0.01) (Figure 8.10 panel (b)), with a maximum presence between 180° and 225°, which is in agreement with the maximum detection of structures with a negative shift (Figure 8.10 panel (e)). The distribution then decreases,

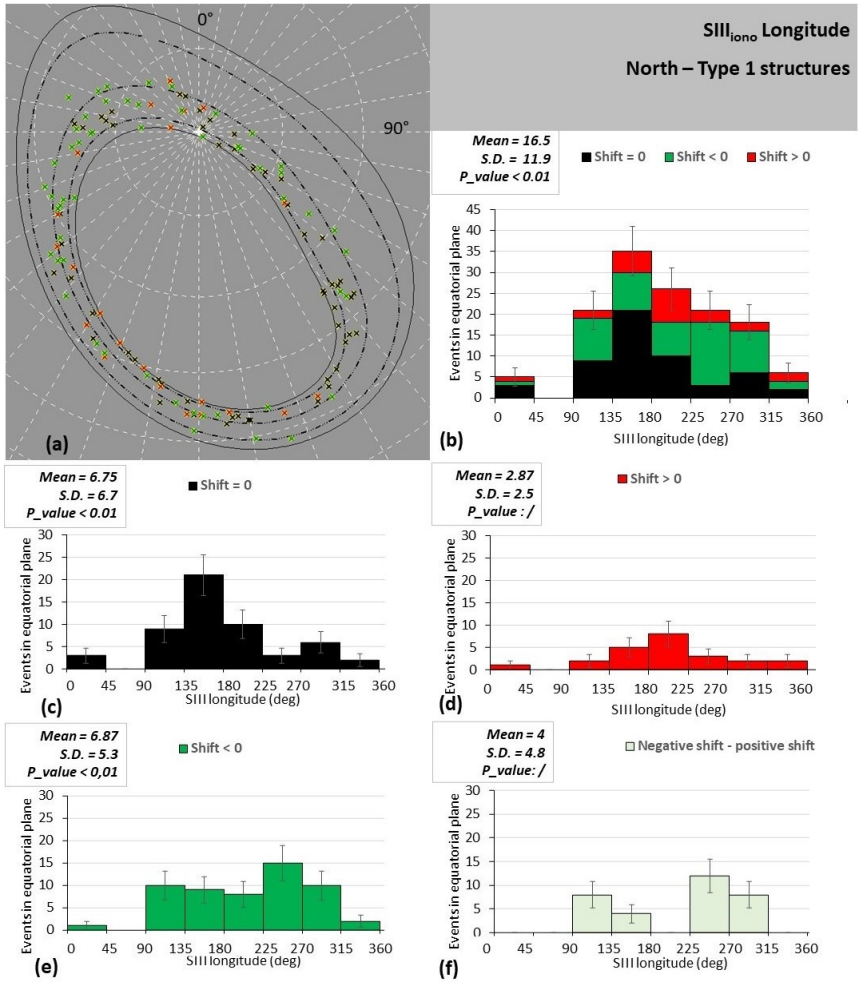

Figure 8.8 – The positions of the Type 1 structures observed in the northern hemisphere (with 0° SIII at the top) are reported in a polar projection (a), where the contour at 5 R_J is the outer contour (solid line), the contour at 30 R_J is the inner contour (solid line), the three footpaths of Io, Europa and Ganymede are the dashed lines. Black crosses correspond to no-shift, green crosses to negative shift and red crosses to positive shift. The distributions of these structures as a function of ionospheric longitude SIII are shown in the histograms with three different shifts combined (b), no-shift (c), positive shift (d), negative shift (e) and finally the difference between the number of structures with negative shift and the number of structures with positive shift (f). The uncertainty bars are derived from the shoot noise of the detection number. The mean and standard deviation (S.D.) of each distribution are given for each histogram. If the number of structures is sufficient, a χ^2 test is performed and the p-value is given, otherwise the p-value = /.

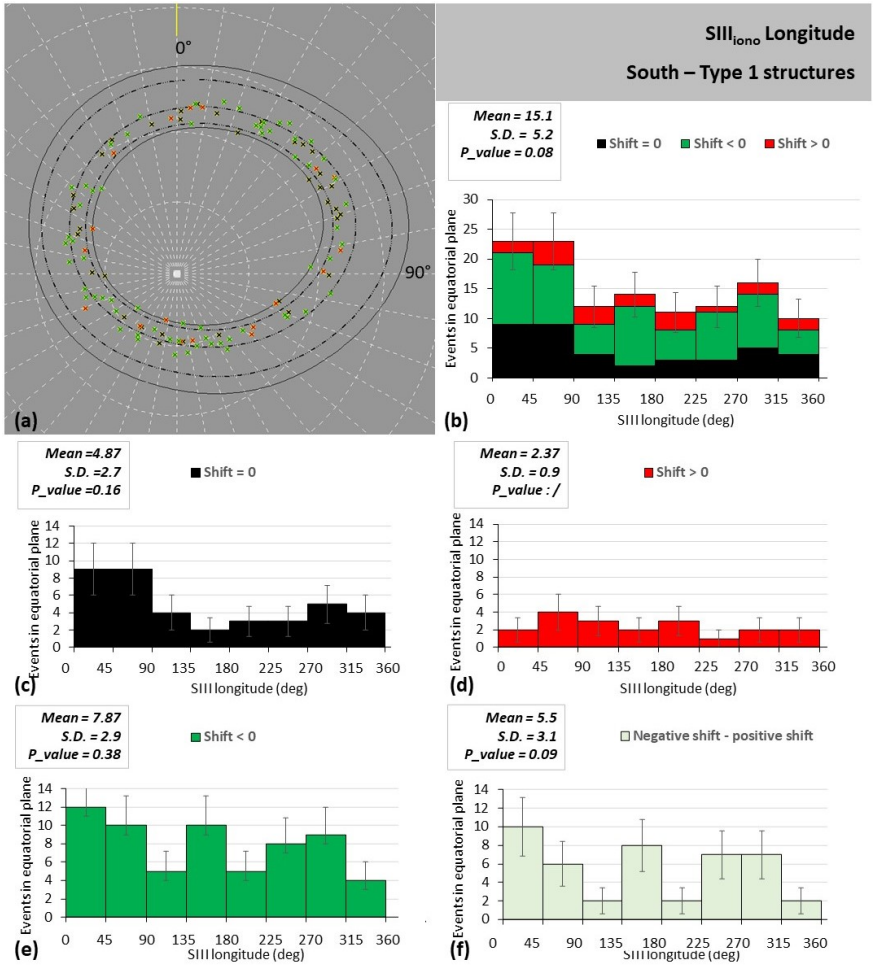

Figure 8.9 – The positions of the Type 1 structures observed in the southern hemisphere (with 0° SIII at the top) are reported in a polar projection (a), where the contour at 5 R_J is the outer contour (solid line), the contour at 30 R_J is the inner contour (solid line), the three footpaths of Io, Europa and Ganymede are the dashed lines. Black crosses correspond to no-shift, green crosses to negative shift and red crosses to positive shift. The distributions of these structures as a function of ionospheric longitude SIII are shown in the histograms with three different shifts combined (b), no-shift (c), positive shift (d), negative shift (e) and finally the difference between the number of structures with negative shift and the number of structures with positive shift (f). The uncertainty bars are derived from the shoot noise of the detection number. The mean and standard deviation (S.D.) of each distribution are given for each histogram. If the number of structures is sufficient, a χ^2 test is performed and the p-value is given, otherwise the p-value = /.

with a zone of no detection between 0° and 90°. For structures with a no-shift (Figure 8.10 panel (c)), the maximum detection is between 135° and 180°. In the southern hemisphere (Figure 8.11 panel (b)), the combined distribution is quasi-homogeneous (χ^2 test, p-value = 0.07), with only the structures with no-shift showing an inhomogeneous distribution (χ^2 test, p-value = 0.03) with a detection maximum between 0° and 90° (Figure 8.11 panel (c)). Few structures with a positive shift are found in both north and south (Figures 8.10 and 8.11 panel (d)). In both hemispheres, the distribution of the number of structures with a negative shift minus those with a positive shift (Figures 8.10 and 8.11 panel (f)) follows the distribution trend for structures with a negative shift. This is consistent with the low detection count of structures with a positive shift.

For both Type 1 and Type 2 structures, more were detected in the north than in the south. However, the difference is not significant (4.4 % and 10.8 % more structures of Type 1 and 2 respectively in the north). One possible explanation is that for the first 18 PJ the spatial resolution of the southern hemisphere observations is always slightly lower than that of the northern hemisphere observations, due to the trajectory of the spacecraft. During the first PJs, the spatial resolution is equivalent in both hemispheres. As the PJ evolves, Juno's perijove gets closer and closer to the north pole, which increases the resolution in the northern hemisphere, compared to the southern hemisphere, but the spatial coverage of the aurora is smaller (Gladstone et al. 2017). The distribution of structures is always more homogeneous in the southern hemisphere than in the northern hemisphere. This inhomogeneity of the distribution in the north may be explained by two different elements. The first is geometric: between 0° and 90°, the observed area is very small due to its proximity to the pole, as can be seen in Figures 8.8 and 8.10 panel (a). The second is related to the intensity of the surface

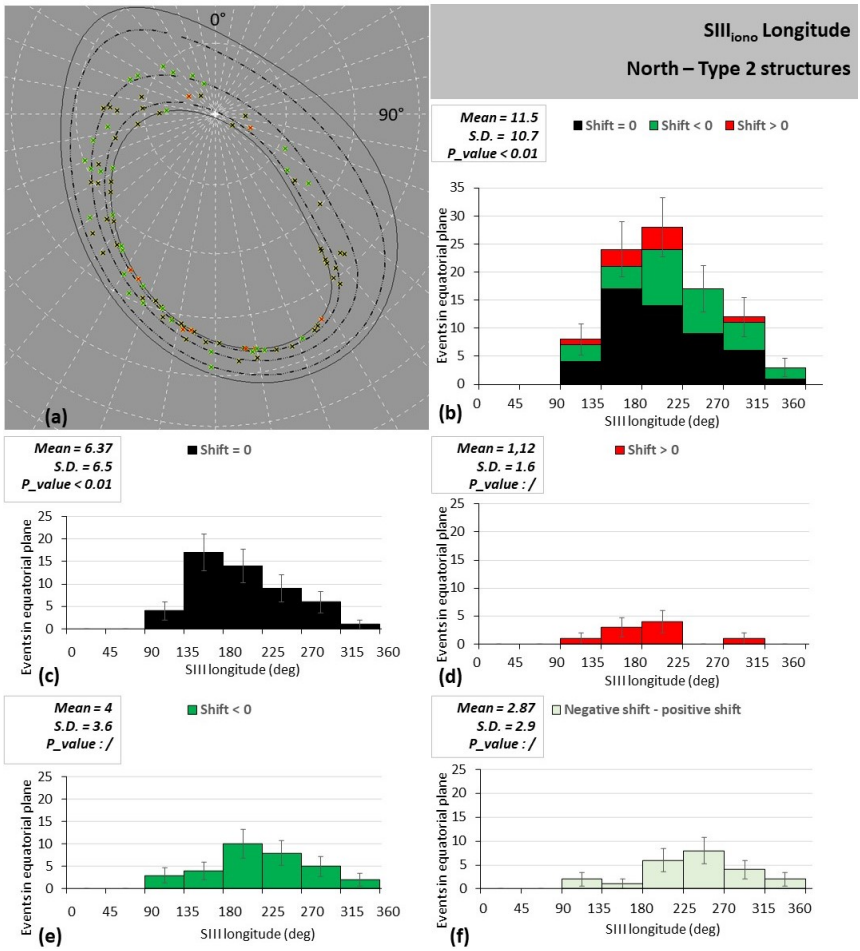

Figure 8.10 – The positions of the Type 2 structures observed in the northern hemisphere (with 0° SIII at the top) are reported in a polar projection (a), where the contour at 5 R_J is the outer contour (solid line), the contour at 30 R_J is the inner contour (solid line), the three footpaths of Io, Europa and Ganymede are the dashed lines. Black crosses correspond to no-shift, green crosses to negative shift and red crosses to positive shift. The distributions of these structures as a function of ionospheric longitude SIII are shown in the histograms with three different shifts combined (b), no-shift (c), positive shift (d), negative shift (e) and finally the difference between the number of structures with negative shift and the number of structures with positive shift (f). The uncertainty bars are derived from the shoot noise of the detection number. The mean and standard deviation (S.D.) of each distribution are given for each histogram. If the number of structures is sufficient, a χ^2 test is performed and the p-value is given, otherwise the p-value = /.

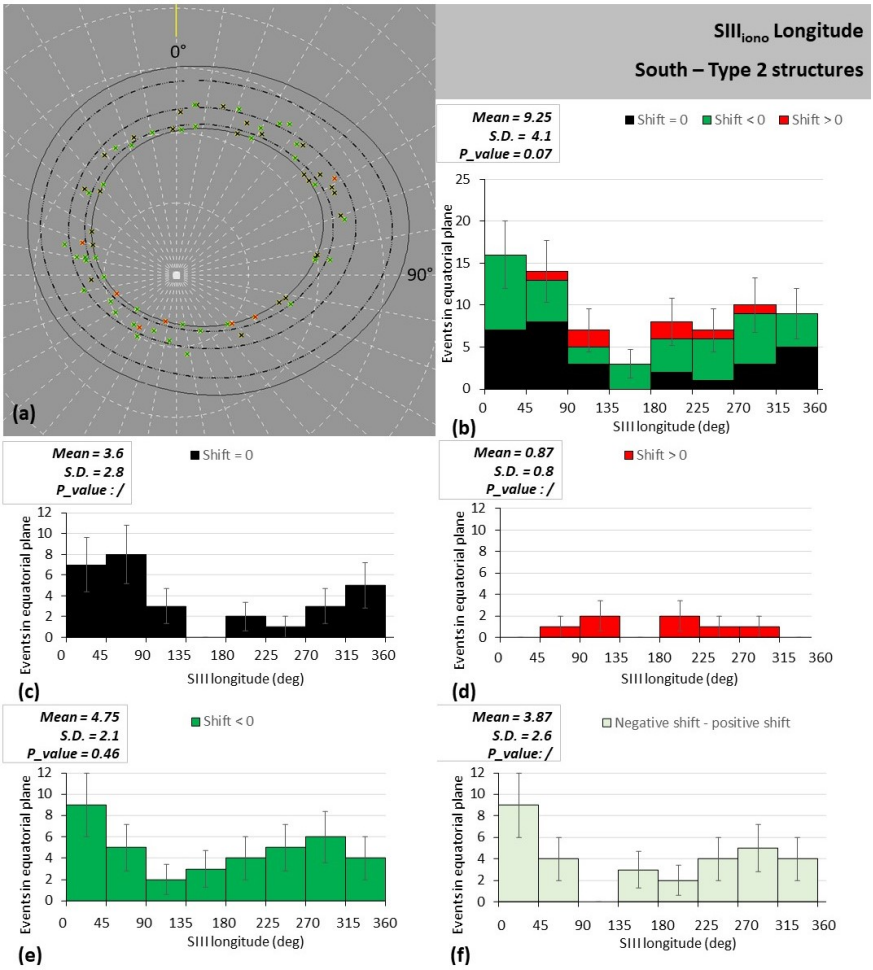

Figure 8.11 – The positions of the Type 2 structures observed in the southern hemisphere (with 0° SIII at the top) are reported in a polar projection (a), where the contour at 5 R_J is the outer contour (solid line), the contour at 30 R_J is the inner contour (solid line), the three footpaths of Io, Europa and Ganymede are the dashed lines. Black crosses correspond to no-shift, green crosses to negative shift and red crosses to positive shift. The distributions of these structures as a function of ionospheric longitude SIII are shown in the histograms with three different shifts combined (b), no-shift (c), positive shift (d), negative shift (e) and finally the difference between the number of structures with negative shift and the number of structures with positive shift (f). The uncertainty bars are derived from the shoot noise of the detection number. The mean and standard deviation (S.D.) of each distribution are given for each histogram. If the number of structures is sufficient, a χ^2 test is performed and the p-value is given, otherwise the p-value = /.

magnetic field, which is not uniform (Connerney et al. 2022) (more details in Section 1.3.1). The distribution of fresh structures appears to be related to the magnetic intensity, as the frequency of detection of fresh structures (no-shift) increases with the magnetic field. This suggests that the mechanism associated with the auroral signatures of plasma injections is related to magnetic field intensity. In addition, the distributions are homogeneous in the southern hemisphere, which further supports this hypothesis because the magnetic field in the southern hemisphere is much more homogeneous than in the northern hemisphere (Connerney et al. 2022). Until now, the favoured mechanism to explain the brightness of the injection signatures was the pitch angle diffusion/scattering. In this process, the altitude of the mirror point increases as the surface magnetic field increases, so that fewer auroral electrons can reach the ionosphere (Grodent et al. 2008), which is not consistent with our observations. On the other hand, we consider the notion of "mirror ratio", which is defined as the ratio between the magnetic field strength in the (ionospheric) acceleration region and the magnetic field strength in the corresponding region (along the field lines) of the equatorial plane (Vasyliūnas 2004). For Io's footprint, Hess et al. (2013) showed a dependence between the efficiency of energy transfer from Alfvén waves to electrons and the intensity of the magnetic field strength in the acceleration region. When the mirror ratio increases, the magnetic flux in the acceleration region increases; when the magnetic flux of the precipitation zone increases, so does that of the acceleration region. This implies an increase flow of precipitated electrons in the ionosphere which means more auroral emission. It therefore appears that the Alfvén wave acceleration process is more consistent with the detection of auroral structures that we obtain in this study. The transfer of energy from Alfvén waves to electrons is therefore more efficient when the mirror ratio is high, which is exactly the opposite of the pitch angle diffusion process, which involves a smaller

loss cone (i.e. less auroral emission) when the mirror ratio is high.

8.4 Analysis of auroral signatures of plasma injections projected in the equatorial plane

Using the JRM09 magnetic field model, the ionospheric results are projected in the equatorial plane in order to cancel the effect of the magnetic field topology on the location of the auroral structures. Furthermore, it makes it possible to compare the properties of the auroral signatures derived from Juno-UVS with the statistical characteristics of plasma particles, associated with magnetospheric injections, previously made with the Galileo spacecraft near Jupiter's equatorial plane. The analysis of the results will be according to the type of structure: Type 1 and Type 2 structures projected in the equatorial plane, for each of the parameters studied: SIII longitude, LT and radial distance. All the results are then discussed for each parameter studied.

8.4.1 Magnetospheric SIII longitude

Generally the distribution of Type 1 structures in SIII longitude in the equatorial plane is not homogeneous (χ^2 test, p-value = 0.01), even when the uncertainty bars are taken into account (Figure 8.12). On average, 31.6 structures were detected per 45° longitude sector[1], with a standard deviation of 8.3. If we look separately at the three types of shift: the negative

[1]These longitude sectors are the same range as those used for the Galileo (Mauk et al. 1999) and HST (Chapter 4) studies.

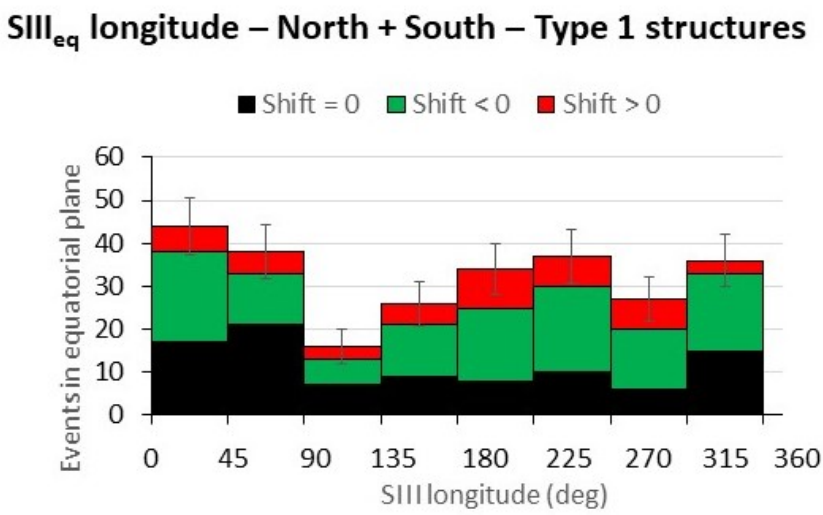

Figure 8.12 – The distributions of the positions of Type 1 structures observed in the northern and southern hemispheres, magnetically mapped in the equatorial plane using the JRM09 magnetic field mode, as a function of equatorial longitude SIII are shown in the histograms with three different shifts combined : no-shift (black), negative shift (green) and positive shift (red). The uncertainty bars are derived from the shoot noise of the detection number.

shift and the positive shift show a homogeneous distribution (χ^2 tests, respectively, p-value = 0.11; p-value = 0.62) with an average of 14.7 mature structures detected per sector with a standard deviation of 5 and an average of 5.2 structures with a positive shift per sector with a standard deviation of 2.1. As for the no-shift, the distribution is inhomogeneous (χ^2 test, p-value = 0.01), with an average per sector of 11.6 and a standard deviation of 5.4. The distribution density is twice as small between 90° and 315° as in the rest of the distribution (between 315 and 90°: mean = 17.66 per 45° interval and between 90° and 315°: mean = 8 per 45°).

In each hemisphere, the data collected for Type 1 structures are analysed separately. In the northern hemisphere, the distribution of Type 1 structures detected and projected in the equatorial plane (Figure 8.13) is inhomogeneous (χ^2 test, p-value = 0.03). The distribution of structures with no-shift is almost homogeneous (χ^2 test, p-value = 0.08) and the one with positive shift appears homogeneous, although the χ^2 test is not applicable for the latter due to insufficient numbers. The inhomogeneity of the combined distribution is due to the inhomogeneity of the distribution of structures with a negative shift (χ^2 test, p-value = 0.03). The distribution consists of 10 structures detected between 0° and 45° and the number of detections decreases until it reaches a minimum of one structure detected between 90° and 135°, before gradually increasing to 315° and 360° with 13 structures detected. The histogram of the difference between the number of structures with a negative shift and the number of structures having a positive shift is intended to show that structures with a negative shift predominate and that the observed phenomenon is real, as discussed in Section 8.3. Their distribution is relatively inhomogeneous, with the difference in structures showing a greater frequency between 315° and 360°.

In the southern hemisphere, the distribution of Type 1 structures detected in the equatorial plane (Figure 8.14) is statistically homogeneous (χ^2 test, p-value = 0.53). The distribution of structures with a no-shift is statistically homogeneous (χ^2 test, p-value = 0.13), but there is a variation in detection ranging from 1 structure between 90° and 135° to a maximum of 9 detections between 45° and 90° and between 315° and 360°. The distribution of structures with a negative shift is homogeneous (χ^2 test, p-value = 0.25), with a minimum of 5 structures detected between 90° and 135° and between 270° and 360°, and a maximum of 12 structures between 180° and 270°. The histogram of the difference between the number of structures with a

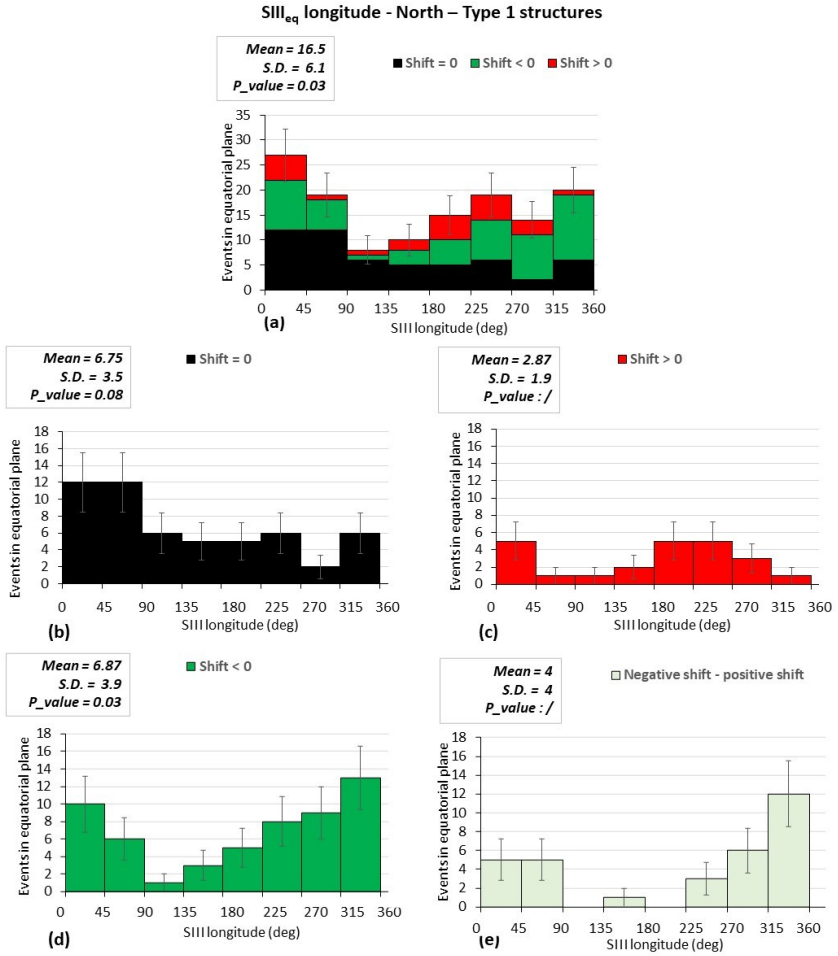

Figure 8.13 – The positions of Type 1 structures observed in the northern hemisphere are magnetically projected in the equatorial plane using the JRM09 magnetic field model. The distributions of these events in the equatorial plane as a function of equatorial longitude SIII are shown in the histograms with three different shifts combined (a), no-shift (b), positive shift (c) negative shift (d) and finally the difference between the number of structures with a negative shift and the number of structures with a positive shift (e). The uncertainty bars are derived from the shoot noise of the detection number. The mean and the standard deviation (S.D.) of each distribution are given for each histogram. If the number of structures is sufficient, a χ^2 test is performed and the p-value is given, otherwise the p-value = /.

negative shift and the number of structures having a positive shift shows that structures with negative shift are predominant and their distribution is inhomogeneous (χ^2 test, p-value = 0.02), with two detections maxima between 0° and 90° and between 225° and 270°.

In general, in SIII longitude in the equatorial plane, the distribution of Type 2 structures (Figure 8.15) is not homogeneous (χ^2 test, p-value = 0.04). On average, 20.75 structures were detected per 45° longitude sector. Considering the three types of shifts separately, the no-shift has a homogeneous distribution (χ^2 test, p-value = 0.33) and the positive shift appears homogeneous, although the χ^2 test may not be meaningful because of the paucity of data points. As for the negative shift, its distribution is inhomogeneous (χ^2 test, p-value = 0.02). The density of the distribution is 8 times greater between 225° and 270° than between 90° and 135°, which corresponds to the minimum number of structures detected, of which there are two in the latter sector.

Splitting the analysis by hemisphere, the distribution of the projection in the equatorial plane of the Type 2 structures detected in the northern hemisphere (Figure 8.16) is homogeneous overall (χ^2 test, p-value = 0.13). The distribution of structures with a no-shift is homogeneous (χ^2 test, p-value = 0.58) and that with a positive shift appears homogeneous, however, it is possible that the χ^2 test is not significant due to the small number of data points. The distribution of Type 2 structures with negative shift appears to be inhomogeneous. No structures were detected between 90° and 135°, while a maximum of 9 structures were detected between 225° and 270°. The distribution of the difference between the number of structures with a negative shift and the number of structures with a positive shift is inhomogeneous. This distribution maximizes between 215° and 315°.

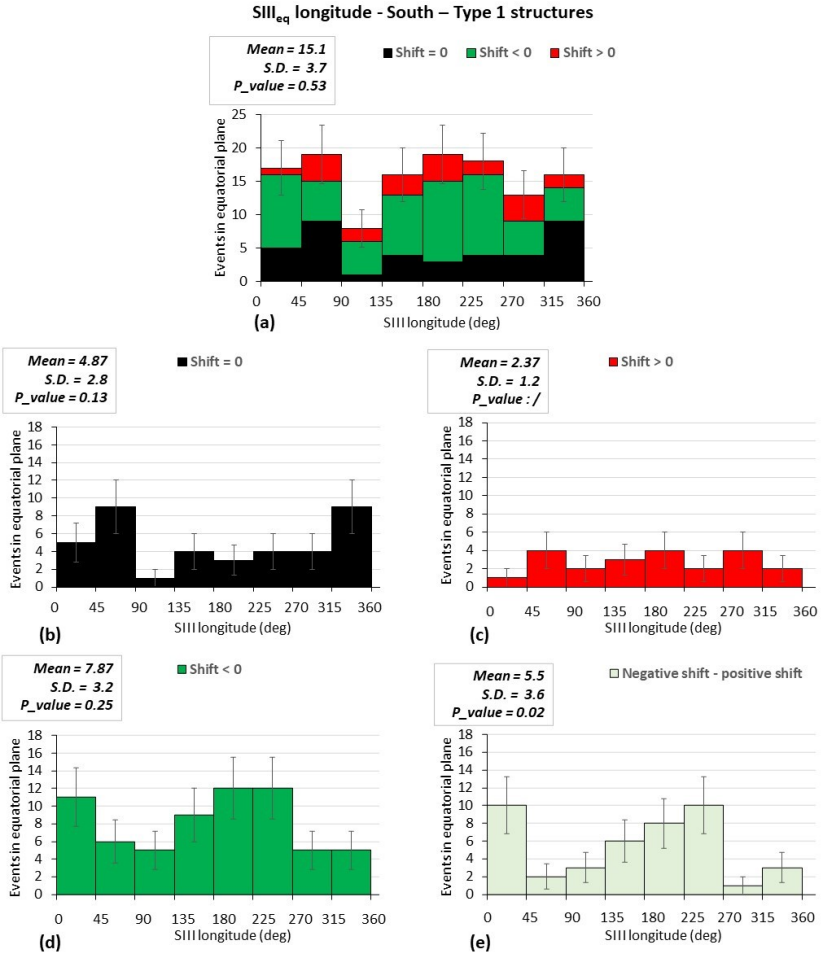

Figure 8.14 – The positions of Type 1 structures observed in the southern hemisphere are magnetically projected in the equatorial plane using the JRM09 magnetic field model. The distributions of these events in the equatorial plane as a function of equatorial longitude SIII are shown in the histograms with three different shifts combined (a), no-shift (b), positive shift (c) negative shift (d) and finally the difference between the number of structures with a negative shift and the number of structures with a positive shift (e). The uncertainty bars are derived from the shoot noise of the detection number. The mean and the standard deviation (S.D.) of each distribution are given for each histogram. If the number of structures is sufficient, a χ^2 test is performed and the p-value is given, otherwise the p-value = /.

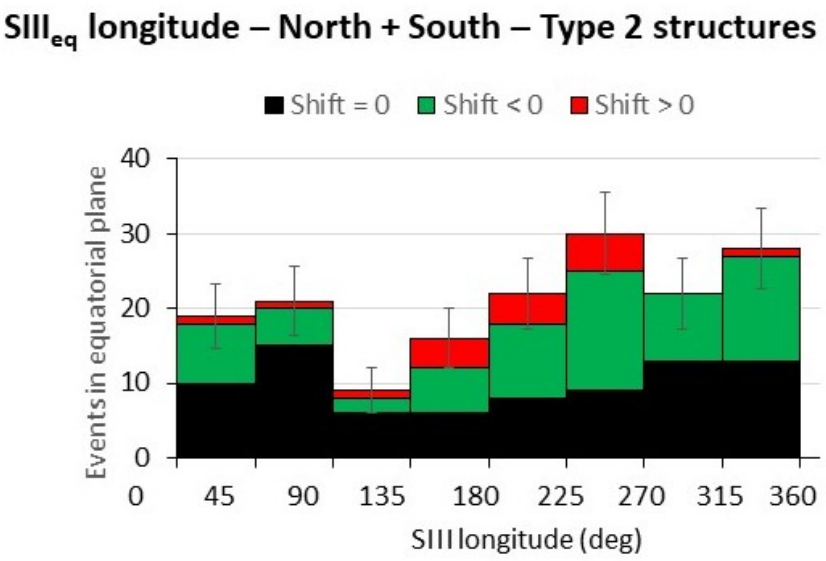

Figure 8.15 – The distributions of he positions of Type 2 structures observed in the northern and southern hemispheres, magnetically mapped in the equatorial plane using the JRM09 magnetic field mode, as a function of equatorial longitude SIII are shown in the histograms with three different shifts combined : no-shift (black), negative shift (green) and positive shift (red). The uncertainty bars are derived from the shoot noise of the detection number.

In the southern hemisphere, the distribution of Type 2 structures projected in the equatorial plane (Figure 8.17) is statistically homogeneous (χ^2 test, p-value = 0.19). The distribution of structures with a negative shift is statistically quasi-homogeneous (χ^2 test, p-value = 0.08). However, for the no-shift, no structures were detected between 180° and 225° and a maximum of 7 structures were detected between 315° and 360°. The distribution of negative shift structures is at least 2 per detection interval ([90° ;180°] and [270° ;315°]), with a maximum of 9 detections between 315°

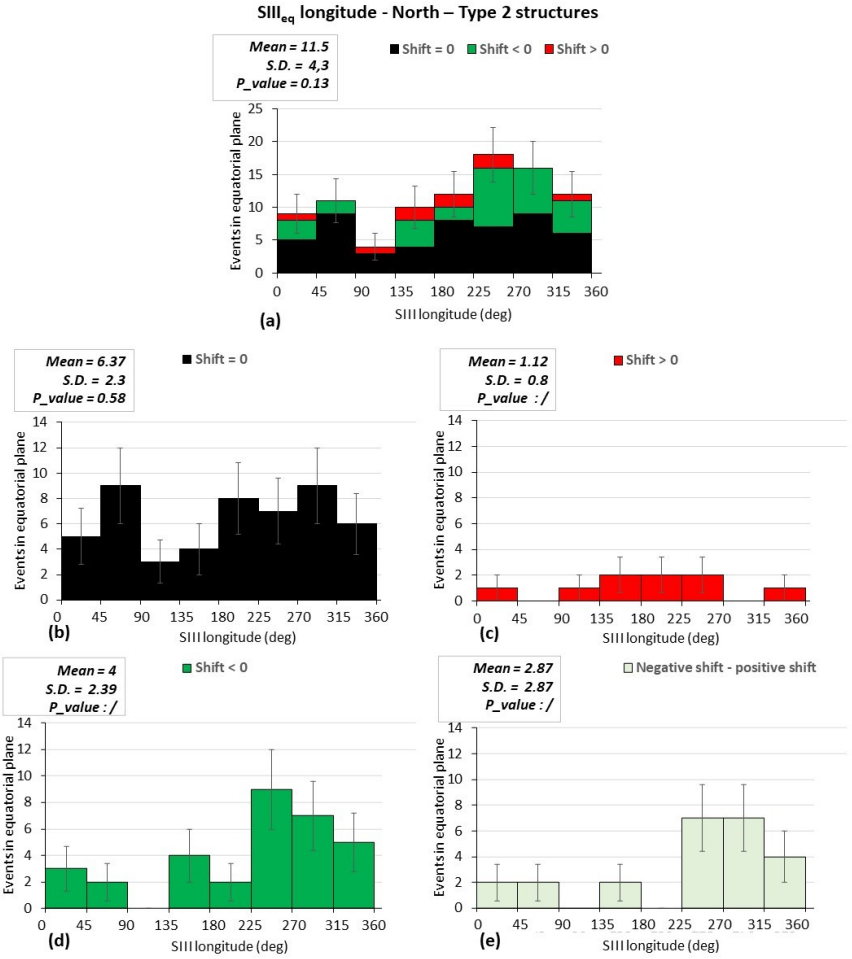

Figure 8.16 – The positions of Type 2 structures observed in the northern hemisphere are magnetically projected in the equatorial plane using the JRM09 magnetic field model. The distributions of these events in the equatorial plane as a function of equatorial longitude SIII are shown in the histograms with three different shifts combined (a), no-shift (b), positive shift (c) negative shift (d) and finally the difference between the number of structures with a negative shift and the number of structures with a positive shift (e). The uncertainty bars are derived from the shoot noise of the detection number. The mean and the standard deviation (S.D.) of each distribution are given for each histogram. If the number of structures is sufficient, a χ^2 test is performed and the p-value is given, otherwise the p-value = /.

and 360°. There are few structures with a positive shift, with a maximum of 3 detected per zone and an average of only one. The distribution of the number of structures with a negative shift minus those with a positive shift is inhomogeneous with a maximum of detections between 315° and 360°.

The Type 1 and Type 2 structures magnetically projected in the equatorial plane are present on all magnetospheric SIII longitudes. The distribution of young structures is relatively homogeneous across all SIII longitudes. The distribution of more mature structures is more inhomogeneous, with no specific area of predilection, which may simply be the result of the drift of the structures over time. In Chapter 4, the region between 45° and 135° for structures detected in the northern hemisphere and the region between 45° and 90° for those detected in the southern hemisphere were highlighted as preferential detection zones. However, the Juno observations, used in this thesis, do not confirm the existence of preferential detection zones. Our statistical analysis of the location of the auroral signatures projected in the equatorial plane is fully consistent with the in situ observations by Galileo of magnetospheric injections. Our results, derived from remote observation of UV auroral signatures of injections, thus confirm the Galileo result that injections occur at no preferential SIII longitude. In addition, our study demonstrates that this trend is also verified at radial distances less than 9 R_J that were not explored by Galileo.

8.4.2 Magnetospheric LT

In general, when considered according to the LT in the equatorial plane, the distribution of the projection of Type 1 structures (Figure 8.18) is homogeneous (χ^2 test, p-value = 0.67) where, on average, there are 31.6 struc-

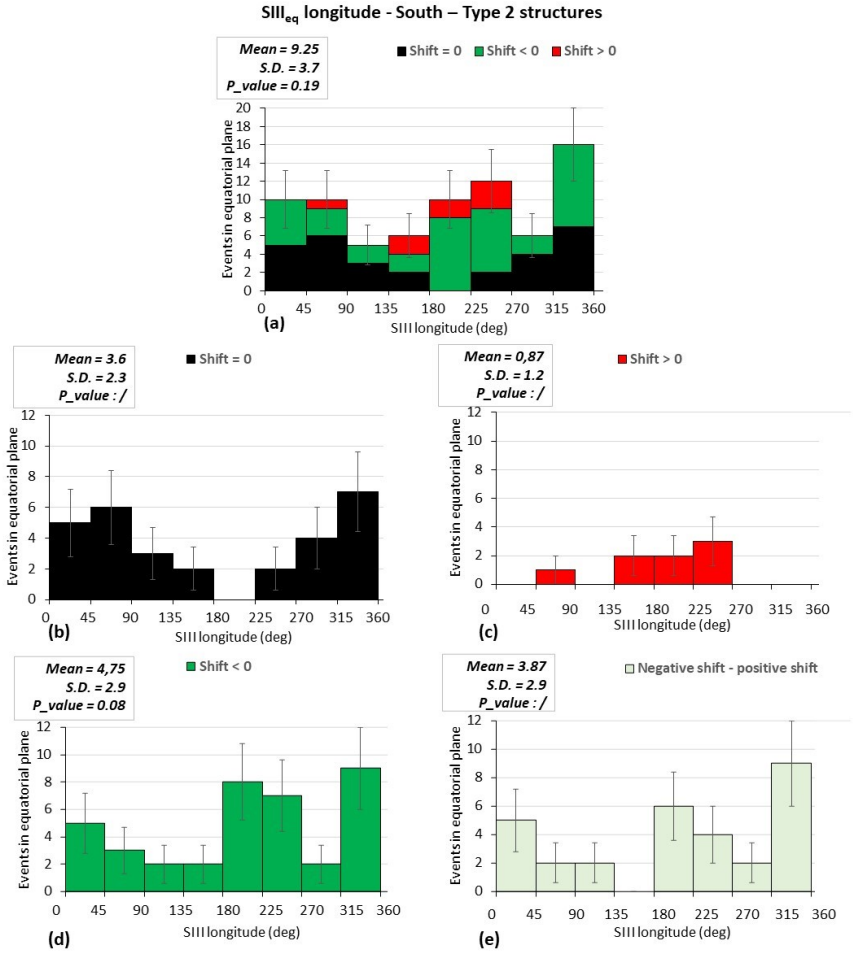

Figure 8.17 – The positions of Type 2 structures observed in the southern hemisphere are magnetically projected in the equatorial plane using the JRM09 magnetic field model. The distributions of these events in the equatorial plane as a function of equatorial longitude SIII are shown in the histograms with three different shifts combined (a), no-shift (b), positive shift (c) negative shift (d) and finally the difference between the number of structures with a negative shift and the number of structures with a positive shift (e). The uncertainty bars are derived from the shoot noise of the detection number. The mean and the standard deviation (S.D.) of each distribution are given for each histogram. If the number of structures is sufficient, a χ^2 test is performed and the p-value is given, otherwise the p-value = /.

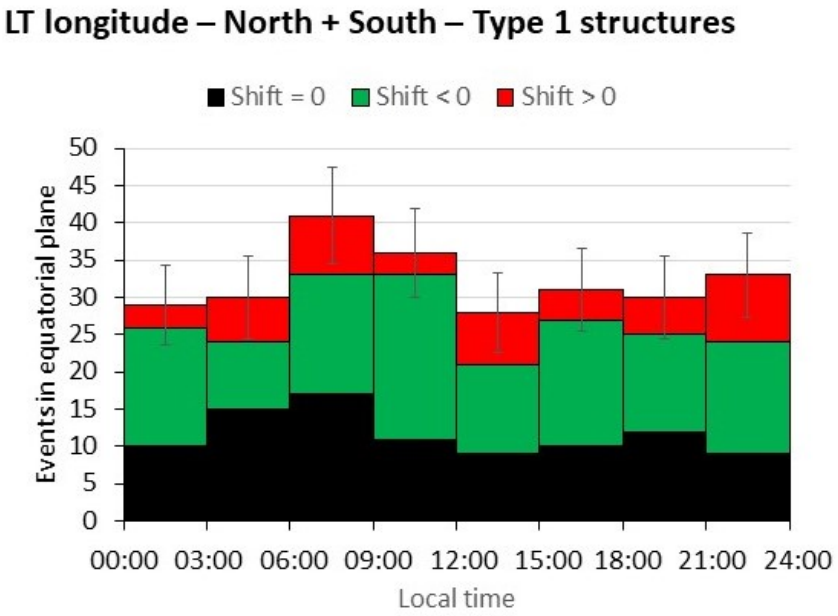

Figure 8.18 – The distributions of he positions of Type 1 structures observed in the northern and southern hemispheres, magnetically mapped in the equatorial plane using the JRM09 magnetic field mode, as a function of equatorial LT are shown in the histograms with three different shifts combined : no-shift (black), negative shift (green) and positive shift (red). The uncertainty bars are derived from the shoot noise of the detection number.

tures detected per 3-hour wide sector. For all the sub-populations, i.e. the structures with a negative, nul or positive shift, each of the distributions is homogeneous (χ^2 test, p-value (negative) = 0.44, p-value (zero) = 0.64, p-value (positive) = 0.5).

Focusing only on the projection of Type 1 structures detected in the northern hemisphere, the combined distribution (Figure 8.19 panel (a)) is homogeneous (χ^2 test, p-value = 0.14).The distribution of no-shift structures is

homogeneous (χ^2 test, p-value = 0.87) with an average of 6.75 structures detected per sector and a standard deviation of 1.8. Maximum detection occurred between 09:00 and 12:00 LT. The distribution of structures with a negative shift is homogeneous (χ^2 test, p-value = 0.76) with an average of 6.87 structures detected per sector and a standard deviation of 2. The same applies to structures with a positive shift, their distribution appears almost homogeneous, although the χ^2 test is not applicable due to the small number of structures. Finally, for the distribution of the difference between the number of structures with a negative shift and the number of structures with a positive shift, there are too few structures per sector to be able to rely on the p-value of a χ^2 test. This distribution appears inhomogeneous, but it can be seen that structures are detected in every LT sector[2] visited.

For the projection of Type 1 structures detected in the southern hemisphere (Figure 8.20), we observed a combined homogeneous distribution (χ^2 test, p-value = 0.69). The same is true for structures with a negative shift (χ^2 test, p-value =0.19). The distribution of structures with a positive shift appears to be homogeneous, but the small number of structures means that we cannot use a χ^2 test. For structures with no-shift, the distribution is inhomogeneous (χ^2 test, p-value = 0.04) with a detection peak between 03:00 and 09:00 LT. The distribution of the difference between the number of structures with a negative shift and the number of structures with a positive shift was inhomogeneous (χ^2 test, p-value = 0.01) with a peak between 09:00 and 12:00 LT.

The global LT distribution for projection of Type 2 structures (Figure 8.21) is inhomogeneous (p-value < 0.01), with an average of 20.75 structures

[2]One LT sector corresponds to 3 hours. These LT sectors are the same range as those used for the Galileo (Mauk et al. 1999) and HST (Chapter 4) studies.

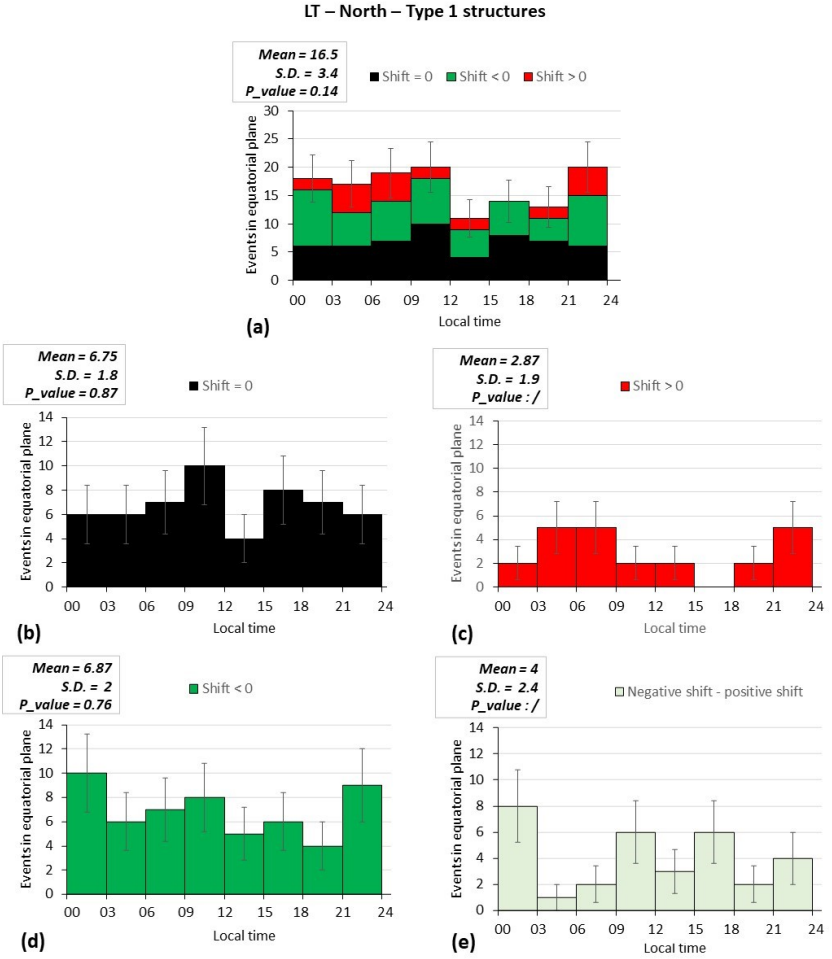

Figure 8.19 – The positions of Type 1 structures observed in the northern hemisphere are magnetically projected in the equatorial plane using the JRM09 magnetic field model. The distributions of these events in the equatorial plane as a function of equatorial LT are shown in the histograms with three different shifts combined (a), no-shift (b), positive shift (c) negative shift (d) and finally the difference between the number of structures with a negative shift and the number of structures with a positive shift (e). The uncertainty bars are derived from the shoot noise of the detection number. The mean and the standard deviation (S.D.) of each distribution are given for each histogram. If the number of structures is sufficient, a χ^2 test is performed and the p-value is given, otherwise the p-value = /.

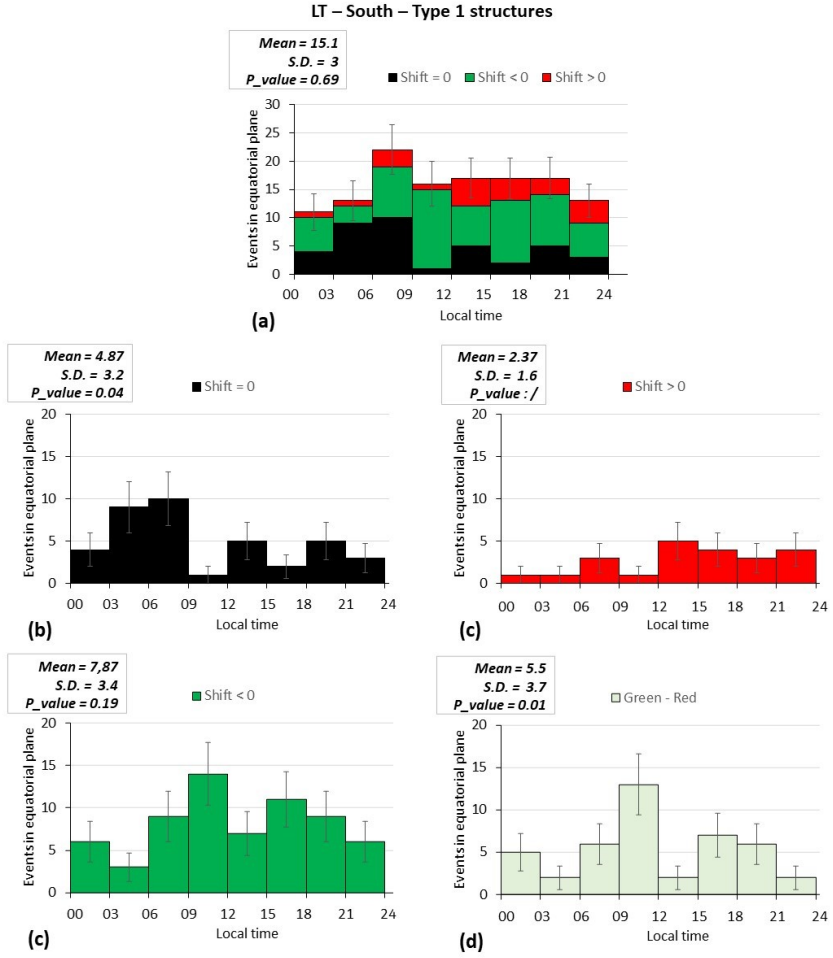

Figure 8.20 – The positions of Type 1 structures observed in the southern hemisphere are magnetically projected in the equatorial plane using the JRM09 magnetic field model. The distributions of these events in the equatorial plane as a function of equatorial LT are shown in the histograms with three different shifts combined (a), no-shift (b), positive shift (c) negative shift (d) and finally the difference between the number of structures with a negative shift and the number of structures with a positive shift (e). The uncertainty bars are derived from the shoot noise of the detection number. The mean and the standard deviation (S.D.) of each distribution are given for each histogram. If the number of structures is sufficient, a χ^2 test is performed and the p-value is given, otherwise the p-value = /.

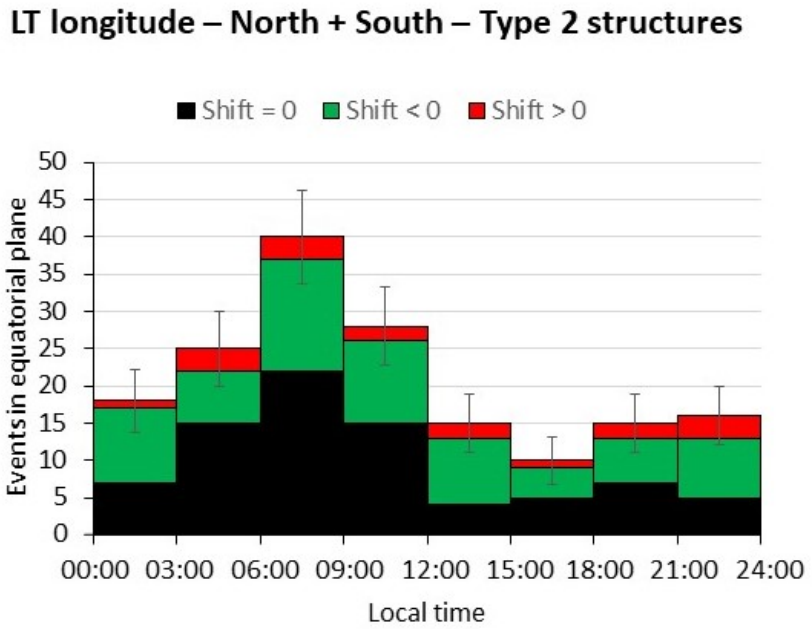

Figure 8.21 – The distributions of he positions of Type 2 structures observed in the northern and southern hemispheres, magnetically mapped in the equatorial plane using the JRM09 magnetic field mode, as a function of equatorial LT are shown in the histograms with three different shifts combined : no-shift (black), negative shift (green) and positive shift (red). The uncertainty bars are derived from the shoot noise of the detection number.

detected per sector and a standard deviation of 9.6. The structures with a negative shift have a homogeneous distribution (χ^2 test, p-value = 0.25), while those with a positive shift are too few in number to perform a χ^2 test, but their distribution nevertheless appears homogeneous. This result implies that the overall inhomogeneity is due to the inhomogeneity of the structures with a no-shift.

The projection of Type 2 structures detected in the northern and southern

hemispheres have the same characteristics as the combined northern and southern global distribution. The distribution is inhomogeneous (χ^2 test, p-value = 0.01). This inhomogeneity is due to the inhomogeneity of the distribution of structures with a no-shift. This distribution shows a detection peak between 03:00 and 12:00 LT, and this observation is valid for the structures detected to the north and to the south. The other distributions appear homogeneous (Figures 8.22 and 8.23). It should simply be noted that the number of structures with a positive shift, both to the north and to the south, is so small that a χ^2 test can only be performed even though the distribution is considered to be relatively homogeneous.

The behaviour in LT in the equatorial plane of Type 1 and Type 2 structures is not entirely identical.The young Type 2 structures have an inhomogeneous distribution, with the preferred detection in dawn side, between 03:00 and 12:00 LT. This preferred zone can be associated with the dawn storm region. As shown by Bonfond et al. (2021), dawn storms can be at the origin of the birth of auroral signatures of plasma injections. However, these signatures of fresh injections are present at all LT. This opens up two possibilities. The first is that the signatures of fresh injections are not exclusively associated with dawn storms, which is consistent with the observations of Bonfond et al. in 2017, who saw an auroral signature of plasma injection appear in the Juno spacecraft observations when no dawn storm had previously occurred. We can therefore assume that the plasma interchange phenomenon could be associated with the plasma injections signatures, as proposed by Mauk et al. in 2002. The second possible explanation is that dawn storms generate more sustainable disturbances that do not only occur at the location where the dawn storm appears.The dawn storm could be a source of disturbances at different LT throughout its existence, but of lesser intensity than when it occurs in the dawn sector. These disturbances

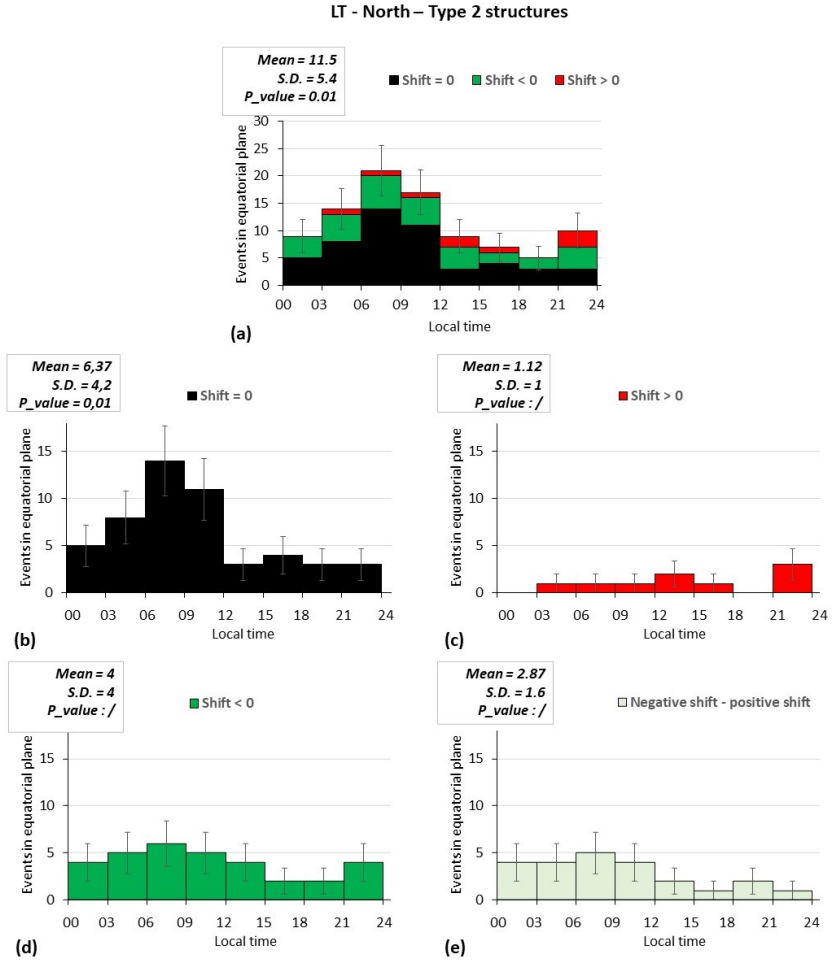

Figure 8.22 – The positions of Type 2 structures observed in the northern hemisphere are magnetically projected in the equatorial plane using the JRM09 magnetic field model. The distributions of these events in the equatorial plane as a function of equatorial LT are shown in the histograms with three different shifts combined (a), no-shift (b), positive shift (c) negative shift (d) and finally the difference between the number of structures with a negative shift and the number of structures with a positive shift (e). The uncertainty bars are derived from the shoot noise of the detection number. The mean and the standard deviation (S.D.) of each distribution are given for each histogram. If the number of structures is sufficient, a χ^2 test is performed and the p-value is given, otherwise the p-value = /.

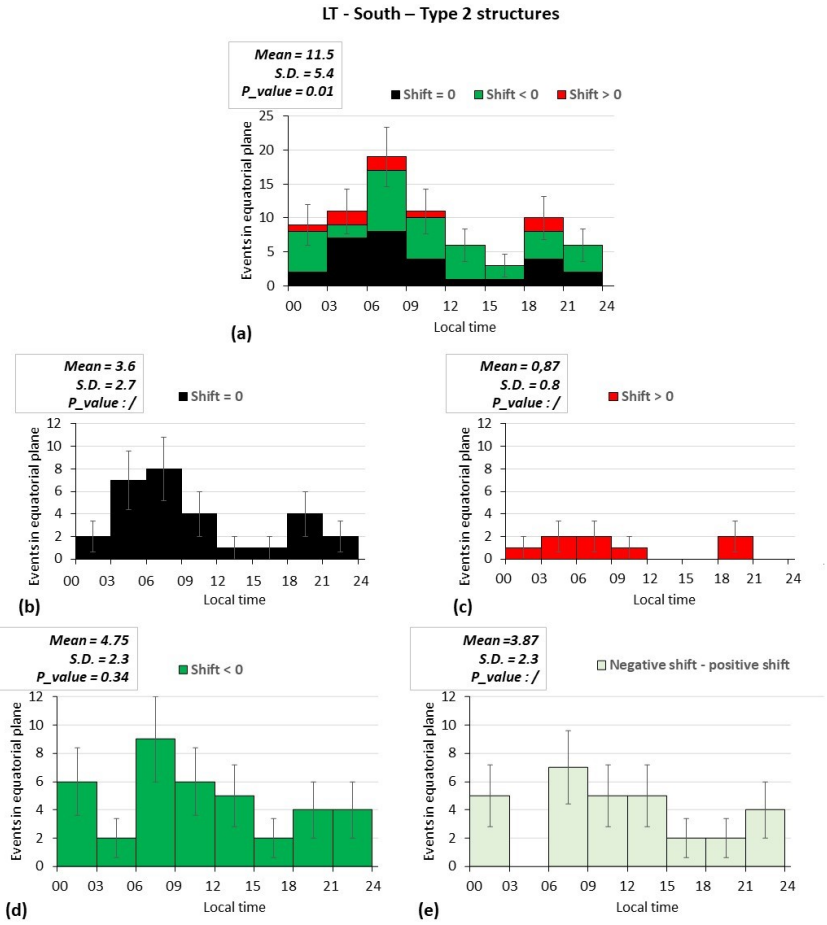

Figure 8.23 – The positions of Type 2 structures observed in the southern hemisphere are magnetically projected in the equatorial plane using the JRM09 magnetic field model. The distributions of these events in the equatorial plane as a function of equatorial LT are shown in the histograms with three different shifts combined (a), no-shift (b), positive shift (c) negative shift (d) and finally the difference between the number of structures with a negative shift and the number of structures with a positive shift (e). The uncertainty bars are derived from the shoot noise of the detection number. The mean and the standard deviation (S.D.) of each distribution are given for each histogram. If the number of structures is sufficient, a χ^2 test is performed and the p-value is given, otherwise the p-value = /.

could therefore continue to generate plasma injections throughout the evolution of the dawn storm. It should be noted that it is not impossible for these two proposed phenomena to coexist but above all that in the second scenario, interchange is also involved, but in a more subtle way, as a permanent phenomenon of plasma transport in the magnetosphere. Type 1 fresh structures have a much more homogeneous distribution than those of Type 2. They therefore appear to be less dependent on LT, suggesting that Type 1 structures may be more associated with a local-time-homogeneous plasma interchange process than with dawn storms.

For both Type 1 and Type 2 structures, the distribution in the equatorial plane of structures associated with more mature injections is uniform, which is consistent with a quasi-corotating motion of the old injections over time. Given the life time of the auroral structures, which may be greater than one rotation of Jupiter (Chapter 4), it is expected to observe these signatures at all LT.

The results obtained from the HST data in Chapter 4 showed a relatively uniform distribution of structures in the southern hemisphere and a preferential zone for structures detected in the north between 12 LT and 18 LT. This preferential zone has not been confirmed in the present analysis based on Juno-UVS observations. We have already mentioned in Chapter 4 the risk that this preferential zone might be related to the observational bias associated with the presence of the northern magnetic anomaly, which facilitated the discrimination of auroral features that were detached from the rest of the emission. We can therefore confirm that the preferential zone highlighted by the HST observations was indeed linked to observational bias.

8.4.3 Radial distance magnetically projected in the equatorial plane

To analyse the different distributions of auroral structures as a function of the radial distance in the equatorial plane, the data obtained were resampled over 1 R_J, so that the distributions that are described below are given in units of number of structures per R_J. This step was essential because the distance grid is not uniform (Section 8.2). The distribution of Type 1 structures per R_J (Figure 8.24) is inhomogeneous (χ^2 test: $p < 0.01$). If we look at the distributions with a nul, positive or negative shift, each of these distributions is inhomogeneous (χ^2 tests: all $p< 0.01$). The structures magnetically mapped in the equatorial plane are detected at all radial distances (from 5 to 30 R_J), with a larger frequency between 7 and 16 R_J.

In the northern and southern hemispheres, the distribution over the radial distance of Type 1 structures with a no-shift (Figures 8.25 and 8.26 panel (b)) are detected from 7 R_J and up to 30 R_J. The majority of the distribution is detected between 7 R_J and 16 R_J (81% of the distribution in the north and 86% of the distribution in the south). Type 1 structures with a negative shift show a detection peak in the distribution of structures at 9 R_J. This statement is correct for structures detected in both hemispheres. The majority of structures detected are located between 8 and 16 R_J (85% of the distribution in the north and 91% of the distribution in the south). This information is confirmed by the radial distribution of the difference between the number of structures with a negative shift and the number of structures with a positive shift. In the northern hemisphere, the radial distribution of the structures with a positive shift is close to that of those with a negative shift, but there are far fewer of them, as already mentioned.

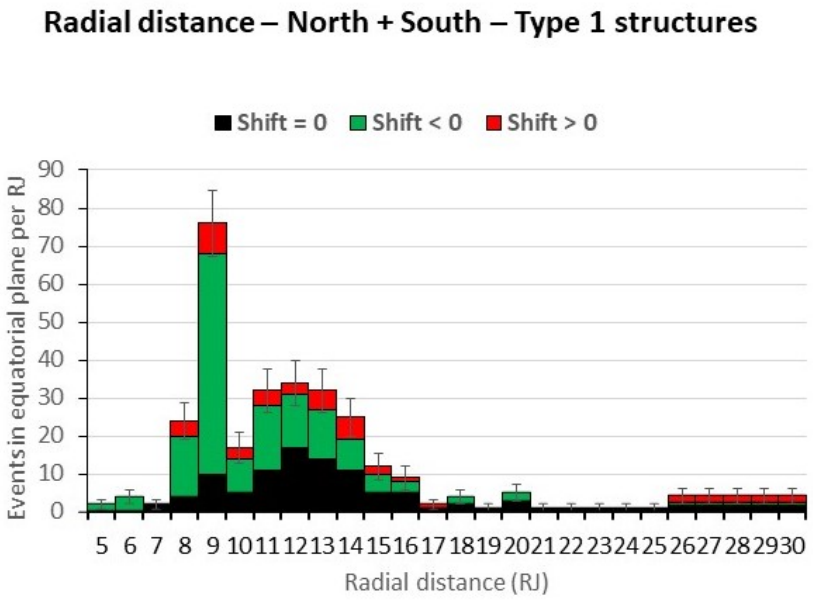

Figure 8.24 – The distributions of the position of Type 1 structures observed in the northern and southern hemispheres, magnetically mapped in the equatorial plane using the JRM09 magnetic field mode, as a function of radial distance are shown in the histograms with three different shifts combined : no-shift (black), negative shift (green) and positive shift (red). The uncertainty bars are derived from the shoot noise of the detection number.

The radial distribution for Type 2 structures is obtained in the same way as for Type 1 structures. The global distribution (Figure 8.27) is inhomogeneous (χ^2 tests: all p-value < 0.01). Looking at the distributions with a nul, positive or negative shift, each of these distributions is inhomogeneous (χ^2 tests: all p-value < 0.01). It can be seen that structures are detected from 6 to 30 R_J.

The young structures detected in the northern hemisphere (Figure 8.28) are

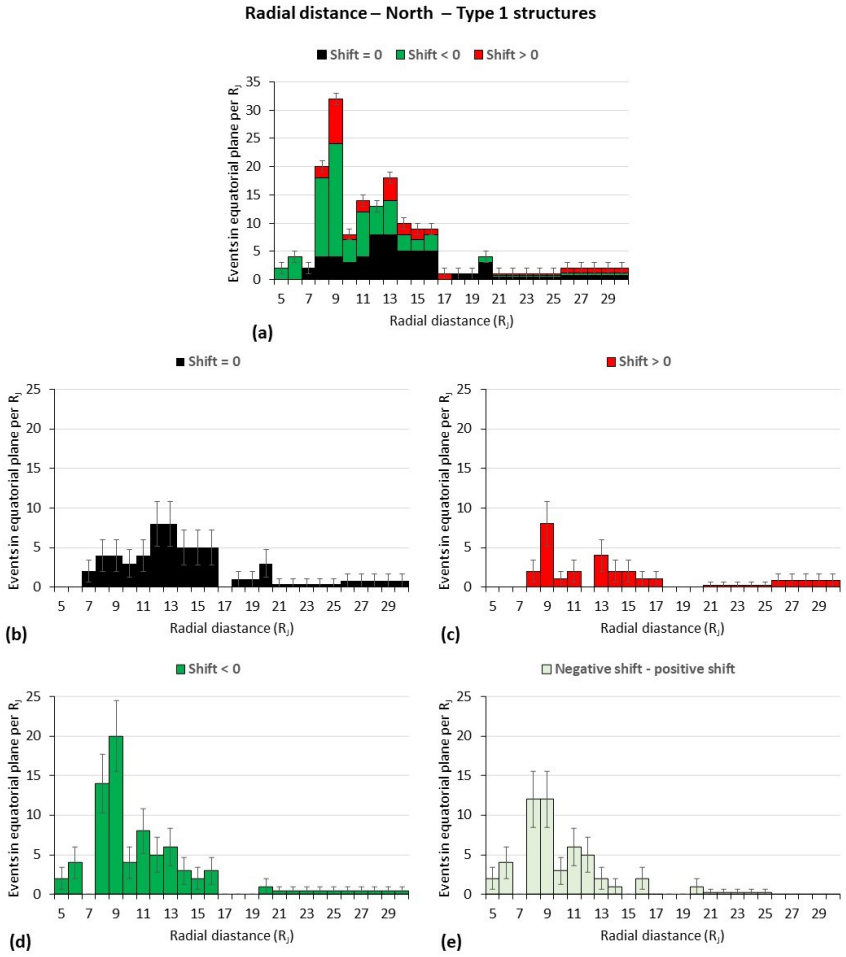

Figure 8.25 – The positions of Type 1 structures observed in the northern hemisphere are magnetically projected in the equatorial plane using the JRM09 magnetic field model. The distributions of these events in the equatorial plane as a function of radial distance are shown in the histograms with three different shifts combined (a), no-shift (b), positive shift (c) negative shift (d) and finally the difference between the number of structures with a negative shift and the number of structures with a positive shift (e). The uncertainty bars are derived from the shoot noise of the detection number. The mean and the standard deviation (S.D.) of each distribution are given for each histogram. If the number of structures is sufficient, a χ^2 test is performed and the p-value is given, otherwise the p-value = /.

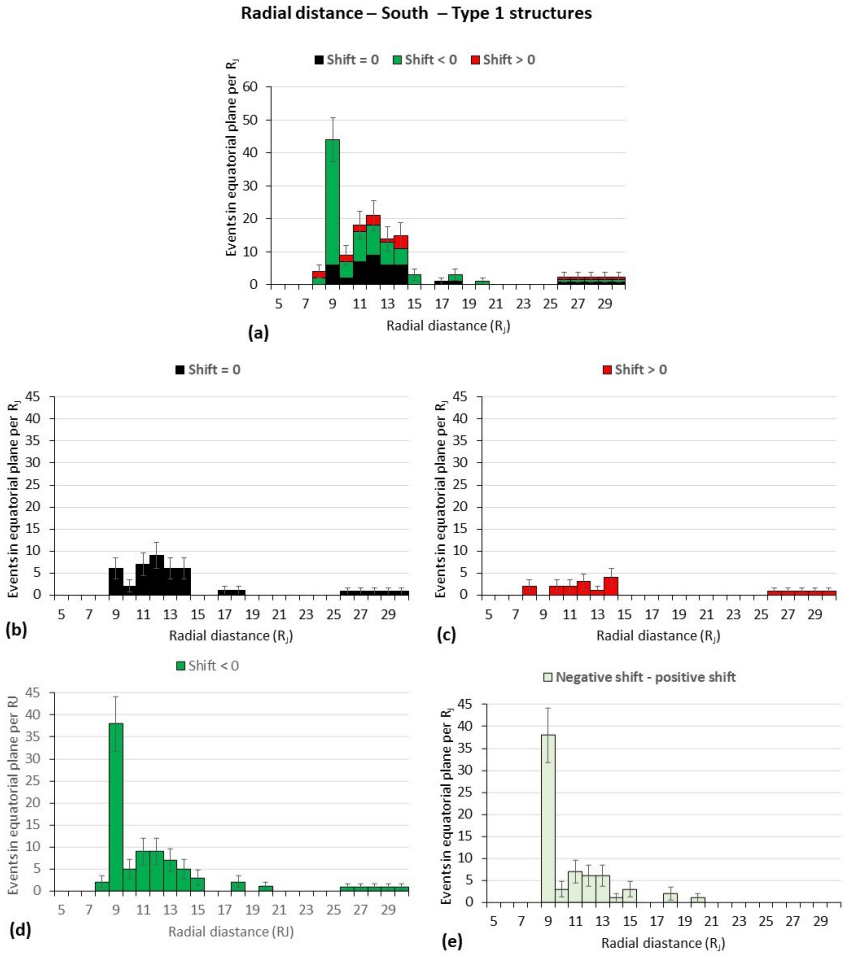

Figure 8.26 – The positions of Type 1 structures observed in the southern hemisphere are magnetically projected in the equatorial plane using the JRM09 magnetic field model. The distributions of these events in the equatorial plane as a function of radial distance are shown in the histograms with three different shifts combined (a), no-shift (b), positive shift (c) negative shift (d) and finally the difference between the number of structures with a negative shift and the number of structures with a positive shift (e). The uncertainty bars are derived from the shoot noise of the detection number. The mean and the standard deviation (S.D.) of each distribution are given for each histogram. If the number of structures is sufficient, a χ^2 test is performed and the p-value is given, otherwise the p-value = /.

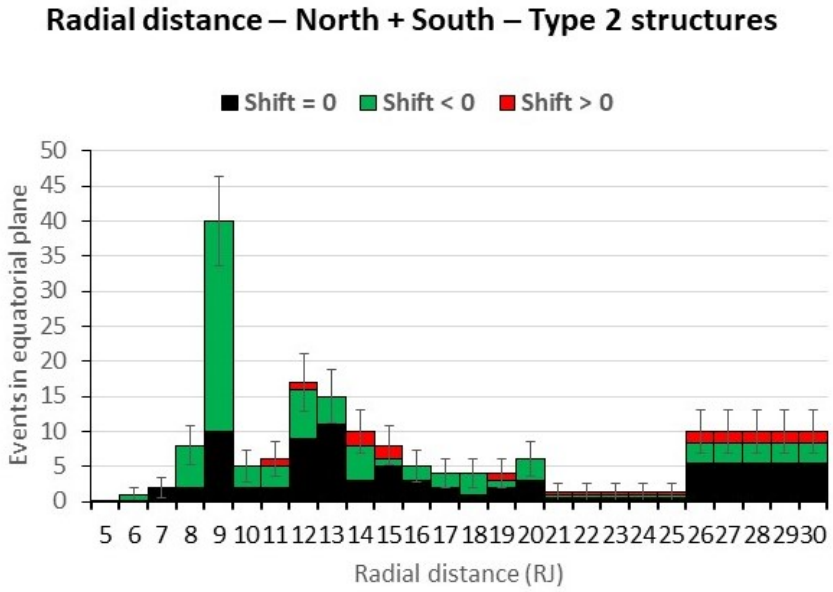

Figure 8.27 – The distributions of the positions of Type 2 structures observed in the northern and southern hemispheres, magnetically mapped in the equatorial plane using the JRM09 magnetic field mode, as a function of radial distance are shown in the histograms with three different shifts combined : no-shift (black), negative shift (green) and positive shift (red). The uncertainty bars are derived from the shoot noise of the detection number.

present between 7 and 30 R_J, with no detection by R_J at 11 R_J and a detection peak between 12 and 13 R_J. More mature structures are detected between 6 and 30 R_J, with no detection at 7, 14 and 15 R_J and a peak detection at 9 R_J. This peak at 9 R_J is confirmed by the difference between structures with a negative shift and those with a positive shift.

In the southern hemisphere (Figure 8.29) , the young structures are detected between 11 and 15 R_J, at 20 R_J and between 26 and 30 R_J. These struc-

tures have a peak of 13 R_J. Negative shift structures are present between 9 and 30 R_J, with no detection at 10 R_J, 19 R_J and between 21 and 25 R_J. A detection of peak is observed at 9 R_J, and this peak is confirmed by the distribution of the number of the number of structures with a negative shift minus those with a positive shift.

For Type 1 structures, our observations are identical for structures detected in both hemispheres. The fresh structures are present between 7 R_J and up to 30 R_J, which is consistent with a process triggered by a dawn storm, which can extend from the main emission to equatorward emissions (Bonfond et al. 2021). It is also consistent with auroral signatures of plasma injections whose birth is spontaneous, this type of birth being associated with the interchange phenomenon (Bonfond et al. 2017). These data also suggest that the auroral process is not incompatible with the Alfvén wave-dependent auroral process. Indeed, the region of wave-particle interaction associated with Alfvén waves in Jupiter's magnetosphere is located on magnetic field lines with equatorial distances of less than 40 R_J (Saur et al. 2018, Gershman et al. 2019). The majority of the radial distribution for the young structures is detected between 7 R_J and 16 R_J, this observation is the translation of the radial displacement in the equatorial plane of the injection signatures. This radial displacement continues with time, which explains why structures with a negative shift show a detection peak in the radial distribution of structures at smaller radial distance, i.e. 8 and 9 R_J.

The detection of Type 2 structures highlights structures between 6 and 30 R_J, corresponding to the radial region where Alfvén waves are most likely to interact with magnetospheric particles. The young structures have a peak in the north between 12 and 13 R_J and at 13 R_J in the south and are detected up to 30 R_J. The analysis and conclusions are therefore the same as for type

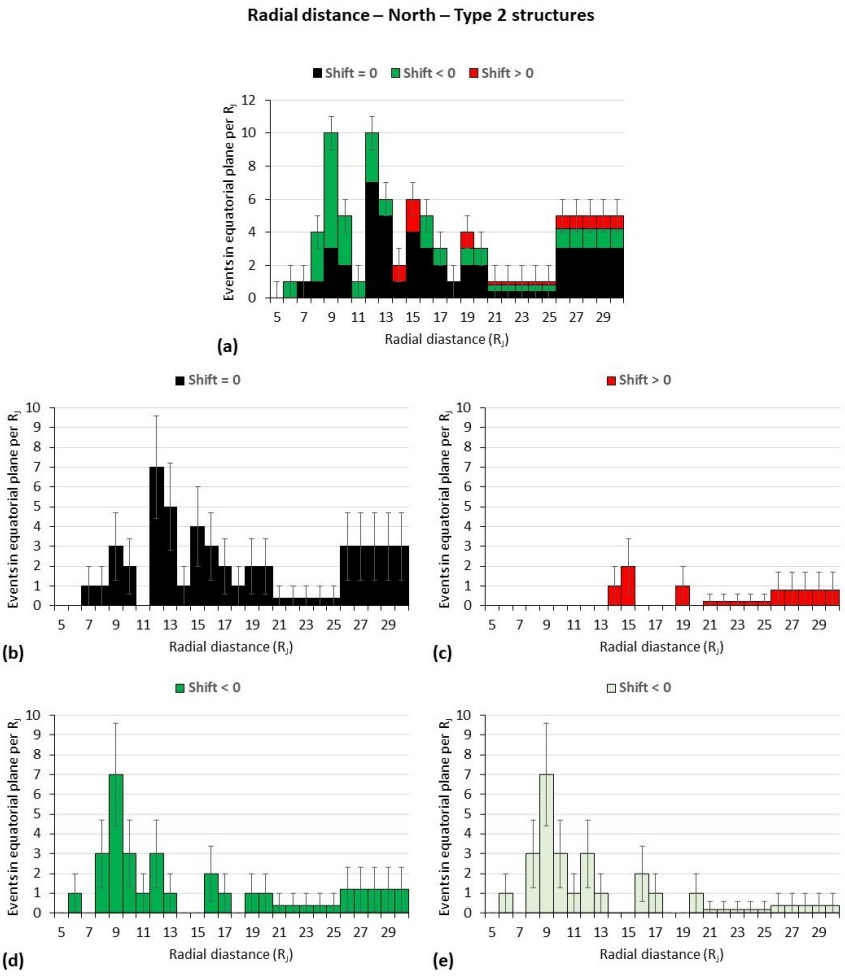

Figure 8.28 – The positions of Type 2 structures observed in the northern hemisphere are magnetically projected in the equatorial plane using the JRM09 magnetic field model. The distributions of these events in the equatorial plane as a function of radial distance are shown in the histograms with three different shifts combined (a), no-shift (b), positive shift (c) negative shift (d) and finally the difference between the number of structures with a negative shift and the number of structures with a positive shift (e). The uncertainty bars are derived from the shoot noise of the detection number. The mean and the standard deviation (S.D.) of each distribution are given for each histogram. If the number of structures is sufficient, a χ^2 test is performed and the p-value is given, otherwise the p-value = /.

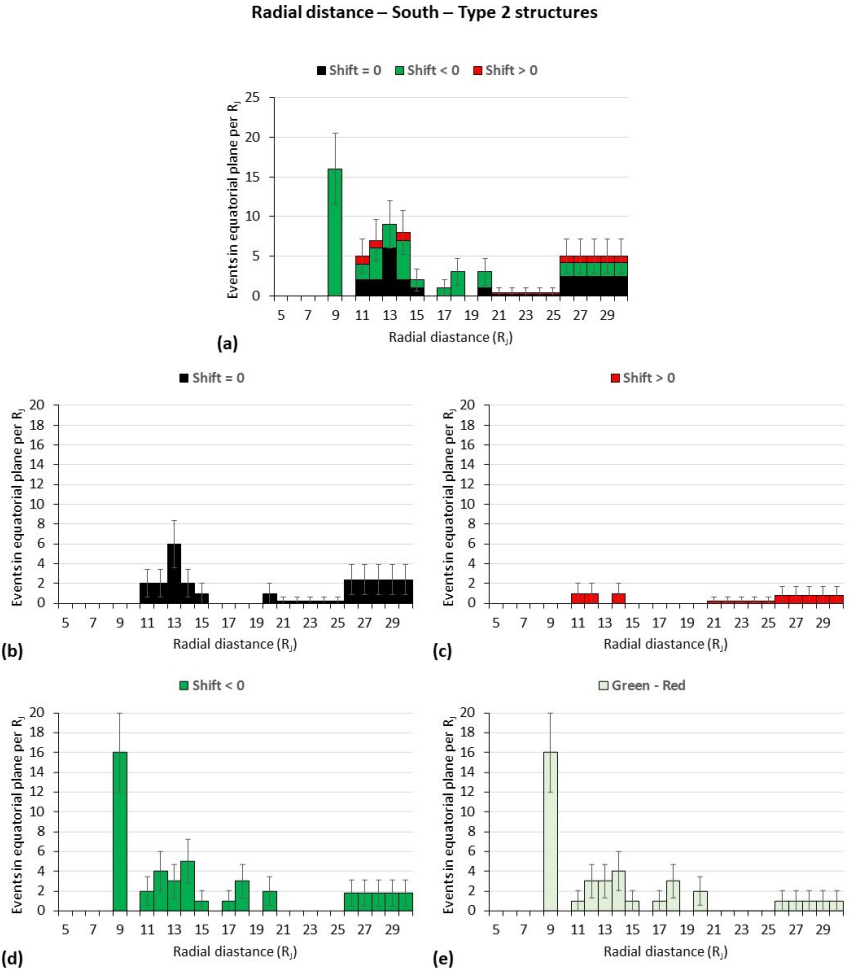

Figure 8.29 – The positions of Type 2 structures observed in the southern hemisphere are magnetically projected in the equatorial plane using the JRM09 magnetic field model. The distributions of these events in the equatorial plane as a function of radial distance are shown in the histograms with three different shifts combined (a), no-shift (b), positive shift (c) negative shift (d) and finally the difference between the number of structures with a negative shift and the number of structures with a positive shift (e). The uncertainty bars are derived from the shoot noise of the detection number. The mean and the standard deviation (S.D.) of each distribution are given for each histogram. If the number of structures is sufficient, a χ^2 test is performed and the p-value is given, otherwise the p-value = /.

1 structures, given their similar radial distribution. The origin of these auroral signatures can be linked to dawn storms and to the phenomenon of interchange. For the most mature structures, we observed maximum detection at 9 R_J in the north and in the south (corresponding to~ 22% and ~35% of the detected structures in each hemisphere, respectively). This peak has a shorter radial distance than the younger structures and could be related to the radial evolution of the structures over time as they approach Jupiter.

In all cases, regardless of the type of structure or hemisphere, a peak for mature structures was detected at 9 R_J. These peaks of the different radial distributions can not be assimilated to the Europa's footprint. The brightness of satellite footprints can be highly variable in time and space, with the brightness of Io's footprint showing variations between 2500 kR and 20,000 kR Bonfond et al. 2013b. We know that the brightness of Io's UV footprint is about 10 times larger than that of Ganymede, which is itself about 10 times larger than Europa (a few kR) (Bonfond et al. 2017). It seems obvious that if the peak at 9 R_J was assimilated to the presence of Europa's footprint, we should observe a peak at 15 R_J reflecting the same type of detection for Ganymede's footprint. However, it cannot be ruled out that Europa could play a role in revealing auroral signatures of plasma injections. However, this is only a hypothesis that should be explored in the future.

8.5 Summary and conclusions

In this chapter, we report a statistical study of auroral signatures associated with injection signatures in Jupiter's magnetosphere, based on auroral data collected by the Juno UVS during the first 18 PJ. Using the JRM09

magnetic field model, we magnetically map the auroral structures in the equatorial plane and study their characteristics. We relate the selected UV auroral features to plasma injections into the Jovian magnetosphere. We use the evidence of the shift between the brightness peak and the CR peak as reasonable proof that the studied signatures are indeed related to the plasma injection phenomenon in the equatorial plane of the magnetosphere. It is interesting to add that very recently, Nichols et al. (2023) compared Jovian auroral observations from HST and contemporary in situ data from Juno present in the equatorial plane in the middle magnetosphere. They have shown that the equatorward auroral structures are associated with plasma injections. This is the first direct evidence that the auroral morphology known as "strong injections" (see family defined by Grodent et al. (2018)) is in fact a manifestation of magnetospheric injections.

We show that the detection of Type 1 or Type 2 auroral structures is not favoured by the presence of the magnetic anomaly in the northern hemisphere. On the other hand, the distribution of fresh structures seems to be related to the magnetic field strength, their frequency of detection increases with the magnetic field, which leads us to suggest that the auroral mechanism associated with the auroral signatures of plasma injections is related to the magnetic field strength. More precisely, we suggest that the acceleration process due to Alfvén waves is at the origin of the detected auroral signatures, because the higher magnetic field strength, the more efficient the energy transfer by Alfvén waves and hence the more auroral emission. Furthermore, we show that these auroral features are common, since they appear in all the observations.

In the magnetosphere, our analysis shows that the coordinates of Type 1 and Type 2 auroral structures projected in the equatorial plane are observed

at all equatorial SIII longitudes. We compare these Juno UVS observations with in situ injection signatures obtained from Galileo energetic particle data and find that auroral detections projected in the equatorial plane and those detected in situ are consistent with previous studies. Looking at the LT positions of the studied structures, we find that the signatures of fresh injections are present at all LT. However, depending on the brightness detection threshold and the CR detection threshold, we found a different distribution of young structures. Type 2 structures show a predilection for the dawn side, which suggests an association of these young structures with dawn storms. This tendency is much less pronounced for Type 1 structures. This observation led us to propose two possible processes to explain the injection phenomenon: (1) the process is associated with the dawn storm phenomenon, and (2) it is associated with a local-time-homogeneous plasma interchange process. Looking at the LT distribution of the structures, the process associated with the dawn storm phenomenon seems to be more involved in the presence of the young Type 2 structures, whereas the young Type 1 structures are more associated with the interchange phenomenon. In addition, the Type 1 and Type 2 structures associated with the more mature auroral signatures of plasma injections are homogeneously distributed. This observation is consistent with a quasi-corotating motion of the old injections over time. The majority of young structures are detected before 17 R_J. More mature Type 1 and Type 2 structures are detected mainly at shorter radial distances, with a peak at 9 R_J. This last observation reflects the radial shift in the equatorial plane of the injection signatures with time. In general, the radial position of the structures is consistent with the distance at which the Alfvén waves are observed in the Jovian magnetosphere.

9 Conclusions and perspectives

9.1 Conclusions

In this thesis, we have studied auroral features of Jupiter, observed with HST and Juno, which are interpreted as signatures of plasma injections. This interpretation is supported by three assertions:

1. The auroral signatures have the same characteristics as the auroral signature of an injection observed by Mauk et al. (2002).

2. The spectral analysis of these auroral signatures, show a differential drift of electrons as a function of their energy, in agreement with the distribution of energetic electrons within a magnetospheric injection detected in the equatorial plane with an in situ probe (Mauk et al. 1997).

3. When we project the position of these auroral features in the equatorial plane along magnetic field lines, their location is in agreement with the distribution of injection detections made by the Galileo probe orbiting Jupiter.

The auroral signatures of plasma injections are continuously observed during single HST observing sequences (~45 min). When several consecutive

sequences were available, amounting to several hours of observations, these auroral structures were present from the beginning to the end. This strongly suggests that their lifetime is greater than 45 minutes. The lifetimes have also been estimated from simulations, assuming that they correspond to the lifetimes of the injected population of electrons that are precipitating in the atmosphere and generating an auroral signature. Simulations of the auroral signatures of plasma injections suggest that the auroral characteristics are compatible with the process of pitch angle scattering. These simulations suggest that their lifetimes are between 0.5 and 1 rotation of Jupiter (i.e. from 5 to 10 hours). However, this lifetime is most probably underestimated, since Haggerty et al. (2019) have shown, using Juno in situ data, that the plasma injections can begin several hours before the auroral signatures are observed. In other words, they have shown that the presence of in situ injections does not necessarily translate into auroral injection signatures. We also estimated the incoming magnetic flux associated with the injections of plasma related to these auroral signatures, it corresponds to 30% of the outgoing flux. We suggested in 2014 that this low ratio was perhaps the result of (i) overly restrictive selection criteria for auroral features or (ii) underestimation of their lifetime or (iii) a detection threshold issue. So Haggerty et al. (2019) confirm hypotheses (ii) and (iii).

The results obtained, in Chapter 4, show that auroral signatures of plasma injections are common since they appear in more than half of the HST data sample used. Most observations showed only one unmistakable such auroral feature per day. Occasionally multiple auroral structures were observed in the same HST image, indicating multiple magnetospheric event generation regions, rather than a single localised source region. Subsequently, thanks to the observations made by Juno, it was confirmed that this was a common phenomenon, detected in every PJ, and that their detection did not

increase in the region of the magnetic anomaly in the northern hemisphere. On the other hand, the detection of auroral signatures of fresh plasma injections seems to be related to the magnetic field strength, as they suggest that their auroral mechanism should be more effective when the magnetic field strength is strong. More precisely, the acceleration process due to Alfvén waves could play a role in generating the auroral signatures detected. This suggestion is supported by the detection of Alfvén waves at high-latitude, mapping the inner magnetosphere, associated with auroral emission highlighted by Gershman et al. (2019). In addition, we have estimated the temporal variations of the emitted power of the auroral signatures of the plasma injections (~8 min), which have the same typical time scale as those of the injections observed in the radio domain (18 min) (Louarn et al. 2001). This time scale also appears to be consistent with the period of oscillation expected from the travel time of Alfvén waves between the ionosphere (close the main emission) and the upper edge of the equatorial plasma sheet Nichols2017 .

The latitudinal and azimuthal movements of the auroral signatures of the plasma injections were analysed from the HST data. We have shown that magnetospheric injections move towards the planet and lag behind corotation. The simulations described in Chapter 5 provide a better understanding of the size, spectral index and evolution of the population of electrons injected into the Jovian magnetosphere. They show that during a typical HST sequence, the spatial extension of the injection signature due to scattering is limited. They also suggest that the old injections are quasi-corotating and that they show a very small displacement equatorward. In addition, there are some equatorward bright patchy auroral features, which present wider azimuthal and radial displacements than observed at the beginning of Chapter 4 for the old injections. These structures are also known in au-

roral morphology as "strong injections" (see the auroral family defined by Grodent et al. (2018)). If the radial velocity is indicative of the evolution of the plasma injection, then these structures should be linked to young magnetospheric injections. Very recently, Nichols et al. (2023) compared HST Jovian auroral observations with contemporaneous in situ data from Juno in the equatorial plane of the middle magnetosphere. They have established the first direct evidence that “strong injections” are in fact a manifestation of magnetospheric injections, confirming our 2014 analysis.

Finally the locations of the injection structures in the equatorial plane were obtained using the VIPAL and JRM09 magnetic field models for the HST and Juno data, respectively. We magnetically mapped the auroral structures in the equatorial plane and studied their characteristics. Irrespective of the database used, auroral signatures projected in the equatorial plane are observed at all SIII longitudes, independently of their age. Looking at the LT positions of the structures that have been considered, we find that signatures of fresh injections are present at all LTs. However, these results must be nuanced. Depending on the brigthness detection threshold and the CR detection threshold imposed to the Juno data that we used, we found a different distribution of young structures. This difference implies distinct characteristics for Type 1 and Type 2 structures:

- Type 2 structures (thresholds: luminosity > 250 kR and CR > 3) show a predilection for the dawn side, which is consistent with the scenario where dawn storms trigger these young injections,
- This tendency is much less pronounced for Type 1 structures (thresholds: brightness > 50 kR and CR > 5), and their distribution seems more homogeneous across all the LTs, suggesting an origin linked to a local-time-homogenous process. This suggests that they are more

closely associated with the plasma interchange process.

This observation has led us to propose two possible processes to explain the injection phenomenon: the first associated with the dawn storm phenomenon, in agreement with Bonfond et al. (2021) and Yao et al. (2020), and the second associated with a local-time-homogeneous plasma interchange process. In other words, looking at the LT distribution of the structures, the process associated with the dawn storm phenomenon seems to be more involved in the presence of young Type 2 structures, whereas young Type 1 structures are more associated with the interchange phenomenon. In addition, the Type 1 and Type 2 structures associated with the more mature auroral signatures of plasma injections are homogeneously distributed. This observation is consistent with a quasi-corotating motion of the old injections over time. The existence of both processes is also consistent with the idea of multiple regions of magnetospheric event generation, as discussed above. From the analysis of the HST data, we concluded that the signatures are preferentially present at distances between 7 R_J and 40 R_J. The data acquired from Juno have enabled us to refine our perception of the distribution of structures as a function of their age: Type 1 and 2 structures are detected up to 30 R_J, which corresponds to our radial detection threshold in the Juno data. The majority of young structures are detected before 17 R_J. The more mature Type 1 and 2 structures are mainly detected at shorter radial distances, with a peak at 9 R_J. This last observation reflects the radial shift in the equatorial plane of the injection signatures over time. In general, the radial position of the structures is consistent with the distance at which Alfvén waves are observed in the Jovian magnetosphere, which seems to support the hypothesis of the involvement of these waves in the auroral process associated with auroral signatures of plasma injection.

9.2 Perspectives

The above-mentioned results of this thesis have led to a better understanding of the magnetospheric and ionospheric processes that may be involved in plasma injections and their auroral signatures. This raises new questions that can be addressed in the future in order to complement the results obtained in this thesis and to validate the proposed hypotheses.

To date, we have not been able to observe the birth, evolution and disappearance of one auroral signature of plasma injection during a single observing sequence. This complete observation would give us access to the full dynamics of these auroral structures, by analysing their evolution in size, brightness, CR, displacement and real lifetime. In addition, this study could have two distinct strands, one based on injections originating in a dawn storm and the other with a spontaneous birth, in order to compare whether the two distinct types of birth have an impact on the auroral and energetic characteristics of the injections, as hypothesised in this thesis.

Using our method of image reconstruction with observations acquired by Juno, we have been confronted with detections of auroral signatures of plasma injections composed of two (or more) observations that are spatially close but not acquired simultaneously. It would be interesting to repeat the last study of this thesis, but with knowledge of the regions of interest to be targeted, i.e. with knowledge of the location of the auroral signatures of the plasma injections. The aim of this new study will no longer be to reconstruct the entire aurora in order to obtain a global view of the injection phenomenon. The aim will be to follow the injection signatures detected in their entirety, with a small temporal gap between the swaths captured by the UVS that make up the auroral signature. This approach to auroral

emissions will enable us to carry out case studies, focusing in particular on the movement of the structures, their size and the distribution of their CR over time. This will complement the global analysis carried out in Chapter 8.

In Chapter 8 it was suggested that the presence of Europa could be a trigger for auroral signatures of plasma injections. Using HST and/or Juno, or in the near future JUICE, this hypothesis could be tested by establishing a link between Europa's position and the occurrence of auroral signatures along Europa's footpath and its neighbourhood.

This list is indicative and based solely on the elements discovered during this thesis. No further analysis has yet been carried out, and many questions remain unanswered. We can only hope that further exploitation of the available data on plasma injections will provide additional information to support the conclusions of this thesis.

List of acronyms and abbreviations

ACS	Advanced Camera for Surveys
AU	Astronomical Unit
CCD	charge coupled device
CML	Central Meridian Longitude
CR	color ratio
EPD	Energetic Particles Detector
EUV	extreme ultraviolet
F115LP	Long Pass MgF_2
F125LP	Long Pass CaF_2
FAC	Field-aligned currents
FUV	far ultraviolet
GAM	Grodent anomaly model
HST	Hubble Space Telescope
ICP	Initial Center Position
IMF	interplanetary magnetic field
IR	infrared
JADE	Jovian Auroral Distribution Experiment
JEDI	Jovian Energetic Particle Detector Instrument

JIRAM	Jupiter InfraRed Auroral Mapping
JRM09	Juno Reference Model through Perijove 9
LPAP	Laboratory for Planetary and Atmospheric Physics
LT	Local Time
MAMA	Multi Anode Microchannel Array
NIR	near infrared
NUV	near ultraviolet
PJ	perijove
R_J	Jovian radius
R_S	Saturnian radius
SBC	solar blind channels
SIII	System III
SrF2	Strontium Fluoride
STIS	Space Telescope Imaging Spectrograph
SWP	solar wind pressure
UT	Universal Time
UV	ultraviolet
UVS	Ultraviolet Spectrograph
VIPAL	Voyager Io Pioneer Anomaly Longitude

Bibliography

Akasofu, S.-I., 1964, The development of the auroral substorm, Planetary and Space Science, 12, 273 – 282, doi:https://doi.org/10.1016/0032-0633(64)90151-5

Allegrini, F., Bagenal, F., Bolton, S., Connerney, J., Clark, G., Ebert, R. W., Kim, T. K., Kurth, W. S., Levin, S., Louarn, P., Mauk, B., McComas, D. J., Pollock, C., Ranquist, D., Reno, M., Szalay, J. R., Thomsen, M. F., Valek, P., Weidner, S., Wilson, R. J., Zink, J. L., 2017, Electron beams and loss cones in the auroral regions of Jupiter, Geophys. Res. Lett., 44, 7131–7139, doi:10.1002/2017GL073180

Atreya, S., Mahaffy, P., Niemann, H., Wong, M., Owen, T., 2003, Composition and origin of the atmosphere of jupiter—an update, and implications for the extrasolar giant planets, Planetary and Space Science, 51, 105 – 112, doi:https://doi.org/10.1016/S0032-0633(02)00144-7

Azari, A. R., Liemohn, M. W., Jia, X., Thomsen, M. F., Mitchell, D. G., Sergis, N., Rymer, A. M., Hospodarsky, G. B., Paranicas, C., Vandegriff, J., 2018, Interchange injections at saturn: Statistical survey of energetic h+ sudden flux intensifications, Journal of Geophysical Research: Space Physics, 123, 4692–4711, doi:https://doi.org/10.1029/2018JA025391

Bagenal, F., Delamere, P. A., 2011, Flow of mass and energy in the magnetospheres of jupiter and saturn, Journal of Geophysical Research, 116, A05 209, doi:10.1029/2010ja016294

Bagenal, F., Shemansky, D. E., McNutt Jr., R. L., Schreier, R., Eviatar, A., 1992, The abundance of o++ in the jovian magnetosphere, Geophysical Research Letters, 19, 79–82, doi:https://doi.org/10.1029/92GL00070

Bagenal, F., Adriani, A., Allegrini, F., Bolton, S. J., Bonfond, B., Bunce, E. J., Connerney, J. E. P., Cowley, S. W. H., Ebert, R. W., Gladstone, G. R., Hansen, C. J., Kurth, W. S., Levin, S. M., Mauk, B. H., McComas, D. J., Paranicas, C. P., Santos-Costa, D., Thorne, R. M., Valek, P., Waite, J. H., Zarka, P., 2017, Magnetospheric Science Objectives of the Juno Mission, Space Sci. Rev., 213, 219–287, doi:10.1007/s11214-014-0036-8

Baumjohann, W., et al., 2012, Basic Space Plasma Physics (Revised Edition)

Baumjohann, W., Treumann, R. A., 1996, Basic Space Plasma Physics, PUBLISHED BY IMPERIAL COLLEGE PRESS AND DISTRIBUTED BY WORLD SCIENTIFIC PUBLISHING CO.

Bhardwaj, A., Gladstone, G. R., 2000, Auroral emissions of the giant planets, Reviews of Geophysics, 38, 295–353, doi:https://doi.org/10.1029/1998RG000046

Bhattacharyya, D., Clarke, J. T., Montgomery, J., Bonfond, B., Gérard, J.-C., Grodent, D., 2018, Evidence for Auroral Emissions From Callisto's Footprint in HST UV Images, Journal of Geophysical Research (Space Physics), 123, 364–373, doi:10.1002/2017JA024791

Birn, J., Thomsen, M. F., Borovsky, J. E., Reeves, G. D., McComas, D. J., Belian, R. D., 1997, Characteristic plasma properties during dispersionless substorm injections at geosynchronous orbit, Journal of Geophysical Research: Space Physics, 102, 2309–2324, doi:10.1029/96JA02870

Blanc, M., Andrews, D. J., Coates, A. J., Hamilton, D. C., Jackman, C. M., Jia, X., Kotova, A., Morooka, M., Smith, H. T., Westlake, J. H., 2015, Saturn plasma sources and associated transport processes, Space Science Reviews, 192, 237–283, doi:10.1007/s11214-015-0172-9

Bolton, S. J., Bagenal, F., Blanc, M., Cassidy, T., Chané, E., Jackman, C., Jia, X., Kotova, A., Krupp, N., Mililllo, A., Plainaki, C., Smith, H. T., Waite, H., 2015, Jupiter's Magnetosphere: Plasma Sources and Transport, Space Sci. Rev., 192, 209–236, doi:10.1007/s11214-015-0184-5

Bonfond, B., Grodent, D., Gérard, J. C., Radioti, A., Saur, J., Jacobsen, S., 2008, UV Io footprint leading spot: A key feature for understanding the UV Io footprint multiplicity?, Geophys. Res. Lett., 35, L05107, doi:10.1029/2007GL032418

Bonfond, B., Grodent, D., Gerard, J. C., Radioti, A., Dols, V., Delamere, P. A., Clarke, J. T., 2009, The io uv footprint: location, inter-spot distances and tail vertical extent, Journal of Geophysical Research, 114, A07 224, doi:10.1029/2009ja014312

Bonfond, B., Vogt, M. F., Gérard, J. C., Grodent, D., Radioti, A., Coumans, V., 2011, Quasi-periodic polar flares at jupiter: A signature of pulsed dayside reconnections?, Geophysical Research Letters, 38, L02 104, doi:10.1029/2010GL045981

Bonfond, B., Grodent, D., Gérard, J. C., Stallard, T., Clarke, J. T., Yoneda, M., Radioti, A., Gustin, J., 2012, Auroral evidence of io's control over the magnetosphere of jupiter, Geophysical Research Letters, 39, L01 105, doi:10.1029/2011GL050253

Bonfond, B., Hess, S., Bagenal, F., Gérard, J. C., Grodent, D., Radioti, A., Gustin, J., Clarke, J. T., 2013a, The multiple spots of the Ganymede auroral footprint, Geophys. Res. Lett., 40, 4977–4981, doi:10.1002/grl.50989

Bonfond, B., Hess, S., Gérard, J. C., Grodent, D., Radioti, A., Chantry, V., Saur, J., Jacobsen, S., Clarke, J. T., 2013b, Evolution of the Io footprint brightness I: Far-UV observations, Planet. Space Sci., 88, 64–75, doi:10.1016/j.pss.2013.05.023

Bonfond, B., Gustin, J., Gérard, J. C., Grodent, D., Radioti, A., Palmaerts, B., Badman, S. V., Khurana, K. K., Tao, C., 2015, The far-ultraviolet main auroral emission at Jupiter - Part 2: Vertical emission profile, Annales Geophysicae, 33, 1211–1219, doi:10.5194/angeo-33-1211-2015

Bonfond, B., Grodent, D., Badman, S. V., Gérard, J. C., Radioti, A., 2016, Dynamics of the flares in the active polar region of Jupiter, Geophys. Res. Lett., 43, 11,963–11,970, doi:10.1002/2016GL071757

Bonfond, B., Gladstone, G. R., Grodent, D., Greathouse, T. K., Versteeg, M. H., Hue, V., Davis, M. W., Vogt, M. F., Gérard, J. C., Radioti, A., Bolton, S., Levin, S. M., Connerney, J. E. P., Mauk, B. H., Valek, P., Adriani, A., Kurth, W. S., 2017, Morphology of the uv aurorae jupiter during juno's first perijove observations, Geophysical Research Letters, 44, 4463–4471, doi:10.1002/2017GL073114

Bonfond, B., Yao, Z., Grodent, D., 2020, Six Pieces of Evidence Against the Corotation Enforcement Theory to Explain the Main Aurora at Jupiter, Journal of Geophysical Research (Space Physics), 125, e28152, doi:10.1029/2020JA028152

Bonfond, B., Yao, Z. H., Gladstone, G. R., Grodent, D., Gérard, J. C., Matar, J., Palmaerts, B., Greathouse, T. K., Hue, V., Versteeg, M. H., Kammer, J. A., Giles, R. S., Tao, C., Vogt, M. F., Mura, A., Adriani, A., Mauk, B. H., Kurth, W. S., Bolton, S. J., 2021, Are Dawn Storms Jupiter's Auroral Substorms?, AGU Advances, 2, e00275, doi:10.1029/2020AV000275

Broadfoot, A. L., Belton, M. J. S., Takacs, P. Z., Sandel, B. R., Shemansky, D. E., Holberg, J. B., Ajello, J. M., Atreya, S. K., Donahue, T. M., Moos, H. W., Bertaux, J. L., Blamont, J. E., Strobel, D. F., McConnell, J. C., Dalgarno, A., Goody, R., McElroy, M. B., 1979, Extreme ultraviolet observations from voyager 1 encounter with jupiter, Science, 204, 979–982, doi:10.1126/science.204.4396.979

Bunce, E. J., Cowley, S. W. H., Wright, D. M., Coates, A. J., Dougherty, M. K., Krupp, N., Kurth, W. S., Rymer, A. M., 2005, In situ observations of a solar wind compression-induced hot plasma injection in saturn's tail, Geophysical Research Letters, 32, doi:https://doi.org/10.1029/2005GL022888

Burch, J. L., Goldstein, J., Hill, T. W., Young, D. T., Crary, F. J., Coates, A. J., André, N., Kurth, W. S., Sittler Jr., E. C., 2005, Properties of local plasma injections in saturn's magnetosphere, Geophysical Research Letters, 32, doi:10.1029/2005GL022611

Burke, B. F., Franklin, K. L., 1955, Observations of a variable radio source associated with the planet jupiter, Journal of Geophysical Research (1896-1977), 60, 213–217, doi:https://doi.org/10.1029/JZ060i002p00213

Caldwell, J., Halthore, R., Orton, G., Bergstralh, J., 1988, Infrared polar brightenings on Jupiter IV. Spatial properties of methane emission, Icarus, 74, 331–339, doi:10.1016/0019-1035(88)90045-0

Chané, E., Saur, J., Poedts, S., 2013, Modeling jupiter's magnetosphere: Influence of the internal sources, Journal of Geophysical Research: Space Physics, 118, 2157–2172, doi:https://doi.org/10.1002/jgra.50258

Chen, Y., Hill, T. W., 2008, Statistical analysis of injection/dispersion events in saturn's inner magnetosphere, Journal of Geophysical Research: Space Physics, 113, doi:https://doi.org/10.1029/2008JA013166

Chen, Y., Hill, T. W., Rymer, A. M., Wilson, R. J., 2010, Rate of radial transport of plasma in saturn's inner magnetosphere, Journal of Geophysical Research: Space Physics, 115, doi:https://doi.org/10.1029/2010JA015412

Clark, G. B., Mauk, B., Paranicas, C., Haggerty, D. K., Kollmann, P., Rymer, A. M., Westlake, J. H., Allegrini, F., Bagenal, F., Bolton, S. J., Connerney, J. E. P., Ebert, R. W., Elliott, S., Gershman, D. J., Gladstone, R., Hospodarsky, G. B., Imai, M., Kurth, W. S., Kotsiaros, S., Levin, S., Saur, J., Szalay, J. R., 2019, Energetic particle observations in Jupiter's polar magnetosphere: new discoveries by Juno, in AGU Fall Meeting Abstracts, vol. 2019, pp. P42A–01

Clarke, J. T., Ajello, J., Ballester, G., Ben Jaffel, L., Connerney, J., Gérard, J. C., Gladstone, G. R., Grodent, D., Pryor, W., Trauger, J., Waite, J. H., 2002, Ultraviolet emissions from the magnetic footprints of Io, Ganymede and Europa on Jupiter, Nature, 415, 997–1000

Clarke, J. T., Grodent, D., Cowley, S. W. H., Bunce, E. J., Zarka, P., Connerney, J. E. P., Satoh, T., 2004, Jupiter's aurora, in Jupiter. The Planet, Satellites and Magnetosphere, (Eds.) F. Bagenal, T. E. Dowling, W. B. McKinnon, vol. 1, pp. 639–670

Clarke, J. T., Nichols, J., Gérard, J. C., Grodent, D., Hansen, K. C., Kurth, W., Gladstone, G. R., Duval, J., Wannawichian, S., Bunce, E., Cowley, S. W. H., Crary, F., Dougherty, M., Lamy, L., Mitchell, D., Pryor, W., Retherford, K., Stallard, T., Zieger, B., Zarka, P., Cecconi, B., 2009, Response of jupiter's and saturn's auroral activity to the solar wind, Journal of Geophysical Research: Space Physics, 114, A05 210, doi:10.1029/2008JA013694

Connerney, J. E. P., Acuña, M. H., Ness, N. F., Satoh, T., 1998, New models of Jupiter's magnetic field constrained by the Io flux tube footprint, J. Geophys. Res., 103, 11 929–11 940, doi:10.1029/97JA03726

Connerney, J. E. P., Kotsiaros, S., Oliversen, R. J., Espley, J. R., Joergensen, J. L., Joergensen, P. S., Merayo, J. M. G., Herceg, M., Bloxham, J., Moore, K. M., Bolton, S. J., Levin, S. M., 2018, A new model of jupiter's magnetic field from juno's first nine orbits, Geophysical Research Letters, 45, 2590–2596, doi:10.1002/2018GL077312

Connerney, J. E. P., Timmins, S., Herceg, M., Joergensen, J. L., 2020, A Jovian Magnetodisc Model for the Juno Era, Journal of Geophysical Research (Space Physics), 125, e28138, doi:10.1029/2020JA028138

Connerney, J. E. P., Timmins, S., Oliversen, R. J., Espley, J. R., Joergensen, J. L., Kotsiaros, S., Joergensen, P. S., Merayo, J. M. G., Herceg, M., Bloxham, J., Moore, K. M., Mura, A., Moirano, A., Bolton, S. J., Levin, S. M., 2022, A new model of jupiter's magnetic field at the completion of juno's prime mission, Journal of Geophysical Research: Planets, 127, e2021JE007 055, doi: https://doi.org/10.1029/2021JE007055

Cooper, J. F., Johnson, R. E., Mauk, B. H., Garrett, H. B., Gehrels, N., 2001, Energetic Ion and Electron Irradiation of the Icy Galilean Satellites, Icarus, 149, 133–159, doi:10.1006/icar.2000.6498

Cowley, S. W. H., Bunce, E. J., 2001, Origin of the main auroral oval in jupiter's coupled magnetosphere-ionosphere system, Planetary and Space Science, 49, 1067–1088, doi:10.1016/s0032-0633(00)00167-7

Cowley, S. W. H., Nichols, J. D., Jackman, C. M., 2015, Down-tail mass loss by plasmoids in Jupiter's and Saturn's magnetospheres, Journal of Geophysical Research (Space Physics), 120, 6347–6356, doi:10.1002/2015JA021500

Damiano, P. A., Delamere, P. A., Stauffer, B., Ng, C. S., Johnson, J. R., 2019, Kinetic Simulations of Electron Acceleration by Dispersive Scale Alfvén Waves in Jupiter's Magnetosphere, Geophys. Res. Lett., 46, 3043–3051, doi:10.1029/2018GL081219

DeForest, S. E., McIlwain, C. E., 1971, Plasma clouds in the magnetosphere, Journal of Geophysical Research (1896-1977), 76, 3587–3611, doi:10.1029/JA076i016p03587

Delamere, P. A., Bagenal, F., 2003, Modeling variability of plasma conditions in the Io torus, Journal of Geophysical Research (Space Physics), 108, 1276, doi:10.1029/2002JA009706

Delamere, P. A., Bagenal, F., 2010, Solar wind interaction with Jupiter's magnetosphere, Journal of Geophysical Research (Space Physics), 115, A10201, doi:10.1029/2010JA015347

Delamere, P. A., Bagenal, F., 2013, Magnetotail structure of the giant magnetospheres: Implications of the viscous interaction with the solar wind, Journal of Geophysical Research (Space Physics), 118, 7045–7053, doi:10.1002/2013JA019179

Delamere, P. A., Bagenal, F., Paranicas, C., Masters, A., Radioti, A., Bonfond, B., Ray, L., Jia, X., Nichols, J., Arridge, C., 2015, Solar Wind and Internally Driven Dynamics: Influences on Magnetodiscs and Auroral Responses, Space Sci. Rev., 187, 51–97, doi:10.1007/s11214-014-0075-1

Delamere, P. A., Otto, A., Ma, X., Bagenal, F., Wilson, R. J., 2015, Magnetic flux circulation in the rotationally driven giant magnetospheres, Journal of Geophysical Research: Space Physics, 120, 4229–4245, doi:https://doi.org/10.1002/2015JA021036

Desroche, M., Bagenal, F., Delamere, P. A., Erkaev, N., 2012, Conditions at the expanded Jovian magnetopause and implications for the solar wind interaction, Journal of Geophysical Research (Space Physics), 117, A07202, doi:10.1029/2012JA017621

Divine, N., Garrett, H. B., 1983, Charged particle distributions in Jupiter's magnetosphere, J. Geophys. Res., 88, 6889–6903, doi:10.1029/JA088iA09p06889

Dols, V., Gerard, J. C., Paresce, F., Prange, R., Vidal-Madjar, A., 1992, Ultraviolet imaging of the Jovian aurora with the Hubble Space Telescope, Geophys. Res. Lett., 19, 1803–1806, doi:10.1029/92GL02104

Drake, F. D., Hvatum, S., 1959, Non-thermal microwave radiation from Jupiter., AJ, 64, 329–330, doi:10.1086/108047

Drossart, P., Maillard, J. P., Caldwell, J., Kim, S. J., Watson, J. K. G., Majewski, W. A., Tennyson, J., Miller, S., Atreya, S. K., Clarke, J. T., Waite, J. H., Wagener, R., 1989, Detection of H_3^+ on Jupiter, Nature, 340, 539–541, doi:10.1038/340539a0

Dumont, M., Grodent, D., Radioti, A., Bonfond, B., Gérard, J. C., 2014, Jupiter's equatorward auroral features: Possible signatures of magnetospheric injections, Journal of Geophysical Research: Space Physics, 119, 10,068–10,077, doi:10.1002/2014JA020527

Dumont, M., Grodent, D., Radioti, A., Bonfond, B., Roussos, E., Paranicas, C., 2018, Evolution of the auroral signatures of jupiter's magnetospheric injections, Journal of Geophysical Research: Space Physics, 123, 8489–8501, doi:10.1029/2018JA025708

Dungey, J. W., 1961, Interplanetary magnetic field and the auroral zones, Phys. Rev. Lett., 6, 47–48, doi:10.1103/PhysRevLett.6.47

Ebert, R. W., Greathouse, T. K., Clark, G., Hue, V., Allegrini, F., Bagenal, F., Bolton, S. J., Bonfond, B., Connerney, J. E. P., Gladstone, G. R., Imai, M., Kotsiaros, S., Kurth, W. S., Levin, S., Louarn, P., Mauk, B. H., McComas, D. J., Paranicas, C., Sulaiman, A. H., Szalay, J. R., Thomsen, M. F., Wilson, R. J., 2021, Simultaneous UV Images and High-Latitude Particle and Field Measurements During an Auroral Dawn Storm at Jupiter, Journal of Geophysical Research (Space Physics), 126, e29679, doi:10.1029/2021JA029679

Ebihara, Y., 2019, Simulation study of near-Earth space disturbances: 2. Auroral substorms, Progress in Earth and Planetary Science, 6, 24, doi:10.1186/s40645-019-0273-2

Elliott, S. S., Gurnett, D. A., Kurth, W. S., Mauk, B. H., Ebert, R. W., Clark, G., Valek, P., Allegrini, F., Bolton, S. J., 2018, The acceleration of electrons to high energies over the jovian polar cap via whistler mode wave-particle interactions, Journal of Geophysical Research: Space Physics, 123, 7523–7533, doi:https://doi.org/10.1029/2018JA025797

Feldman, U., Landi, E., Schwadron, N. A., 2005, On the sources of fast and slow solar wind, Journal of Geophysical Research (Space Physics), 110, A07109, doi:10.1029/2004JA010918

Field, G. B., 1959, The Source of Radiation from Jupiter at Decimeter Wavelengths, J. Geophys. Res., 64, 1169–1177, doi:10.1029/JZ064i009p01169

Ford, H. C., Feldman, P. D., Golimowski, D. A., Tsvetanov, Z., Bartko, F., Crocker, J. H., Bely, P. Y., Brown, R. A., Burrows, C. J., Clampin, M., Hartig, G. F., Postman, M., Rafal, M. D., Sparks, W. B., White, R. L., Broadhurst, T., Illingworth, G., Kelly, T., Woodruff, R. A., Cheng, E., Kimble, R. A., Krebs, C. A., Neff, S. G., Lesser, M. P., Miley, G., 1996, Advanced camera for the Hubble Space Telescope, in Space Telescopes and Instruments IV, (Eds.) P. Y. Bely, J. B. Breckinridge, vol. 2807 of Society of Photo-Optical Instrumentation Engineers (SPIE) Conference Series, pp. 184–196, doi:10.1117/12.255099

Gérard, J.-C., Saglam, A., Grodent, D., Clarke, J. T., 2006, Morphology of the ultraviolet Io footprint emission and its control by Io's location, Journal of Geophysical Research (Space Physics), 111, A04202, doi:10.1029/2005JA011327

Gérard, J. C., Grodent, D., Radioti, A., Bonfond, B., Clarke, J. T., 2013, Hubble observations of Jupiter's north-south conjugate ultraviolet aurora, Icarus, 226, 1559–1567, doi:10.1016/j.icarus.2013.08.017

Gérard, J. C., Bonfond, B., Mauk, B. H., Gladstone, G. R., Yao, Z. H., Greathouse, T. K., Hue, V., Grodent, D., Gkouvelis, L., Kammer, J. A., Versteeg, M., Clark, G., Radioti, A., Connerney, J. E. P., Bolton, S. J., Levin, S. M., 2019, Contemporaneous Observations of Jovian Energetic Auroral Electrons and Ultraviolet Emissions by the Juno Spacecraft, Journal of Geophysical Research (Space Physics), 124, 8298–8317, doi:10.1029/2019JA026862

Gershman, D. J., Connerney, J. E. P., Kotsiaros, S., DiBraccio, G. A., Martos, Y. M., -Viñas, A. F., Hue, V., Clark, G., Bagenal, F., Levin, S., Bolton, S. J., 2019, Alfvénic Fluctuations Associated With Jupiter's Auroral Emissions, Geophys. Res. Lett., 46, 7157–7165, doi:10.1029/2019GL082951

Gladstone, G. R., Persyn, S. C., Eterno, J. S., Walther, B. C., Slater, D. C., Davis, M. W., Versteeg, M. H., Persson, K. B., Young, M. K., Dirks, G. J., Sawka, A. O., Tumlinson, J., Sykes, H., Beshears, J., Rhoad, C. L., Cravens, J. P., Winters, G. S., Klar, R. A., Lockhart, W., Piepgrass, B. M., Greathouse, T. K., Trantham, B. J., Wilcox, P. M., Jackson, M. W., Siegmund, O. H. W., Vallerga, J. V., Raffanti, R., Martin, A., Gérard, J. C., Grodent, D. C., Bonfond, B., Marquet, B., Denis, F., 2017, The Ultraviolet Spectrograph on NASA's Juno Mission, Space Sci. Rev., 213, 447–473, doi:10.1007/s11214-014-0040-z

Gray, R. L., Badman, S. V., Bonfond, B., Kimura, T., Misawa, H., Nichols, J. D., Vogt, M. F., Ray, L. C., 2016, Auroral evidence of radial transport at jupiter during january 2014, Journal of Geophysical Research: Space Physics, 121, 9972–9984, doi:10.1002/2016JA023007

Gray, R. L., Badman, S. V., Woodfield, E. E., Tao, C., 2017, Characterization of jupiter's secondary auroral oval and its response to hot plasma injections, Journal of Geophysical Research: Space Physics, 122, 6415–6429, doi:10.1002/2017JA024214

Greathouse, T., Gladstone, R., Versteeg, M., Hue, V., Kammer, J., Giles, R., Davis, M., Bolton, S., Levin, S., Connerney, J., Gérard, J.-C., Grodent, D., Bonfond, B., Bunce, E., Vogt, M. F., 2021, Local Time Dependence of Jupiter's Polar Auroral Emissions Observed by Juno UVS, Journal of Geophysical Research (Planets), 126, e06954, doi:10.1029/2021JE006954

Grodent, D., 2015, A Brief Review of Ultraviolet Auroral Emissions on Giant Planets, Space Sci. Rev., 187, 23–50, doi:10.1007/s11214-014-0052-8

Grodent, D., Waite, J. Hunter, J., Gérard, J.-C., 2001, A self-consistent model of the Jovian auroral thermal structure, J. Geophys. Res., 106, 12 933–12 952, doi:10.1029/2000JA900129

Grodent, D., Clarke, J. T., Kim, J., Waite, J. H., J., Cowley, S. W. H., 2003a, Jupiter's main auroral oval observed with hst-stis, Journal of Geophysical Research, 108, 1389, doi:10.1029/2003ja009921

Grodent, D., Clarke, J. T., Kim, J., Waite Jr., J. H., Cowley, S. W. H., 2003b, Jupiter's main auroral oval observed with hst-stis, Journal of Geophysical Research: Space Physics, 108, doi:https://doi.org/10.1029/2003JA009921

Grodent, D., Clarke, J. T., Waite, J. H., J., Cowley, S. W. H., Gerard, J. C., Kim, J., 2003c, Jupiter's polar auroral emissions, Journal of Geophysical Research, 108, 1366, doi:10.1029/2003ja010017

Grodent, D., Bonfond, B., Gérard, J.-C., Radioti, A., Gustin, J., Clarke, J. T., Nichols, J., Connerney, J. E. P., 2008, Auroral evidence of a localized magnetic anomaly in jupiter's northern hemisphere, Journal of Geophysical Research: Space Physics, 113, A09 201, doi:10.1029/2008JA013185

Grodent, D., Bonfond, B., Radioti, A., Gérard, J.-C., Jia, X., Nichols, J. D., Clarke, J. T., 2009, Auroral footprint of ganymede, Journal of Geophysical Research: Space Physics, 114, A07 212, doi:10.1029/2009JA014289

Grodent, D., Bonfond, B., Yao, Z., Gérard, J. C., Radioti, A., Dumont, M., Palmaerts, B., Adriani, A., Badman, S. V., Bunce, E. J., Clarke, J. T., Connerney, J. E. P., Gladstone, G. R., Greathouse, T., Kimura, T., Kurth, W. S., Mauk, B. H., McComas, D. J., Nichols, J. D., Orton, G. S., Roth, L., Saur, J., Valek, P., 2018, Jupiter's Aurora Observed With HST During Juno Orbits 3 to 7, Journal of Geophysical Research (Space Physics), 123, 3299–3319, doi:10.1002/2017JA025046

Guillot, T., Stevenson, D. J., Hubbard, W., Saumon, D., 2004, Jupiter. The Planet, Satellites and Magnetosphere, chap. The Interior of Jupiter, pp. p35–p57, Cambridge Cambrigde University Press, ISBN 0 521 81808 7

Guo, R. L., Yao, Z. H., Wei, Y., Ray, L. C., Rae, I. J., Arridge, C. S., Coates, A. J., Delamere, P. A., Sergis, N., Kollmann, P., Grodent, D., Dunn, W. R., Waite, J. H., Burch, J. L., Pu, Z. Y., Palmaerts, B., Dougherty, M. K., 2018, Rotationally driven magnetic reconnection in Saturn's dayside, Nature Astronomy, 2, 640–645, doi:10.1038/s41550-018-0461-9

Gustin, J., Bonfond, B., Grodent, D., Gérard, J. C., 2012, Conversion from hst acs and stis auroral counts into brightness, precipitated power, and radiated power for h2 giant planets, Journal of Geophysical Research: Space Physics, 117, A07 316, doi:10.1029/2012JA017607

Gustin, J., Grodent, D., Ray, L. C., Bonfond, B., Bunce, E. J., Nichols, J. D., Ozak, N., 2016, Characteristics of north jovian aurora from stis fuv spectral images, Icarus, 268, 215–241, doi: https://doi.org/10.1016/j.icarus.2015.12.048

Gérard, J. C., Bonfond, B., Grodent, D., Radioti, A., Clarke, J. T., Gladstone, G. R., Waite, J. H., Bisikalo, D., Shematovich, V. I., 2014, Mapping the electron energy in jupiter's aurora: Hubble spectral observations, Journal of Geophysical Research: Space Physics, 119, 9072–9088, doi:10.1002/2014JA020514

Haewsantati, K., 2022, Characteristics of Jupiter's Polar Auroral Bright Spot based on Juno in situ and Remote Sensing Observations, Ph.D. thesis, ULiège - Université de Liège, Belgium

Haewsantati, K., Bonfond, B., Wannawichian, S., Gladstone, G. R., Hue, V., Versteeg, M. H., Greathouse, T. K., Grodent, D., Yao, Z., Dunn, W., Gérard, J. C., Giles, R., Kammer, J., Guo, R., Vogt, M. F., 2021, Morphology of Jupiter's Polar Auroral Bright Spot Emissions via Juno UVS Observations, Journal of Geophysical Research (Space Physics), 126, e28586, doi: 10.1029/2020JA028586

Haggerty, D. K., Mauk, B. H., Paranicas, C. P., Clark, G., Kollmann, P., Rymer, A. M., Gladstone, G. R., Greathouse, T. K., Bolton, S. J., Levin, S. M., 2019, Jovian injections observed at high latitude, Geophysical Research Letters, 46, 9397–9404, doi:https://doi.org/10.1029/2019GL083442

Hamilton, D. C., Gloeckler, G., Krimigis, S. M., Lanzerotti, L. J., 1981, Composition of nonthermal ions in the Jovian magnetosphere, J. Geophys. Res., 86, 8301–8318, doi:10.1029/JA086iA10p08301

Hess, S., Bonfond, B., Zarka, P., Grodent, D., 2011, Model of the jovian magnetic field topology constrained by the io auroral emissions, Journal of Geophysical Research - Part A - Space Physics, 116, A05 217, doi:10.1029/2010ja016262

Hess, S., Bonfond, B., Chantry, V., Gérard, J.-C., Grodent, D., Jacobsen, S., Radioti, A., 2013, Evolution of the io footprint brightness ii: Modeling, Planetary and Space Science, 88, 76–85, doi: https://doi.org/10.1016/j.pss.2013.08.005

Hess, S. L. G., Delamere, P., Dols, V., Bonfond, B., Swift, D., 2010, Power transmission and particle acceleration along the Io flux tube, Journal of Geophysical Research (Space Physics), 115, A06205, doi:10.1029/2009JA014928

Hill, T. W., 2001, The Jovian auroral oval, J. Geophys. Res., 106, 8101–8108, doi:10.1029/2000JA000302

Hill, T. W., 2016, Penetration of external plasma into a rotation-driven magnetosphere, Journal of Geophysical Research: Space Physics, 121, 10,032–10,036, doi:10.1002/2016JA023430

Hill, T. W., Dessler, A. J., Michel, F. C., 1974, Configuration of the jovian magnetosphere, Geophysical Research Letters, 1, 3–6, doi:https://doi.org/10.1029/GL001i001p00003

Hill, T. W., Rymer, A. M., Burch, J. L., Crary, F. J., Young, D. T., Thomsen, M. F., Delapp, D., André, N., Coates, A. J., Lewis, G. R., 2005, Evidence for rotationally driven plasma transport in saturn's magnetosphere, Geophysical Research Letters, 32, doi:10.1029/2005GL022620

Hill, T. W., Thomsen, M. F., Henderson, M. G., Tokar, R. L., Coates, A. J., McAndrews, H. J., Lewis, G. R., Mitchell, D. G., Jackman, C. M., Russell, C. T., Dougherty, M. K., Crary, F. J., Young, D. T., 2008, Plasmoids in saturn's magnetotail, Journal of Geophysical Research: Space Physics, 113, doi:https://doi.org/10.1029/2007JA012626

Huddleston, D. E., Russell, C. T., Kivelson, M. G., Khurana, K. K., Bennett, L., 1998, Location and shape of the Jovian magnetopause and bow shock, J. Geophys. Res., 103, 20 075–20 082, doi:10.1029/98JE00394

Hue, V., Gladstone, G. R., Greathouse, T. K., Kammer, J. A., Davis, M. W., Bonfond, B., Versteeg, M. H., Grodent, D. C., Gérard, J.-C., Bolton, S. J., Levin, S. M., Byron, B. D., 2019, In-flight Characterization and Calibration of the Juno-ultraviolet Spectrograph (Juno-UVS), AJ, 157, 90, doi:10.3847/1538-3881/aafb36

Johnson, V. E., 2013, Revised standards for statistical evidence, Proceedings of the National Academy of Sciences, 110, 19 313–19 317, doi:10.1073/pnas.1313476110

Joy, S. P., Kivelson, M. G., Walker, R. J., Khurana, K. K., Russell, C. T., Ogino, T., 2002, Probabilistic models of the Jovian magnetopause and bow shock locations, Journal of Geophysical Research (Space Physics), 107, 1309, doi:10.1029/2001JA009146

Kennel, C. F., Scarf, F. L., Fredricks, R. W., McGehee, J. H., Coroniti, F. V., 1970, VLF electric field observations in the magnetosphere, J. Geophys. Res., 75, 6136–6152, doi:10.1029/JA075i031p06136

Kennelly, T. J., Leisner, J. S., Hospodarsky, G. B., Gurnett, D. A., 2013, Ordering of injection events within saturnian sls longitude and local time, Journal of Geophysical Research: Space Physics, 118, 832–838, doi:10.1002/jgra.50152

Khurana, K. K., Kivelson, M. G., Vasyliunas, V. M., Krupp, N., Woch, J., Lagg, A., Mauk, B. H., Kurth, W. S., 2004, The configuration of Jupiter's magnetosphere, vol. 1, pp. 593–616

Kidder, A., Winglee, R. M., Harnett, E. M., 2009, Regulation of the centrifugal interchange cycle in saturn's inner magnetosphere, Journal of Geophysical Research: Space Physics, 114, A02 205, doi:10.1029/2008JA013100

Kimura, T., Badman, S. V., Tao, C., Yoshioka, K., Murakami, G., Yamazaki, A., Tsuchiya, F., Bonfond, B., Steffl, A. J., Masters, A., Kasahara, S., Hasegawa, H., Yoshikawa, I., Fujimoto, M., Clarke, J. T., 2015, Transient internally driven aurora at jupiter discovered by hisaki and the hubble space telescope, Geophysical Research Letters, 42, 1662–1668, doi:10.1002/2015GL063272

Kimura, T., Nichols, J. D., Gray, R. L., Tao, C., Murakami, G., Yamazaki, A., Badman, S. V., Tsuchiya, F., Yoshioka, K., Kita, H., Grodent, D., Clark, G., Yoshikawa, I., Fujimoto, M., 2017, Transient brightening of Jupiter's aurora observed by the Hisaki satellite and Hubble Space Telescope during approach phase of the Juno spacecraft, Geophys. Res. Lett., 44, 4523–4531, doi: 10.1002/2017GL072912

Kimura, T., Hiraki, Y., Tao, C., Tsuchiya, F., Delamere, P. A., Yoshioka, K., Murakami, G., Yamazaki, A., Kita, H., Badman, S. V., Fukazawa, K., Yoshikawa, I., Fujimoto, M., 2018, Response of Jupiter's Aurora to Plasma Mass Loading Rate Monitored by the Hisaki Satellite During Volcanic Eruptions at Io, Journal of Geophysical Research (Space Physics), 123, 1885–1899, doi: 10.1002/2017JA025029

Kivelson, M., Russell, C., 1995, Introduction to Space Physics, Cambridge University Press, ISBN 9780521457149

Kivelson, M., Bagenal, F., Kurth, W., Neubauer, F., Paranicas, C., Saur, J., 2004, Jupiter: The planet, satellites, and magnetosphere

Kivelson, M. G., 2015, Planetary Magnetodiscs: Some Unanswered Questions, Space Sci. Rev., 187, 5–21, doi:10.1007/s11214-014-0046-6

Kivelson, M. G., Southwood, D. J., 2005, Dynamical consequences of two modes of centrifugal instability in Jupiter's outer magnetosphere, Journal of Geophysical Research (Space Physics), 110, A12209, doi:10.1029/2005JA011176

Knight, S., 1973, Parallel electric fields, Planet. Space Sci., 21, 741–750, doi:10.1016/0032-0633(73)90093-7

Kostiuk, T., Romani, P., Espenak, F., Livengood, T. A., Goldstein, J. J., 1993, Temperature and abundances in the Jovian auroral stratosphere 2. Ethylene as a probe of the microbar region, J. Geophys. Res., 98, 18 823–18 830, doi:10.1029/93JE01332

Kotsiaros, S., Connerney, J. E. P., Clark, G., Allegrini, F., Gladstone, G. R., Kurth, W. S., Mauk, B. H., Saur, J., Bunce, E. J., Gershman, D. J., Martos, Y. M., Greathouse, T. K., Bolton, S. J., Levin, S. M., 2019, Birkeland currents in Jupiter's magnetosphere observed by the polar-orbiting Juno spacecraft, Nature Astronomy, 3, 904–909, doi:10.1038/s41550-019-0819-7

Kronberg, E. A., Woch, J., Krupp, N., Lagg, A., Khurana, K. K., Glassmeier, K. H., 2005, Mass release at jupiter: Substorm-like processes in the jovian magnetotail, Journal of Geophysical Research: Space Physics, 110, A03 211, doi:10.1029/2004JA010777

Krupp, N., 2014, Giant magnetospheres in our solar system: Jupiter and Saturn compared, A&A Rev., 22, 75, doi:10.1007/s00159-014-0075-x

Krupp, N., Woch, J., Lagg, A., Wilken, B., Livi, S., Williams, D. J., 1998, Energetic particle bursts in the predawn jovian magnetotail, Geophysical Research Letters, 25, 1249–1252, doi:10.1029/98GL00863

Krupp, N., Vasyliūnas, V. M., Woch, J., Lagg, A., Khurana, K. K., Kivelson, M. G., Mauk, B. H., Roelof, E. C., Williams, D. J., Krimigis, S., Kurth, W. S., Frank, L., Paterson, W., 2004, The dynamics of the Jovian magnetosphere, vol. 1, book section 25, Cambrigde University Press, ISBN 0-521-81808-7

Kurth, W. S., Hospodarsky, G. B., Kirchner, D. L., Mokrzycki, B. T., Averkamp, T. F., Robison, W. T., Piker, C. W., Sampl, M., Zarka, P., 2017, The Juno Waves Investigation, Space Sci. Rev., 213, 347–392, doi:10.1007/s11214-017-0396-y

Lenchek, A. M., Singer, S. F., Wentworth, R. C., 1961, Geomagnetically trapped electrons from cosmic ray albedo neutrons, Journal of Geophysical Research (1896-1977), 66, 4027–4046, doi:https://doi.org/10.1029/JZ066i012p04027

Lew, J. S., 1961, Drift rate in a dipole field, Journal of Geophysical Research (1896-1977), 66, 2681–2685, doi:https://doi.org/10.1029/JZ066i009p02681

Li, W., Thorne, R. M., Ma, Q., Zhang, X.-J., Gladstone, G. R., Hue, V., Valek, P. W., Allegrini, F., Mauk, B. H., Clark, G., Kurth, W. S., Hospodarsky, G. B., Connerney, J. E. P., Bolton, S. J., 2017, Understanding the origin of jupiter's diffuse aurora using juno's first perijove observations, Geophysical Research Letters, 44, 10,162–10,170, doi:10.1002/2017GL075545

Li, W., Ma, Q., Shen, X. C., Zhang, X. J., Mauk, B. H., Clark, G., Allegrini, F., Kurth, W. S., Hospodarsky, G. B., Hue, V., Gladstone, G. R., Greathouse, T. K., Bolton, S. J., 2021, Quantification of Diffuse Auroral Electron Precipitation Driven by Whistler Mode Waves at Jupiter, Geophys. Res. Lett., 48, e95457, doi:10.1029/2021GL095457

Liu, X., Hill, T. W., Wolf, R. A., Sazykin, S., Spiro, R. W., Wu, H., 2010, Numerical simulation of plasma transport in saturn's inner magnetosphere using the rice convection model, Journal of Geophysical Research: Space Physics, 115, doi:https://doi.org/10.1029/2010JA015859

Lorch, C. T. S., Ray, L. C., Wilson, R. J., Bagenal, F., Crary, F., Delamere, P. A., Damiano, P. A., Watt, C. E. J., Allegrini, F., 2022, Evidence of alfvénic activity in jupiter's mid-to-high latitude magnetosphere, Journal of Geophysical Research: Space Physics, 127, e2021JA029 853, doi:https://doi.org/10.1029/2021JA029853

Louarn, P., Mauk, B. H., Kivelson, M. G., Kurth, W. S., Roux, A., Zimmer, C., Gurnett, D. A., Williams, D. J., 2001, A multi-instrument study of a jovian magnetospheric disturbance, Journal of Geophysical Research: Space Physics, 106, 29 883–29 898, doi:10.1029/2001JA900067

Louarn, P., Andre, N., Jackman, C., Kasahara, S., Kronberg, E., Vogt, M., 2014, Magnetic reconnection and associated transient phenomena within the magnetospheres of jupiter and saturn, Space Science Reviews, pp. 1–47, doi:10.1007/s11214-014-0047-5

Ma, X., Delamere, P. A., Otto, A., 2016, Plasma transport driven by the rayleigh-taylor instability, Journal of Geophysical Research: Space Physics, 121, 5260–5271, doi:https://doi.org/10.1002/2015JA022122

Masters, A., 2017, Model-Based Assessments of Magnetic Reconnection and Kelvin-Helmholtz Instability at Jupiter's Magnetopause, Journal of Geophysical Research (Space Physics), 122, 11,154–11,174, doi:10.1002/2017JA024736

Mauk, B. H., Saur, J., 2007, Equatorial electron beams and auroral structuring at Jupiter, Journal of Geophysical Research (Space Physics), 112, A10221, doi:10.1029/2007JA012370

Mauk, B. H., Williams, D. J., McEntire, R. W., 1997, Energy-time dispersed charged particle signatures of dynamic injections in jupiter's inner magnetosphere, Geophysical Research Letters, 24, 2949–2952, doi:10.1029/97gl03026

Mauk, B. H., Williams, D. J., McEntire, R. W., Khurana, K. K., Roederer, J. G., 1999, Storm-like dynamics of jupiter's inner and middle magnetosphere, Journal of Geophysical Research, 104, 22 759–22 778, doi:10.1029/1999ja900097

Mauk, B. H., Clarke, J. T., Grodent, D., Watte, J. H., J., Paranicas, C. P., Williams, D. J., 2002, Transient aurora on jupiter from injections of magnetospheric electrons, Nature, 415, 1003–1005, doi:10.1038/4151003a

Mauk, B. H., Mitchell, D. G., McEntire, R. W., Paranicas, C. P., Roelof, E. C., Williams, D. J., Krimigis, S. M., Lagg, A., 2004, Energetic ion characteristics and neutral gas interactions in Jupiter's magnetosphere, Journal of Geophysical Research (Space Physics), 109, A09S12, doi:10.1029/2003JA010270

Mauk, B. H., Saur, J., Mitchell, D. G., Roelof, E. C., Brandt, P. C., Armstrong, T. P., Hamilton, D. C., Krimigis, S. M., Krupp, N., Livi, S. A., Manweiler, J. W., Paranicas, C. P., 2005, Energetic particle injections in Saturn's magnetosphere, Geophys. Res. Lett., 32, L14S05, doi: 10.1029/2005GL022485

Mauk, B. H., Haggerty, D. K., Jaskulek, S. E., Schlemm, C. E., Brown, L. E., Cooper, S. A., Gurnee, R. S., Hammock, C. M., Hayes, J. R., Ho, G. C., Hutcheson, J. C., Jacques, A. D., Kerem, S., Kim, C. K., Mitchell, D. G., Nelson, K. S., Paranicas, C. P., Paschalidis, N., Rossano, E., Stokes, M. R., 2017, The Jupiter Energetic Particle Detector Instrument (JEDI) Investigation for the Juno Mission, Space Sci. Rev., 213, 289–346, doi:10.1007/s11214-013-0025-3

Mauk, B. H., Haggerty, D. K., Paranicas, C., Clark, G., Kollmann, P., Rymer, A. M., Peachey, J. M., Bolton, S. J., Levin, S. M., Adriani, A., Allegrini, F., Bagenal, F., Bonfond, B., Connerney, J. E. P., Ebert, R. W., Gladstone, G. R., Kurth, W. S., McComas, D. J., Ranquist, D., Valek, P., 2018, Diverse electron and ion acceleration characteristics observed over jupiter's main aurora, Geophysical Research Letters, 45, 1277–1285, doi:https://doi.org/10.1002/2017GL076901

Mauk, B. H., Clark, G., Gladstone, G. R., Kotsiaros, S., Adriani, A., Allegrini, F., Bagenal, F., Bolton, S. J., Bonfond, B., Connerney, J. E. P., Ebert, R. W., Haggerty, D. K., Kollmann, P., Kurth, W. S., Levin, S. M., Paranicas, C. P., Rymer, A. M., 2020, Energetic Particles and Acceleration Regions Over Jupiter's Polar Cap and Main Aurora: A Broad Overview, Journal of Geophysical Research (Space Physics), 125, e27699, doi:10.1029/2019JA027699

McIlwain, C. E., 1974, Substorm injection boundaries, in Magnetospheric Physics, (Ed.) B. M. McCormac, pp. 143–154, Springer Netherlands, Dordrecht, ISBN 978-94-010-2214-9

McNutt, R. L., Haggerty, D. K., Hill, M. E., Krimigis, S. M., Livi, S., Ho, G. C., Gurnee, R. S., Mauk, B. H., Mitchell, D. G., Roelof, E. C., McComas, D. J., Bagenal, F., Elliott, H. A., Brown, L. E., Kusterer, M., Vandegriff, J., Stern, S. A., Weaver, H. A., Spencer, J. R., Moore, J. M., 2007, Energetic Particles in the Jovian Magnetotail, Science, 318, 220, doi:10.1126/science.1148025

McPherron, R. L., Russell, C. T., Kivelson, M. G., Coleman Jr., P. J., 1973, Substorms in space: The correlation between ground and satellite observations of the magnetic field, Radio Science, 8, 1059–1076, doi:10.1029/RS008i011p01059

Menager, H., Barthélemy, M., Lilensten, J., 2010, H Lyman α line in Jovian aurorae: electron transport and radiative transfer coupled modelling, A&A, 509, A56, doi:10.1051/0004-6361/200912952

Metzger, A. E., Gilman, D. A., Luthey, J. L., Hurley, K. C., Schnopper, H. W., Seward, F. D., Sullivan, J. D., 1983, The detection of x rays from jupiter, Journal of Geophysical Research: Space Physics, 88, 7731–7741, doi:https://doi.org/10.1029/JA088iA10p07731

Mitchell, D., Krimigis, S., Paranicas, C., Brandt, P., Carbary, J., Roelof, E., Kurth, W., Gurnett, D., Clarke, J., Nichols, J., Gérard, J.-C., Grodent, D., Dougherty, M., Pryor, W., 2009, Recurrent energization of plasma in the midnight-to-dawn quadrant of saturn's magnetosphere, and its relationship to auroral uv and radio emissions, Planetary and Space Science, 57, 1732–1742, doi: https://doi.org/10.1016/j.pss.2009.04.002

Mitchell, D. G., Brandt, P. C., Roelof, E. C., Dandouras, J., Krimigis, S. M., Mauk, B. H., Paranicas, C. P., Krupp, N., Hamilton, D. C., Kurth, W. S., Zarka, P., Dougherty, M. K., Bunce, E. J., Shemansky, D. E., 2005, Energetic ion acceleration in saturn's magnetotail: Substorms at saturn?, Geophysical Research Letters, 32, doi:https://doi.org/10.1029/2005GL022647

Moncuquet, M., 1997, Équilibre et confinement du tore de plasma d'Io dans la magnétosphère de Jupiter : observations d'Ulysse et modélisation, Ph.D. thesis, L'UNIVERSITÉ PARIS VII - Denis DIDEROT, France

Moses, J. I., Fouchet, T., Yelle, R. V., Friedson, A. J., Orton, G. S., Bézard, B., Drossart, P., Gladstone, G. R., Kostiuk, T., Livengood, T. A., 2004, The stratosphere of Jupiter, in Jupiter. The Planet, Satellites and Magnetosphere, (Eds.) F. Bagenal, T. E. Dowling, W. B. McKinnon, vol. 1, pp. 129–157

Mura, A., Adriani, A., Altieri, F., Connerney, J. E. P., Bolton, S. J., Moriconi, M. L., Gérard, J. C., Kurth, W. S., Dinelli, B. M., Fabiano, F., Tosi, F., Atreya, S. K., Bagenal, F., Gladstone, G. R., Hansen, C., Levin, S. M., Mauk, B. H., McComas, D. J., Sindoni, G., Filacchione, G., Migliorini, A., Grassi, D., Piccioni, G., Noschese, R., Cicchetti, A., Turrini, D., Stefani, S., Amoroso, M., Olivieri, A., 2017, Infrared observations of Jovian aurora from Juno's first orbits: Main oval and satellite footprints, Geophys. Res. Lett., 44, 5308–5316, doi:10.1002/2017GL072954

Mura, A., Adriani, A., Connerney, J. E. P., Bolton, S., Altieri, F., Bagenal, F., Bonfond, B., Dinelli, B. M., Gérard, J. C., Greathouse, T., Grodent, D., Levin, S., Mauk, B., Moriconi, M. L., Saur, J., Waite, J. H., Amoroso, M., Cicchetti, A., Fabiano, F., Filacchione, G., Grassi, D., Migliorini, A., Noschese, R., Olivieri, A., Piccioni, G., Plainaki, C., Sindoni, G., Sordini, R., Tosi, F., Turrini, D., 2018, Juno observations of spot structures and a split tail in Io-induced aurorae on Jupiter, Science, 361, 774–777, doi:10.1126/science.aat1450

Müller, A. L., Saur, J., Krupp, N., Roussos, E., Mauk, B. H., Rymer, A. M., Mitchell, D. G., Krimigis, S. M., 2010, Azimuthal plasma flow in the kronian magnetosphere, Journal of Geophysical Research: Space Physics, 115, doi:https://doi.org/10.1029/2009JA015122

Ng, C. S., Delamere, P. A., Kaminker, V., Damiano, P. A., 2018, Radial Transport and Plasma Heating in Jupiter's Magnetodisc, Journal of Geophysical Research (Space Physics), 123, 6611–6620, doi: 10.1029/2018JA025345

Nichols, J. D., Clarke, J. T., Gérard, J. C., Grodent, D., Hansen, K. C., 2009, Variation of different components of Jupiter's auroral emission, Journal of Geophysical Research (Space Physics), 114, A06210, doi:10.1029/2009JA014051

Nichols, J. D., Badman, S. V., Bagenal, F., Bolton, S. J., Bonfond, B., Bunce, E. J., Clarke, J. T., Connerney, J. E. P., Cowley, S. W. H., Ebert, R. W., Fujimoto, M., Gérard, J. C., Gladstone, G. R., Grodent, D., Kimura, T., Kurth, W. S., Mauk, B. H., Murakami, G., McComas, D. J., Orton, G. S., Radioti, A., Stallard, T. S., Tao, C., Valek, P. W., Wilson, R. J., Yamazaki, A., Yoshikawa, I., 2017, Jovian magnetospheric injections observed by the Hubble Space Telescope and Juno, Geophys. Res. Lett., 44, 7643–7652, doi:10.1002/2017GL073029

Nichols, J. D., Allegrini, F., Bagenal, F., Bonfond, B., Clark, G. B., Clarke, J. T., Connerney, J. E. P., Cowley, S. W. H., Ebert, R. W.and Gladstone, G. R., Grodent, D., Haggerty, D. K., Mauk, B.and Orton, G. S., Provan, G., Wilson, R. J., 2023, Jovian magnetospheric injections observed by the Hubble Space Telescope and Juno

Pallier, L., Prange, R., 2001, Dynamics of high latitude structures of the Jovian Aurorae., in AAS/Division for Planetary Sciences Meeting Abstracts #33, vol. 33 of AAS/Division for Planetary Sciences Meeting Abstracts, p. 18.07

Palmaerts, B., Radioti, A., Grodent, D., Chané, E., Bonfond, B., 2014, Transient small-scale structure in the main auroral emission at Jupiter, Journal of Geophysical Research (Space Physics), 119, 9931–9938, doi:10.1002/2014JA020688

Paranicas, C., Mitchell, D. G., Roelof, E. C., Mauk, B. H., Krimigis, S. M., Brandt, P. C., Kusterer, M., Turner, F. S., Vandegriff, J., Krupp, N., 2007, Energetic electrons injected into saturn's neutral gas cloud, Geophysical Research Letters, 34, doi:https://doi.org/10.1029/2006GL028676

Paranicas, C., Mitchell, D. G., Roussos, E., Kollmann, P., Krupp, N., Müller, A. L., Krimigis, S. M., Turner, F. S., Brandt, P. C., Rymer, A. M., Johnson, R. E., 2010, Transport of energetic electrons into saturn's inner magnetosphere, Journal of Geophysical Research: Space Physics, 115, doi:https://doi.org/10.1029/2010JA015853

Paranicas, C., Thomsen, M., Achilleos, N., Andriopoulou, M., Badman, S., Hospodarsky, G., Jackman, C., Jia, X., Kennelly, T., Khurana, K., Kollmann, P., Krupp, N., Louarn, P., Roussos, E., Sergis, N., 2016, Effects of radial motion on interchange injections at saturn, Icarus, 264, 342–351, doi:https://doi.org/10.1016/j.icarus.2015.10.002

Paranicas, C. P., Mauk, B. H., Krimigis, S. M., 1991, Pressure anisotropy and radial stress balance in the jovian neutral sheet, Journal of Geophysical Research, 96, 21 135–21 140, doi:10.1029/91ja01647

Parker, E. N., 1958, Dynamics of the Interplanetary Gas and Magnetic Fields., ApJ, 128, 664, doi:10.1086/146579

Pensionerov, I. A., Alexeev, I. I., Belenkaya, E. S., Connerney, J. E. P., Cowley, S. W. H., 2019, Model of jupiter's current sheet with a piecewise current density, Journal of Geophysical Research: Space Physics, 124, 1843–1854, doi:https://doi.org/10.1029/2018JA026321

Pollock, C., C:son-Brandt, P., Burch, J., Henderson, M., Jahn, J.-M., McComas, D., Mende, S., Mitchell, D., Reeves, G., Scime, E., Skoug, R., Thomsen, M., Valek, P., 2003, The Role and Contributions of Energetic Neutral Atom (ENA) Imaging in Magnetospheric Substorm Research, vol. 109, pp. 155–182, doi:10.1023/B:SPAC.0000007518.93331.d5

Radioti, A., Grodent, D., Gerard, J. C., Bonfond, B., Clarke, J. T., 2008, Auroral polar dawn spots: signatures of internally driven reconnection processes at jupiter's magnetotail, Geophysical Research Letters, 35, L03 104, doi:10.1029/2007gl032460

Radioti, A., Grodent, D., Gérard, J. C., Roussos, E., Paranicas, C., Bonfond, B., Mitchell, D. G., Krupp, N., Krimigis, S., Clarke, J. T., 2009a, Transient auroral features at saturn: Signatures of energetic particle injections in the magnetosphere, Journal of Geophysical Research: Space Physics, 114, A03 210, doi:10.1029/2008JA013632

Radioti, A., Tomás, A. T., Grodent, D., Gérard, J. C., Gustin, J., Bonford, B., Krupp, N., Woch, J., Menietti, J. D., 2009b, Equatorward diffuse auroral emissions at jupiter: Simultaneous hst and galileo observations, Geophysical Research Letters, 36, L07 101, doi:10.1029/2009GL037857

Radioti, A., Grodent, D., Gérard, J. C., Bonfond, B., 2010, Auroral signatures of flow bursts released during magnetotail reconnection at jupiter, Journal of Geophysical Research: Space Physics, 115, A07 214, doi:10.1029/2009JA014844

Radioti, A., Roussos, E., Grodent, D., Gérard, J. C., Krupp, N., Mitchell, D. G., Gustin, J., Bonfond, B., Pryor, W., 2013, Signatures of magnetospheric injections in saturn's aurora, Journal of Geophysical Research: Space Physics, 118, 1922–1933, doi:10.1002/jgra.50161

Ray, L. C., Ergun, R. E., Delamere, P. A., Bagenal, F., 2010, Magnetosphere-ionosphere coupling at Jupiter: Effect of field-aligned potentials on angular momentum transport, Journal of Geophysical Research (Space Physics), 115, A09211, doi:10.1029/2010JA015423

Rodrigo, C., Solano, E., 2020, The SVO Filter Profile Service, in XIV.0 Scientific Meeting (virtual) of the Spanish Astronomical Society, p. 182

Roederer, J., 1970, Dynamics of geomagnetically trapped radiation, Springer, Heidelberg

Rymer, A. M., Mauk, B. H., Hill, T. W., Paranicas, C., André, N., Sittler, E. C., Mitchell, D. G., Smith, H. T., Johnson, R. E., Coates, A. J., Young, D. T., Bolton, S. J., Thomsen, M. F., Dougherty, M. K., 2007, Electron sources in Saturn's magnetosphere, Journal of Geophysical Research (Space Physics), 112, A02201, doi:10.1029/2006JA012017

Salveter, A., Saur, J., Clark, G., Mauk, B. H., 2022, Jovian Auroral Electron Precipitation Budget—A Statistical Analysis of Diffuse, Mono-Energetic, and Broadband Auroral Electron Distributions, Journal of Geophysical Research (Space Physics), 127, e30224, doi:10.1029/2021JA030224

Saur, J., 2004, Turbulent Heating of Jupiter's Middle Magnetosphere, ApJ, 602, L137–L140, doi: 10.1086/382588

Saur, J., Janser, S., Schreiner, A., Clark, G., Mauk, B. H., Kollmann, P., Ebert, R. W., Allegrini, F., Szalay, J. R., Kotsiaros, S., 2018, Wave-particle interaction of alfvén waves in jupiter's magnetosphere: Auroral and magnetospheric particle acceleration, Journal of Geophysical Research: Space Physics, 123, 9560–9573, doi:https://doi.org/10.1029/2018JA025948

Schulz, M., Lanzerotti, L., 1974, Particle diffusion in the radiation belt, vol. 7 of Physics and chemistry in space, Springer, New York, ISBN 3540063986

Siscoe, G. L., Summers, D., 1981, Centrifugally driven diffusion of iogenic plasma, Journal of Geophysical Research, 86, 8471–8479, doi:10.1029/JA086iA10p08471

Smith, E. J., Davis, L., J., Jones, D. E., 1976, Jupiter's magnetic field and magnetosphere, in IAU Colloq. 30: Jupiter: Studies of the Interior, Atmosp here, Magnetosphere and Satellites, (Eds.) T. Gehrels, S. Matthews, pp. 788–829

Southwood, D. J., Kivelson, M. G., 2001, A new perspective concerning the influence of the solar wind on the Jovian magnetosphere, J. Geophys. Res., 106, 6123–6130, doi:10.1029/2000JA000236

Sulaiman, A. H., Mauk, B. H., Szalay, J. R., Allegrini, F., Clark, G., Gladstone, G. R., Kotsiaros, S., Kurth, W. S., Bagenal, F., Bonfond, B., Connerney, J. E. P., Ebert, R. W., Elliott, S. S., Gershman, D. J., Hospodarsky, G. B., Hue, V., Lysak, R. L., Masters, A., Santolík, O., Saur, J., Bolton, S. J., 2022, Jupiter's Low-Altitude Auroral Zones: Fields, Particles, Plasma Waves, and Density Depletions, Journal of Geophysical Research (Space Physics), 127, e30334, doi:10.1029/2022JA030334

Sulaiman, A. H., Szalay, J. R., Clark, G., Allegrini, F., Bagenal, F., Brennan, M. J., Connerney, J. E. P., Hue, V., Kurth, W. S., Lysak, R. L., Nichols, J. D., Saur, J., Bolton, S. J., 2023, Poynting Fluxes, Field-Aligned Current Densities, and the Efficiency of the Io-Jupiter Electrodynamic Interaction, Geophys. Res. Lett., 50, e2023GL103456, doi:10.1029/2023GL103456

Swithenbank-Harris, B. G., Nichols, J. D., Allegrini, F., Bagenal, F., Bonfond, B., Bunce, E. J., Clark, G., Kurth, W. S., Mauk, B. H., Wilson, R. J., 2021, Simultaneous observation of an auroral dawn storm with the hubble space telescope and juno, Journal of Geophysical Research: Space Physics, 126, e2020JA028 717, doi:https://doi.org/10.1029/2020JA028717

Szalay, J. R., Bonfond, B., Allegrini, F., Bagenal, F., Bolton, S., Clark, G., Connerney, J. E. P., Ebert, R. W., Ergun, R. E., Gladstone, G. R., Grodent, D., Hospodarsky, G. B., Hue, V., Kurth, W. S.,

Kotsiaros, S., Levin, S. M., Louarn, P., Mauk, B., McComas, D. J., Saur, J., Valek, P. W., Wilson, R. J., 2018, In Situ Observations Connected to the Io Footprint Tail Aurora, Journal of Geophysical Research (Planets), 123, 3061–3077, doi:10.1029/2018JE005752

Taylor, F. W., Atreya, S. K., Encrenaz, T., Hunten, D. M., Irwin, P. G. J., Owen, T. C., 2007, The Composition of the Atmosphere of Jupiter, in Jupiter, p. 59

Thomsen, M. F., Van Allen, J. A., 1980, Motion of trapped electrons and protons in saturn's inner magnetosphere, Journal of Geophysical Research: Space Physics, 85, 5831–5834, doi:https://doi.org/10.1029/JA085iA11p05831

Tomás, A. T., Woch, J., Krupp, N., Lagg, A., Glassmeier, K. H., Kurth, W. S., 2004, Energetic electrons in the inner part of the Jovian magnetosphere and their relation to auroral emissions, Journal of Geophysical Research (Space Physics), 109, A06203, doi:10.1029/2004JA010405

Tsuchiya, F., Kagitani, M., Yoshioka, K., Kimura, T., Murakami, G., Yamazaki, A., Nozawa, H., Kasaba, Y., Sakanoi, T., Uemizu, K., Yoshikawa, I., 2015, Local electron heating in the Io plasma torus associated with Io from HISAKI satellite observation, Journal of Geophysical Research (Space Physics), 120, 10,317–10,333, doi:10.1002/2015JA021420

Vasyliūnas, V. M., 2004, Comparative magnetospheres: lessons for Earth, Advances in Space Research, 33, 2113–2120, doi:10.1016/j.asr.2003.04.051

Vasyliūnas, V. M., 1983, Plasma distribution and flow, Cambridge University Press

Vogt, M. F., Kivelson, M. G., Khurana, K. K., Joy, S. P., Walker, R. J., 2010, Reconnection and flows in the jovian magnetotail as inferred from magnetometer observations, Journal of Geophysical Research: Space Physics, 115, A06 219, doi:10.1029/2009JA015098

Vogt, M. F., Kivelson, M. G., Khurana, K. K., Walker, R. J., Bonfond, B., Grodent, D., Radioti, A., 2011, Improved mapping of Jupiter's auroral features to magnetospheric sources, Journal of Geophysical Research (Space Physics), 116, A03220, doi:10.1029/2010JA016148

Vogt, M. F., Bunce, E. J., Kivelson, M. G., Khurana, K. K., Walker, R. J., Radioti, A., Bonfond, B., Grodent, D., 2015, Magnetosphere-ionosphere mapping at Jupiter: Quantifying the effects of using different internal field models, Journal of Geophysical Research (Space Physics), 120, 2584–2599, doi:10.1002/2014JA020729

Woodgate, B. E., Kimble, R. A., Bowers, C. W., Kraemer, S., Kaiser, M. E., Danks, A. C., Grady, J. F., Loiacono, J. J., Brumfield, M., Feinberg, L., Gull, T. R., Heap, S. R., Maran, S. P., Lindler, D., Hood, D., Meyer, W., Vanhouten, C., Argabright, V., Franka, S., Bybee, R., Dorn, D., Bottema, M., Woodruff, R., Michika, D., Sullivan, J., Hetlinger, J., Ludtke, C., Stocker, R., Delamere, A., Rose, D., Becker, I., Garner, H., Timothy, J. G., Blouke, M., Joseph, C. L., Hartig, G., Green, R. F.,

Jenkins, E. B., Linsky, J. L., Hutchings, J. B., Moos, H. W., Boggess, A., Roesler, F., Weistrop, D., 1998, The Space Telescope Imaging Spectrograph Design, PASP, 110, 1183–1204, doi:10.1086/316243

Xu, C., Prince, J. L., 1998, Snakes, shapes, and gradient vector flow, IEEE Transactions on Image Processing, 7, 359–369, doi:10.1109/83.661186

Yang, Y. S., Wolf, R. A., Spiro, R. W., Hill, T. W., Dessler, A. J., 1994, Numerical simulation of torus-driven plasma transport in the jovian magnetosphere, Journal of Geophysical Research: Space Physics, 99, 8755–8770, doi:10.1029/94JA00142

Yao, Z., Rae, I. J., Lui, A. T. Y., Murphy, K. R., Owen, C. J., Pu, Z. Y., Forsyth, C., Grodent, D., Zong, Q. G., Du, A. M., Kalmoni, N. M. E., 2017, An explanation of auroral intensification during the substorm expansion phase, Journal of Geophysical Research (Space Physics), 122, 8560–8576, doi:10.1002/2017JA024029

Yao, Z. H., Bonfond, B., Clark, G., Grodent, D., Dunn, W. R., Vogt, M. F., Guo, R. L., Mauk, B. H., Connerney, J. E. P., Levin, S. M., Bolton, S. J., 2020, Reconnection- and Dipolarization-Driven Auroral Dawn Storms and Injections, Journal of Geophysical Research (Space Physics), 125, e27663, doi:10.1029/2019JA027663

Yelle, R. V., Miller, S., 2007, Jupiter's Thermosphere and Ionosphere, in Jupiter, p. 185

Yoshikawa, I., Suzuki, F., Hikida, R., Yoshioka, K., Murakami, G., Tsuchiya, F., Tao, C., Yamazaki, A., Kimura, T., Kita, H., Nozawa, H., Fujimoto, M., 2017, Volcanic activity on Io and its influence on the dynamics of the Jovian magnetosphere observed by EXCEED/Hisaki in 2015, Earth, Planets and Space, 69, 110, doi:10.1186/s40623-017-0700-9

Yoshioka, K., Tsuchiya, F., Kimura, T., Kagitani, M., Murakami, G., Yamazaki, A., Kuwabara, M., Suzuki, F., Hikida, R., Yoshikawa, I., Bagenal, F., Fujimoto, M., 2017, Radial variation of sulfur and oxygen ions in the Io plasma torus as deduced from remote observations by Hisaki, Journal of Geophysical Research (Space Physics), 122, 2999–3012, doi:10.1002/2016JA023691

Yoshioka, K., Tsuchiya, F., Kagitani, M., Kimura, T., Murakami, G., Fukuyama, D., Yamazaki, A., Yoshikawa, I., Fujimoto, M., 2018, The Influence of Io's 2015 Volcanic Activity on Jupiter's Magnetospheric Dynamics, Geophys. Res. Lett., 45, 10,193–10,199, doi:10.1029/2018GL079264

Yung, Y. L., Gladstone, G. R., Chang, K. M., Ajello, J. M., Srivastava, S. K., 1982, H2 fluorescence spectrum from 1200 to 1700 A by electron impact - Laboratory study and application to Jovian aurora, ApJ, 254, L65–L69, doi:10.1086/183757

Zhang, B., Delamere, P. A., Yao, Z., Bonfond, B., Lin, D., Sorathia, K. A., Brambles, O. J., Lotko, W., Garretson, J. S., Merkin, V. G., Grodent, D., Dunn, W. R., Lyon, J. G., 2021, How jupiter's unusual

magnetospheric topology structures its aurora, Science Advances, 7, eabd1204, doi:10.1126/sciadv.abd1204

Acknowledgements

Ca fait déjà un petit temps que je pense à ces remerciements. Ne voulant oublier personne, j'ai écrit dans un petit carnet, dès que j'avais une idée ou une personne qui me venait à l'esprit. Mais le nombre de personnes, qui ont d'une manière ou d'une autre fait partie de ma vie de thésarde, est vite devenu faramineux. J'ai alors décidé de taire vos noms, mais chacun de vous se reconnaitra, j'en suis certaine.

Et nous y voilà, au moment où je me rends compte que l'aventure se finit et où l'émotion me submerge. J'avais tellement la tête dans le guidon ces derniers mois, avec pour seul objectif de finir ma thèse, que j'en ai oublié que j'allais vous quitter. On dit que le bonheur est le chemin et non pas la destination. Vous avez été mon bonheur sur le chemin, vous avez été mon refuge, mon exutoire, ma salle de jeux quand j'en avais besoin et grâce à vous j'ai grandi. Enfin, les mauvaises langues diront que j'ai vieilli.

Cette aventure n'était pas gagnée d'avance, et j'ai eu besoin du soutien et de la confiance de celui qui a été au cours toutes ces années mon guide scientifique. Jamais sur mes talons mais jamais bien loin non plus car dès que j'avais besoin de lui, il était là toujours bienveillant et compréhensif malgré mes exubérances. J'ai pu également m'appuyer sur d'autres

bonnes âmes, de celles qui ne ferment jamais la porte même si les questions sont redondantes ou naïves. Vous m'avez mis la pression quand il le fallait et poussée dans mes retranchements pour mon bien. Vous connaissiez le chemin vous y étiez passés avant moi, vous connaissiez les doutes, les épreuves et l'excitation que je traversais.

Et puis, il y a eu tous les autres collègues de l'AGO et de la physique : les oreilles attentives, les épaules compatissantes, les camarades pour le commérage, les collègues devenus des amis inestimables. Nous avons partagé des bouts de vie dans les bons moments, comme les moins bons. Bien au-delà de votre aide apportée au cours de ces nombreuses années, vous vous êtes fait une place dans mon cœur.

Merci à mon "pré-relecteur" en chef, celui qui a sacrifié ses week-ends et ses soirées d'été pour relire ce que j'appelais mon torchon. Ton aide a été très précieuse.

Je voudrais remercier mes amis et les deux femmes indispensables à ma vie avec qui je partage un bout d'ADN. Vous m'avez offert, en cette fin de thèse, votre aide mais surtout des moments de déconnection, des moments hors du temps, de ceux qu'on garde précieusement en nous pour nous réchauffer le cœur les jours de pluie.

Et enfin, il y a vous trois : les « mannekes » de la maison. Vous m'avez supportée et soutenue pendant mes échecs et mes excès de folie. Les plus petits m'ont permis de garder les pieds sur terre et toi tu m'as permis de m'évader dès que j'en avais besoin. Je vous aime.

Merci !

Maïté Dumont : Ultraviolet auroral emissions associated with plasma injections in Jupiter's magnetosphere